EVALUATION OF BIOFIDELITY & REPEATABILITY AND THE INFLUENCE OF DIFFERENT POSITIONING FOR THOR-NT DUMMY

Masayuki Yaguchi
Koshiro Ono
Japan Automobile Research Institute
Japan
Mitsutoshi Masuda
Japan Automobile Manufacturers Association
Japan
Paper Number 07-0286

ABSTRACT

Component tests on the head, neck, thorax, abdomen and face were conducted to evaluate the biofidelity of THOR-NT. HYGE sled tests were also conducted to evaluate repeatability and to investigate the influence of different positioning to dummy responses.
Three frontal HYGE sled tests were conducted under the same conditions with a velocity of 56km/h, acceleration of 270m/s^2, and a designed standard seat position.
Repeatability of dummy responses was evaluated by coefficient of variation (CV) calculated based on the peak values of accelerations, deflections, forces and moments measured. The following three categories were defined as evaluation criteria of repeatability by CV: CV<=5% as good, CV<=10% as acceptable and CV>10% as poor.
The kinematic and dynamic responses of THOR-NT were additionally compared with that of Hybrid-III.
Furthermore, in order to investigate the influence of different positioning to dummy responses, a 56km/h frontal HYGE sled test was conducted on a dummy positioned according to the ATD positioning procedure developed by UMTRI.

In the biofidelity evaluation, only head responses were within the PMHS response corridors.
For repeatability, 10 (32%) out of 31 items in all of the data had an evaluation criteria within CV<=5%. Comparison of dummy responses between UMTRI and standard positioning showed similarity in kinematic responses of the upper body. However, the maximum displacement of ankle in X-direction with respect to the initial position was larger in the UMTRI position compared to the standard position.
In the UMTRI position, the feet which are initially positioned away from the toe board comes in contact with the toe board and slide upward due to the forward movement to the vehicle body during impact. Due to this, difference in dynamic responses of the legs between the UMTRI and standard position was observed.

INTRODUCTION

In October 2003, NHTSA (National Highway Traffic Safety Administration) had released the THOR-NT (Test Device for Human Occupant Restraint - New Technology) as the next generation frontal impact dummy. Almost at the same time, the THOR-FT was also released by the FID (World Frontal Impact Dummy), the European project. Here, FT means "FID Technology."
Although both of these dummies were developed from THOR-alpha, several components of each dummy have been individually improved. Therefore, it is our concern that the responses of these dummies against the impact may differ with each other. If such original development and improvement continue at this pace, two different types will eventually appear as next generation dummies.
Therefore, the harmonization of THOR dummies is now being sought in earnest. From such a background, SAE THOR Evaluation Task Force Group was established in order to harmonize the specifications such as structures and characteristics that are required for dummy. Efforts aimed at the harmonization of two THOR dummies have started.
In order to contribute to the harmonization of THOR dummies, the biofidelity of THOR-NT was evaluated in this study. Furthermore, the repeatability on the responses of THOR-NT in dynamic tests using HYGE sled and the influence on the dummy responses by the different dummy positioning was evaluated.

METHODS

Biofidelity Tests

Biofidelity evaluation tests on the head, neck, thorax, abdomen and face were conducted in accordance with test

procedures for THOR determined by NHTSA and GESAC (General Engineering and Systems Analysis Company), Inc. [1], [2], and responses were compared with PMHS (Post Mortem Human Subjects) response corridors.

Head

Head Drop Test - As shown in Figure 1 a), only the head of the dummy was hanged so that the lowest point on the forehead was held 376 mm above the impact plane, and the base of the head-neck mounting platform was inclined at 29 degrees against the vertical line. Then, free fall of the head was performed onto the horizontal rigid plane. The results were evaluated by the peak of 3-axial resultant acceleration of head center of gravity and its occurrence time.

Head Impact Test - The dummy was sat on a flat plane, and the head of the dummy was hit by the impactor with a mass of 23.4 kg and diameter of 152 mm at a speed of 2.0 m/s. The impact point was where the center-line of the impactor is 30 mm above the horizontal marking line at the lowest point of the forehead (Figure 2 b)). The biofidelity evaluation parameters of this head impact test were the peak of the impact force and its occurrence time.

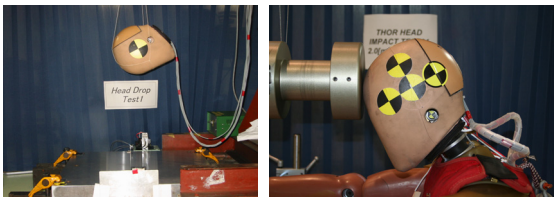

a) Drop test b) Impact test

Figure 1. Setup of biofidelity tests on the head

Neck

Neck Frontal Flexion Test - The head and neck of the dummy are fixed on the HYGE sled by means of fixed attachment as shown in Figure 2, and the dynamic and kinematic responses of the neck at the specified sled pulse were evaluated [3].

With regard to the mini-sled test for the neck in frontal flexion, the correct sled pulse which should be given is the pulse (T1 pulse) as shown in Figure 3. However, since our sled apparatus did not have the ability to generate such complex pulse, the sled pulse (15G) which was used in volunteer testing at the NBDL (Naval Biodynamics Laboratory) as shown in Figure 4 was used in this study.

The evaluation parameters were head rotation angle, resultant acceleration of head center of gravity, back-forth and up-down kinematic displacements and neck moment around Y-axis with respect to the head rotation angle.

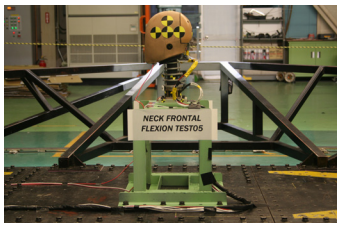

Figure 2. Setup of neck frontal flexion test

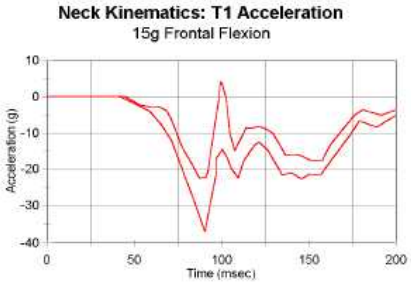

Figure 3. Mini-sled pulse (T1 pulse) in the neck frontal flexion

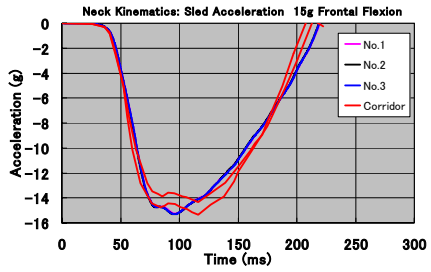

Figure 4. 15G sled pulse in frontal flexion of NBDL

Neck Lateral Flexion Test - Just like the setup of the neck frontal flexion test, the head and neck of the dummy were fixed on the HYGE sled by means of a fixed attachment. The dynamic and kinematic responses of the neck at the specified sled accelerations were evaluated.

With regard to the mini-sled test for the neck in lateral flexion, the correct sled pulse which should be given is the pulse (T1 pulse) as shown in Figure 5. However, since our sled apparatus did not have the ability to generate such complex pulse, the sled pulse (7G) which was used in volunteer testing at the NBDL as shown in Figure 6 was used in this study.

The evaluation parameters were head rotation angle, right-left and up-down kinematic displacements of head center of gravity, and neck moment around X-axis with respect to the head rotation angle.

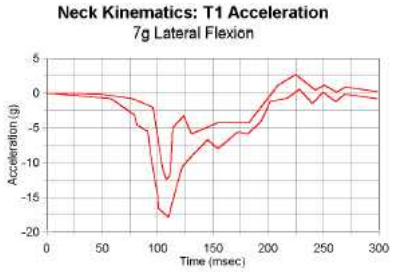

Figure 5. Mini-sled pulse (T1 pulse) in the neck lateral flexion

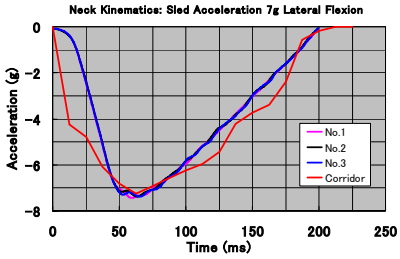

Figure 6. 7G sled pulse in lateral flexion of NBDL

Thorax

Kroell Test - The dummy was sat on a flat plane, and the thorax of the dummy was hit by the impactor with a mass of 23.4 kg and diameter of 152 mm at 4.3m/s and 6.7m/s. The impact point was where the center line of the impactor coincides with the vertical level of the middle of dummy rib #3, and positioned over the mid-line of the sternum (Figure 7). The biofidelity evaluation parameter was the response of impact force versus thorax deflection.

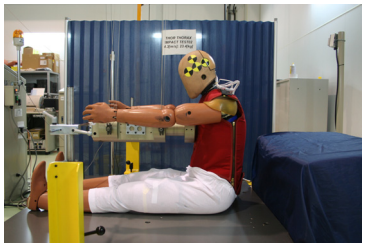

Figure 7. Setup of Kroell test

Abdomen

Upper Abdomen Impact Test - The dummy was sat on a flat plane, and the upper abdomen of the dummy was hit by the rigid steering wheel impactor with a mass of 18 kg and angle against the vertical line of 30 degrees at 8.0m/s. The impact point was where the leading edge of the steering wheel coincides with the center of the seventh rib (Figure 8 a)).

Lower Abdomen Impact Test - The dummy was sat on a flat plane, and the lower abdomen of the dummy was hit by the rigid impactor with a mass of 32 kg, diameter of 25 mm, and length of 300 mm at 6.1m/s. The impact point was where the center line of the impactor coincided with the vertical level of the line joining the centers of the attachment nuts of the right and left DGSPs and aimed at the mid-point of this line (Figure 8 b)).

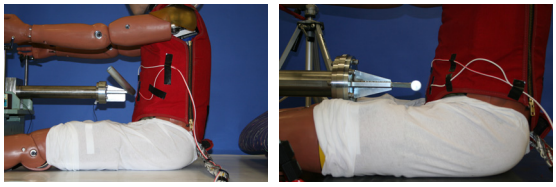

a) Upper abdomen b) Lower abdomen

Figure 8. Setup of biofidelity tests on the abdomen

Face

Disk Impact Test - The dummy was sat on a flat plane, and the face of the dummy was hit by the impactor with a mass of 13 kg and diameter of 152 mm at a speed of 6.7 m/s. The center of the disk was configured to impact at the mid-point of the line joining the two maxilla plates on the face (Figure 9 a)).

Rigid Bar Impact Test - The dummy was sat on a flat plane, and the face of the dummy was hit by the rigid bar impactor with a mass of 32 kg, diameter of 25 mm, and length of 300 mm at a speed of 3.6 m/s. The rod was configured to impact along the mid-line of the left and right maxilla plates on the face (Figure 9 b)).

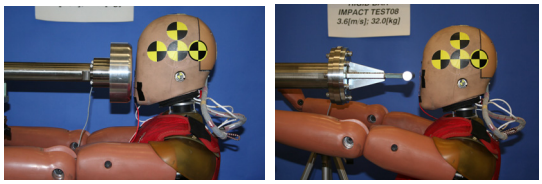

a) Disk impact b) Rigid bar impact

Figure 9. Setup of biofidelity tests on the face

HYGE Sled Tests

The white-body of a passenger car was fixed on the sled and the white-body which seated the dummy was given an impact at 35 mph (56 km/h). The accelerations and forces, etc of the dummy was measured by each sensor. The motion of the dummy was recorded by high speed video cameras and analyzed. Figure 10 indicates the acceleration curve and the velocity curve of the sled.

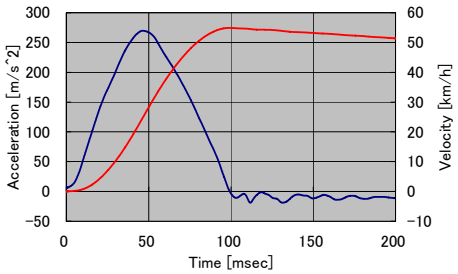

Figure 10. Acceleration and velocity of the sled

Measurements - The accelerations and forces, etc of the dummy were measured. These data were recorded by the data acquisition system attached to the sled and were filtered based on SAE J211 [4]. The behavior of the dummy was recorded by three high speed video cameras from the side view of the sled, and the motion of the target mark of each component of the dummy was analyzed.

Test Conditions

a) Evaluation of Repeatability - In order to evaluate the repeatability of the dynamic responses of THOR-NT, three tests were conducted under the same conditions. The dummy was set according to the positioning procedure for Hybrid-III specified in FMVSS 208 (Federal Motor Vehicle Safety Standard No. 208, Occupant Crash Protection) [5]. The dummy seating position, the seat position, and the restraint devices were as follows:

1) The dummy seating position: driver's seat
2) The seat slide position: at the mid position
3) The seat lifter position: at the lowest position
4) The seat back position: at the designed standard position
5) Restraint devices: airbag, and seatbelt with pretensioner and force limiter

Hereafter, this seat position is called "standard position".

b) Investigation on the influence of different positioning to dummy responses - In order to investigate the influence of different positioning to dummy responses, tests were conducted on a dummy positioned according to the ATD positioning procedure, developed by UMTRI (University of Michigan Transportation Research Institute) [6]. The positioned posture and response of the dummy in this test were compared with those in the tests to evaluate repeatability. The seating position of dummy, the seat position, and the restraint device were as follows:

1) The seating position of dummy: driver's seat
2) The position of the seat slide: 50 mm rearward from the middle position
3) The position of the seat lifter: 18 mm above the lowest position
4) The position of the seat back: a designed standard position
5) Restraint device: a seatbelt with force limiter and pretensioner, and an airbag

Hereafter, this seat position is called "UMTRI position".

Definition for Evaluation of Repeatability - The repeatability of the dynamic responses of the dummy was evaluated by means of coefficients of Variation (CV). As shown in (Equation 1), CV is the percentile of the standard deviation of the peak value of data which measured in three tests divided by the average of those. In addition, it can be considered that CV equal to or less than 5% is "Good", equal to or less than 10% is "Acceptable", and exceeding 10% is "Poor" [7].

$$CV = \left[\frac{S}{\bar{X}}\right] * 100\ (\%) \qquad (1)$$

S : Standard deviation of the measured peak value

$\bar{X}$: Average of the measured peak value

RESULTS

Biofidelity Tests

Biofidelity on the head, neck thorax abdomen and face were compared with PMHS response corridors.

Head

Head Drop Test - Figure 11 indicates the results of the head drop test. The method of biofidelity test and that of certification test are the same [1], [2]. However, since the corridors of these tests were different, both biofidelity corridor and certification corridor are shown in this figure. The responses of the head were within the range of biofidelity corridor in all three tests, indicating good repeatability. However, with regard to certification corridor, the peak occurrence time of the head resultant acceleration was out of the corridor.

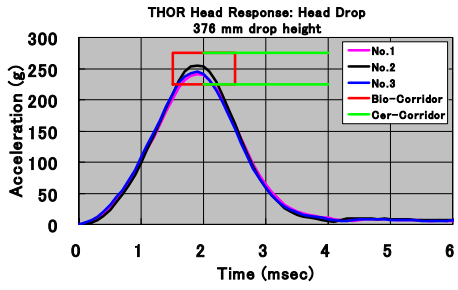

Figure 11. Response on head drop

Head Impact Test - Figure 12 indicates the results of the head impact test. The method of biofidelity test and that of certification test are the same [1], [2]. However, since the corridors of these tests were different, both biofidelity corridor and certification corridor are shown in this figure.

With regard to the repeatability, the results of No. 2 and No. 3 were quite similar, whereas the undulation of No. 1 rose up more gently, and the peak occurrence time of the impact force of No. 1 was slightly late. It can be presumed that this difference stemmed from a little variation of the test setup such as the sitting posture of the dummy and the impact position. However, in all the three tests, responses were within the biofidelity corridor and certification corridor.

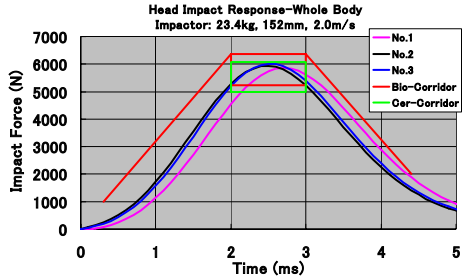

Figure 12. Response on head impact

Neck

Neck Frontal Flexion Test - Figure 13 to Figure 17 respectively indicates the results of the neck frontal flexion tests concerning following evaluation items:

1) Head rotation angle (Figure 13)
2) 3-axial resultant acceleration of head center of gravity (Figure 14)
3) Kinematic displacement of head center of gravity in the X-direction (back-forth) (Figure 15)
4) Kinematic displacement of head center of gravity in the Z-direction (up-down) (Figure 16)
5) Neck moment around Y-axis (My) with respect to the head rotation angle (Figure 17)

The results indicate that the responses were outside the corridors in all the evaluation items. With regard to the sled acceleration corridor, the sled does not accelerate at time 0 and begins to accelerate at around 20 to 30 ms as shown in Figure 4. On the other hand, biofidelity corridors of neck begin to respond at around 50 to 80 ms. Therefore, in the tests conducted in this study, although the sled actually began to accelerate at time 0, the time 0 of the test data was shifted so that it could be synchronized with the sled acceleration corridor. Likewise, time 0 of the dummy data was also shifted in order to synchronize with the time shift of the sled acceleration data. However, the results in all the evaluation items were outside the corridors. Note: These results take notices that were responses where not T1 pulse but 15 G sled pulse of NBDL was used.

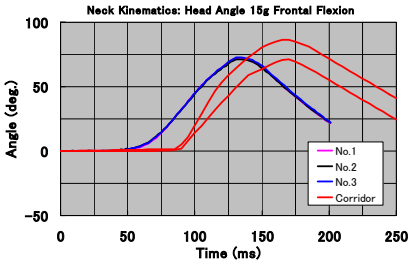

Figure 13. Head rotation angle

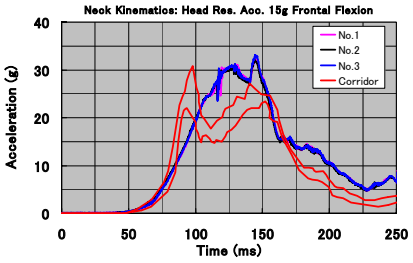

Figure 14. 3-axial res. acceleration of head C.G.

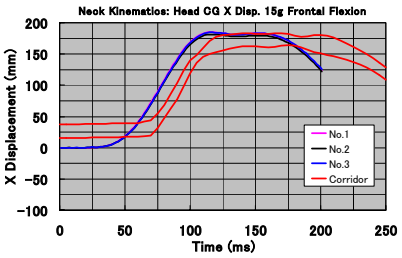

Figure 15. Disp. of head C.G. in the X-direction

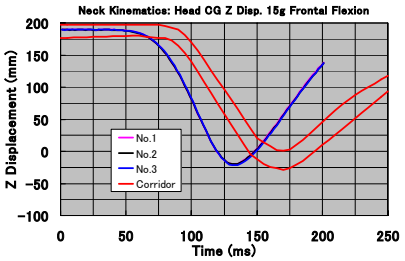

Figure 16. Disp. of head C.G. in the Z-direction

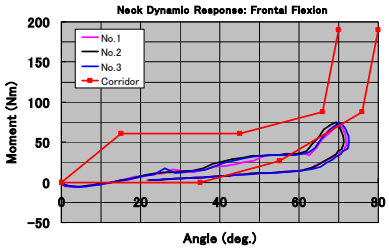

Figure 17. Neck moment around Y-axis (My) w.r.t. the head rotation angle

Neck Lateral Flexion Test - Figure 18 to Figure 21 respectively indicates the results of the neck lateral flexion tests concerning the following evaluation items:

1) Head rotation angle (Figure 18)
2) Kinematic displacement of head center of gravity in the Y-direction (right-left) (Figure 19)
3) Kinematic displacement of head center of gravity in the Z-direction (up-down) (Figure 20)
4) Neck moment around X-axis (Mx) with respect to the head rotation angle (Figure 21)

The results indicate that the responses were outside the corridors in all the evaluation items. In particular, the Y and Z-direction displacements of the head C.G. deviated from these corridors. However, these results take notices that were responses where not T1 pulse but 7 G sled pulse of NBDL was used.

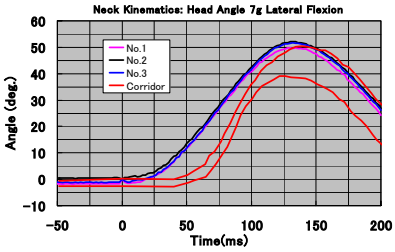

Figure 18. Head rotation angle

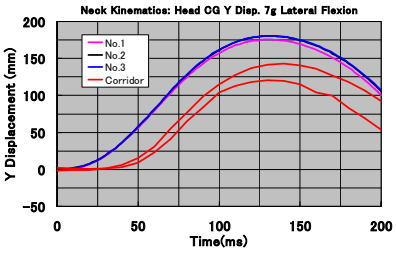

Figure 19. Disp. of head C.G. in Y-direction

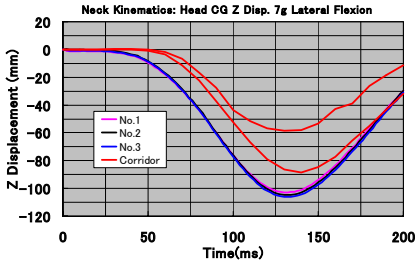

Figure 20. Disp. of head C.G. in Z-direction

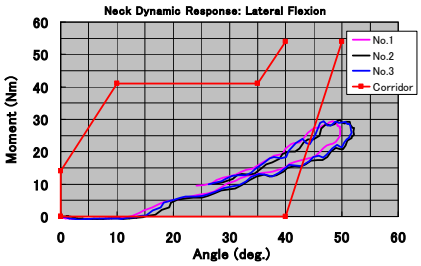

Figure 21. Neck moment around X-axis w.r.t. head rotation angle

Thorax

Kroell Test - Figure 22 indicates the results of the Kroell test at 4.3m/s. In the Kroell test, the method of biofidelity test and that of certification test were the same [1], [2]. However, since the corridors of these tests are different, both biofidelity corridor and certification corridor are shown in this figure.

The repeatability of the three tests was good; however, all of them deviated from both the biofidelity corridor and the certification corridor. It can be presumed that the reason why chest deflection was smaller than that of the corridor was because when the thorax of the dummy was hit, the lowest point of the impactor may have come in contact with its upper abdomen and thereby the intrusion of the impactor may have been restricted.

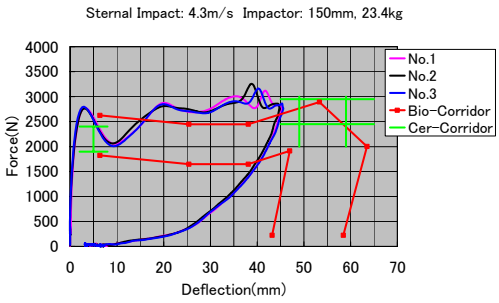

Figure 22. Response of Kroell test at 4.3m/s

Figure 23 indicates the results of the Kroell test at 6.7m/s. The repeatability of the three tests was good. Although

the response near the maximum impact force greatly deviated from the biofidelity corridor, the response approximately fell within the corridor at the deflection of 0 to 60 mm. On the other hand, the response fell within both the first and the second certification corridors. However, as shown in this figure, the impact force suddenly increased at approximately 55 mm of the chest deflection. It can be presumed that because there were vestiges that indicate the contact between the mid sternum mass assembly and the spine (Figure 24), the impact force suddenly increased due to the metal contact caused by bottoming out of thorax.

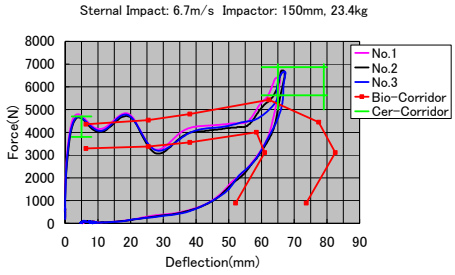

Figure 23. Response of Kroell test at 6.7m/s

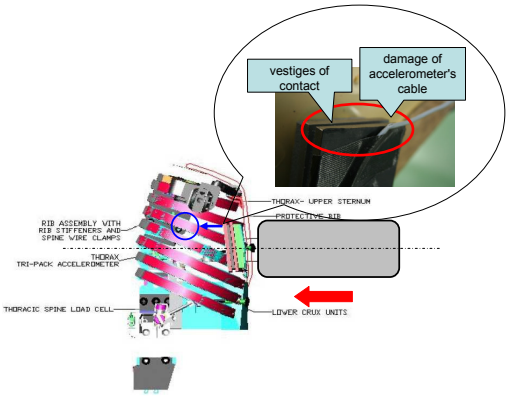

Figure 24. Vestiges of contact between mid sternum mass assembly and spine

Abdomen

Upper Abdomen Impact Test - Figure 25 indicates the results of the upper abdomen impact test. The response on deflection from 50 to 100 mm was within biofidelity corridor, but force on deflection at 120 mm was greater than biofidelity corridor. Therefore, it was found that the upper abdomen of THOR-NT had stiffer characteristics than that of a human body.

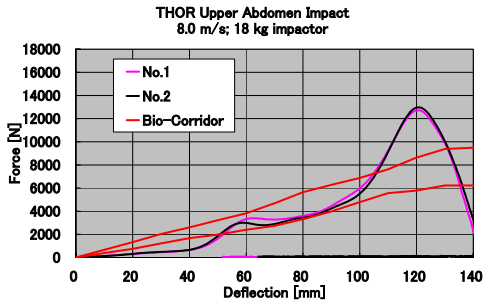

Figure 25. Response of upper abdomen impact

Lower Abdomen Impact Test - Figure 26 indicates the results of the lower abdomen impact test. The response on deflection from 0 to 100 mm was within biofidelity corridor, but force on deflection at 120 mm was far greater than biofidelity corridor. Therefore, it was found that the lower abdomen of THOR-NT had stiffer characteristics than that of a human body.

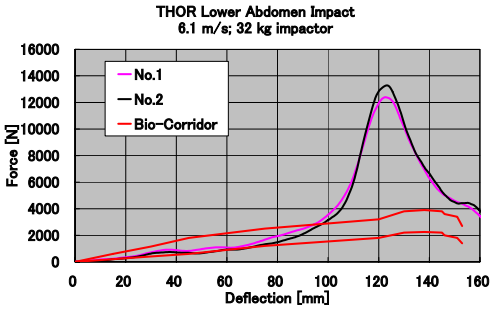

Figure 26. Response of lower abdomen impact

Face

Disk Impact Test - Figure 27 indicates the results of the face disk impact test. In the face disk impact test, the method of biofidelity test and that of certification test were the same [1], [2]. However, since the corridors of these tests are different, both biofidelity corridor and certification corridor are shown in this figure.

Not only the early section of response slightly deviated from the biofidelity corridor, but also the peak impact force was higher than the corridor. In addition, the peak impact force was also higher than certification corridor.

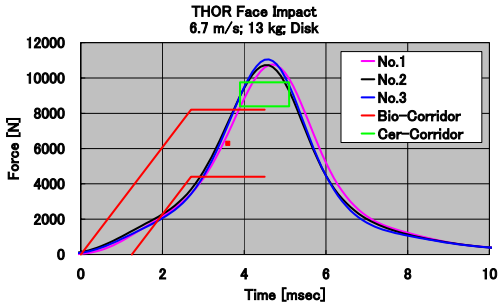

Figure 27. Response of face disk impact

Rigid Bar Impact Test - Figure 28 indicates the results of the face rigid bar impact test. In the face rigid bar impact test, the method of biofidelity test and that of certification test were the same [1], [2]. However, since the corridors of these tests are different, both biofidelity corridor and certification corridor are shown in this figure. The results of all the three tests greatly deviated from biofidelity corridor, and the peak impact force was higher than that of the certification corridor.

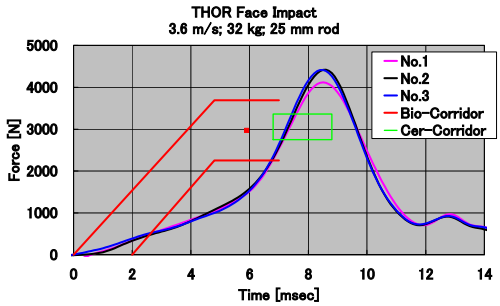

Figure 28. Response of face rigid bar impact

HYGE Sled Tests

In this chapter, it states the results of the evaluation on repeatability of dynamic responses for THOR-NT, and the results of the investigation on influence on responses by the difference of dummy positioning. Furthermore, it states the results of the dynamic and kinematic responses compared between THOR-NT and Hybrid-III.

Positioning of Dummy

Figure 29 indicates the comparison of the positioning of the head, shoulder, hip point (H.P.), knee, and ankle in the three tests on the standard position and one test on the UMTRI position, for THOR-NT. In addition, the positioning in one test on the standard position for Hybrid-III is plotted in this figure.

The repeatability of THOR-NT positioning was good. Even at the maximum, difference in positioning of the head in the vertical direction was only 12 mm.

Comparing the UMTRI position with the average of three tests in the standard position, in the X-direction, the difference of H.P. was the largest, namely, the H.P. in the UMTRI position was positioned 43 mm rearward with respect to that in the standard position. In the Z-direction, the difference of the shoulder was the largest, namely, the shoulder in the UMTRI position was positioned 37 mm above with respect to that in the standard position.

Comparing the positioning of THOR-NT with that of Hybrid-III on the standard position, in the X-direction, the H.P. of THOR-NT was approximately close position to that of Hybrid-III, but the head of THOR-NT was more rearward than that of Hybrid-III while the knee of THOR-NT was more forward than that of Hybrid-III. In the Z-direction, on the whole, each component of THOR-NT was positioned above than that of Hybrid-III.

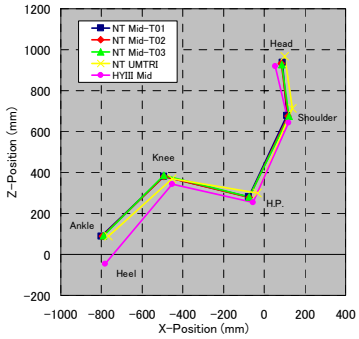

Figure 29. Comparison of the positioning among THOR-NT/Hybrid-III on the standard position, and THOR-NT on the UMTRI position

Kinematic Response

Figure 30 indicates the behavior of each component of the dummy in the three tests on the standard position and one test on the UMTRI position, for THOR-NT. Furthermore, the behavior in one test on the standard position for Hybrid-III is drawn in this figure.

The behavior of THOR-NT was quite similar in the three tests on the standard position. However, as for the head, whose maximum displacement was the most different, the maximum difference in the three tests was 35 mm in both back-forth and up-down directions. As for the other components, the difference in the back-forth direction was 8 to 16 mm, and that in up-down direction was 3 to 6 mm.

The behavior in the UMTRI position and that in the standard position were similar, comparing the kinematics of each part of THOR-NT. However, with regard to the difference in the maximum displacements (X, Z) with

respect to the initial position, there were (31mm, 17mm) at the head, (2mm, 3mm) at the shoulder, (2mm, 7mm) at the H.P., (13mm, 10mm) at the knee, and (46mm, 14mm) at the ankle. The difference in the maximum displacement of the ankle in X-direction was the largest.

Comparing the behavior of THOR-NT with that of Hybrid-III on the standard position, both behavior was similar. However, the forward displacements of the head and shoulder for THOR-NT were larger than that of Hybrid-III. Furthermore, since the knee of THOR-NT was initially positioned on the forward and the upward to that of Hybrid-III, the knee of THOR-NT came hard in contact with instrument panel, compared with Hybrid-III.

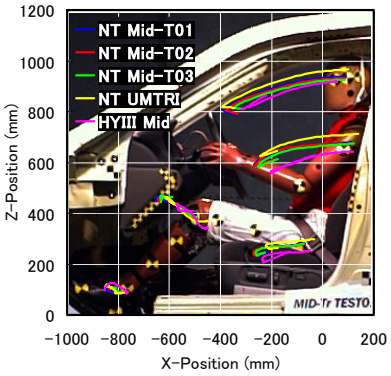

Figure 30. Comparison of the behavior among THOR-NT/Hybrid-III on the standard position, and THOR-NT on the UMTRI position

Dynamic Response

Acceleration Response - Figure 31 indicates the acceleration responses of the dummies' head, thorax, and pelvis. In each of these three components, the acceleration appearance, duration, and the peak value were quite similar in the three tests for THOR-NT. The occurrence situation and duration of acceleration were also similar for the standard position and the UMTRI position. Furthermore, the acceleration responses were also similar between THOR-NT and Hybrid-III.

Figure 32 indicates HIC36 ms and clip 3msG on the head acceleration, and Figure 33 indicates clip 3msG on the chest acceleration and maximum 3-axial resultant acceleration of pelvis. The average (Ave.) ± standard deviation (S.D.), and CV of the data of the three tests is also shown in these figures. The clip 3msG of the head (CV=1.7%) and pelvis acceleration (CV=1.9%) were approximately the same in the three tests. On the other hand, HIC36ms (CV=8.7%) and the clip 3msG of the chest (CV=5.8%) increased in repeated tests.

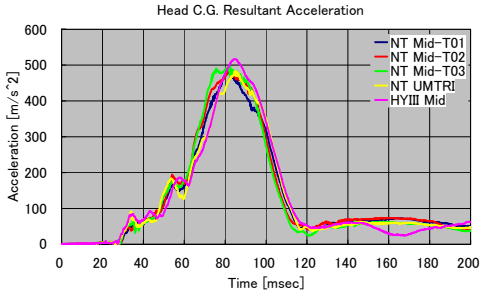

a) Head resultant acceleration

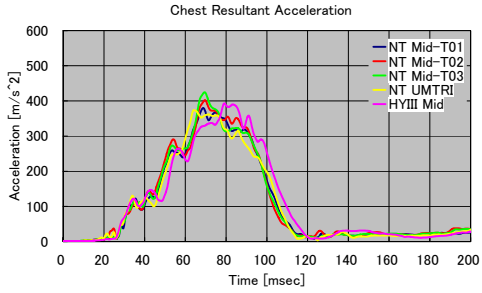

b) Chest resultant acceleration

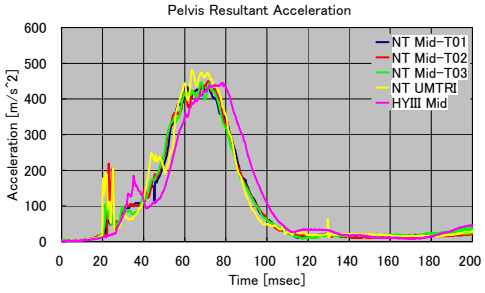

c) Pelvis resultant acceleration

Figure 31. Acceleration responses of the head, thorax, and pelvis

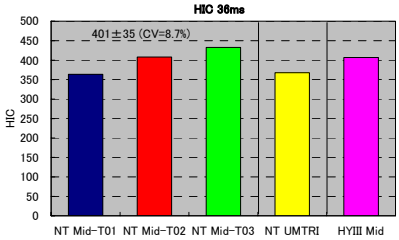

a) HIC36ms

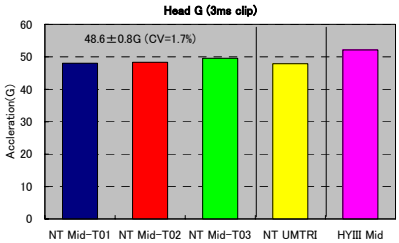

b) Clip 3ms G of head

Figure 32. Injury Criteria of the head, and CV

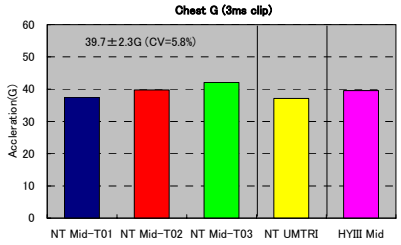

a) Clip 3ms G of chest

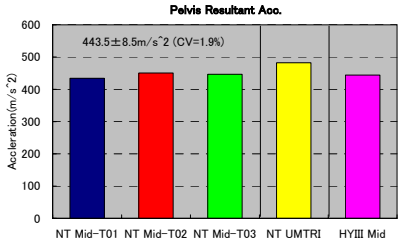

b) Peak acceleration of pelvis

Figure 33. Injury Criteria of the chest, peak acceleration of the pelvis, and CV

Force and Moment Responses of Neck - Figure 34 indicates the neck responses of the shear force (Fx), the tension/compression force (Fz), and the flexion/extension moment around Y-axis (My). With regard to the Fx in the first test (Mid-T01), noises were detected near the peak both in the plus (+) side output (the head backward and the thorax forward) and in the minus (-) side output (the head forward and the thorax backward). The presumed reason is that the cable of the upper neck load cell had already deteriorated. Due to this, even a light touch on the cable caused noise when the functions of the sensor were confirmed after the test. Therefore, the ineffective contact of the wires in the cable caused the noise when the cable was wagged during impact. However, except for the noises of Fx, regarding both Fx and Fz, the responses were similar in the three tests. With regard to My, its appearance was similar in the three tests, but the peak near 90ms in the minus (-) side output (extension) in the first test (Mid-T01) was slightly lower than that in the other two tests. On the other hand, in the plus (+) side output (flexion), the peak in the third test (Mid-T03) was slightly lower than that in the other two tests.

With regard to the repeatability of Fz, both tensile force and compression force were good in the three tests (CV<=2.5%). In the minus (-) side of Fx, repeatability was acceptable (CV=7.7%), but in the plus (+) side, CV exceeded the acceptable criteria (CV=11.7%). In the flexion side of My, repeatability was narrowly acceptable (CV=9.6%). However, in the extension side, the value increased after repeated tests and, as a result, CV greatly exceeded the acceptable criteria (CV=16.8%).

In all the measured points, the occurrence situations of force and moment were similar between the UMTRI position and the standard position. In the response of Fx on the UMTRI position, noise was detected as well as the result in the first test on the standard position.

The circumstances in which the neck force and moment were generated were similar between the THOR-NT and Hybrid-III. However, generation level of Fx in the minus side output of THOR-NT from 0 to 60ms was smaller than that of Hybrid-III, while generation level of that from 110 to 160ms was larger than that of Hybrid-III. As for Fz (tension), although the occurrence of the peak force was similar between the THOR-NT and Hybrid-III on the standard position, the circumstance during falling of force was different between them. If anything, the response on UMTIR position was close to that of Hybrid-III. My (flexion) tended to be larger in the Hybrid-III.

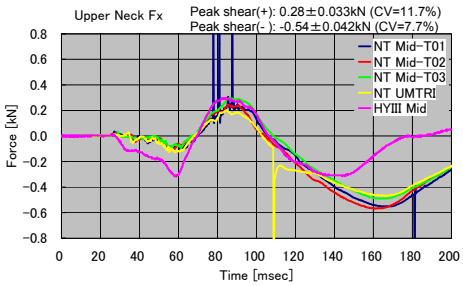

a) Neck force Fx

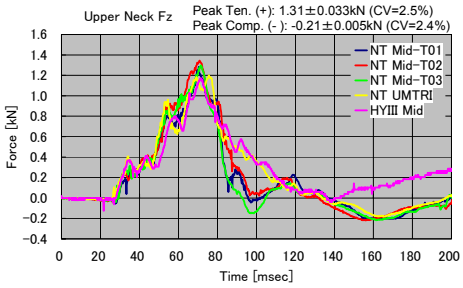

b) Neck force Fz

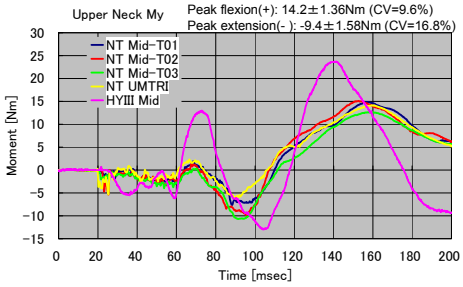

c) Neck moment My

Figure 34. Force and moment responses of neck

Deflection Responses of the Thorax and Abdomen - Figure 35 indicates responses of the upper thorax deflection in X-direction, and Figure 36 indicates

responses of the lower thorax deflection. With regard to repeatability, deflection appearance was similar in the three tests on the standard position, but the maximum values of the right and left side of the chest deflections vary. However, we would like to note that the result of the upper right side in the second test (Mid-T02) was obviously extraordinary. The CV to evaluate repeatability is indicated in this figure. Here, it should be noted that the CV of the upper right deflection was calculated from the results of the first and second tests only. The upper right deflection exhibited the biggest value of the four measuring points, and when compared between the right and the left deflections, the deflections of right side were twice as big as those of the left ones.

As for the repeatability, the CV of the upper right deflection was 0.5% (n=2) and the CV of the lower right deflection was 1.6%, both indicating good results with regard to the right side of the dummy. On the other hand, the CV of the upper left deflection was 19.7% and the CV of the lower left deflection was 17.8%, both indicating that the deflections of the left side of the dummy greatly deviated from the acceptable range.

As for the deflections of the upper area on the thorax, both the timing of the deflection occurrence and the maximum deflection were similar between the UMTRI position and the standard position. However, for the two deflections of the lower area on the thorax, although the timing of the deflection occurrence was similar, a difference in the maximum deflection level was observed probably due to the different positioning. With regard to the maximum values of the four measured points, there was a difference of about 2 mm on the upper left. The deflection on the lower left in the UMTRI position was smaller by about 5 mm than that of the standard position, and oppositely, the deflection on the lower right in the UMTRI position was larger by about 5 mm than that of the standard position.

When the right side deflections in THOR-NT are compared with Hybrid-III measurement taken at the center sternum, the deflection of THOR-NT was larger than that of Hybrid-III.

Figure 37 indicates responses of the abdomen deflection.

With regard to repeatability, both deflection occurrence situations and the maximum values of the left side of the lower abdomen were quite similar in all the three tests. The deflections of the upper abdomen were quite similar from the start of the undulation to the maximum deflection, but the result of the first test was slightly different from that of the other two tests. In addition, with regard to the deflection of the lower right abdomen, the maximum value of the first test was slightly smaller than that of the other two tests.

The deflection of the left side of the lower abdomen was quite similar in all the three tests, having CV value of 1.1%, indicating very good repeatability. Likewise, the deflection of the right side of the lower abdomen indicated good repeatability with a CV of 4.2%. Even the upper abdomen which indicated the greatest deflection fluctuation had a CV of 5.3%.

From the beginning of deflection occurrence to the peak deflection, the deflection response of the upper abdomen was quite similar between the UMTRI position and the standard position. However, after the peak deflection, the response curve of the UMTRI position decreased slowly compared with that of the standard position. As for the deflection responses of the lower abdomen, from 50 ms to 130 ms, the deflection of the left side in the UMTRI position was slightly lower than that of the standard position. While the responses in other time ranges were approximately the same between the UMTRI position and the standard position. The difference in the maximum deflection level between the UMTRI position and the standard position was larger in the right side than in the left side. The maximum deflection value of the upper abdomen was approximately the same in both seat positions. As for the lower abdomen, the maximum deflection values of the UMTRI position were smaller by 4 mm on the left side and by 10 mm on the right side than those of the standard position.

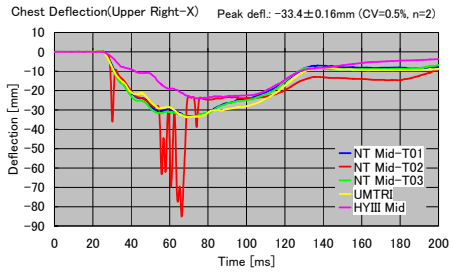

a) Thorax upper right

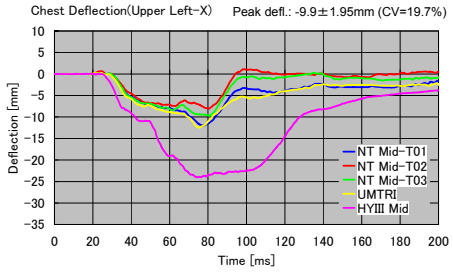

b) Thorax upper left

Figure 35. Deflection responses of upper thorax

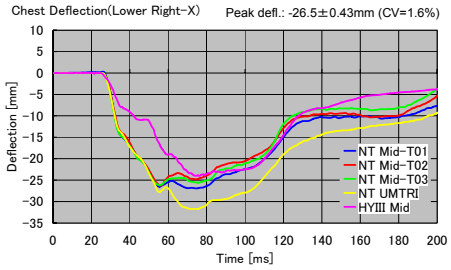

a) Thorax lower right

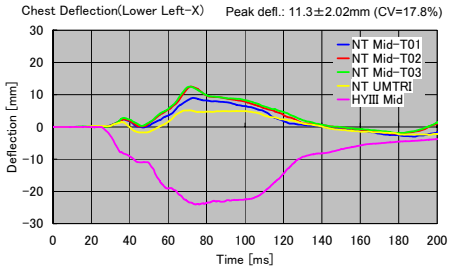

b) Thorax lower left

Figure 36. Deflection responses of lower thorax

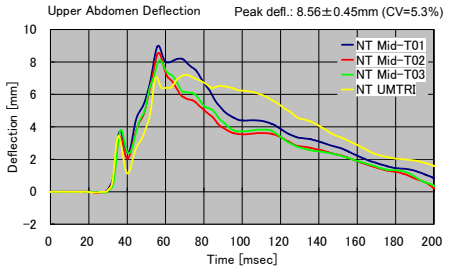

a) Upper abdemen

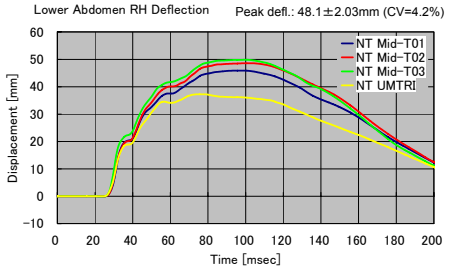

b) Lower abdomen right

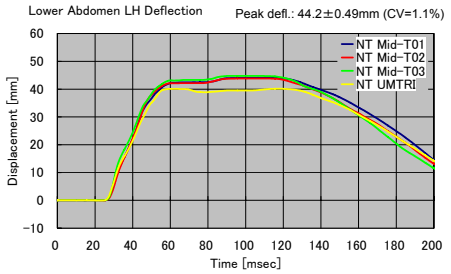

c) Lower abdomen left

Figure 37. Deflection responses of abdomen

Force and Moment Responses of the Legs - Figure 38 indicates the responses of the tension and compression forces on the femur. The compression force (-) of the left femur of THOR-NT was very low and the tension force (+) was high. The compression and tension forces of the right femur were similar.

With regard to repeatability, the force appearance situation of the right and left femur were similar in all the three tests. The repeatability of the compression force of the right femur was good (CV=3.4%), but the compression force of the left femur greatly deviated from the acceptable range (CV=18.8%).

In the occurrence of the compression force (in the minus output) in the beginning of the impact, the left femur force at the UMTRI position was slower than that at the standard position and the force indicated higher value. However, for the tension force (in the plus output), the time of the maximum force occurrence and force level were approximately the same in both positions. In the occurrence of the right femur force in the standard position, the compression force occurred at about 50 ms, and then changed into tension force by about 80 ms. On the other hand, the compression force of the right femur in the UMTRI position occurred before 50 ms, and changed into tension force immediately after that. The maximum compression force of the left femur in the UMTRI position was higher than that in the standard position, however, opposite results were obtained in the right femur.

Comparing the responses of the THOR-NT and Hybrid-III, the occurrence situation from 0 to 60ms of right femur was similar, whereas left femur became completely different situation.

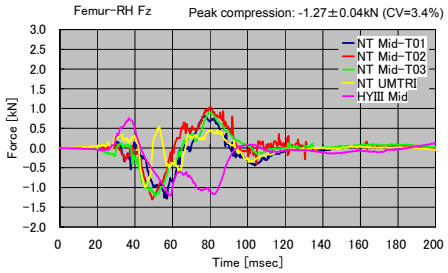

a) Right femur force

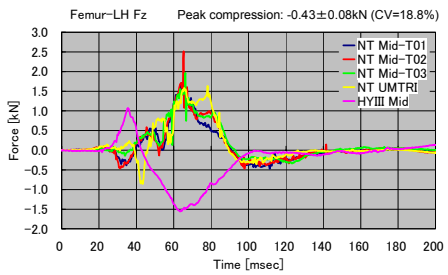

b) Left femur force

Figure 38. Force responses of femur

Figure 39 indicates the axial force responses of the tibia. The axial force was similar in both the right and left tibia. However, the axial force of the upper tibia was larger than that of the lower tibia. In addition, in all the four measuring points, both force occurrence situation and the maximum force were similar in the first and the second tests. But in the third test, the force at the first peak (about 40 ms) was smaller than that of the other two tests. It can be presumed that this difference was due to the slight fluctuation on the setup of the legs in the dummy positioning.

The tibia force was approximately the same at the four measuring points in the tibia (the upper and lower on right tibia and the upper and lower on left tibia). With regard to the repeatability, the lower tibia force on the right leg fell within the acceptable range (CV=7.2%), but the upper tibia force on the right leg, and the upper and lower tibia force on the left leg deviated from the acceptable range, i.e., all of the CVs were higher than 10%.

At the four measured points (upper right, lower right, upper left, and lower left), the occurrence situation of tibia axial force was different between the UMTRI position and the standard position. While the first peak force in the standard position occurred at about 35 ms, the first peak force in the UMTRI position occurred at about 45 ms, and the force level was higher than that of the standard position.

Comparing the responses of the THOR-NT and Hybrid-III on the standard position, the occurrence situation of femur force was similar. However, the peak forces of Hybrid-III were higher than that of THOR-NT.

Figure 40 indicates the moment responses around Y-axis of the tibia. In the three tests of THOR-NT on the standard position, the moment occurrence situations were similar in both the right and left tibia. The maximum moment of the lower tibia was smaller than that of the upper tibia. Also in the three tests, the lower moment of the right tibia tended to indicate smaller values than other three measuring points. Moreover, in all the measuring points on the tibia moments, the values decreased by repeating the test. However, the CVs of the upper and lower tibia moment of the left leg and the lower tibia moment of the right leg were within the range (4% to 6%), while the CV of the upper tibia moment of the right leg was 9.8%. All the CVs fell within the acceptable range of repeatability.

At the four measured points (upper right, lower right, upper left, and lower left), the moment began to appear approximately at the same time in both the UMTRI position and the standard position. However, the undulations from the moment occurrence to the maximum moment were different. In addition, the occurrence time of the maximum moment of the UMTRI position was slightly later than that of the standard position. The maximum tibia moment of the UMTRI position tended to be higher than that of the standard position.

Comparing the responses of the THOR-NT and Hybrid-III on the standard position, in the upper of the right and left tibia, the first peak of Hybrid-III occurred at early timing than THOR-NT.

On the other hand, in the lower tibia, Hybrid-III shifted toward minus after it responded toward plus at early timing, and thereby responses between THOR-NT and Hybrid-III were different.

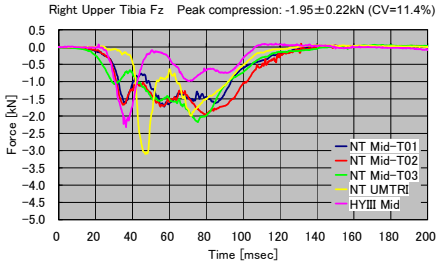

a) Right upper Fz

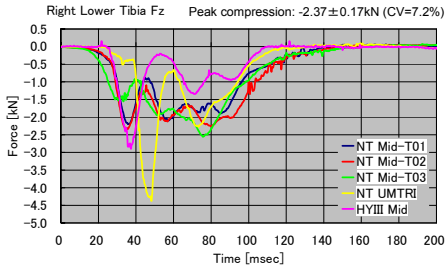

b) Right lower Fz

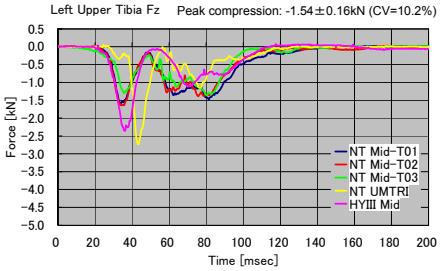

c) Left upper Fz

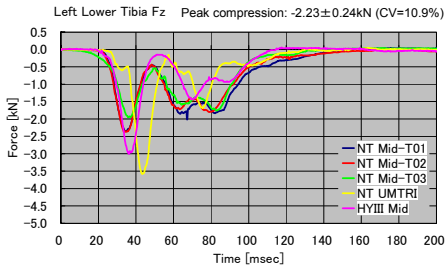

d) Left lower Fz

Figure 39. Force responses of tibia

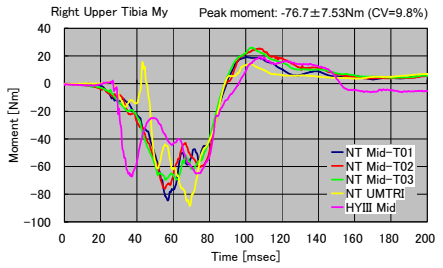

a) Right upper My

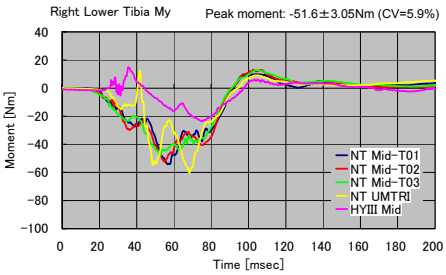

b) Right lower My

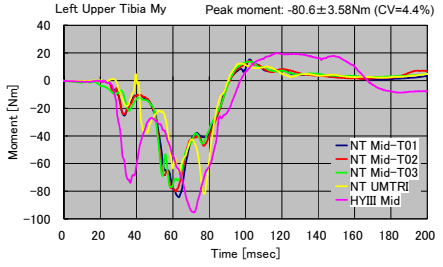

c) Left upper My

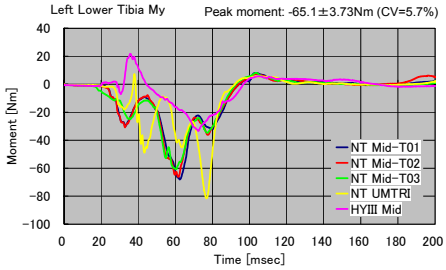

d) Left lower My

Figure 40. Moment responses of tibia

Figure 41 indicates the time history data of the tibia index. In both right and left legs, the curves of the tibia index were similar. As for the maximum values in the tibia index, the value of the upper tibia of the right leg fluctuated larger than that of other three measuring points (CV=9.1%). The CVs of the other three points were from 5.1% to 6.2%.

At the four measured points (upper right, lower right, upper left, and lower left), both the undulation of the UMTRI position and that of the standard position began to appear approximately at the same time, however, the undulations from the starting point to the maximum point of tibia index curves were different. Furthermore, the occurrence time of the maximum tibia index of the UMTRI position was slightly later than that of the standard position. The maximum tibia index of the UMTRI position tended to be slightly higher than that of the standard position.

Comparing the responses of the THOR-NT and Hybrid-III on the standard position, in the upper of the right and left tibia, the first peak of Hybrid-III occurred at early timing than THOR-NT. However, with regard to the maximum values of tibia index, THOR-NT and Hybrid-III were similar. On the other hand, in the lower tibia, tibia index of THOR-NT was higher than that of Hybrid-III.

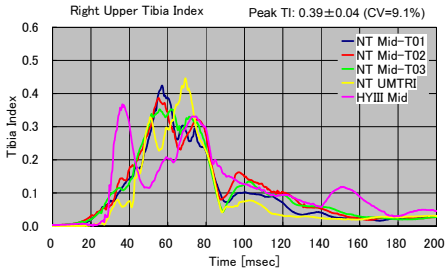

a) Right upper

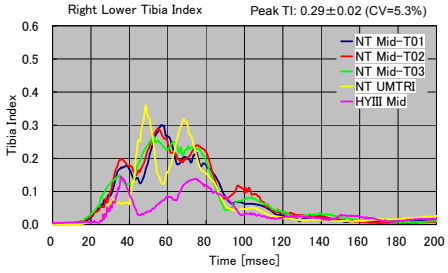

b) Right lower

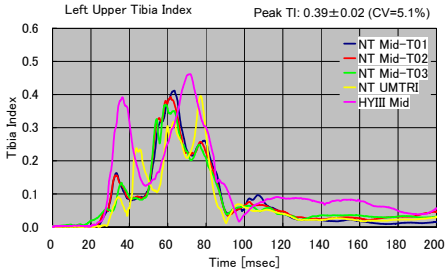

c) Left upper

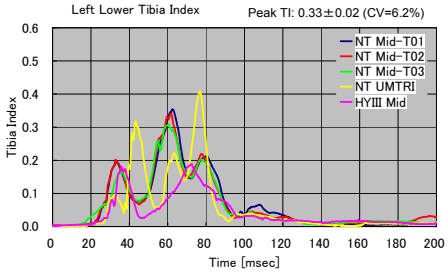

d) Left lower

Figure 41. Tibia Index

DISCUSSIONS

Difference between Biofidelity and Certification Corridors

With regard to the head, thorax and face, the method of biofidelity test and that of certification test are the same. However, the corridors of these tests are different. Therefore, even if the response falls within the one corridor, the response will deviate from another corridor.
It is required how it arranges corridor based on PMHS data.

Suggestion to Improve the Obscure Test Procedures on the Biofidelity and Certification Tests

In biofidelity tests, if it was only the description of the test procedures in the THOR biofidelity/certification test manuals, there was the difficult case of set-up of the test conditions. For instance, as for the head impact test, the test procedure is described in certification manual following as: "The head of the dummy is placed, such that the axis of the impactor is aimed at a point on the forehead on the midsagittal plane and 30 mm above the horizontal line marking the division with the face skin" [2]. However, authors could not correctly judge "the horizontal line marking the division with the face skin". Therefore, authors conducted test assuming that 30 mm above the horizontal line to be approximate point.
Also, as for the rigid bar impact test on the face, the test procedure is described in certification manual following as: "The rod is configured to impact along the mid-line of the left and right maxilla plates on face" [2]. Likewise, as for the disk impact test on the face, the test procedure is described in certification manual following as: "The center of the disk is configured to impact between the cheek and chin plates on the face" [2]. However, authors could not correctly judge "the mid-line of the left and right maxilla plates on face" and "the point between the cheek and chin plates on the face". Therefore, authors conducted these tests, judging the impact point from photographs in the certification manual.
It can be presumed that the slight differences in the test set-up appeared as slightly different result between authors and GESAC. Note: The results of tests which were conducted by GESAC are indicated in the publication of reference [1].
It could be pointed out that it is necessary to arrange the manual such that it is possible to duplicate more faithfully test procedures.

Influence of Different Positioning to Dummy Responses on HYGE Sled Test

With regard to the seat of the white-body of a passenger car used in this test, the seat-slide position in accordance with the ATD positioning procedure of UMTRI was positioned 50 mm rearward with respect to the seat-slide position of the standard position. Therefore, the positioning of the dummy in the UMTRI position was positioned rearward than that in the standard position. The behavior of the dummy was basically similar in both the UMTRI position and the standard position. However, the moving distance of the dummy before coming in contact with the airbag and/or the instrument panel was longer in the UMTRI position than that of the standard position. The clearance between the body of the dummy and the steering wheel/ instrument panel at the initial positioning of the dummy was wider in the UMTRI position compared to the standard position. Therefore, the maximum displacements of each body-part with respect to the initial positioning of the dummy in the UMTRI position were larger relative to the standard position. In particular, there was a difference of about 31 mm at the head and 46 mm at the ankle in the back-forth direction.
With regard to the dynamic responses of the upper body of the dummy, there were little differences observed between the UMTRI position and the standard position. On the other hand, the occurrence situations of force and moment at the femur and the tibia were different relative to those at the upper body probably due to the difference in the behavior of the ankle as stated above.
When the behavior of the dummy in the UMTRI position was checked by means of a video camera, it showed that the ankles moved forward during 0ms to about 40ms and the heels came in contact with the toe board (at the initial position the heels were away from the toe board), and then the feet slide on the toe board at about 40ms to 80ms. On the other hand, in the standard position, the heels were on the toe board at the initial position, and the feet did not slide on the toe board. Instead, the feet appeared to brace against the toe board.
However, the toe board used in the HYGE sled tests series was not the toe board of a real vehicle but a jig-attachment which imitated the real toe board and its surface was covered by a floor carpet of a real vehicle. Therefore, it can be considered that the behavior of the lower legs in these tests did not necessarily reproduce the one in the real driver seat where the lower legs were positioned on the accelerator and the brake pedals.
In addition, the white-body of a passenger car used in

these tests had a rather spacious interior space, and thereby even in the standard position, the clearance between the dummy's knees and the instrument panel was relatively wide. Therefore, it is presumed that this is the reason why conspicuous differences of dummy responses did not appear between the standard position and the UMTRI position.

CONCLUSIONS

The biofidelity of the head, neck, thorax and abdomen of the THOR-NT was evaluated according to the biofidelity test procedures of THOR.

- Only the head responses of the Thor-NT were within the PMHS corridors.
- It was found that the thorax characteristic of Thor-NT dummy was stiffer than the human body. In the test at 6.7m/s, it can be presumed that the maximum force became higher due to the metal contact inside thorax bottomed out.
- With regard to the abdomen, the responses of both upper and lower deviated from each corridor, namely, it was found that the abdomen characteristics of the dummy are stiffer than that of the human body.
- In the head, thorax and face, the test procedures of the biofidelity and certification test are quite same. However, corridors for evaluation in both tests do not overlap with each other. This would cause the result that even if the dummy response is within the corridor of either test, it is outside the corridor of another test. It is required how it arranges corridor based on PMHS data.

In order to obtain the impact response properties of the full assembly of the dummy, four HYGE sled tests were conducted. Evaluation of the repeatability of dynamic response and investigation of the influence on the dummy response by different positioning was performed. In order to evaluate repeatability, three tests were conducted under the same conditions.

- The kinematic responses of the dummy were similar in the three tests.
- As for the dynamic responses of the dummy, coefficient of variation (CV) was used as the evaluation criteria of the repeatability, which was calculated by dividing the standard deviation (SD) of the maximum value of the measured data by the average value. In this study, repeatability was evaluated in the measured data and injury criteria of 31 items. As a result, 10 items (32%) in all the measured data and the injury criteria (31 items) indicated the result that CV is less than 5% as good for repeatability. 23 items (74%) in 31 items indicated the result that CV is less than 10% as acceptable. Thus, the remaining 8 items (26%) indicated that CV is larger than 10% as poor.
- In order to investigate the influence of different positioning to dummy responses, a test was conducted on a dummy positioned according to the ATD positioning procedure developed by UMTRI, and then repeatability was evaluated. When comparing the dummy positioning in the standard and UMTRI position, the dummy in the UMTRI was positioned 50 mm rearward and 18 mm above with respect to the standard seat position. In the back-forth direction, the difference of the H.P. was the largest, namely, the H.P. in the UMTRI position was 43 mm rearward compared with the standard position. In the up-down direction, the difference of the shoulder was the largest, namely, the shoulder in the UMTRI seat position was approximately 37 mm upward compared with the standard seat position.
- The behavior of the dummy was basically similar in both seat positions, but the maximum displacement with respect to the initial position differed in the head and the ankle. The difference in the dummy response due to different positioning was small in the upper body, but large in the femur, legs, and ankles. This is presumed to be due to the difference in the behavior of the ankles.

ACKNOWLEDGMENTS

THOR-NT dummy which evaluated in this study had been leased from NHTSA. The authors would like to express our gratitude to NHTSA for supporting the lease of THOR-NT dummy, and the instructive comments to our manuscript.

REFERENCES

[1] GESAC, Inc. 2005. "Biomechanical Response Requirements of the Thor NHTSA Advanced Frontal Dummy (Revision 2005.1)." Report No.GESAC-05-03

[2] GESAC, Inc. 2005. "Thor Certification Manual (Revision 2005.2)." Report No. GESAC-05-04

[3] M. Hoofman, M. van Ratingen and J. Wismans. 1998. "Evaluation of the Dynamic and Kinematic Performance of the Thor Dummy: Neck Performance." 1998 IRCOBI Conference, 497-511

[4] SAE. 1995. "(R) Instrumentation for Impact Test – Part 1 – Electronic Instrumentation." SAE J211/1 MAR95

[5] NHTSA. 2004. "Code of Federal Regulations, 49 CFR

Part 571 FMVSS No.208; Occupant Crash Protection.”
[6] IIHS. 2004. “Guidelines for Using the UMTRI ATD Positioning Procedure for ATD and Seat Positioning (Version V).”
[7] J. S. H. M. Wismans E.G. Janssen, R. Happee, P.H.M. Bovendeerd, H.G. Mooi and M.R. van Ratingen. 2000 “TU/e technische universiteit eindhoven Injury Biomechanics, Third Edition.”

OOP Air Bag Tests using the THOR-NT

Zi Lu
Philemon Chan
L-3/Jaycor
San Diego, CA, USA

Stephen A. Ridella
Peter G. Martin
National Highway Traffic Safety Administration
U.S. Department of Transportation
Washington, D.C., USA

Paper Number 07-0293

ABSTRACT

An experimental study of driver side air bag loads for out-of-position (OOP) occupants at the ISO-1 (chin on bag) position was performed using the 50th percentile THOR-NT dummy. The main objective was to observe the response of the dummy under exposures to various types of air bags. Dummy sensitivity to the air bags was evaluated in terms of upper neck loads and head acceleration. Five types of late-model fleet air bag modules were used in a total of ten tests (two repeat tests per air bag). Sealed tank tests were also performed to characterize the five different air bag inflators. For one bag, the THOR-NT produced very repeatable measurements. For other bag types, the THOR-NT exposed the variability of the air bags, especially in its upper neck moment measurements. The high-speed videos confirmed the inflation variability of those air bags. The THOR-NT was able to segregate the moment at the head/neck pin joint (representing human occipital condyles) from the total head/neck cross-sectional moment. The THOR-NT performed smoothly throughout the test and was generally user-friendly. A limitation is recognized that only two air bags for each model were used for repeat tests.

INTRODUCTION

The THOR (Test device for Human Occupant Restraint) dummy is an anthropomorphic test device (ATD) developed for advancing the study of biomechanical phenomena and the development of new injury criteria supported by other efforts in human volunteer tests, cadaver tests and modeling [1-3]. The notable new features of THOR include a neck design that segregates load paths within the cervical spine, and the use of multiple potentiometers for measuring chest and abdomen deformations at distributed locations. The current THOR version, denoted as THOR-NT, has an improved design to overcome the limitations of the previous version.

The study herein focuses on the performance of air bags as measured within the THOR-NT head/neck complex. As shown in Figure 1, the THOR-NT distinct neck subassemblies reflect a design premise that human necks are loaded along multiple paths, and that loads are borne by both ligamentous tissues and musculature. Loads that pass through a human neck are presumed to include those borne by "external" musculature only (represented in THOR-NT by the two cable subassemblies), and those borne by both "internal" muscles and ligaments (represented in THOR-NT by the molded neck subassembly and the pin joint/nodding block subassembly).

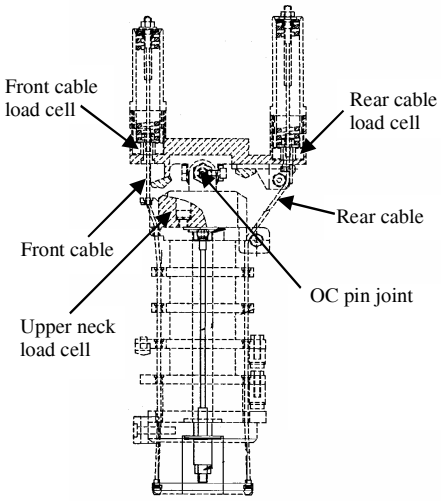

Figure 1. THOR-NT neck structure.

The THOR-NT design philosophy also presumes that human neck injuries occur when ligamentous tissues become overloaded. Hence, a THOR-NT injury crite-

rion will be based on measurements in its upper neck load cell alone, which is mounted on the neck rather than in the head (Fig. 1). Forces measured in the load cells attached to THOR-NT anterior and posterior cables represent "external" noninjurious loads borne by musculature alone (and not ligamentous tissues). These load cell measures are contemplated as reference measures only, and may not be directly linked to an injury criterion.

Other previous work has been performed showing favorable biofidelity evaluation of the head/neck complex of THOR-NT. These tests include a comparison of THOR-NT loads against muscle and occipital condyle (OC) loads measured in tests run by the Medical College of Wisconsin (MCW) using post mortem human subjects [4]. A favorable comparison of the THOR-NT neck response against a human model was also demonstrated by Duke University [5].

Previous tests by L-3/Jaycor using the Air bag Test Simulator (ATS) with a previous version of THOR-NT has shown highly repeatable head/neck responses to well-controlled air bag deployments in out-of-position (OOP) conditions [6-8]. The ATS is a device developed by L-3/Jaycor that deploys air bags in a very repeatable fashion and with the same deployment characteristics as an actual production air bag module [9]. Using the ATS, the air bags were pneumatically inflated and two air bags with conventional folding were used with tests conducted at the ISO-1 (chin on bag) and ISO-2 (chin on upper steering wheel rim) positions [10]. At least five repeat tests were conducted at the same condition, respectively, for both the 50th percentile Hybrid-III and THOR dummies, for data comparison. Data showed that the THOR neck design could carry loads through the cable elements and the head/neck pin joint akin to the way loads are transferred through and around the occipital condyles of a human neck.

This paper presents results from testing the THOR-NT using fleet driver side air bag modules in the laboratory. As the THOR-NT is a relatively new dummy, this paper also serves to provide an evaluation of the dummy itself under well controlled conditions. The tests conducted do not represent standard regulatory tests since there is no standard OOP position or injury metrics established for THOR-NT.

METHODS

Five models of fleet driver side air bags were used, which are labeled as Bag A, B, C, D, and E, respectively (Table 1). Other than Bag E that has a single-stage inflator, the other four models have dual-stage inflators (Table 1).

Table 1. Five driver side air bag modules.

Bag	Model	Position	Stage
A	compact	driver	dual
B	SUV	driver	dual
C	sedan	driver	dual
D	sedan	driver	dual
E	light truck	driver	single

The air bag inflators were characterized using the SAE standard sealed tank test as specified in SAE J2238 [11]. The inflator was separated from the air bag unit, connected to the tank, and electrically discharged. The tank gas pressure and temperature histories were recorded. Pressure and temperature gauges were mounted on the top, side and bottom of the tank (Fig. 2a). To characterize both stages of a dual-stage inflator in a single tank test, the second stage was triggered about 0.12 sec after the first stage (Fig. 2b). This 0.12-sec trigger delay for the second stage was only used for the tank tests to characterize the dual inflators in a single test.

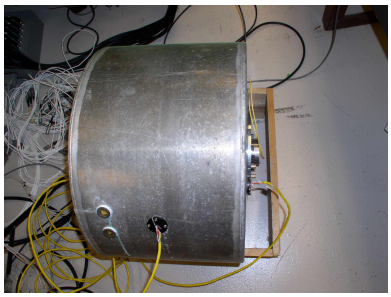

(a) Sealed tank and instrumentation

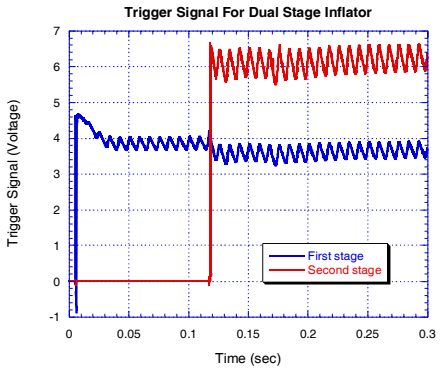

(b) Trigger signal for dual stage inflator

Figure 2. Sealed tank test setup.

For the OOP air bag impact tests, the 50th percentile male THOR-NT dummy was placed in the adjustable seat fixture of the ATS platform (Fig. 3). The dummy was placed at the ISO-1 position (Fig. 3). The position of the dummy was accurately controlled using fixed position markers on the seat and the adjustable neck positioning arm for each test. The transducers used in THOR-NT included accelerometers, load cells, displacement string potentiometers, and rotary potentiometers. All signals were recorded using a digital data acquisition system with a sampling rate of 10 kHz. A high-speed digital camera recorded the air bag-dummy interaction at 1000 frames per second. Signal conditioning, filtering, and recording techniques complied with the SAE J211 standard [12]. A complete new air bag module with the original steering wheel was used for each test.

Figure 3. THOR-NT test setup at ISO-1 position.

Stage-by-stage comparison. OOP tests using the 50th percentile male Hybrid-III dummy were first performed to examine the effects of full deployment vs. first stage only using Bag A. The Hybrid-III dummy was also placed at the ISO-1 position. Two tests were performed separately using deployments from the 1st stage inflator and from both stages. For the full deployment test, both stages were triggered simultaneously. Based on the results observed, it was decided to conduct all THOR-NT dummy tests using deployments from both stages for all the dual-stage air bag modules.

Full-stage air bag tests. Full-deployment air bag impact tests were carried out for all five models for the THOR-NT dummy. For dual-stage models, both stages were triggered simultaneously for each test. Two repeat tests were performed for each air bag model. Head/neck load time-history data comparison was performed for each air bag model. Air bag inflation repeatability or variability for each model was confirmed and analyzed using the high-speed video recordings. Values of Head Injury Criterion based on the 15-ms time interval (HIC_{15}) were computed for comparison.

As stated earlier, the THOR-NT has a unique neck construction in which muscles and osteoligamentous structures are represented by separate mechanical components (Fig. 1). The primary structural component of the THOR-NT neck is the segmented molded rubber column which is designed based on the responses of the human cervical spine. A six-axis load cell is placed at the top of this component to directly measure the loads at the head/neck pin joint, which represents human occipital condyles. In the results presented herein, all neck loads (or upper head/neck loads) refer to the OC pin joint location (Fig. 1). Cross-sectional loads refer to loads including the front and rear cable loads with respect to the head coordinate system.

The THOR-NT instrumentation allows one to compute its "cross-sectional load" by accounting for the cable loads. The dummy has a rotary potentiometer that measures rotation of the head with respect to the neck. Using data from this potentiometer, one may translate THOR-NT's cross-sectional neck loads to the head coordinate system using the THORTEST program [13]. In the results herein, cross-sectional loads are always given in the head coordinate system. The THOR-NT neck load data can also be presented in the neck coordinate system as will be indicated.

RESULTS

Comparison of single and dual-stage inflations. The sealed tank test data for each inflator are shown in Table 2, with the two pressure values indicating the outputs from the first and both stages, respectively, for Bags A-D, while only one value is shown for Bag E with single-stage inflator. For a dual-stage inflator, the tank pressure history shows that the combustion of the first stage usually completes in 50 ms and a fairly stable tank pressure level is sustained for a long time until the second stage is ignited (Fig. 4). For dual-stage inflators, the first stage generally contains the larger portion of the total energy with the second stage contributing about 6-30% of the total energy output (Table 2; Fig. 4). The tank test data justify the use of 0.12-sec trigger delay to collect dual-stage data without sacrificing additional inflators.

Table 2. Tank test results

Bag	Model	Stage	Pressure, KPa
A	compact	dual	100/150
B	SUV	dual-	125/140
C	sedan	dual	165/175
D	sedan	dual	140/190
E	light truck	single	160

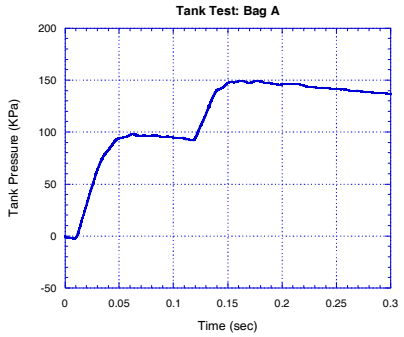

(a) Bag A

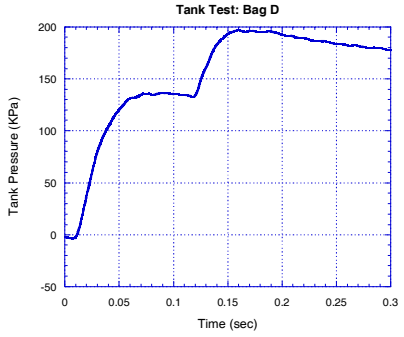

(b) Bag D

Figure 4. Sealed tank test pressure data.

Tests conducted using Bag A and the Hybrid-III dummy showed air bag loads from the 1st stage and both stages resulted in significant differences in the dummy response (Fig. 5). Inflation from both stages deploying simultaneously delivers a much stronger load to the dummy than that just from the 1st stage (Fig. 5). The results are consistent with the tank data showing the tank pressure increasing from 100 to 150 KPa when the 2nd stage is triggered (Fig. 4a and Table 2). To achieve the maximum impact load for dummy evaluation, the remaining tests with the THOR-NT were conducted by deploying both stages simultaneously for all dual-stage modules.

Data repeatability and variability. It was found that the bag inflation variation was a dominant factor affecting the data repeatability of the air bag impact test results (Figs. 6-10). Bag A produced data with excellent repeatability as observed from the two tests for the THOR-NT dummy (Fig. 6). However, the other four types of bags produced significant variability in dummy metrics (Figs. 7-10).

For illustration, large inflation variability was observed for Bag C deploying against the THOR-NT dummy (Fig. 7). The upper head/neck load data shown in Figure 7 are in the head coordinates. For test 1, the air bag pushed the chin backwards, which

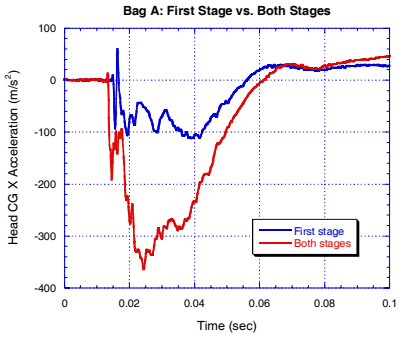

(a) Head CG X-acceleration

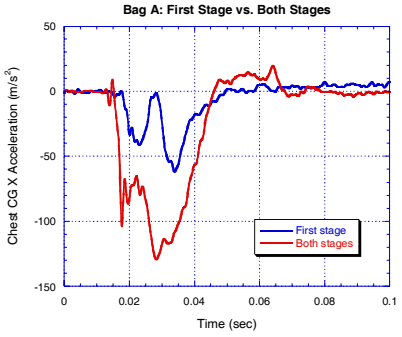

(b) Chest CG X-acceleration

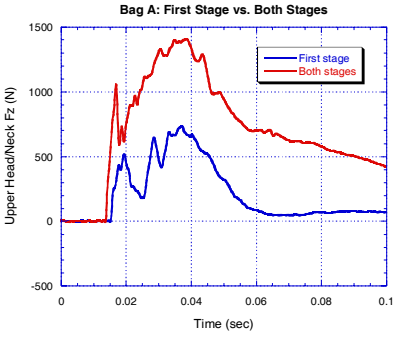

(c) Upper head/neck Fz

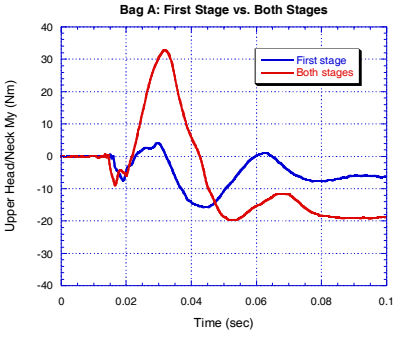

(d) Upper head/neck My

Figure 5. Hybrid-III responses to first stage and full deployments for Bag A.

generated large positive upper head/neck shear Fx and moment My (flexion) at 20 ms (Figs. 7a-b). For test 2, the air bag was trapped under the chin and pushed it upwards, which generated large negative Fx

and My (extension) at 40 ms (Figs. 7a-b). The air bag also slipped behind the steering wheel for test 2, which did not happen in test 1 (Fig. 8a vs. 8b).

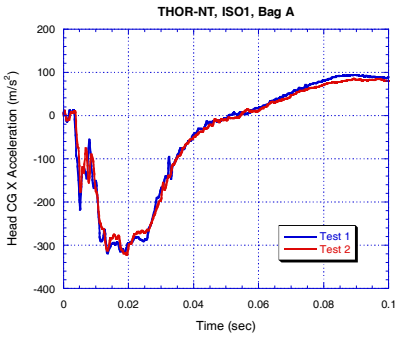

(a) Head CG X-acceleration

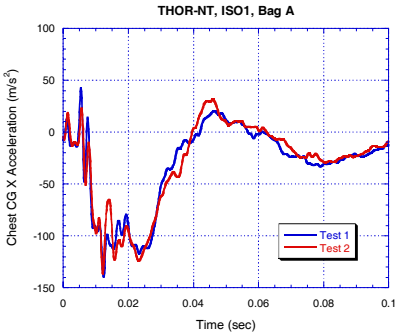

(b) Chest CG X-acceleration

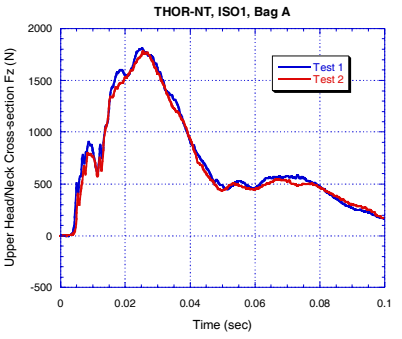

(c) Upper head/neck Fz

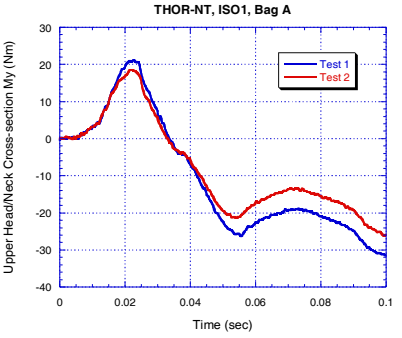

(d) Upper head/neck My

Figure 6. Excellent data repeatability observed for bag A.

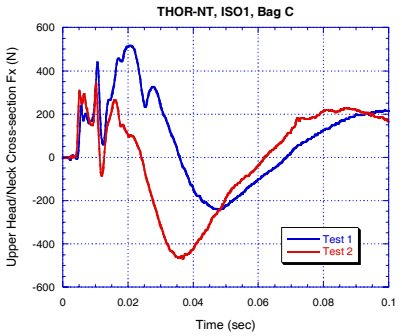

(a) Upper head/neck Fx

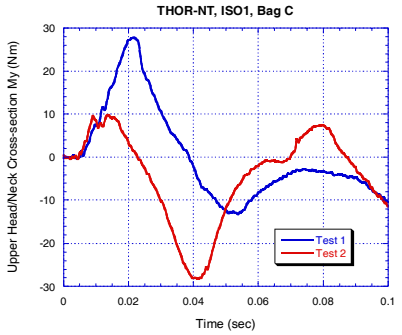

(b) Upper head/neck My

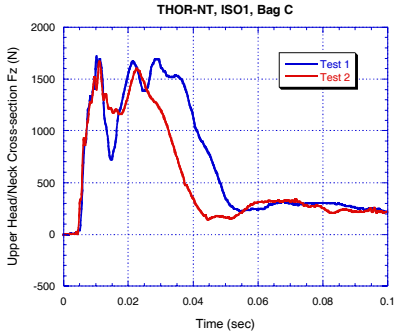

(c) Upper head/neck Fz

Figure 7. Head/neck load data comparison for Bag C (head coordinates).

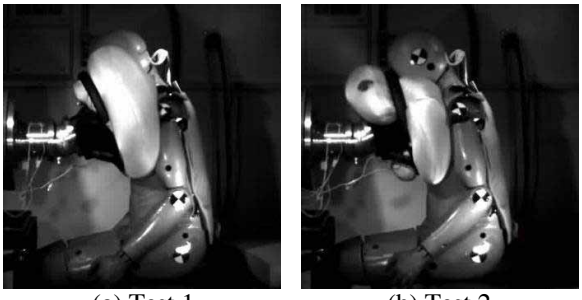

(a) Test 1 (b) Test 2

Figure 8. Inflation variability for Bag C deployed against THOR-NT.

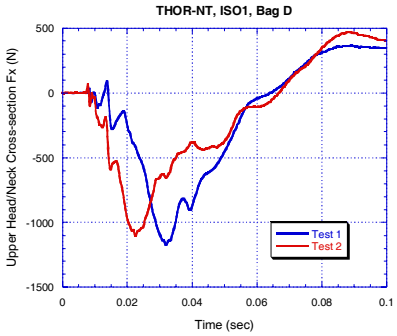

(a) Upper head/neck Fx

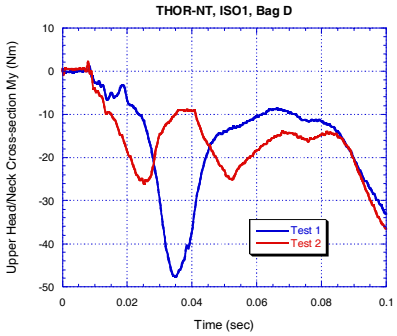

(b) Upper head/neck My

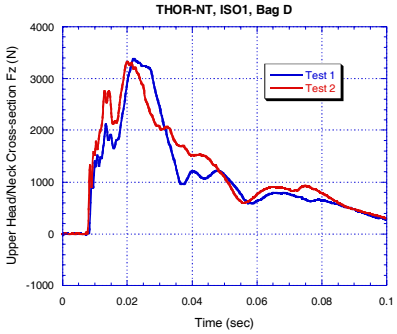

(c) Upper head/neck Fz

Figure 9. Head/neck load data comparison for Bag D (head coordinates).

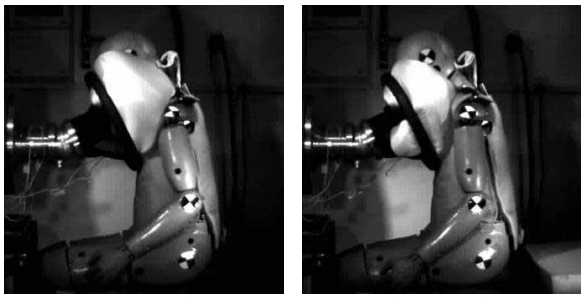

(a) Test 1 (b) Test 2

Figure 10. Inflation variability observed for Bag D deployed against THOR-NT.

Inflation variability was also observed for tests using other air bags. For Bag D, high-speed video data showed the air bag was trapped under the dummy chin and pushed it upwards, which generated large negative My (extension) for test 1 at 35 ms (Figs. 9b and 10a). This neck trapping situation was less severe for test 2 as indicated by the much smaller negative My (Fig. 9b). In addition, the air bag slipped behind the steering wheel more for test 2 than for test 1 as shown by the high-speed video data (Figs. 10a vs. 10b). This partially explains why test 2 delivered a softer load on the neck than test 1 (Fig. 9b).

The inherent bag inflation variability manifested itself mostly in upper head/neck Fx and My. The head/neck axial force Fz was fairly consistent (Figs. 7c and 9c). The Fz forces are positive most of the time (Figs. 6c, 7c and 9c), which means the neck pulls the head downwards in tension. This tensile upper head/neck Fz is a combined effect of the external air bag load and the centrifugal rearward rotation of the head.

Injury metrics for various air bags. For the head, a HIC_{15} = 700 injury reference value may be used to assess injury risk. All five air bags produced HIC_{15} values of less than 200 and significantly below this threshold, although Bag D produced the highest HIC_{15} values (Fig. 11). This seems to be consistent with the tank pressure data showing Bag D generating the highest dual-stage pressure (190 KPa) among the five models (Table 2).

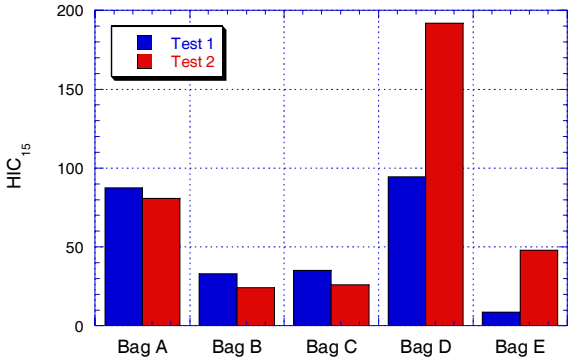

Figure 11. HIC_{15} data comparison.

Table 3 provides the critical injury assessment values for human spine tolerance [5]. While the THOR-NT is designed to mimic the human neck, it is stiffer than the human spine; thus it is likely that some adjustment of the human cervical spine tolerance values will be necessary before they can be used as injury reference values in the THOR-NT. Nonetheless, the human threshold values may be used for experimental purposes.

Table 3. Critical Values for Neck, M_Y and F_Z

	Human
Compression, F_C (N)	3640
Tension, F_T (N)	2520
Flexion, M_F (Nm)	48
Extension, M_E (Nm)	72

The neck load data for all five bags are shown from Figures 12-16. These "OC" neck loads as shown are in the neck coordinate system as measured by the upper neck load cell excluding the cable effects, with the moment, My, moved up to the level of the head/ neck pin joint (the load cell is located 2.54 cm below the joint). The THOR-NT data are presented as such consistent with the way the neck data are expected to be used for injury assessment. Furthermore, the range of variability for each data metric is indicated by the shaded region bounded by the time-history data recorded from the two repeat tests for each bag.

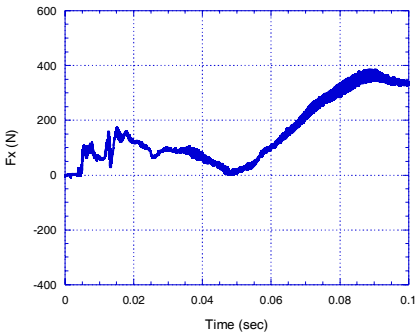

(a) Fx

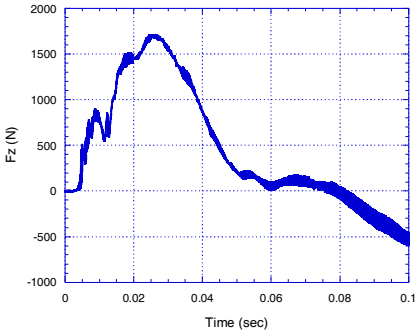

(b) Fz

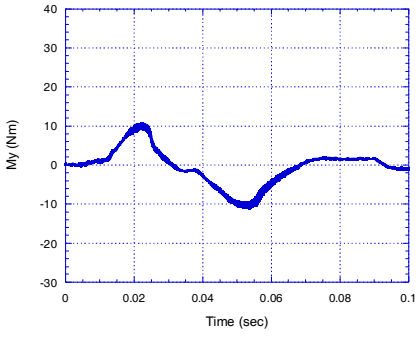

(c) My

Figure 12. Neck load for Bag A (neck coordinates).

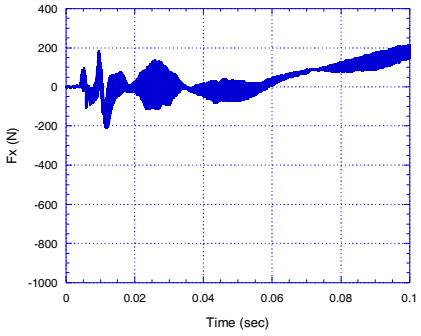

(a) Fx

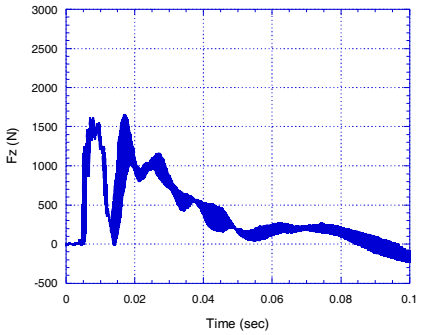

(b) Fz

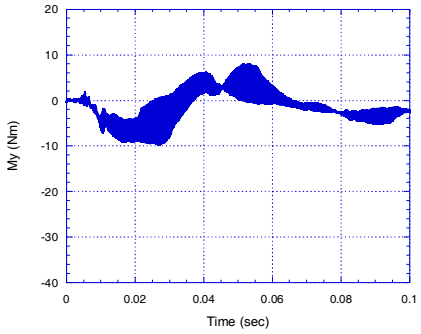

(c) My

Figure 13. Neck load for Bag B (neck coordinates).

The data comparison shown from Figures 12-16 indicates some clear trends even though only two tests were performed for each bag. The data spread for Fz is much smaller than that for Fx and My. The shear force Fx shows consistency with My, with both generally staying positive or negative simultaneously, for flexion or extension, respectively. Other than for Bag D, the neck moment cycled from flexion to extension or vice-versa smoothly within the safe critical values indicated in Table 3 (Figs. 12-16).

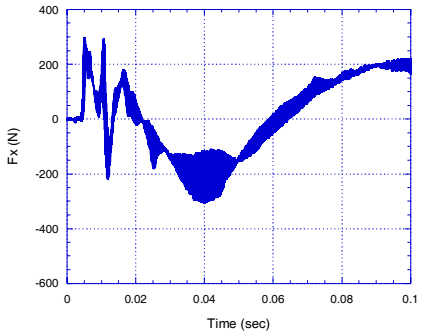

(a) Fx

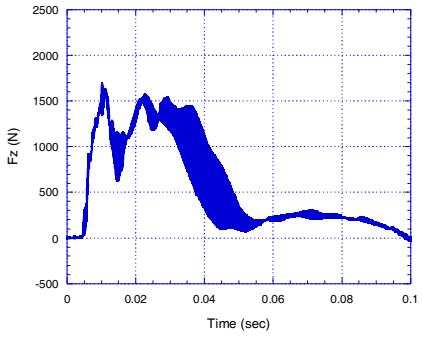

(b) Fz

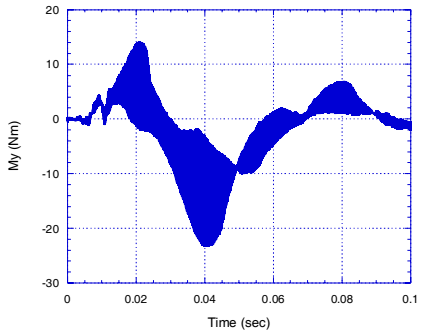

(c) My

Figure 14. Neck load for Bag C (neck coordinates).

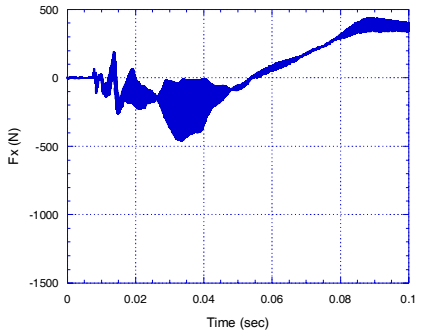

(a) Fx

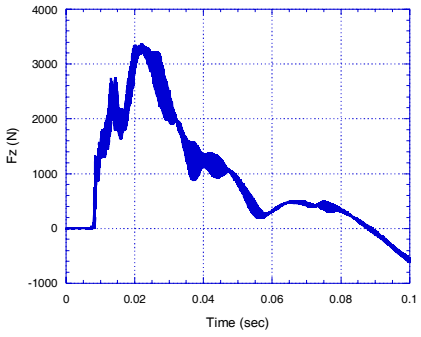

(b) Fz

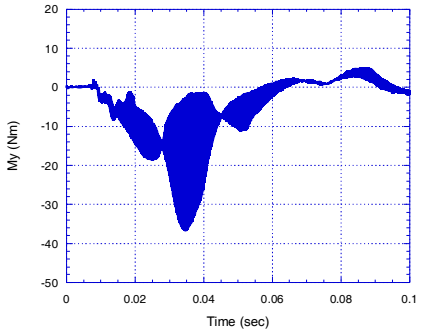

(c) My

Figure 15. Neck load for Bag D (neck coordinates).

Of the five types of air bags tested with the THOR-NT, Bag D exceeded the critical value for neck tension given in Table 3. For Bag D, the axial tension force Fz recorded by THOR-NT reached 3300 N (Fig. 15b), which exceeded the human critical value of 2520 N shown in Table 3. This air bag also produced the highest inflation pressure in the tank test (Table 2). Compared to the other bags, Bag D also produced the largest extension moment reaching -38 Nm and the neck moment was dominated by extension throughout the entire bag-dummy interaction process (Fig. 15c).

Cross-sectional vs OC My comparison. With the exception of Bag A, each air bag had inflation variability that certainly contributed to the differences in dummy responses for a given air bag type. Nonetheless, there were some consistent trends that can be illustrated comparing the OC neck moment against the cross-sectional neck moment calculated by including the cable load effects.

As shown in Figure 17 using data from Bag A and Bag D, the OC moment at the pin joint recorded by THOR-NT is considerably smaller than the total cross-sectional moment (Fig. 17). This trend is consistent for all five air bags tested. This further confirms the intended capability of the THOR-NT neck design to distinguish the musculature from the ligamentous load.

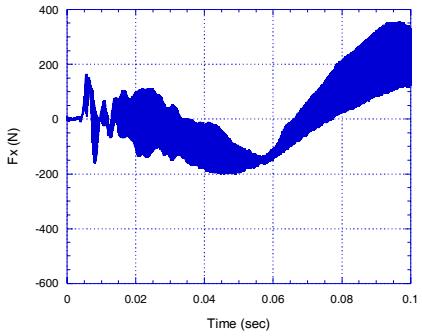

(a) Fx

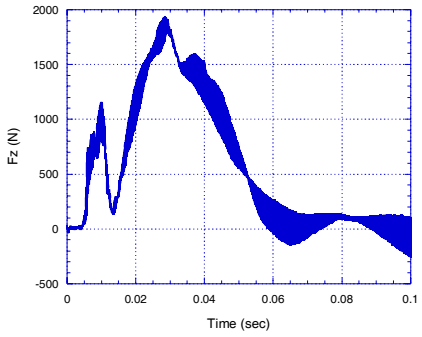

(b) Fz

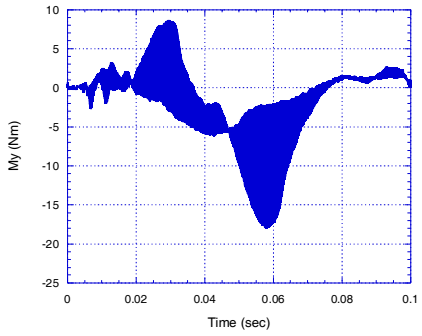

(c) My

Figure 16. Neck load for Bag E (neck coordinates).

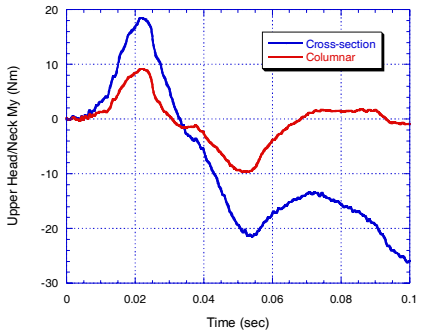

(a) Bag A

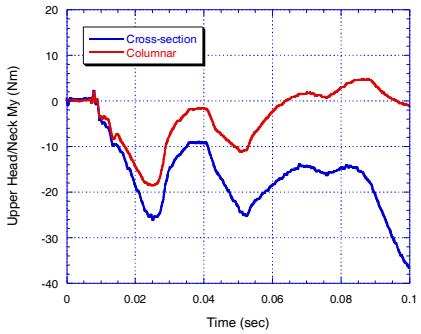

(b) Bag D

Figure 17. Upper head/neck moment comparison.

DISCUSSION

The present study has shown that the head/neck complex of the THOR-NT dummy is capable of capturing the detailed air bag load effects due to the variability of bag inflation on the occupant head and neck in OOP conditions. The variability of the early inflation behavior of the fleet air bag modules tested was confirmed by the high-speed video data. Nevertheless, all HIC_{15} values calculated from the tests are well below the injury threshold. Our previous studies for the THOR and Hybrid-III dummies have shown that highly repeatable dummy responses can be obtained if the inflation and bag folding can be tightly controlled for each test in the laboratory [6-8]. Other studies have also demonstrated the importance of dummy position control [14]. The dummy position was well controlled for the present work. On the other hand, the variability of the pyrotechnics and bag folding in the fleet air bag modules is something that may not be as easily controlled by the scientific researcher in laboratory tests.

Data variability can be an important issue for scientific research and dummy evaluation. It is likely that the range of bag inflation variability is within the manufacturer's expectation, and in terms of standard safety evaluation, it may not result in any significant differences in injury metrics such as that demonstrated by the HIC_{15} values that are all well below the injury threshold. One way to circumvent data variability is to tightly control the inflation process. However, it is probably a reality that some fleet air bags will not inflate with high repeatability as the present work has demonstrated. When these bags are used for research, it is desirable that a significant number of repeat tests are performed with the statistical variation of the results quantified.

By its design nature, the THOR-NT neck separates the musculature load from the spinal ligamentous load on the neck, which results in a lower OC moment than the total cross-sectional value. The test data obtained confirmed the expected performance of the THOR-NT head/neck complex design.

The tests performed are not standard regulatory tests but rather scientific studies for the evaluation of the THOR-NT dummy. It should also be noted that there are no injury criteria defined for the THOR-NT dummy, nor are there standard OOP positions defined for using the THOR-NT dummy. Part of the purpose for the present work is to collect scientific data to understand the attributes to the variability in the dummy responses so that well-defined OOP positions for the THOR-NT dummy can be established in the future. In addition, injury criteria for the THOR-NT will still need to be established and the present work contributes to the understanding of air bag load paths to the neck in OOP conditions.

A limitation of the present work is that the number of repeat tests for each case is small. In addition, a limited range of driver side air bags was tested and only at one OOP position.

CONCLUSIONS

Comparative tests have been carried out successfully for five late model driver side air bag models using THOR-NT in the ISO-1 position. The major findings are that the inflation variation in four of the five air bags was the cause of highly variable neck moment responses in the THOR-NT. Neck tension, on the other hand, was not influenced nearly as much by the inflation variation. However, neck tension appears to be the most critical load and almost all of the tension is passed through the ligamentous spine, with very little load borne by musculature. Neck tension was shown to approach the human threshold value for one of the bags. The THOR-NT dummy has shown good usability for the test effort and was successful in capturing the effects of inflation variability on head/neck responses.

ACKNOWLEDGEMENTS

This research effort was sponsored by the National Highway Traffic Safety Administration (NHTSA) through a Joint Cooperative Research Agreement with the US Army Medical Research and Materiel Command under contract W81XWH-06-C-0051. The support from Dr. Erik Takhounts from NHTSA as COTR for this investigation is appreciated.

REFERENCES

1. Haffner, M., Eppinger, R., Rangarajan, N., Shams, T., Artis, M., and Deach, D., (2001) “Foundations and Elements of the NHTSA THOR Alpha ATD Design,” Paper #458, 17th International Technical Conference on the Enhanced Safety of Vehicles, HS 809 220 (U.S. DOT, 2001).

2. Kent, R., Lessley, D., Shaw, G., and Crandall, J., (2003) “The Utility of Hybrid-III and THOR Chest Deflection for Discriminating Between Standard and Force-Limiting Belt Systems,” SAE Paper 2003-22-0013, in the 47th Stapp Car Crash Conference Proceedings.

3. Xu, L., Jensen, J., Byrnes, K., Kim, A., Agaram, V., Davis, K.L., Hultman, R.W., Kostyniuk, G., Marshall, M.E., Mertz, H., Nusholtz, G., Rouhana, S. and Scherer, R., (2000) “Comparative Performance Evaluation of THOR and Hybrid-III,” SAE Paper 2000-01-0161, SAE 2000 World Congress, Detroit, Michigan, March 6-9, 2000.

4. Pintar, FA, Yoganandan N, and Baisden J. (2005) “Characterizing occipital condyle loads under high-speed head rotation,” SAE paper 2005-22-0002, in the 49th Stapp Car Crash Journal, 49:33-47.

5. Dibb, A.T., Nightingale, R.W., Chancey, V.C., Fronheiser, L.E., Tran, L., Ottaviano, D., Myers, B.S., (2006) “Comparative Structural Neck Response of the THOR-NT, Hybrid-III, and Human in Combined Tension-Bending and Pure Bending,” Stapp Car Crash Journal, 50:567-581.

6. Chan, P. C. and Lu, Z. (2003) “Evaluation of Hybrid-III and THOR Dummy Head/neck Responses to Airbag Load at Close Proximity,” 2003 IRCOBI Conference, Lisbon, 2003.

7. Chan, P. C. and Lu, Z. (2004) “Laboratory Study of Hybrid-III and THOR Dummy Head/neck Responses to Airbag Load at Close Proximity,” SAE Paper 2004-01-0320, 2004.

8. Lu, Z. and Chan, P. C. (2004) "Out-of-Position Airbag Load Sensitivity Study,” SAE 2004 Transactions Journal of Passenger Cars: Mechanical Systems, 2004-01-0847, pp. 507-520, 2004.

9. Bandak, F., Chan, P. C., Ho, K. H., and Lu, Z. (2002) “An Experimental Air Bag Test System for the Study of Air Bag Deployment Loads.” Int. J. Crashworthiness, 7(2), pp.1-12.

10. National Highway Traffic Safety Administration, U.S. Department of Transportation, Motor Vehicle Safety Standard No. 208, Notice of Proposed Rule Making.

11. SAE J2238 (1995) “Airbag Inflator Ballistic Tank Test Procedure,” SAE Surface Vehicle Recommended Practice, March 1995.

12. SAE J211 (1995) “Instrumentation for Impact Test,” SAE Surface Vehicle Recommended Practice, March 1995.

13. User Manual,“THOR Instrumentation Data Processing Program”, November 2001, GESAC-01-06.

14. Bass, C. R., Crandall, J. R., Bolton, R. R., Pilkey, W. D., Khaewpong N., and Sun, E. (1999). “Deployment of Air Bags into the Thorax of an Out-of-Position Dummy,” SAE Paper 1999-01-0764, Air Bag Technology 1999, SAE SP-1411.

Biomechanical Response of Head/ Neck/ Torso and Cervical Vertebral Motion to Lateral Impact Loading on the Shoulders of Volunteers

Koshiro Ono
Susumu Ejima
Japan Automobile Research Institute
Koji Kaneoka
Makoto Fukushima
Department of Orthopaedic Surgery, University of Tsukuba
Shintaro Yamada
Sadayuki Ujihashi
Tokyo Institute of Technology
Japan
Paper Number 07-0294

ABSTRACT

To understand the response of the head, neck and torso during a lateral collision, and to investigate the relation between cervical vertebral motion and the occurrence of neck injuries, lateral impact experiments were conducted on the shoulder areas of human volunteers. Test subjects consisted of 8 volunteers (5 males and 3 females). For the analysis of cervical vertebral motions of each subject, a cineradiography system was used. A VICON motion photographic device was also used for the three-dimensional analysis of head/neck/torso motions. In the experiment, 3 levels of impact force (400N, 500N, and 600N) were applied considering both the presence and absence of muscle tension.
Cervical vertebral rotations all started at 35 ms, but the time required to reach the peak rotation increased toward the upper vertebrae, with C7 and T1 peaking at 120 ms and the final peak in the head at 120 ms. At around 35-80 ms, the rotation angle of C5 surpassed those of the head and C4 showing that the cervical spine was bending into an S-curve. This phenomenon shows the same type of cervical vertebral motions causing whiplash during a rear-end collision. Also, extreme compression was at work in the vertebral disc and/or the facet joint in C6/C7 and C7/T1, suggesting a high probability of injury occurring in the neck.

INTRODUCTION

Vehicle occupants involved in automobile accidents but saved from fatality with injury severity level reduced to serious - minor are increasing, owing probably to the implementation of automobile safety measures and advances made in emergency medical treatments. It can be deduced that the increase in number of those with severe - minor injuries is attributable to the abovementioned developments. In order to keep pace with this development, active studies are being made for further enhancement of automobile safety, particularly against vehicle frontal collisions. Despite such efforts, the number of those injured by rear-end collisions is increasing significantly (Kraft et al., 2002), which is considered by some researchers as a "trade-off" between the number of fatalities and the number of "severe - minor injuries", with the priority set on the reduction of the fatalities. Regarding neck injuries, such increase were found not only in rear-end collisions but also in lateral-collisions (Hell et al., 2003). The same as in the case of rear-end collisions, the neck injury mechanism in lateral-collisions has not been clearly determined, with many questions still remaining unsolved (Kumar et al., 2005, Ito et al., 2004, Yoganandan et al., 2001). One of the reasons is the scarcity of biomechanical studies conducted on human head/neck/torso impact responses in lateral-collisions. In this regard, a new test equipment called "head/neck inertia impactor" was used in this study in order to analyze the "human head/neck junction" while applying a lateral impact to the shoulder. To be more specific, volunteers were impacted on their shoulders to simulate automobile lateral-collisions, and study human head/neck/torso impact responses as well as cervical vertebral motions. Differences in neck muscle responses between the male and female volunteers were also investigated.

EXPERIMENTAL METHODS

Lateral Inertia Impactor

An inertia impactor (Figure 1) specially designed for this study was used in order to investigate head/neck/torso responses and cervical vertebral motions of subjects submitted to a lateral inertia

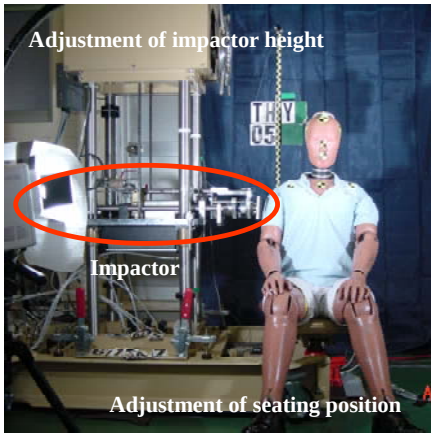

Fig.1 Lateral inertia impactor

impact. The test equipment consists of a compressed air storage/coil spring unit to eject the impactor, the impactor height adjuster, and the test subject sitting position adjuster (forward/ backward & up/down). The front plate, pushed against the impactor front was fixed to the piston through the piston rod. The compressed air is stored in the cylinder with the piston fixed to the air chuck located at the rear end. The impactor mass is 8.5 kg. The impactor is ejected by opening the air chuck, and impact is applied to the back of test subject. A coil spring is provided to control the impactor stroke and the rise of impact load. The stroke setting and the rise of impact load can be varied per test.

Head/Neck/Torso Visual Motions

In order to record the kinematics of the head/neck/torso of each subject during impact, a high-speed video camera with a photographic capability of taking 500 frames/s was used. The head rotation angle and the displacement relative to the torso (the first thoracic vertebra: T1) were calculated by tracing the motion of each marker adhered to the subject according to the photographic images. A VICON motion photographic device (125 frames/s) was also used for the three-dimensional analysis of head/neck/torso motions.

Table 1 Anthropometric data of the subjects

	Age	Sex	Height (cm)	Weight (kg)	Sitting Height (cm)	Mass of head (estimate) (kg)	Inertia of head (estimate) (10^{-2}kgm^2)
1	25	M	172	67	97	4.28	2.21
2	23	M	170	63	94	4.14	2.14
3	22	F	162	46	83	3.63	1.85
4	23	F	166	51	88	3.77	1.93
5	24	F	161	58	86	3.98	2.04
6	23	M	180	85	91	4.97	2.59
7	24	M	174	61	90	4.07	2.10
8	24	M	181	77	96	4.64	2.42

Cervical Vertebral Motions Using Cineradiography System

For the analysis of cervical vertebral motions of each subject during impact, a cineradiography system (Philips: BH500) was used. The system is capable of taking cervical vertebral images at the rate of 60 frames per second with 16.67 ms intervals.

Experimental Conditions

Using five healthy male and three healthy female adults as human volunteers, experiments on the head/neck/torso impact responses and the cervical vertebral motions upon lateral inertia impact was conducted. Table 1 shows anthropometric data on human volunteers. The impact loading direction was set vertical (0 deg inclination) against the shoulder on one side (Figure 2). To be more specific, each test subject sat on one side of the impactor, with the back set practically straight against the stiff seat, so that the impact direction become parallel to the line connecting the acromion and the lower part of the cervical vertebrae. In order to analyze the differences in impact loading directions, the impact was also applied from 15 deg forward and 15 deg backward directions (Figure 2), in addition to the 0 deg direction. The impactor surface is rectangular with an area of 100 mm x 150 mm. The impact loading location against the subject's shoulder was set so that the position of acromion would become the same as that of the impactor upper surface. In order to find the difference in effects of neck muscle response on the head/neck/torso motions, the states of muscle were set in tensed and relaxed conditions, respectively. The impact load was set at 3 different levels such as 400 N, 500 N and 600 N in order to find the differences in head/neck responses to the lateral impacts. For the direction with 0 deg inclination, impact responses were compared between cadaver tests and those on the volunteers. Table 2 shows the different test conditions classified

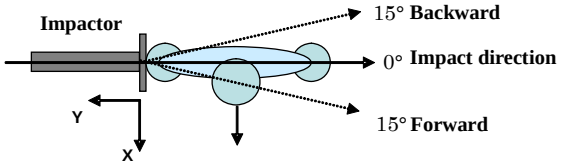

Fig.2 Impact directions

by differences in sex (male and female), impact loading levels, impact directions and states of muscle, with different combinations of test conditions.

Table 2 Test conditions

No. of Subject	Sex	Impact force (N)	Impact direction	Muscle condition
8	Male Female	400	15° forward	Relaxed Tensed
		500	0 degree	
		600	15° backward	

Informed Consent for Volunteers

The informed consent procedure in line with the Helsinki Declaration (WHO/CIOMS, 1988) was conducted in order for the volunteers to be fully informed of the purpose and method of experiments and also to ensure their full consent. The details/contents of the experiments were subjected to the approval of Special Committee of Ethics, Medical Department, Tsukuba University.

ANLYTICAL METHODS

Impact Force Applied to Head/Neck

Head acceleration was measured with the head 9 channel accelerometer, first thoracic vertebra (T1) acceleration was measured with 3-axis accelerometer, and electromyogram was analyzed. The measuring instruments were the head 9ch accelerometer (X, Y & Z), head angular velocity sensor (X, Y & Z), T1 accelerometer (X, Y & Z) and the pelvis accelerometer. The locations where the sensors were attached are shown in Figure 3. A mouth-piece suitable for the teeth profile (teeth impression) was prepared for each test subject. Assuming that the head is rigid, the head coordinate system was set in line with the location of anatomical center of gravity. The 9 channel acceleration measurement method (Ono et al., 1980) was applied according to the coordinates of each accelerometer in this system, and the rotational and linear accelerations at the head CG were calculated.

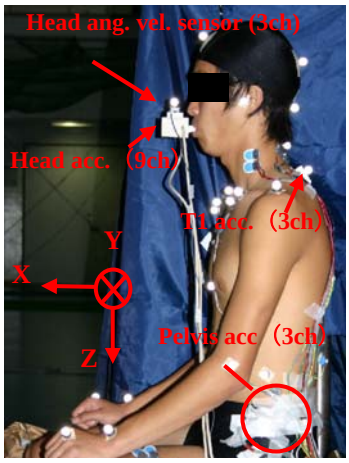

Fig.3 Mounting of accelerometers and rotational velocity sensors

Torso Acceleration (T1)

For the measurement of acceleration at T1, a three-axial accelerometer was attached onto the skin over a spinous process of T1.

Three-dimensional Motions of Head/Neck/Torso

The three-dimensional motions of head/neck/torso were measured by means of a VICON Motion Capture. Then the right-shoulder strain (displacement), left-shoulder strain (displacement), head rotation angles (X, Y & Z), T1 rotation angles (X, Y & Z) and the head rotation angles relative to T1 were analyzed.

RESULTS

Characteristic Aspect of Neck Impact Loading & Visual Motions

A 600 N impact loading experiment (in relaxed muscle condition) is shown in Figure 4, with the sequential photographs of the head/neck/torso motions during impact. X-ray of the neck motions under the same test conditions are shown in Figure 5. Figure 6 shows the corridors of the impact forces, the impact velocities, and the impact accelerations of impactor measured in 600 N impact loading experiment (in relaxed muscle condition). The linear and the angular accelerations at the head CG (X, Y & Z) calculated from the values measured with the head 9 channel accelerometer, the accelerations (X, Y & Z) at the T1 are also shown. Figure 7 shows the neck forces (Fx, Fy, Fz, Mx, My & Mz), and the visual head (head displacements and head rotational angles) motions in relation to the T1. Figure 8 shows the visual motions in relation to the shoulder strains (at the sternum upper end and the right or the left acromion) of the right shoulder (right acromion) and the left acromion). On the other hand, the rear view and the lateral views of spine trajectories by the VICON are shown in Figure 9.

Phase 1 [0-50 ms] - The duration of impact for each one of 8 test subjects were 70 ms or so (Figure 6a). The impact load peak levels were fluctuating, as the impactor and the shoulder were not in complete contact in the initial stage of impact. This presumably resulted in the relatively low impact peak level in the initial stage and the relatively high peak level in the secondary stage. The T1 accelerations, on the other hand, showed that the maximum value was found around 50 ms (Figures 6j-6l), while that of the head

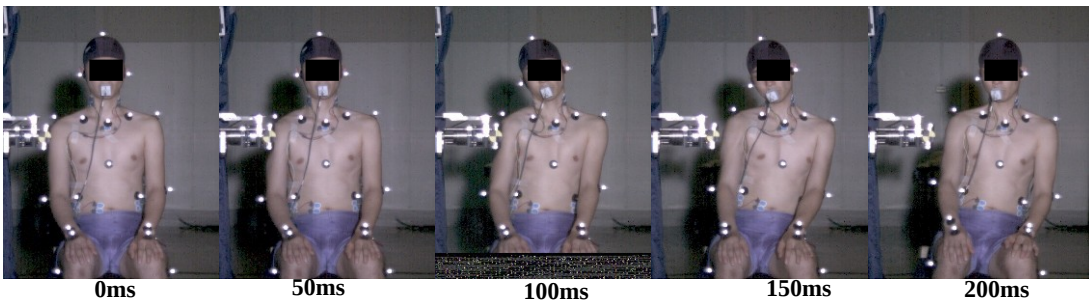

Fig.4 Sequential motions of head/neck/torso (Impact forces: 600N, Relaxed condition)

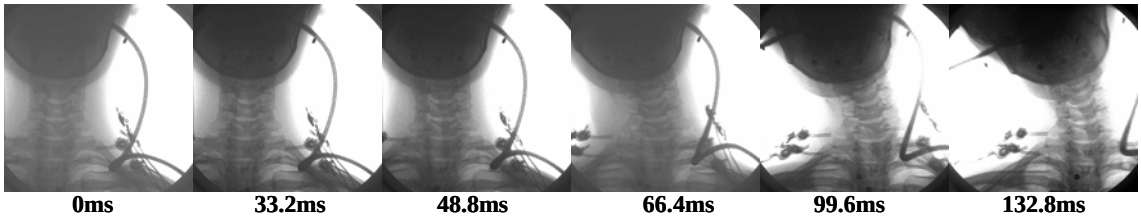

Fig.5 Sequential images of cervical vertebrae by cineradiography (Impact force: 600N, Relaxed condition)

was around 60 ms (Figures 6d-6f). The maximum values of T1 and the head in the Y-axial direction were 55 m/s^2 and 18 m/s^2, respectively. It is deduced that the axial forces between the T1 and the head were acting in opposite direction of compression, as the accelerations of T1 and the head in the Z-axial direction were reversed around 50 ms. The rotations of the head and T1 around the X-axis were reversed around 30 ms. The rotations around the Z-axis were also reversed. The neck shear force (in Y-axial direction) and the neck moments around X-axis and Z-axis did not show their maximum values around 50 ms (Figures 7m), 7q), 7r)), but the axial force of neck in Z-axis showed the maximum value at 50 ms or so. The right shoulder strain (on the impact side) showed the maximum value around 70 ms (Figure 8a). A slight torsion of upper cervical vertebrae was found around the Z-axis (Figure 5).

Phase 2 [50-100 ms] - The impact was continually set up to 70 ms or so (Figure 6a), and the shoulder was separated from the impactor due to the torso inertia. Hence, the acceleration at each portion of the head drops thereafter (Figures 6d-6f). However, the head rotates laterally against the torso, and the acceleration in the X-axial direction starts to increase around 90 ms, as the head is subjected to a restriction by the lateral bending at the same time. The head rotation angles found from the three-dimensional motion analysis by means of VICON Motion Capture showed the maximum values around 100 ms in both X and Z axial directions (Figures 9a-9b). The timing was roughly the same as the timing when the head rotational angle relative to T1 was highest. The maximum value around the X-axis was 32 deg, and 25 deg around the Z-axis. Similar to this trend of head acceleration, the neck shear force decreases around 90 ms, but increases again as the head acceleration was restricted by the lateral bending. The displacements of right and left shoulders and the strains start resuming at the initial states around 80 ms, while the upper cervical vertebral torsion and the lateral extension which occurs mainly at the lower cervical vertebra also started (Figure 5).

Phase 3 [100-300 ms] - The impact loading already stopped, but the entire body keeps rotating clockwise due to inertia. The T1 acceleration in Y-axial direction converged around 150 ms, whereas the head acceleration remains up to 200 ms or so (Figures 6d-6f). The T1 rotation angle around the Y-axis showed gradual changes after 100 ms, while the head keeps on rotating. The lateral extension of cervical vertebrae starts to end, resuming the initial states while maintaining the torsion in the Z-axial direction. It was found from the three-dimensional motion data obtained with VICON that the torsion angle around the Z-axis resumed the initial state at 300 ms or so (Figure 9b). The lateral extension of cervical vertebrae started to resume in the initial state while maintaining the torsion in the Z-axial direction (Figure 5).

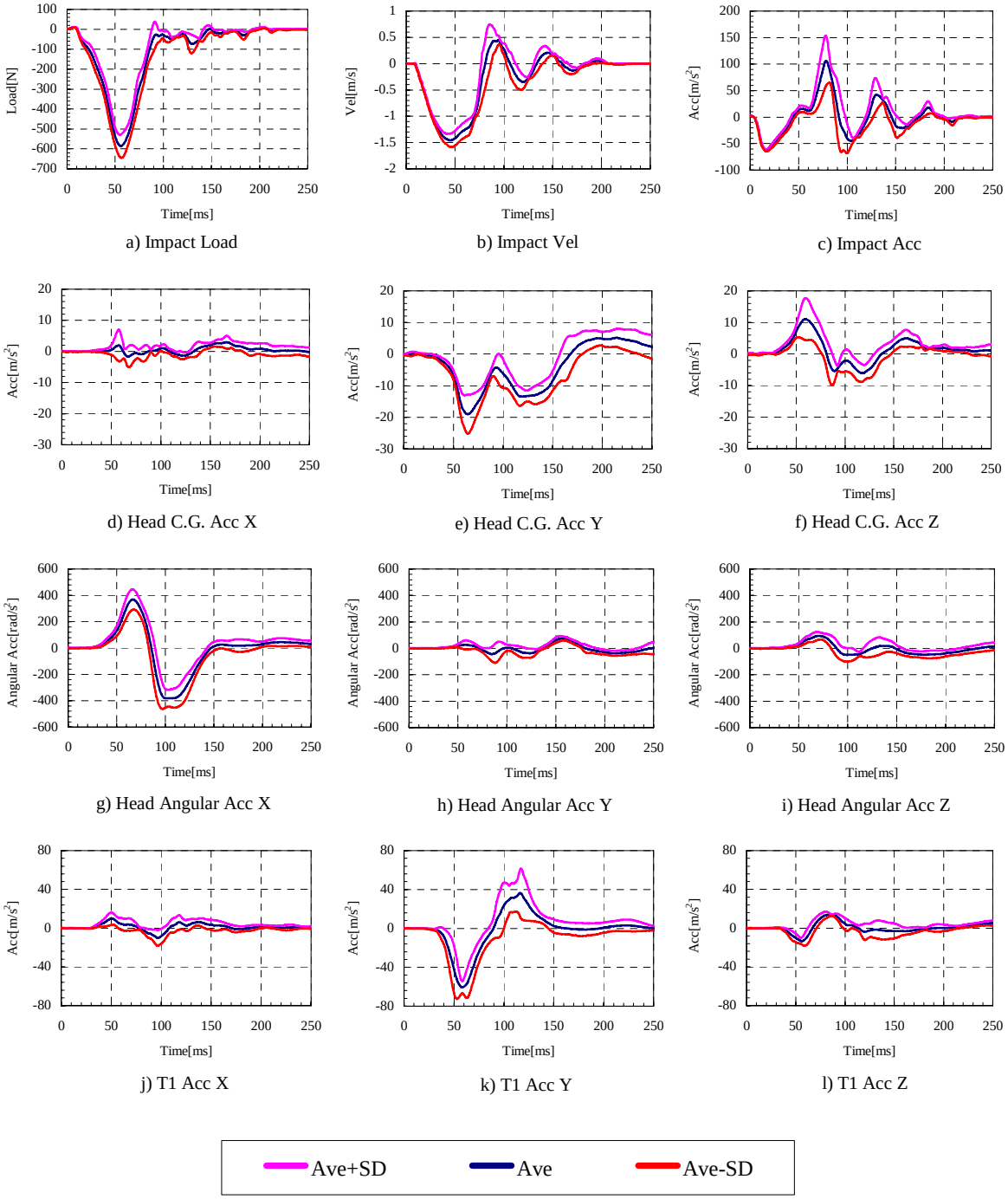

Fig. 6 Impact load, Head C.G. Acc., Head angular Acc., and T1 Acc., (Relax, 600N)

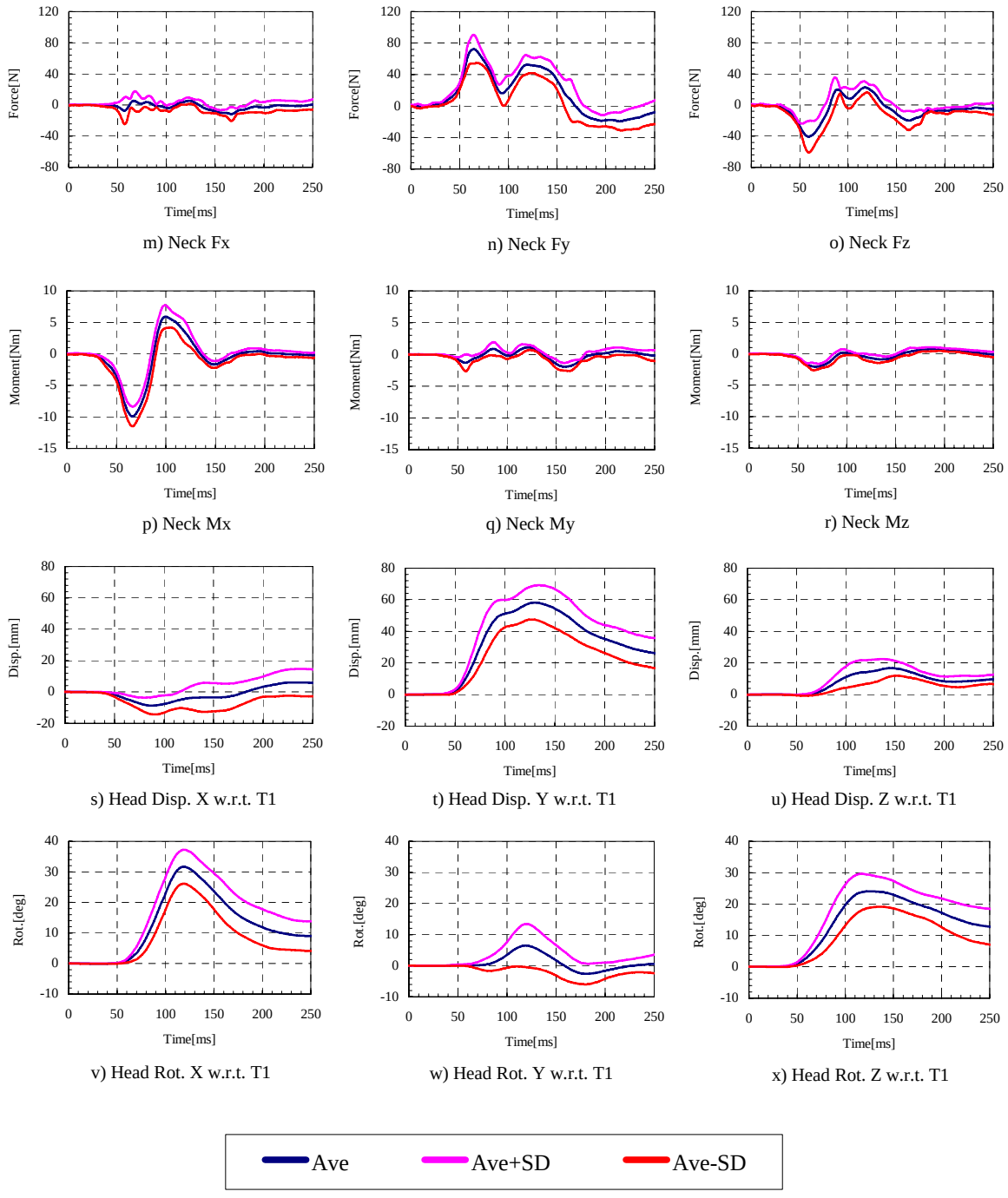

Fig. 7 Neck force, Neck moment, Head Disp. and Rot Ang. w.r.t. T1 (Relax, 600N)

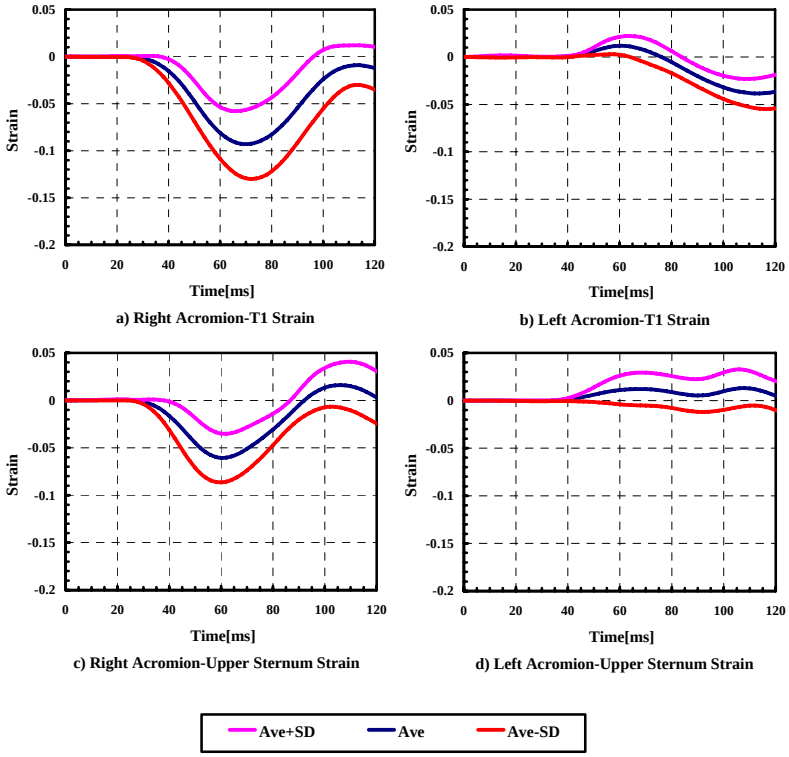

Fig. 8 Shoulder strain at the sternum upper-end and the right or left acromion

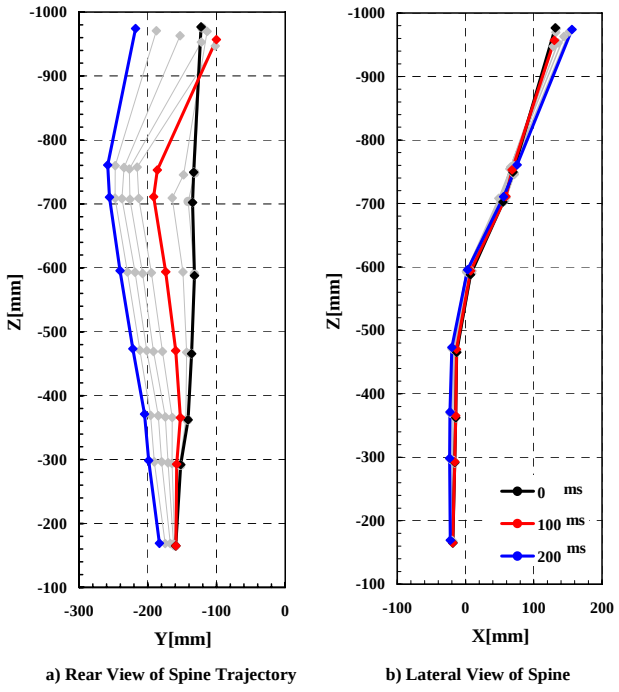

Fig. 9 Views of spine trajectories by the VICON

DISCUSSION

Effect of Differences in Muscle Functions of Head/Neck/Torso Impact Responses

The average value of T1 acceleration for tensed/relaxed muscle conditions with an impact load of 600N is shown in Figure 10. The maximum of T1 acceleration becomes 60m/s^2 in the case of the relaxed muscle condition. On the other hand, the maximum of T1 acceleration becomes 50m/s^2 in the case of tensed muscle condition. Suppression of T1 acceleration under the different muscle conditions was observed. Generally in the case of tensed muscle condition, impact force is transmitted easily to the T1 region when stiffness of the shoulder structure increase. The T1 acceleration rapidly increases according to this phenomenon, and its value becomes greater. Furthermore, effective mass of the shoulder region which was impacted showed higher stiffness. As a result, T1 acceleration decreased and there was an increase in muscle tone, thus, impact force acting on the upper neck is reduced (Fig.11) at an average of 15%. Furthermore, in the case of tensed muscle condition, the motion of head rotation is suppressed so that the stiffness of neck structure itself is increasing (Fig.12 and Fig.13). According to this result, it can be said that the impact motion responses of head/neck/torso easily change based on the different state of muscle conditions.

Effects of Differences between Male & Female on Head/Neck Impact Responses

The maximum of T1 acceleration and head C.G. acceleration under the relaxed muscle condition with impact force of 600N (three males and two females) are shown in Fig.14 and Fig.15. As for the head C.G. acceleration, female subjects showed greater value than male subjects. For the T1 acceleration, no difference was seen between male and female. As a result, even if the force level in lateral impact is

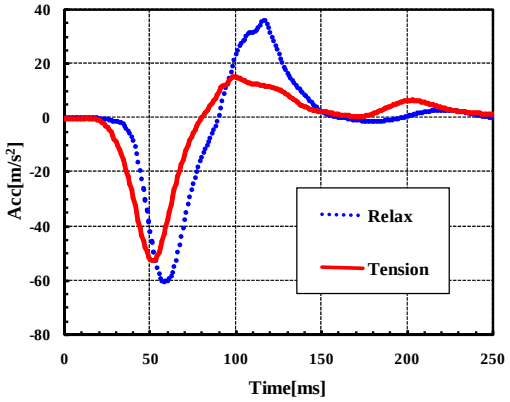

Fig. 10 Comparison of T1 acceleration between relaxed and tensed muscle conditions

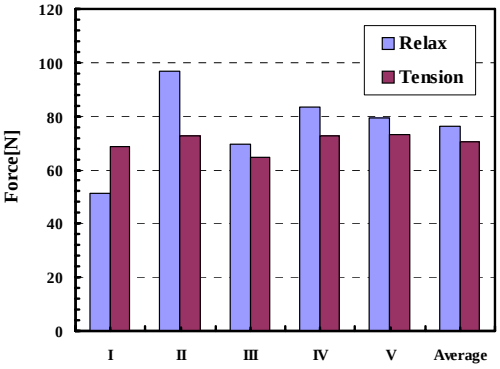

Fig. 11 Comparison of neck shear force (Fy) between relaxed and tensed muscle conditions

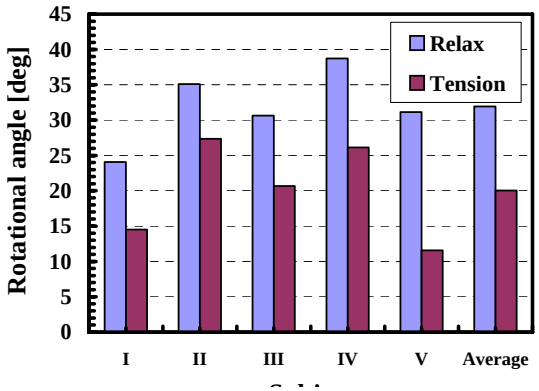

Fig. 12 Comparison of head rot. ang (Y) w.r.t. T1 between relaxed and tensed muscle conditions

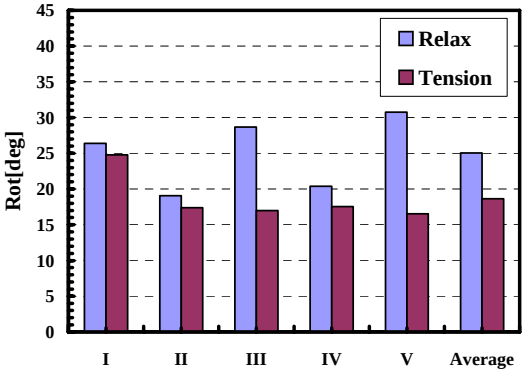

Fig. 13 Comparison of head rot. ang (Z) w.r.t. T1 between relaxed and tensed muscle conditions

almost same, difference of the head/neck motion is observed between male and female. This could probably be due to the smaller head mass of females compared to males. Furthermore, it is thought that the structure size of cervical vertebrae of a female being small might be the cause. The maximum head displacement relative to T1 in the Y-axis and the maximum head rotational angle relative to T1 in the X-axis under the relaxed muscle condition with impact force of 600N are shown in Fig.16 and Fig.17, respectively. The displacement and rotation of head/neck for both male and female were suppressed by doing muscle tone. However, the displacement and the rotation of the head/neck for two female subjects were greater than those of male values under the tensed condition, whereas no difference was observed between male and female under the relaxed condition. According to this situation, it is suggested that under tensed muscle condition, stronger muscular strength of males in general can greatly depress the head/neck/torso motions. On the other hand, females who have weak muscular strength, has difficulty in suppressing the global motion. According to the difference in responses of head/neck/torso between males and females, it is supposed that there will be a higher risk of neck injury for females.

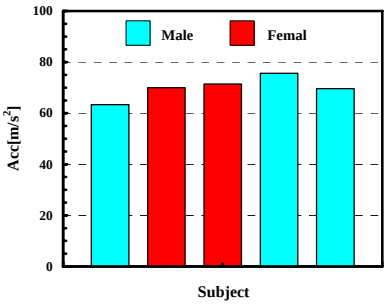

Fig. 14 Max. T1 acc. (Relax, 600N)

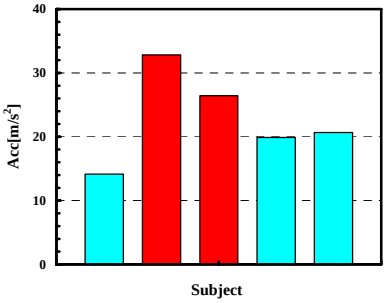

Fig. 15 Head C.G. acc. (Relax, 600N)

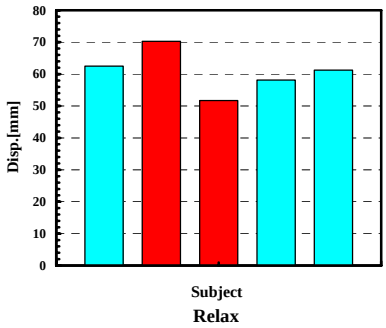

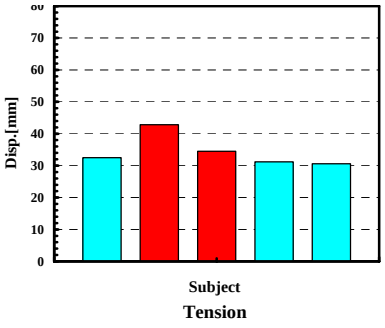

Fig. 16 Head disp. (Y) w.r.t. T1 (600N)

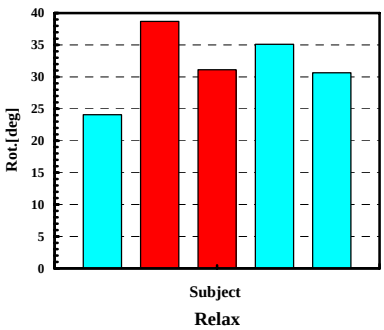

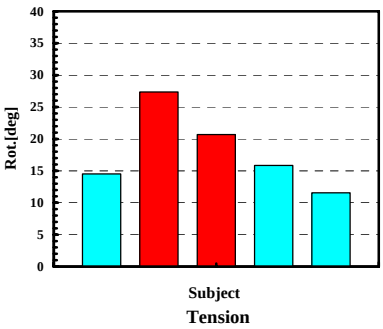

Fig. 17 Head rot. ang. (X) w.r.t. T1 (600N)

Effect of Shoulder Structural Deformation on Head/Neck Impact Responses

Sabine et al (2002, 2003, and 2004) reported that a difference of motion such as the clavicle and the shoulder blade etc. was clarified in the experimental studies on the PMHS lateral shoulder impacts. In the lateral collision, the impact which went from the shoulder takes the influence of the shoulder structure greatly before reaching neck region when an impact acts on the occupant's shoulder region through the vehicle inside structure such as a door panel. And, a change in the impact energy dispersion of the shoulder region, the impact transmission direction of the torso and so on occurs at the same time. The shoulder structure which influences the motion responses of head/neck in the lateral impact was examined here.

When a lateral impact is imposed to the shoulder region, it is transmitted to the clavicle and thorax, the sternum through the shoulder blade, and it influences the neck region consequently through T1 region (Fig.9). The compression strain between the right acromion and the T1 was greater (Fig.8a), Fig.8c)). This corresponds to the result of the PMHS experiment by Sabine et al (2002, 2003, and 2004). It is not compressed comparatively because the clavicle exists between the acromion and the sternum and it is fixed firmly when an impact is imposed from the lateral direction to the shoulder region. The shoulder blade may slide behind the aperture thoracic superior by the impact, and greatly compress in the acromion and the T1. In other words, the acromion and the aperture thoracic superior though an impact is transmitted directly, and the transmission of the impact is delayed in the acromion and the T1. The rising time of the lateral displacement of shoulder markers were shown in Table 3. Displacement between the sternum top-end and the left acromion almost started at the same time, and the motion of T1 was delayed. This shows a difference in the impact transmission mechanism that the neighborhood of the bone structure on the torso front side such as the sternum and clavicle followed by the movement of the neighborhood of the bone structure on the torso rear side such as T1.

Table 3 Rising time of the lateral displacement of the shoulder markers (Relax, 600N)

Subject	Rising Time of Displacement (ms)			
	Right Acromion	Upper Sternum	T1	Left Acromion
I	8	16	26	14
II	8	28	30	22
III	8	18	22	16
IV	10	14	28	22
V	8	20	28	20
Average	8.4	19.2	26.8	18.8

It is understood that the different motion response was due to the structural difference of the rear and front torso as described above. An impact was introduced to the left acromion directly without deformation between the left acromion and the sternum top-end though the impact transmitted to the top-end of the sternum was transmitted to the left acromion through the clavicle on the opposite impact side. In other words, the left acromion was imposed an impact through the top-end of the sternum, and the left acromion was displaced backward. It can be considered that the strain of the left acromion and T1 showed slight tension at first, and as a result showed compression.

Characteristics of Cervical Vertebral Motions during Lateral Impacts

The head rotation was delayed for about 30ms to the neck, after which, head rotation begins. The rotation of C4 was lower than that of C5 in 35-80ms (Fig.18). It can be considered that the torso moves first, and then the left lateral moment acts to the upper neck as shown in Fig.19. Furthermore, C4/C5 which is the relative rotational motion of cervical vertebrae as shown in the Fig.20 showed a negative value in the early stage of impact. This indicated that the tension of the left cervical vertebral joint in C4/C5 and the compression of the right cervical vertebral joint in C4/C5 occurred. It was estimated that the rotational angle of C1～C3 which can not be analyzed in this experiment will be delayed from that of the lower cervical vertebra, and the rotational angle of the upper cervical vertebra will exceed that of the lower cervical vertebra. The rotation angle of C5 suppressed those of the head and C4, showing that the cervical spine has a bi-phases curvature form such as an S-curve. An S-shape form with relative left extension of upper cervical vertebra and relative right flexion of lower cervical vertebra was presented concretely, and it can be considered that the right bending moment was acting on upper cervical vertebra and the left bending moment was also acting on the lower cervical vertebra. This phenomenon shows the same type of cervical vertebral motions causing the whiplash during a rear-end collision.

Moreover, tension on the left side of the cervical vertebra always shows an increase tendency as shown in Fig.21. On the other hand, compression on the right side of the cervical vertebra (C4/C5～C7/T1 in 90-120ms) shows a constant value (Fig.22). The rotation angle of the cervical vertebra was depressed by restricted motion of the facet joint on the right of cervical vertebra, and it can be considered that larger compression acts on this area at the latter half of impact. The compression of the intervertebral disk decreased with the elasticity of the neck itself due to a decrease in compression and the axial force applied on the upper neck shifted to tension force after 130ms (Fig.23).

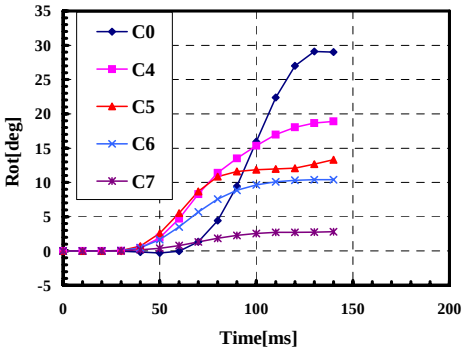

Fig. 18 Vertebral angle w.r.t. T1

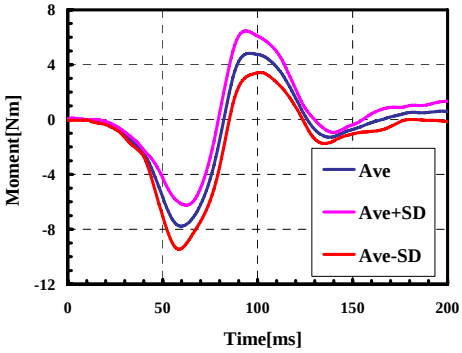

Fig. 19 Neck Moment

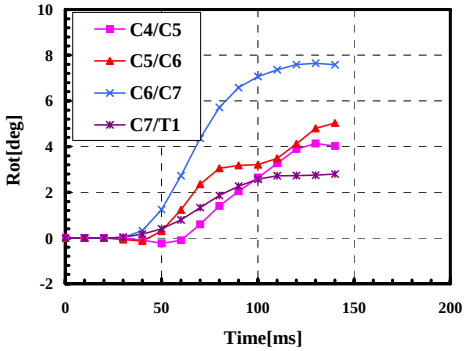

Fig. 20 Vertebral angle w.r.t. lower vertebra

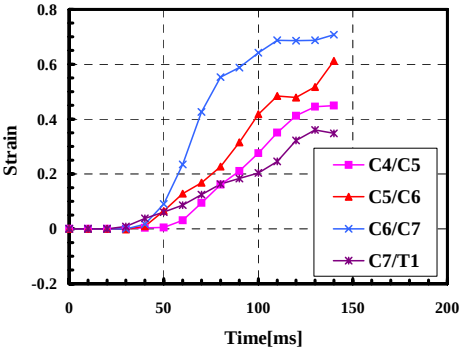

Fig. 21 Left side strain of intervertebral disc

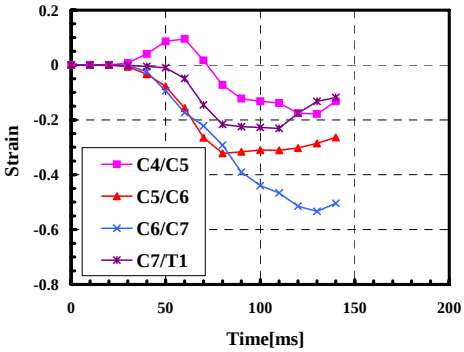

Fig. 22 Right side strain of intervertebral disc

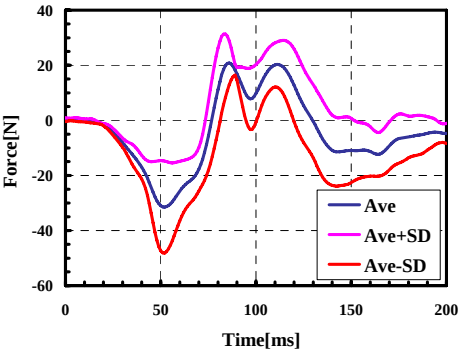

Fig. 23 Neck force Z

CONCLUSIONS

Using five healthy male and three healthy female adults as human volunteers, experiments on the head/neck/torso impact responses and the cervical vertebral motions upon lateral inertia impact have been conducted, with the impact forces set at 400 N, 500 N and 600 N, respectively. The findings obtained from the above are as follows:

Effect of Differences in Muscle Functions of Head/Neck/Torso Impact Responses

The suppression of head/neck/torso motions was greater in tensed muscle than in relaxed condition. The T1 displacement (18%) and the head displacement (48%) relative to T1 were more suppressed in the tensed condition than in relaxed condition.

Effects of Differences between Male & Female on Head/Neck Impact Responses

Regardless of the state of muscle tension, the displacement of acromion with respect to the first thoracic vertebra (T1) tends to be greater for male than for female subjects. As female shoulders tend to have less flexibility against impact than male, the female cervical vertebral motions are likely to show longer lateral extensions than male. It is suggested that the differences in muscle responses should be taken into account, in addition to the differences in shoulder anatomical structures, as marked differences between male and female.

Effect of Shoulder Structural Deformation on Head/Neck Impact Responses

When an impact is applied to a shoulder, the head/neck/neck impact responses become different even if the magnitude of impact on the torso is the same. Thus, it is suggested that the differences in head/neck/torso motions are caused by the differences in shoulder anatomical shape and/or front-rear structural differences. A shoulder has high three-dimensional flexibility and a wide range of movability, owing to the gleno-humeral and sternoclavicular joints, which facilitate vertical and lateral motions against lateral impacts. However, the shoulder movability would be restricted, if the direction of the lateral impact roughly aligns with the line connecting the acromio-clavicular joint and the sternoclavicular joint - i.e., the longitudinal direction of the clavicle.

Characteristics of Cervical Vertebral Motions during Lateral Impacts

Cervical vertebral rotations all started at 35 ms, but the time required to reach the peak rotation increased toward the upper vertebrae, with C7 and T1 peaking at 120 ms and the final peak in the head at 120 ms. At around 35-80 ms, the rotation angle of C5 surpassed those of the head and C4 showing that the cervical spine was bending into an S-curve. This phenomenon shows the same type of cervical vertebral motions causing whiplash during a rear-end collisions. Also, extreme compression was at work in the vertebral disc and/or the facet joint in C6/C7 and C7/T1, suggesting a high probability of injury occurring in the neck.

AKNOWLEGMENTS

The authors would like to give special thanks to the volunteers who understood the aim of the research and its contribution to current social needs.

REFERENCES

Compigne S., Caire Y., and Verriest J., Three Dimensional Dynamic Response of the Human Shoulder submitted to Lateral and Oblique Glenohumeral Joint Impacts, Proceedings of IRCOBI Conference, Sept. 2002, pp.377-379

Compigne S., Caire Y., Quesnel T., and Verriest J., Lateral and Oblique Impact Loading of the Human Shoulder 3D Acceleration and Force-Deflection Data, IRCOBI Conference, Lisbon (Portugal), September, (2003), pp. 265-279

Compigne S., Caire Y., Quesnel T., and Verriest J., Non-Injurious and Injurious Impact Response of the Human Shoulder Three-Dimensional Analysis of Kinematics and Determination of Injury Threshold, Stapp Car Crash Journal, Vol.48 (November 2004), pp.89-123

Hell W., Hopfl, F., Langweider K., and Lang D., Cervical Spine Distortion Injuries in Various Car Collisions and Injury Incidence of Different Car Types in Rear-end Collisions, Proceedings of IRCOBI Conference, 2003, pp.193-206

Kraft M., Kullgren A., Ydenius A., Tingval C., Influence of Crash Pulse Characteristics on Whiplash Associated Disorders in Rear Impact-Crash Recording in Real-Life Crashes. Journal of Crash Prevention and Injury Control, 2002

Narayan Yoganandan, Srirangam Kumaresan, Frank Pinter, Review Paper, Biomechanics of the cervical spine Part2. Cervical spine soft tissue responses and biomechanical modeling, Clinical Biomechanics 16, 2001, pp.1-27

Ono K., Kikuchi A., Nakamura M., Kobayashi H., and Nakamura N., Human Head Tolerance to Sagittal Impact - Reliable Estimation Deduced from Experimental Head Injury Using Subhuman Primates and Human Cadaver Skulls, 1980 Transactions of the Society of Automotive Engineers, SAE Paper No. 801303, 1980, pp.

3837-3866
Shigeki Ito, Paul C. Ivancic, Manohar M. Panjabi, and Bryan W. Cunningham,, Soft Tissue Injury Threshold During Simulated Whiplash A Biomechanical Investigation, SPINE Volume29, Number9 , 2004, pp979–987
Shrawan Kumar, Robert Ferrari, and Yogesh Narayan, Looking Away From Whiplash: Effect of Head Rotation in Rear Impacts, SPINE Volume30, Number7, 2005, pp760–768
WHO/CIOMS proposed guidelines for medical research involving human subjects, and the guidelines on the practice of ethics committees published by the Royal College of Physicians, The Lancet, November 12, 1988, pp.1128-1131

MODELING THE SEAT BELT TO SHOULDER-COMPLEX INTERACTION IN FAR-SIDE CRASHES

Clay A. Douglas
Brian N. Fildes
Monash University Accident Research Centre
Australia
Tom J. Gibson
Human Impact Engineering
Australia
Ola Boström
Autoliv Research
Sweden
Frank A. Pintar
Medical College of Wisconsin and VA Medical Center
United States of America
Paper Number 07-0296

ABSTRACT

Regulations and interventions to protect far-side occupants in crashes do not currently exist, despite these occupants accounting for 43% of the AIS3+ injured persons and 30% of the overall Harm in side impact crashes. Furthermore, no suitable ATDs or mathematical models have been developed to investigate far-side occupant dynamics. The aim of this study was to investigate seat belt to shoulder-complex interaction during the first phase of a far-side impact for incorporation into a multibody occupant model.

The model adaptations were derived based on quasi-static belt slip tests using two volunteers, a standard Hybrid III ATD and a Hybrid III Spring-Spine ATD. The model development was validated for this first phase of impact by comparison with shoulder belt force-time histories and head lateral displacements from lateral far-side sled tests using PMHS and a WorldSID ATD.

The newly adapted model correctly predicted seat belt to shoulder complex interaction in all of the quasi-static belt slip tests, compared to 50% and 67% for Hybrid III and Hybrid III Spring-Spine respectively. Furthermore, the model was able to predict the increasing likelihood of the seat belt engaging the shoulder when the D-ring moved rearward and pretension increased. For the validation tests, the magnitude and phasing of the shoulder-belt force-time and head displacement-time histories were generally within 10% of the PMHS results. In addition, the model was capable of predicting the location of occupant to seat belt interaction observed in the PMHS tests.

INTRODUCTION

Side impacts represent the second most common type of passenger vehicle crash to cause serious injury or death to the occupant behind frontal collisions (Fildes et al., 1991; Otte, 1984). Research into side impact is becoming more critical as it is projected that the number of elderly road users will increase. Elderly road users have an increased likelihood of being involved and seriously injured in a side impact crash compared to other age groups (Chipman, 2004).

In addition, while research attention and government regulations have focused on protecting nearside (or struck side) occupants of the vehicle, little attention has been paid to protecting far-side (or non-struck side) occupants. Research by Gabler et al. (2005a) using NASS/CDS and FARS data from 1997-2002 indicated that far-side occupants account for 43% of the seriously injured persons and 30% of the Harm in US side impact crashes. Furthermore, using MUARC in-depth data (MIDS) from 1993-2002, Gabler et al. (2005b) observed that far-side occupants accounted for 20% of the seriously injured persons and 24% of the Harm in Australian side impact crashes.

The primary form of restraint for a far-side occupant is the outboard mounted three-point seat belt. However, it has been recognized that this design does not provide adequate restraint for this crash configuration. Specifically, by preventing thorax and head excursion towards the struck side of the vehicle. This was most recently highlighted by Gabler et al., (2005a) where head and thorax injuries accounted for over half of the serious injuries sustained in these crashes. Added to that, the seat belt has been recorded as the source of injury in around 86% of

AIS2+ abdominal injuries sustained in far-side crashes (Gabler et al. 2005a).

In an earlier study, Mackay et al., (1993) conducted an analysis of 193 cases of restrained occupants in far-side crashes. It was observed that of those occupants with AIS ≤ 2 head injuries, 35% came out of the shoulder section of the seat belt. The authors suggested that "…as well as the direction of the impact, a number of other factors have a bearing on this event – the position of the upper anchorage, the size of the occupant, the seat position, the adjustment of the upper anchorage, and the looseness of the seat belt". Mackay concluded by stating that these problems may be alleviated through experimental work looking at improving seat belt geometry and pretensioning.

It had long been recognized that the seat belt was not ideal in all crash configurations. Knowing this, early laboratory studies by Adomeit et al., (1977) and Horsch (1980) examined the effect of impact angle on the restraint provided by the seat belt using anthropomorphic test devices (ATDs). Both Adomeit et al., (1977) and Horsch (1980) observed that for far-side impacts up to approximately to 40 degrees, the shoulder belt remained in the clavicular area and did not slip off the shoulder. At angles greater than this the thorax tended to slip out of the shoulder portion of the seat belt, leading to an increase in thoracic and head excursion. Horsch did however note that even at angles of around 60 degrees, significant energy was removed from the thorax by the seat belt before slippage.

In an attempt to reduce this lateral excursion, Horsch et al., (1979) and Kallieris & Schmitt (1990) used Post Mortem Human Subjects (PMHS) to investigate the effect of inboard belts. However, such designs were observed to induce neck injuries. One of the primary concerns with the use of an inboard belt is this neck loading, which can place the neck's vascular system and spinal column at risk of trauma (Sinson et al., 2003).

More recent attempts have been made to reduce occupant excursion towards the vehicle's struck side in a far-side crash (Stolinski et al., 1999; Boström & Haland, 2003; Pintar et al., 2006; Rouhana et al. 2006). Stolinski et al., (1999) investigated the effect of firing pretensioners on reducing lateral excursion using Hybrid III and SID ATDs. Boström and Haland (2003) investigated inboard airbags and a 3+2 seat belt design using a modified BioSID ATD; Pintar et al. (2006) investigated thorax and shoulder supports in addition to inboard belts using a WorldSID ATD; and Rouhana et al. (2006) investigated the use of a four-point seat belt using PMHS, BioSID and SIDIIs ATDs. Each study suggested methods of reducing head and thorax excursion, however, more research is required to ensure that these designs do not induce additional injuries, primarily to the thorax and neck.

Despite these attempts to design better restraints, therein lies a problem, no computer model or ATD is designed specifically for far-side impacts. WorldSID has been suggested to be the best of the available ATDs (Fildes et al., 2002), however, thorough validation is yet to be seen. A major limitation ATDs have is the ability to mimic the seat belt to shoulder complex interaction. This has come primarily from the fact that ATDs are designed to work within a narrow crash configuration band. In frontal crash tests, Hybrid III ATDs only have a single measurement device in the chest to measure the effect of shoulder belt load. However, up to half the belt load gets distributed through the shoulder where no measurement device exists (Kent et al., 2003). In side impacts, ATDs are to a large extent not validated using shoulder belts. As a result, the shoulder region of both frontal and side impact dummies is not ideal.

Tornvall et al., (2005) investigated this very aspect, more specifically looking at the performance of the shoulder complex of THOR in oblique impacts (both near and far-side). Despite a lack of sufficient PMHS tests in far-side configurations, Tornvall's results indicate a weakness in the kinematic shoulder response of the three ATDs, possibly related to limitations in shoulder range-of-motion and the lack of human-like shoulder complex design (Tornvall et al., 2005).

This investigation forms part of a larger study aimed at improving far-side occupant protection (Fildes et al., 2005). A subtask of this larger study involves developing a far-side occupant model. Due to the critical role of seat belt to shoulder-complex interaction in governing upper body kinematics in a far-side crash, it was deemed necessary to explore further.

OBJECTIVE

The aim of this study was to investigate seat belt to shoulder-complex interaction during the first phase of a far-side impact and incorporate this knowledge into a multibody occupant model.

METHODS

This study is separated into four components: quasi-static far-side tests categorizing the seat belt to shoulder-complex interaction; developing a model capable of mimicking this interaction; high-speed lateral far-side sled tests; and validating the model against these sled tests.

1g Quasi-Static Far-Side Tests

The aim of the quasi-static belt slip tests was to characterize the seat belt to shoulder-complex interaction in a far-side impact. Two factors identified by Mackay et al., (1993) – seat belt geometry and pretension, were investigated regarding their role in providing lateral restraint to the subject.

To achieve these aims, a test rig consisting of a rotating seat with appropriate safety measures was designed (Figure 1). It rotated the subject in the frontal plane, about an axis running horizontal to the ground through their thorax. When rotated 90 degrees, the subject experienced a 1g lateral force.

Figure 1. Rotating quasi-static test rig

The test subject was seated normally with the belt in the drivers position in a Volvo V70 seat. The seat back was positioned to the angle used in seat rating tests, the tilt and other chair settings being set to the mid-positions and were kept there throughout testing.

The seat X-position (fore/aft) was instrumented such that 5 positions: 0, 60, 120, 180, and 240 could be determined. These positions (measured in millimeters from most-rearwad) represented 0%, 25%, 50%, 75%, and 100% forward. Similarly, this represents moving the D-ring fore/aft (0 being the most forward D-ring, 240 being the most rear D-ring).

In addition to belt geometry, three belt pretensions were tested. Due to the difficulty in getting reproducible tensions, ranges were used instead of specific tensions. These were 0N, 100-150N, and 200-250N. The tension was produced prior to the test manually (not through actual pretensioner devices) and measured through a standard belt tension measurement system (Figure 2) and monitored from a continuous online display.

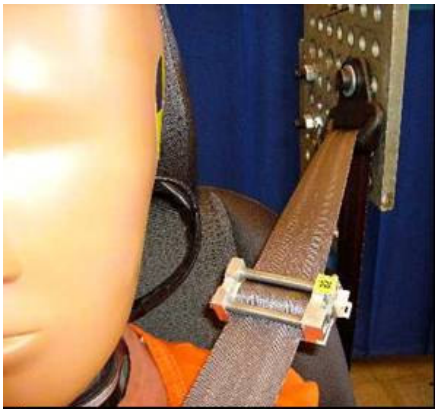

Figure 2. Seat belt tension measurement device and anchorage point

Three different subjects were put through the entire matrix of tests: A standard Hybrid III 50th Percentile Male ATD; A Hybrid III 50th Percentile Male with a Spring-Spine (as seen in Boström et al., 2005); and a male human volunteer of average height and weight. For the volunteer test, muscle tension was neglected as the subject was completely relaxed, with little or no muscle activity.

A second volunteer was exposed only to the X = 120, 0N pretension configuration to highlight the difference body size has on the resulting restraint. The second volunteer was more muscular and broad shouldered than the first volunteer. Volunteer 1's shoulder breadth was approximately 480mm, whereas the second volunteer's was 560mm.

The only measured outcome from these tests was whether the seat belt slipped off the shoulder or not, leading the results to be binary (i.e. yes or no). Five tests were conducted with each subject at the same configuration. As such, a percentage of times the belt slipped off the shoulder for each configuration could be determined. For instance, if the belt slipped off the shoulder in 5 out of 5 cases at a set configuration, the result would be 100%. If the belt only slipped twice, the result would be 40% and so on.

Modeling the 1g Quasi-Static Far-Side Tests

The test set-up geometry (as described in the previous section) was modeled in MADYMO 6.2.2 using the pre-processor Easi-Crash-MAD v5. A geometrically similar seat and seat belt was modeled using facet surfaces and finite elements respectively. Each was given realistic stiffness characteristics.

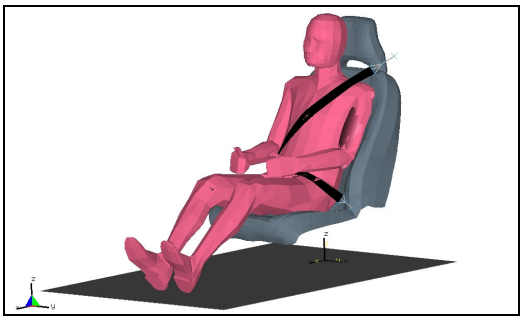

Figure 3. Human model in simulated 1g test

The human model used for these simulations was the TNO Human Facet Model. This model was recently validated against ISO TR9790 requirements for lateral impact by de Lange et al., (2005). The same study also demonstrated that the human facet model showed potential in frontal and oblique impacts (de Lange et al., 2005). The human facet model was identified to be the most suitable MADYMO model for far-side impacts (Digges et al., 2005).

As previously mentioned, modeling the seat belt to shoulder-complex interaction is a critical requirement of a far-side occupant model. The standard TNO Human Facet Model is not capable of replicating the contour variation of the shoulder-complex's boney structures, specifically the junction of the clavicle, scapula and humerus.

To address this issue, rigid ellipsoids were inserted into the region of the shoulder (Figure 4). The shoulder was represented by a sphere (degree 2 ellipsoid) of radius 0.053m. These dimensions coincide with those defined for a 50th percentile male in Tilley et al., (2002). The shoulder breadth of the human model was approximately 460mm.

Two additional ellipsoids were placed in the upper arm adjoining the shoulder ellipsoid to ensure the belt did not deeply penetrate the arm and get caught when the belt slipped off the shoulder. Each was modeled as a sphere of 0.045m radius, which coincides with the same arm thickness defined for arm ellipsoids in earlier versions of the TNO Human Facet Model.

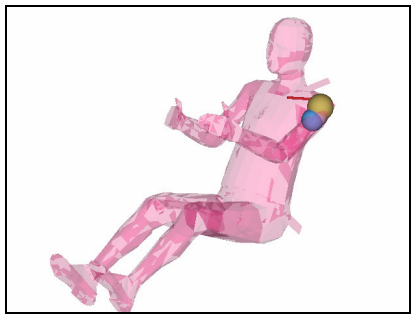

Figure 4. Rigid ellipsoids used to approximate the shoulder on the human model

A MB.FE Kinematic contact was then defined between the seat belt, clavicle and shoulder, so that the belt would not penetrate this region - ensuring the contour of the region (despite being approximated) is maintained. Due to the choice of contact type, a static friction coefficient for the belt and skin interaction could only be defined, rather than a specific velocity dependant function. As such, an approximated friction coefficient of 0.3 was used.

To start the simulation, the human model was firstly sat in the seat under gravity and allowed to come to equilibrium. Belts were then routed across the model such that anchor locations matched those used in the tests. For cases with pretension, simulated loads represented the middle of the ranges defined in the physical tests. To achieve this preload, linear belt segments were attached vertically from the D-ring with 125N and 225N loads added to the ends. This initiated initial penetrations in the model, which provided the preload prior to initiating the lateral 1g pulse.

Once the model was at equilibrium and the belts were in the correct position, a 1g lateral pulse was inserted to the model. This pulse was not a step input, rather a ramp, due to the rotating of the buck in the physical tests. Concurrently, the 1g used for pre-simulation (vertical direction) was ramped down. Each simulation lasted 1 second.

The measured outputs from the model included whether the belt slipped or not, and T1 lateral displacement – to quantify the effect of D-ring position and pretension on excursion.

Far-Side Lateral Sled Tests

Data from lateral far-side sled tests were utilized as means of model validation in this first phase of impact. Tests were conducted at 30km/h using a unique far-side impact buck which included, as a

standard configuration, a center console and outboard three-point belt system (Pintar et al. 2006).

For this study, two configurations of seat belt geometry and pretension were investigated with PMHS and a WorldSID ATD (Table 1). As a realistic worst case scenario, the Forward D-ring was located 120mm above and 30mm rear of the shoulder. The Middle D-ring was located 120mm above and 90mm rear of the shoulder. PMHS tests were conducted using the same procedures as described for the WorldSID tests (Pintar et al., 2006).

Table 1.
Sled Test Matrix

D-Ring Position	Pretension	Test Subject
Middle	100N	PMHS 1, WorldSID
Forward	0N	PMHS 2, WorldSID

For the PMHS tests, 2 unembalmed human cadavers were procured, medical records assessed and tested for Hepatitis A, B, C and HIV. Pretest x-rays and anthropomorphic data were obtained using established procedures (Pintar et al., 1997) (Table 2). PMHS were cleaned then dressed in a tight-fitting leotard with a head/face mask to ensure anonymity.

Table 2.
PMHS Sex and Anthropometry

PMHS	Sex (M/F)	Height (m)	Weight (kg)
1	M	1.73	67
2	F	1.60	70

To quantify occupant-to-seat belt interaction, seat belt force transducers mounted between the shoulder and D-ring measured shoulder belt load. To quantify lateral excursion, retro-reflective targets placed on the head, in addition to reference targets fixed to the sled and buck tracked three-dimensional, 1000 f/s motion (Pintar et al., 2006).

Modeling the Far-Side Sled Tests

The test set-up geometry (as described in Pintar et al. 2006) was modeled in MADYMO 6.2.2 using the pre-processor Easi-Crash-MAD v5 (Figure 5). The sled pulses used from the physical tests were directly inserted into the model. The same human model (including shoulder modifications) was used and executed in the quasi-static tests.

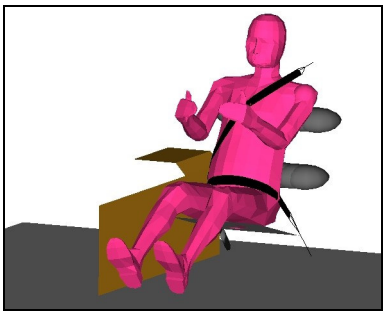

Figure 5. Human model in simulated far-side buck

Seat belts were modeled using finite elements and the center console was modeled using facet surfaces. Force-deflection characteristics for the center console and belts were defined in Pintar et al. (2006).

Within the model, contact between the human model and the center console was defined as a FE.FE (facet-to-facet) COMBINED contact. To achieve this, a stress-strain relationship was required for the paper honeycomb mounted to the console. This was approximated, since the honeycomb's rating was 15psi and 30psi respectively. This approximation can be seen in Figure 6.

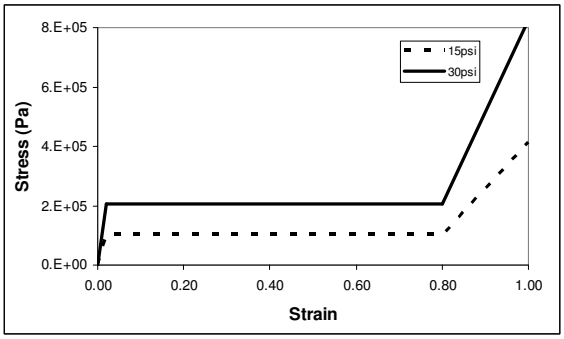

Figure 6. Approximated stress-strain relationship for paper honeycomb

Each simulation was executed for 240ms. The shoulder belt forces and head c.g lateral displacements were obtained from the relevant MADYMO output files.

RESULTS

1g Quasi-Static Far-Side Tests

Results from the physical tests and the simulations can be seen in Table 3. Only results from the four rearmost positions are shown as the most-forward D-ring (X=0) yielded the same result as X=60 Volunteer 1.

Table 3.
1g quasi-static test results. Numbers represent the proportion of time slip occurred at that configuration. Shading represents cases which match volunteer response

VOLUNTEER			
X pos (mm)	0N	100-150N	200-250N
60	*100*	*100*	*100*
120	*100*	*100*	*20*
180	*100*	*0*	*0*
240	*100*	*0*	*0*

HUMAN MODEL			
X pos (mm)	0N	125N	225N
60	*100*	*100*	*100*
120	*100*	*100*	*0*
180	*100*	*0*	*0*
240	*100*	*0*	*0*

HYBRID III SPRING-SPINE			
X pos (mm)	0N	100-150N	200-250N
60	*100*	*60*	*0*
120	*100*	*0*	*0*
180	*0*	*0*	*0*
240	*0*	*0*	*0*

HYBRID III			
X pos (mm)	0N	100-150N	200-250N
60	*60*	*0*	*0*
120	*0*	*0*	*0*
180	*0*	*0*	*0*
240	*0*	*0*	*0*

Results from the volunteer tests indicate that a trend exists between moving the D-ring rearward, increasing pretension, and thus, an increased likelihood of the belt engaging the shoulder. A visual example of cases where belt slip occurred and where the shoulder was engaged can be seen in Figure 7.

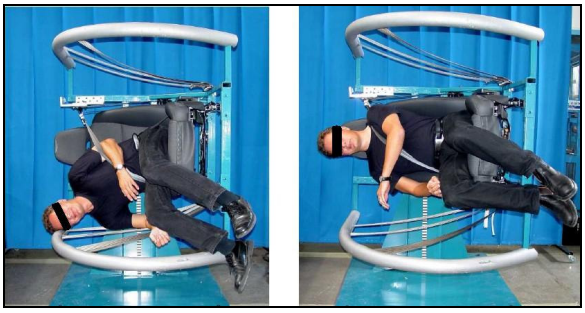

Figure 7. Volunteer in cases indicative of belt slip (left) and shoulder engagement (right)

As previously mentioned, the second volunteer was only tested in the X=120, 0N pretension case. For this configuration, the seat belt effectively restrained the larger occupant. Despite this only being a single configuration, it suggests that human anthropometry plays a major role in whether the belt restrains the human or not. It also suggests that more broad or muscular occupants may be better restrained by an outboard three-point belt in a far-side impact.

Results also highlight that the standard Hybrid III and the Hybrid III Spring-Spine ATDs are much more sensitive to changes in belt geometry and pretension than the human volunteer. Moreover, the standard 50th percentile Hybrid III and Hybrid III Spring-Spine only predicted the same binary outcome of slip or engagement in approximately 50% and 67% of the configurations when compared to the mid-sized volunteer. A visual example for the Hybrid III Spring-Spine in cases of belt slip and restraint can be seen in Figure 8.

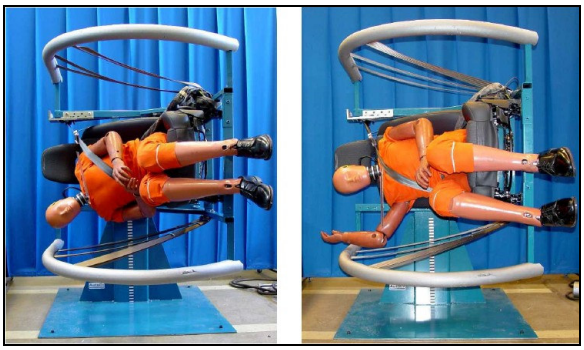

Figure 8. Hybrid III Spring-Spine in cases of belt slip (left) and shoulder engagement (right)

The difference between the way in which the volunteer and the ATDs interacted with the belt was noticeable. Specifically, the belt engaged the ATDs thorax instead of the shoulder complex. Of the two ATDs tested, the Hybrid III Spring-Spine ATD was more biofidelic in how belt slip occurred compared to the standard Hybrid III. However, the Hybrid III Spring-Spine was still more sensitive to D-ring position and pretension than the volunteer. This was related to the solid features of the thorax engaging the belt even when the belt slipped over the shoulder.

Conversely, the human model correctly predicted all of the binary outcomes from the mid-sized volunteer tests, in addition to the trend observed between D-ring position, pretension and belt slip. A visual example of cases where belt slip occurred and where the shoulder was engaged can be seen in Figure 9.

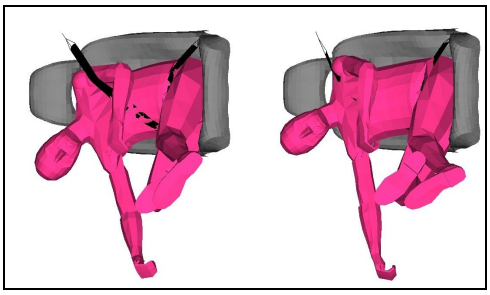

Figure 9. Human model in cases indicative of belt slip (left) and shoulder engagement (right)

Despite the match in binary results, the human model's upper body lateral motion appears stiffer than the volunteer. This is not surprising since this model (like the ATDs) is designed to perform at higher severity impacts than 1g.

In addition to the binary outcomes from the quasi-static tests, T1 lateral displacements were also plotted (Figures 10 and 11). This was done to quantify the effect different D-ring positions and pretensions had on the model's lateral displacement.

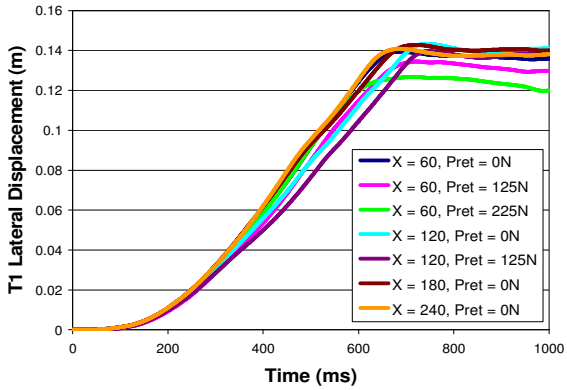

Figure 10. T1 lateral displacement vs. time for cases with belt slip

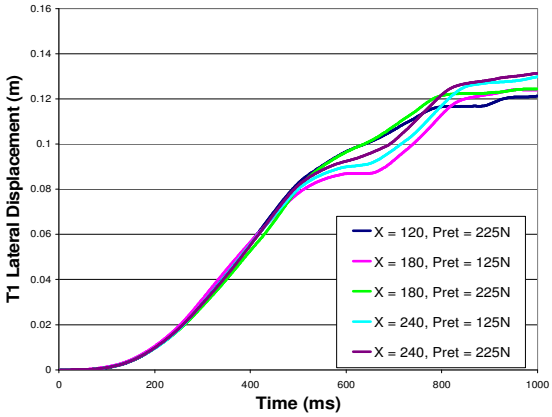

Figure 11. T1 lateral displacement vs. time for cases with belt engaging the shoulder

These results indicate that the crucial factor influencing the magnitude of lateral displacement is whether the belt slips over the shoulder or not. For cases where the belt slips over the shoulder, T1 displacements are all very similar (average displacement = 138mm). When the belt engages the shoulder there is only minor differences between D-ring positions (average displacement = 126mm). What is interesting to note is that this equates to only an average 9% reduction in lateral displacement. It should be noted however that the maximum displacements for cases with slip occurred approximately 200ms earlier that those with engagement.

Far-Side Lateral Sled Tests

For the Middle D-ring configuration, all test subjects indicated that the seat belt engaged the shoulder complex. This can be derived from the shoulder belt force-time histories seen in Figure 12, with an image of the human model response seen in Figure 13.

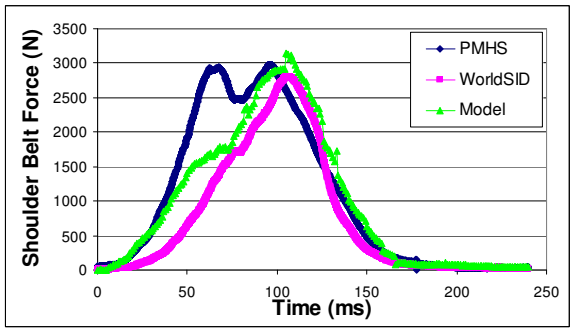

Figure 12. Shoulder belt force – Middle D-Ring, 100N Pretension

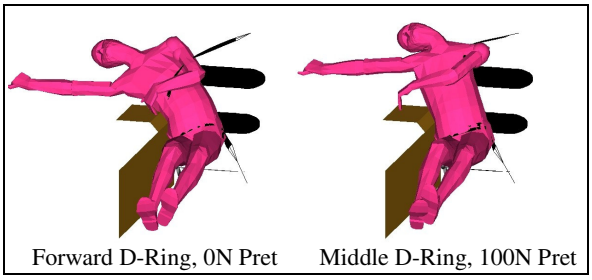

Figure 13. Human model simulated belt interaction in sled tests (175ms)

In the force-time curve, the belt to shoulder-complex interaction is represented by the large peak response at around 100ms. Both the WorldSID and the human Model predicted the magnitude and timing of this event within 10% of the results from the PMHS test. One difference is the initial peak observed in the

response of the PMHS test. This was attributed to thoracic loading prior to slipping across the thorax (drop in response) and then engaging the shoulder. Neither the WorldSID nor human model observed this response to the same magnitude.

For the forward D-ring configuration, all test subjects (PMHS, WorldSID and human model) slipped out of the shoulder portion of the seat belt. In all cases, the belt provided restraint via loading the thorax in the early phases of impact. The belt subsequently slipped past the shoulder and got caught on the upper arm near the elbow. Despite those similarities, the shoulder belt force-time histories are quite different for all three subjects (Figure 14).

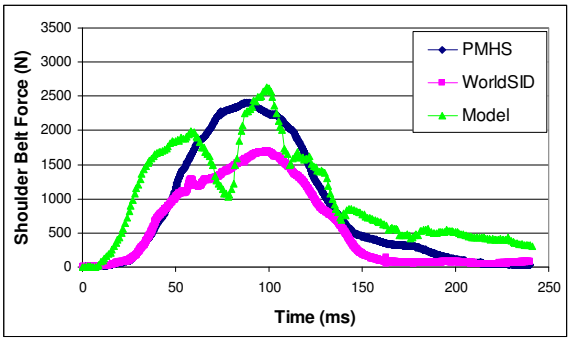

Figure 14. Shoulder belt force – Forward D-Ring, 0N Pretension

The shape and phasing of WorldSID and PMHS traces are similar, however the magnitude of the PMHS belt force is 40% higher than WorldSID. Conversely, the human model made a closer match of the belt force magnitude, however the trace shows a profound double peak. The first peak related to the thorax loading the belt, with the second peak for contact with the upper arm. This suggests that the thorax of the PMHS and WorldSID took nearly all the belt load. Whereas in the model, belt load dropped whilst the belt slipped over the shoulder.

To quantify excursion, head lateral displacements were plotted versus time for both test configurations (Figures 15 and 16).

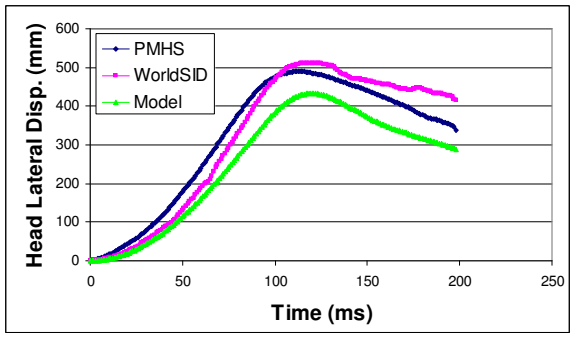

Figure 15. Head lateral displacement – Middle D-ring, 100N Pretension

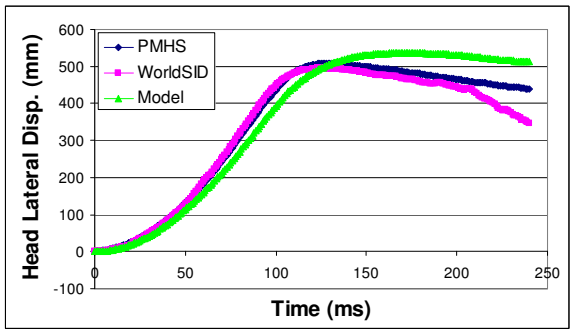

Figure 16. Head lateral displacement – Forward D-ring, 0N Pretension

For the Middle D-ring configuration, the human model predicted a slightly slower velocity to maximum displacement than both the PMHS and WorldSID. The maximum head displacement of the human model was 12% less than the PMHS and 15% less than that of WorldSID. The timing of maximum displacement was within 5ms for all three subjects. All three subjects also predicted rebound of similar velocities subsequent to maximum excursion.

For the Forward D-ring configuration, all the subjects predicted a similar level of maximum displacement (within 5%), and the speed at which they arrive there. When the PMHS reached maximum displacement, the human model's displacement magnitude was within 1% and WorldSID's within 3%.

In contrast to the physical test results, the human model spent in excess of 100ms at 95% of maximum displacement, whereas the PMHS and WorldSID only spent 60ms and 65 ms respectively. This was related to the human model continuing to slip and not rebound in the same way the PMHS and WorldSID did.

DISCUSSION

The aim of this study was to investigate seat belt to shoulder-complex interaction during the first phase of a far-side impact and incorporate this knowledge into a multibody occupant model. After incorporating this into the model, it was to be validated against a series of lateral sled tests using PMHS and WorldSID ATD.

The first aspect of this study involved 1g quasi-static tests using human volunteers, a Hybrid III ATD, a Hybrid III Spring-Spine ATD and the TNO Human Facet Model (with shoulder modifications). From the volunteer quasi-static tests two interesting findings were observed. Firstly, thorax lateral restraint appears to be dependent on seat belt geometry and the level of pretension applied to the belt. Secondly, the critical relationship between the shoulder engaging the belt (or slipping) and seat belt geometry and pretension is highly dependent on human anthropometry. Only two volunteers were needed to demonstrate the uniqueness of humans in this sense.

Due to the effect of anthropometry, it should not be necessary to validate ATDs or human models to a specific human for specific belt pretensions and geometries. It is to be expected that there should be similar restraining effects depending on the level of pretension or belt geometry for human surrogates of similar anthropometry. However, these levels are not possible to estimate until a much larger sample set and higher impact speeds are investigated.

For the meantime, it should be demonstrated that the model or ATD has a critical (or almost critical) slip relation depending on seat belt geometry and pretension levels. Specifically, that it can predict the increasing likelihood of shoulder engagement by the seat belt as the D-ring moves rearward and pretension increases.

The 1g quasi-static simulations indicated that the newly adapted human model was able to demonstrate an increasing level of restraint as D-ring moved rearward and pretension increased. The ATDs tested also predicted this trend, however they were much more sensitive to seat belt geometry changes and pretension. Further to that, the way in which the ATDs loaded the belt was not the same as the volunteer, or the human model for that matter. Restraint in the ATD tests was provided through the belt loading the thorax, whereas the volunteer and human model also loaded the shoulder-complex.

The dimensions of the shoulder ellipsoid added to the human model were derived from the arm radius at the axilla for of a 50^{th} percentile male defined in Tilley et al., (2002). Tilley et al., showed that this 53mm radius coincides with a shoulder breadth of 465mm, very similar to that of this human model. When compared to other anthropometries, a 95^{th} percentile male with a shoulder breadth of 523mm has a radius of 58mm (Tilley et al., 2002). Thus it is reasonable to suggest that the dimensions of the shoulder ellipsoid defined in this study are similar to those of Volunteer 1. Volunteer 2 on the other hand, who had a shoulder breadth of 560mm, is likely to have a larger arm radius at the axilla.

These simulations also indicated that the most critical factor influencing thorax lateral displacement was whether belt slip occurred or not. If the shoulder engaged the belt, displacement levels remained the same regardless of belt geometry or pretension. Similarly, if the belt slipped off the shoulder, there was little influence of belt geometry and pretension.

It was firstly thought that the minor differences observed in overall lateral displacement for cases of belt slip and engagement may be have been a factor of the low test speed (1g). This being related to the fact that occupant models are typically validated at much higher speeds than 1g.

In the high speed sled tests, it was also observed that lateral excursion was only slightly less during shoulder engagement compared to when the belt slipped off the shoulder. The small differences noted in these tests are likely to be influenced by the difference in anthropometry between subjects. Specifically, the PMHS which slipped out of the belt was 13cm shorter than the subject which engaged the belt at the shoulder. While all three subjects distinguished differences in magnitude between the two configurations, the human model showed the largest difference.

The other notable difference between the subjects in the high speed tests related to the shoulder belt loading. This was most pronounced in the case where the belt slipped over the shoulder. The force-time trace for the human model showed two obvious peaks, one related to thorax loading and the other due to arm contact. The same event did not happen in the physical tests. Results from more tests where the belt slips over the shoulder would need to be conducted to see whether this is an artifact of the model or not.

In light of the results put forward in this study, it possible to suggest most likely and least likely configurations for occupants to slip out of the shoulder portion of the seat belt. The most likely configuration being with a forward mounted D-ring, no pretension and slim anthropometry. Conversely, a rear mounted D-ring, pretension and a more solidly built person is less likely to slip out of the shoulder portion of the seatbelt.

Another factor, not investigated in this study, likely to influence belt slip and lateral excursion is occupant height. A taller person is likely to have larger lateral displacement purely based on the belt loading the thorax lower on the inboard side, the increased inertia of the longer body segments and the extra distance their body will occupy when positioned horizontally. As seat belt geometry and occupant size are closely related, further research should be undertaken to gain a better understanding of the effect D-ring position has on lateral excursion.

FUTURE WORK

The next step in this research is for more detailed validation demonstrating that this model is capable of mimicking additional human responses such as neck, thoracic, abdominal and pelvic loading in far-side impacts. This should also be conducted at 60 degrees, as these impacts represent the greatest source of Harm in far-side crashes (Gabler et al., 2005a). The effect of D-ring position and pretension at various impact directions is also to be investigated. Additionally, this model should be validated against tests like those seen in Pintar et al., (2006) to evaluate whether it is capable of identifying which body regions are suitable to load, should inboard countermeasures be proposed.

CONCLUSIONS

The newly adapted human model has been demonstrated to exhibit a critical element of what is required for a far-side occupant model. Specifically, the ability to model seat belt to shoulder-complex interaction. This ability was firstly established using low speed data from volunteer tests and subsequently validated against high speed data obtained from PMHS and WorldSID tests.

This study has also demonstrated that a trend exists between seat belt geometry and pretension on the level of restraint provided to occupants in far-side impacts. It has also been highlighted that human anthropometry has a major effect on the restraint provided by the seat belt in far-side impacts.

ACKNOWLEDGMENTS

The funding for this study is provided in part by the Australian Research Council with cost sharing and support from the other participants. Additional funding for this research has been provided by private parties, who have selected Dr. Kennerly Digges (and the FHWA/NHTSA National Crash Analysis Center at the George Washington University) to be an independent solicitor of and funder for research in motor vehicle safety, and to be one of the peer reviewers for the research projects and reports. Neither of the private parties have determined the allocation of funds or had any influence on the content.

REFERENCES

Adomeit D, Goegler H, Vu Han V. (1977) “Expected Belt-Specific Injury Patterns Dependent on the Angle of Impact”. 3rd International Conference on Impact Trauma, International Research Council on Biokinetics of Impacts, Bron, France, pp. 242-250.

Boström O, Haland Y. (2003) “Benefits of a 3+2 Point Belt System and an Inboard Torso Side Support in Frontal, Far-Side, and Rollover Crashes”. Proceedings of the 18th International Conference on Enhanced Safety of Vehicles, Nagoya, Japan.

Boström O, Haland Y, Soderstrom P. (2005) “Seat Integrated 3-Point Belt with Reversed Geometry and an Inboard Torso Side-Support Airbag for Improved Protection in Rollover”. Proceedings of the 19th International Conference on Enhanced Safety of Vehicles, Washington, DC, USA.

Chipman M. (2004) “Side Impact Crashes - Factors Affecting Incidence and Severity: Review of the Literature”. Traffic Injury Prevention, 5:67–75.

Digges K, Gabler H, Mohan P, Alonso B. (2005) “Characteristics of the Injury Environment in Far-Side Crashes”. Proceedings of the 49th Annual Conference, Association for the Advancement of Automotive Medicine. pp 185 - 197

Fildes B, Lane J, Lenard J, Vulcan A. (1991) “Passenger Cars and Occupant Injury”. Federal Office of Road Safety, Report CR95

Fildes B, Sparke L, Boström O, Pintar F, Yoganandan N, Morris A. (2002) “Suitability of Current Side Impact Test Dummies in Far-Side Impacts”. Proceedings of the 19th International Conference on the Biomechanics of Impact. pp 43-66

Fildes B, Linder A, Douglas C, Digges K, Morgan R, Pintar F, Yoganandan N, Gabler H, Duma S, Stitzel J, Boström O, Sparke L, Smith S, Newland C. (2005) "Occupant Protection in Far Side Crashes". Proceedings of the 19th International Conference on Enhanced Safety of Vehicles, Washington, DC, USA.

Gabler H, Digges K, Fildes B, Sparke L. (2005a) "Side Impact Injury Risk for Belted Far Side Passenger Vehicle Occupants". Society of Automotive Engineers, Paper 2005-01-0287.

Gabler H, Fitzharris M, Scully J, Fildes B, Digges K, Sparke L. (2005b) "Far Side Impact Injury Risk for Belted Occupants in Australia and the United States". Proceedings of the 19th International Conference on Enhanced Safety of Vehicles, Washington, DC, USA

Horsch J, Schneider D, Kroell C, and Raasch F, (1979) Response of Belt Restrained Subjects in Simulated Lateral Impact. Proceedings of the 23rd Stapp Car Crash Conference, SAE Technical Paper No. 791005, pp. 69-103.

Horsch JD. (1980) "Occupant Dynamics as a Function of Impact Angle and Belt Restraint". Proceedings of the 24th Stapp Car Crash Conference, SAE Technical Paper No. 801310, pp. 417–438.

Kallieris D, Schmidt G. (1990) "Neck Response and Injury Assessment Using Cadavers and the US-SID for Far-Side Lateral Impacts of Rear Seat Occupants with Inboard-Anchored Shoulder Belts", Proceedings of the 34th Stapp Car Crash Conference, SAE Technical Paper No. 902313, pp. 93–100.

Kent R, Shaw G, Lessley D, Crandall J, Svensson M. (2003) Comparison of Belted Hybrid III, THOR, and Cadaver Thoracic Responses in Oblique Frontal and Full Frontal Sled Tests. Society of Automotive Engineers, Paper 2003-01-0160.

de Lange R., van Rooij L., Mooi H., Wismans J. (2005) "Objective Biofidelity Rating of a Numerical Human Occupant Model in Frontal to Lateral Impact". Proceedings of 49th Stapp Car Crash Conference, SAE Technical Paper No. 2005-22-0020, pp. 457-479

Mackay G, Hill J, Parkin S, Munns J. (1993) "Restrained Occupants on the Nonstruck Side in Lateral Collisions". Accident Analysis and Prevention. Vol. 25, No. 2, pp. 147-152.

Otte D, Suren E, Appel H, Nehmzov J. "Vehicle Parts Causing Injuries to Front-Seat Car Passengers in Lateral Impact". Proceedings of 28th Stapp Car Crash Conference, pp. 13–24.

Pintar F, Yoganandan N, Hines M, Maltese M, McFadden J, Saul R, Eppinger R, Khaewpong N, Kleinberger M. (1997) "Chestband Analysis of Human Tolerance to Side Impact", Proceedings of 41st Stapp Car Conference, pp. 63–74.

Pintar F, Yoganandan N, Stemper B, Boström O, Rouhana S, Smith S, Sparke L, Fildes B, Digges K. (2006) "WorldSID Assessment of Far Side Impact Countermeasures", Proceedings of the 50th Annual Conference, Association For The Advancement Of Automotive Medicine.

Rouhana S, Kankanala S, Prasad P, Rupp J, Jeffreys T, Schneider L. (2006) "Biomechanics of 4-Point Seat Belt Systems in Farside Impacts", Proceedings of the 50th Stapp Car Crash Conference, SAE Technical Paper No. 2006-22-0012, pp. 267-298

Sinson G, Yoganandan N, Pintar F. (2003) "Carotid Artery Trauma in Motor Vehicle Crashes: Investigation of the Local Tensile Loading Mechanism". Proceedings of the 20th International Conference on the Biomechanics of Impact. pp 207-216.

Stolinski R, Grzebieta R, Fildes B, Judd R. Wawrzynczak J, Gray I, Mcgrath P, Case M. (1999) "Response of Far Side Occupants in Car-to-Car Impacts with Standard and Modified Restraint Systems using HIII and US SID", SAE Technical Paper No. 1999-01-1321.

Tilley, A. R and Henry Dreyfuss Associates (2002). "The Measure of Man and Woman: Human Factors Design". Revised Edition. Published by John Wiley and Sons, Inc. United Sates of America.

Tornvall F, Svensson M, Davidsson J, Flogard A, Kallieris D, Haland Y. (2005) "Frontal Impact Dummy Kinematics in Oblique Frontal Collisions: Evaluation Against Post Mortem Human Subject Test Data". Traffic Injury Prevention, 6:340–350.

WORLDSID SMALL FEMALE SIDE IMPACT DUMMY SPECIFICATIONS AND PROTOTYPE EVALUATION

Bernard Been
First Technology Safety Systems Europe
Riske Meijer
TNO Science & Industry
The Netherlands
Francois Bermond
INRETS - LBMC
France
Klaus Bortenschlager
PDB
Germany
David Hynd
TRL limited
United Kingdom
Luis Martinez
Gustavo Ferichola
University Institute for Automobile Research, Polytechnic University of Madrid (UPM-INSIA)
Spain
Paper Number 07-0311

ABSTRACT

The WorldSID program was set up to develop a new, worldwide acceptable, advanced technology, side impact crash test dummy for improved assessment of injury risk to car occupants in lateral collisions. Following the release of the mid-sized male WorldSID, the development of the small female WorldSID dummy was initiated by the EC 6th Framework collaborative research project 'APROSYS' in 2004.
The main specifications and requirements of the new dummy have been defined in terms of anthropometry, biomechanical response and instrumentation capabilities in general and per body segment. An overview of the specification is given in this paper. Two prototype dummies have been evaluated against a first set of test conditions. Test results are presented here, including pendulum impactor, linearly guided impactor, drop and sled tests. For a prioritised matrix of biomechanical test conditions, the dummy responses were compared against the biomechanical human response requirements. Furthermore, the dummy's repeatability in well-controlled test conditions and its sensitivity to temperature were studied and its compliance to anthropometric requirements is reported. Following the assessment of the dummy's current biofidelity and maturity, recommendations for further dummy improvements are given in the conclusions.

INTRODUCTION

In recent years there have been a number of developments in the field of side impact crash test dummy technology. The WorldSID 50th percentile male dummy was developed between 1997 and 2001 and evaluated against a number of biofidelity and sensitivity criteria.
After the development of the 50th percentile male dummy, the focus was put on the small (5th percentile) female size. The aim was to develop a dummy with the same biofidelity, functionality, handling and injury assessment capabilities as the WorldSID 50th percentile male dummy. The results of the WorldSID 50th percentile prototype testing were taken into account in the 5th female development. The specification of the WorldSID 5th female, including the selection of scaled biofidelity requirements, was undertaken in the Aprosys EC project (Barnes *et al.*, 2005). Five prototype dummies were built according to these specifications, two of which have been extensively evaluated in the Aprosys EC project.
This paper provides an overview of the biofidelity and anthropometry assessment of the dummy as well as assessment the dummy's repeatability, sensitivity to environmental temperature, its handling and robustness. The dummy's characteristics are evaluated against the requirements and recommendations are made as to potential improvements to the design and usability of the dummy to make it suitable for use in a regulatory test environment.

MAIN SPECIFICATIONS

The WorldSID small female requirements were published in a detailed document prepared in the Aprosys EC project (Barnes *et al.*, 2005). Further, the specifications of the WorldSID small female prototypes that were built according to these requirements were published by Wang *et.al.* (2007). The current paper only provides a brief overview of the main characteristics of the dummy.

Anthropometry

The small female WorldSID dummy was designed in order to represent a small-size adult female and adolescent car occupant. The dummy anthropometry was based on the UMTRI data set (Schneider *et al.*, 1983). This data set includes many anthropometry details for a small-sized female in an automotive seating posture, such as the external 3D surface, joint centre locations, external and internal anatomical reference points, and mass and inertia properties of the body segments. The dummy target mass is 45.8 kg ± 1.2 kg (~2.5%) including two half arms, excluding dummy suit and shoes.

Biofidelity

The biomechanical performance requirements of the WorldSID 5th female are based on impact responses as specified in ISO Technical Report 9790 (ISO, 1997) for lateral biofidelity, scaled for 5th percentile female according the formulas specified by Irwin *et al.* (2002).
ISO Technical Report 9790 includes a large set of dynamic biofidelity performance specifications for the head, neck, shoulder, thorax, abdomen and pelvis of a 50th percentile male side impact dummy in sled tests, drop tests and pendulum tests. This report includes a (weighted) biofidelity rating methodology that enables quantification of the ability of a certain dummy to meet the performance requirements. The target biofidelity rating for the WorldSID dummy family, including the small female, is to achieve "Good to Excellent Biofidelity", i.e. B $\geq$ 6.5 out of 10. The Irwin study gives scaling formulae and scaled responses for all body segments in all test conditions of ISO TR9790 for all available anthropometric sizes between a large 95th percentile male down to new born child. The 5th percentile female biofidelity response requirements as published by Irwin were applied to the 5th percentile female WorldSID dummy.

Instrumentation

The instrumentation options of the WorldSID 5th female dummy are given in Table 1. A total of 125 dynamic measurement parameters are available in the dummy, completed with static measurements for tilt angle and temperature in head, thorax and pelvis.

Table 1.
Instrumentation options WorldSID small female

Segment	Parameter	Nr.
Head	Acceleration ($a_{x,y,z}$)	3
	Rotational acceleration ($\alpha_{x,y,z}$)	3
Neck	Upper loads ($F_{x,y,z}$, $M_{x,y,z}$)	6
	Lower loads ($F_{x,y,z}$, $M_{x,y,z}$)	6
Shoulder	Loads ($F_{x,y,z}$)	2*3
	Deflection (δ_y)	1
	Acceleration ($a_{x,y,z}$)	3
Thorax	T1 acceleration ($a_{x,y,z}$)	3
	T4 acceleration ($a_{x,y,z}$)	3
	T12 acceleration ($a_{x,y,z}$)	3
	Rib deflection (δ_y)	3
	Rib acceleration ($a_{x,y,z.}$)	3*3
	Rotational acceleration (α_x)	1
Abdomen	Deflection (δ_y)	2
	Acceleration ($a_{x,y,z}$)	2*3
Lumbar	Loads ($F_{y,z}$, $M_{x,z}$)	4
Pelvis	Sacro-iliac loads ($F_{x,y,z}$,$M_{x,y,z}$)	2*6
	Pubic loads (F_y)	1
	Acceleration ($a_{x,y,z}$)	3
	Rotational acceleration (α_x)	1
Femur	Femoral neck load ($F_{x,y,z}$)	2*3
	Femur load ($F_{x,y,z}$ $M_{x,y,z}$)	2*6
	Knee load (Fy)	2*2
Tibia	Upper load ($F_{x,y,z}$ $M_{x,y,z}$)	2*6
	Lower load ($F_{x,y,z}$ $M_{x,y,z}$)	2*6

EVALUATION METHOD

Anthropometry

The objective of this study was to determine actual dummy anthropometric details, such as joint-, landmark- and center of gravity locations; mass of body segments and total dummy, and external shape of the flesh components. Based on measured dummy dimensions, a complete and accurate CAD model was reconstructed by measuring components with a caliper, a FARO ARM 3D measurement machine and by digitising the external shapes of dummy flesh components. The actual components were weighed and the mass was applied to the CAD model components. The actual dummy was set up in the UMTRI reference position, using the internal tilt sensors of the dummy at zero tilt read out. Anthropometric reference points of the actual dummy assembly were measured with a FARO ARM and used to set up the reconstructed CAD model in 3D space. Centre of gravity (CoG) locations of actual dummy assemblies were obtained on a scale according Figure 1 and Equation 1.

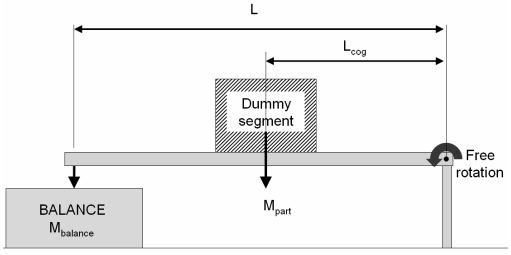

Figure 1. CoG location process.

$$L_{cog} = \frac{M_{balance} * L}{M_{part}} \quad (1)$$

The reconstructed dummy CAD model was then analysed to obtain the dummy anthropometric characteristics, such as location of the joints, instrumentation and CoG and mass. Also the CAD model enabled comparison of the external shape of components in 3D space with the UMTRI "Golden Shell", the target outer surface of the small female anthropometry. The details obtained were compared to the UMTRI anthropometric targets and deviations between target and actual dummy anthropometric data were identified.

Biomechanical response

Test matrix - The test matrix for the biomechanical response evaluation of the small female WorldSID is given in Table 2. Note that the complete set of ISO TR9790 tests was not performed. In the ISO TR9790 rating system, test conditions and body segments are prioritised by weighting factors. The selection of test conditions for the Aprosys evaluation was based on the test condition weighting factors (V_{ij}), test severity and available skill and equipment within the Aprosys consortium. Drop tests, low weighting factor tests and high risk tests (in terms of dummy damage) were omitted.

Table 2.
Prioritised test matrix Aprosys

Body region	Impact condition	V_{ij}
Head		
Head test 1	200 mm rigid drop	8
Frontal drop	376 mm rigid drop	0
Neck		
Neck test 1 shoulder test 2	7.2 g sled impact	7
Neck test 2	6.7 G sled impact	6
Shoulder		
Shoulder test 1	4.5 m/s pendulum	6
Shoulder 4, Thorax 6, Abdomen 5, pelvis 13	8.9 m/s padded WSU	7
Thorax		
Thorax test 1	lateral 4.3 m/s pendulum	9
Thorax test 2	oblique 6.7 m/s pendulum	9
Thorax test 5 pelvis 7	6.8 m/s Heidelberg rigid sled	7
Abdomen		
Abdomen test 3	8.9 m/s WSU padded sled	3
Pelvis		
Pelvis test 1	6.0 m/s impactor	8
Pelvis test 2	10 m/s impactor	9
Pelvis test 9 thorax 6	8.9 m/s Heidelberg padded sled	8
Pelvis test 10	6.8 m/s WSU rigid sled	3

Sled velocity - The EEVC Heidelberg test procedure (Roberts *et al.*, 1991) specifies the dummy to load cell wall impact velocity as 7.6 and 10.3 $m.s^{-1}$, rather than the sled velocity of 6.8 and 8.9 $m.s^{-1}$ used in the ISO TR9790 documentation. The difference is because the EEVC analysis used the relative speed of impact between the dummy and the load plates (which included the rebound velocity of the sled), and the ISO analysis used only the velocity of the sled at t_0. Note that there is no difference in the actual loading condition between ISO and EEVC. Therefore the data obtained in these tests can be analysed applying EEVC as well as ISO corridors. However, when applying sled velocity as test parameter in a rebounding sled (e.g. Heidelberg), the dummy to load plate contact velocity is likely to be less accurately controlled as it will depend on the performance of the sled deceleration and stopping mechanism.

Scaling of force plates - To achieve similar force plate interaction with the small female dummy as the original PMHS test set up, the force plates in both sled test conditions - Heidelberg and Wayne State University (WSU) - were scaled using the same method. The vertical scale factor was determined from the ratio between Occiptal Condyle joint to seat pan distance of small female and mid size male, resulting in scale factor of 0.895. Both the location of the beams and the height of the beams were scaled in a direction perpendicular to the seat pan. The scaled and original beam locations are illustrated in Figure 2 for the WSU configuration. To calculate the location of the knee plate and the dimension of the pelvis beam a scale factor of 0.917 was applied. The scale factor is based on ratio of the UMTRI 5^{th} and 50^{th} femur lengths.

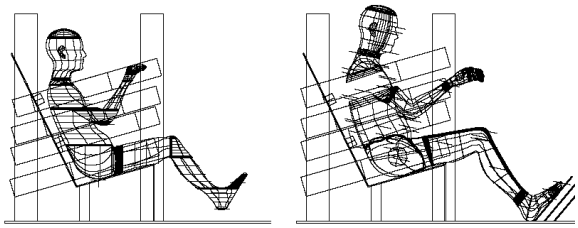

Figure 2. WSU beam configurations and human body models. Left 5^{th} % female, right 50^{th} % male.

Normalisation - The dummy responses were normalised according the procedures used for normalising PMHS raw data to obtain ISO TR9790 and EEVC response corridors. The small female standard mass was determined using the ISO standard body segment mass (50^{th} male) per test condition scaled by the ratio of UMTRI body segment mass 5F/50M. No stiffness scaling was applied as ratios of characteristic lengths of the dummy equal 1

.

Pendulum tests - The effective mass in each test was calculated using Equation (2):

$$M_e = \frac{\int F dt}{V_0} \quad (2)$$

Where M_e = effective mass of the segment (kg);
F = pendulum force (N);
V_0 = pendulum velocity ($m.s^{-1}$).
The integration interval was taken to be from first positive pendulum force to the end of the impact.

The shoulder and pelvis pendulum forces were normalised according to Equation (3):

$$F_N = F_p \sqrt{\frac{M_s}{M_e}} \quad (3)$$

where F_N = normalised pendulum force (N);
F_p = pendulum force (N);
M_s = standard segment mass (kg);
M_e = effective segment mass (kg).

The shoulder displacement was normalised according to the Equation (4):

$$D_N = D_s \sqrt{\frac{M_s}{M_e}} \quad (4)$$

where D_N = normalised deflection (mm);
D_s = measured shoulder deflection (mm).

The thoracic pendulum responses were normalised using the two mass system methods as applied in ISO TR9790 according to Equation (5). Time factor scaling was applied to the HSRI and WSU/GML thoracic pendulum responses according Equation (6). The T1 acceleration responses in the 4.3 m/s HSRI thorax tests were normalised according Equation (7).

$$F_N = F_p \sqrt{\frac{M_s}{M_e}} \times \sqrt{(14 + M_e)} / \sqrt{(14 + M_s)} \quad (5)$$

$$t_N = t_p \sqrt{\frac{M_s}{M_e}} \times \sqrt{(14 + M_e)} / \sqrt{(14 + M_s)} \quad (6)$$

$$a_N = a_{T1} \sqrt{\frac{M_e}{M_s}} \times \sqrt{(14 + M_e)} / \sqrt{(14 + M_s)} \quad (7)$$

where t_N = normalised time (s);
a_N = normalised T1 acceleration (G);
a_{T1} = T1 acceleration (G);
14 = the pendulum mass (kg).

Shoulder - The APR lateral shoulder tests were normalised using a standard mass of 20.5 kg. 5th %-ile UMTRI shoulder-thorax segment mass is 12.983 kg, 50th %-ile UMTRI shoulder-thorax segment mass is 23.763 kg. The 5th female standard shoulder mass Ms = 20.5*12.983/23.763 = 11.20 kg. The average effective mass Me in three tests was 12.663 kg. The shoulder normalisation factor applied was 0.940 for both pendulum force and deflection.

Thorax - The HSRI lateral thorax tests were normalised using a standard mass of 20.8 kg for the thorax. 5th %-ile UMTRI shoulder-thorax segment mass is 12.983 kg and 50th %-ile UMTRI shoulder-thorax segment mass is 23.763 kg. The 5th female standard shoulder mass M_s = 20.8*12.983/23.763 = 11.364 kg. The average effective mass M_e in three 4.3 m/s tests was 13.351 kg. The thorax 4.3 m/s normalisation factor applied was 0.958. The WSU/GMR lateral thorax tests were normalised using a standard mass of 15.2 kg for the thorax. 5th %-ile UMTRI shoulder-thorax segment mass is 12.983 kg and 50th %-ile UMTRI shoulder-thorax segment mass is 23.763 kg. The 5th female standard thorax mass M_s = 15.2*12.983/23.763 = 8.305 kg. The average effective mass M_e in three 6.0 m/s tests was 12.988 kg. The thorax 6.0 m/s normalisation factor applied was 0.880.

Pelvis - The pelvis pendulum tests were run with a 14 kg mass and the linear guided impactor tests were performed with a 10.26 kg mass. The prescribed pendulum mass is 10.14 kg for small female pelvis impacts. The data were scaled applying scale factor according Equation (8):

$$F_p = F_{imp} * \sqrt{(10.14 * (M_i + 48)} / (M_i * (10.14 + 48)) \quad (8)$$

where M_i = mass of impactor used in the test (kg);
F_{imp} = impactor force (N).

As second step the data were normalised following the ONSER lateral pelvis tests according to Equation (2) and (3). A standard mass of 14.5 kg was applied for the pelvis. 5th %-ile UMTRI pelvis segment mass (including femur heads) is 8.5 kg and 50th %-ile UMTRI pelvis segment mass (including femur heads) is 14.5 kg. The 5th female standard pelvis mass applied was M_s = 14.5*8.5/14.5 = 8.5 kg.

Sled tests - In the Heidelberg tests the force plates were mounted on the sled. Therefore the readings were inertia compensated as follows:

$$F_i = F_{plate} + (M_{plate} \times A_{plate}) \quad (9)$$

Where F_i = inertia compensated plate force (N);
F_{plate} = sum of plate load cell forces (N);
M_{plate} = mass of plate forward of the centre of the load cells (kg);
A_{plate} = acceleration of plate, where acceleration is positive in the direction of impact of the dummy ($m.s^{-2}$).

The WSU force plates were mounted statically and no inertia compensation was applied. The Heidelberg inertia compensated and WSU registered plate forces were normalised according to Equation (10).

$$F_N = F_i \sqrt{\frac{M_s}{M_e}} \qquad (10)$$

where F_N = normalised wall force (N);
F_i = inertia compensated force

Dummy measurements were normalised according to the Equations (11), (12) and (13).

$$F_N = F_i \sqrt{\frac{M_s}{M_e}} \qquad (11)$$

$$x_N = x_i \sqrt{\frac{M_s}{M_e}} \qquad (12)$$

$$A_N = A_i \sqrt{\frac{M_e}{M_s}} \qquad (13)$$

where x_N = normalised displacement (m);
x_i = displacement (m);
A_N = normalised acceleration ($m.s^{-2}$);
A_i = acceleration ($m.s^{-2}$).

Standard mass - For Heidelberg sled tests, EEVC normalisation applied a 37 kg segment mass for the thorax and 24 kg for the pelvis. The ISO normalisation used a 38 kg thorax segment and the whole dummy mass to normalise the pelvis responses. The ratio of the 5th to 50th %-ile total body masses was used to scale all segment masses to 23.5kg thorax mass and 15.2 kg pelvis mass for the EEVC and 24.1 kg thorax for ISO. A ratio of specified 5th %-ile mass to actual dummy mass was used in the ISO normalisation of the pelvis responses. In the Wayne State University sled tests small female standard masses were applied as follows: thorax 15.2 kg, abdomen 6.7 kg and pelvis 10.8 kg.

RESULTS

Anthropometry

Segment mass - The target body segment masses and those obtained for WorldSID 5th female are given in Table 3. Note that the WorldSID masses given are from (not necessarily functional-) sub-assemblies that match UMTRI segmentation planes as closely as possible. The CAD model and UMTRI segmentation planes are shown in Figure 3. The main deviations are in abdomen (-1.3 kg) and lower legs and feet (+1.2 kg). The other large deviation of 2.5 kg in the pelvis/upper leg is due to the mismatch between the UMTRI segmentation plane and dummy components. The dummy pelvis extends forward of the UMTRI segmentation plane and contains a large portion of the thigh. The overall dummy mass is well within the tolerance specification.

Table 3.
Target and dummy body segment mass [gram]

Body segment	UMTRI	WorldSID 5th	Deviation
Head	3697	3660	-37
Neck	601	541	-60
Thorax including only upper arms	15231	15452	222
Abdomen	1610	305	-1305
Pelvis	6976	9475	2499
Upper legs	11828	9160	-2668
Lower legs	4720	5486	766
Feet	1276	1724	448
Total	**45939**	**45804**	**-135**

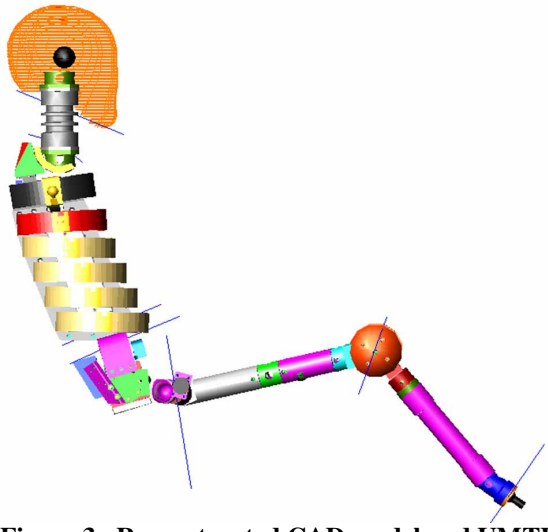

Figure 3. Reconstructed CAD model and UMTRI segmentation planes.

Table 4.
Target and dummy centre of gravity [mm]

	UMTRI			WorldSID 5th		
Body segment	X	Y	Z	X	Y	Z
Head	-184	0	578	-177	-1	580
Neck	-172	0	460	-185	1	446
Thorax	-147	0	238	-170	-1	258
Pelvis	-76	0	25	-36	0	19
Upper leg	147	±104	-4	232	±92	38
Lower leg	444	±82	-56	491	±83	-81
Feet	653	±101	-178	654	±93	-171
Whole body	24	0.0	129	48	-0.5	136

Centre of Gravity - The target and dummy centres of gravity are shown in Table 4 and Figure 4. The black balls represent target CoG's and the green balls the CoG of the dummy segments.
Main deviations are found in the thorax: +20 mm in vertical and horizontal direction. The whole body

CoG is too far forward and the dummy lower legs CoG are too far backward and too high up. The high thorax CoG is due to the low abdomen mass. The forward position of the whole body CoG is due to the high mass in the lower leg and feet. Redistribution of these masses would bring the whole body CoG and the thorax CoG closer to the targets. There is also a deviation in the pelvis and upper leg in the X direction. This deviation is due to the segmentation plane deviation between dummy and UMTRI. This is not a problem with the dummy.

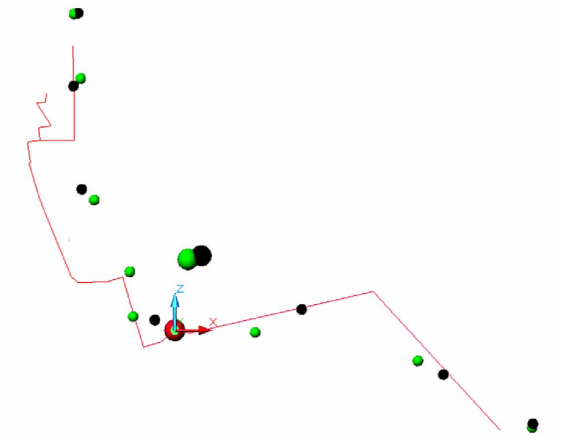

Figure 4. Target (black) and dummy (grey) centre of gravity.

Table 5.
UMTRI targets and dummy joint locations [mm]

	UMTRI			WorldSID		
	X	Y	Z	X	Y	Z
OC	-189	0	519	-187	-1	519
T1	-183	0	429	-184	1	424
Shoulder	-174	±146	354	-194	±147	348
T12/L5 joint	-149	0	140	-86	0	67
L5/S1 joint	-80	0	46	-86	0	67
H-point	0	0	0	0	0	0
Hip	0	±80	0	0	±80	0
Knee	363	±75	71	362	±75	71
Ankle	593	±86	-182	594	±86	-182

Joint locations - The UMTRI target and dummy joint locations are given in Table 5. The dummy was seated with 0º angle tilt sensor reading for this study. The table shows that there is a very good match between the dummy posture and the UMTRI reference posture. Deviations are found in the shoulder joint (rearward 20mm). This is a deviation by design, as the dummy construction did not allow matching the shoulder joint target entirely. The downward (-6mm) position of the shoulder joint may have to do with slight sagging of the shoulder rib due to the arm weight and/or the compression of the lumbar spine. The latter is confirmed by slightly low T1 position. However the OC joint precisely matches the vertical target. The lumbar joint does not match the human targets by design. The dummy lumbar spine is much shorter than human because of design constraints. In the analyses the mid point of the lumbar component was assumed as the joint location, therefore the same numbers appear twice for dummy T12/L5 and L5/S1 joints in the table.

Outer surfaces - A comparison of the outer surface of UMTRI and the reconstructed CAD model (Figure 5) shows a very good match between the two. However some deviations appear as well. First of all the abdomen ribs are wider than the UMTRI target. The thorax and abdomen ribs were designed to be the same width on purpose to avoid discontinuity, which was anticipated to give response or sensitivity problems. A further rationale is that the dummy should not only represent 5th percentile females, but also adolescent males (13 year old). Further deviations are found in T1, clavicle and the knee area. These are all known design compromises. Close study also reveals deviation at the foot surface, but this is considered a minor issue. Figure 6 shows a deviation between the dummy half arm and bone which are much shorter than their UMTRI targets. This deviation appears as a problem in the sled tests; see abdomen responses, page 11.

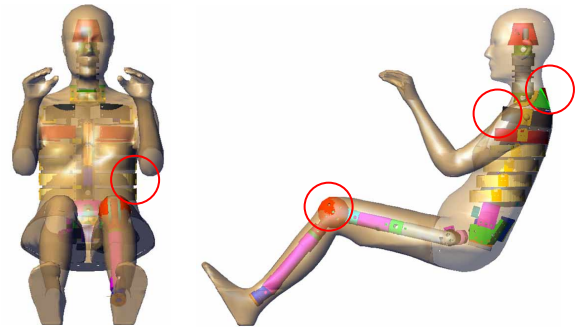

Figure 5. Reconstructed CAD model inside UMTRI 5th female "Golden Shell" surface model.

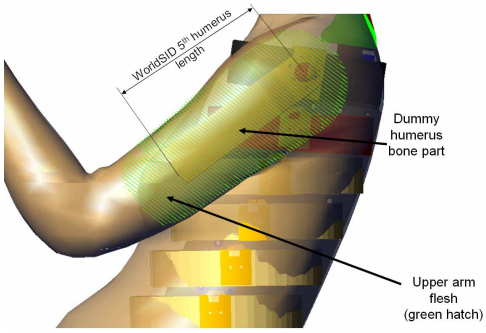

Figure 6. Dummy upper arm and humerus profile.

Biomechanical response

In the following chapters the results will be discussed per body segment rather than per test condition to allow making body segment conclusions based on multiple test conditions.

Head - The results of the head drop tests are given in Table 6. In the original PMHS tests the head impact accelerations were measured directly on the skull; on a point on the non-struck side of the head coincident with a lateral axis through the head CoG. To match the PMHS response, the dummy acceleration results at the non-struck side of the head were calculated from the linear and rotational accelerations measured at the head CoG. The equations are given in (Wang *et al.*, 2007). Note that the frontal head response is just below the corridor and the lateral response is within the corridor. As the ISO TR9790 only applies a lateral performance requirement, the head biofidelity achieved a 10 rating.

Table 6.
Results head drop tests [G]

Condition	Resultant acceleration [G]		Corridor	Criteria
	CoG	Side		
Lateral	120.1	139.5	107-161	pass
Lateral	118.9	135.9		pass
Frontal	244.2	NA	250-300	fail
Frontal	235.7	NA		fail

Neck - The WorldSID small female head-neck responses to NBDL and Patrick and Chou (P&C) conditions are presented in Figure 7 through Figure 16. Four tests were performed with different belt configurations to optimise the dummy T1 acceleration (Figure 15). The traces are differentiated by colours as follows: *black* tight 5-point belt with lateral torso belt; *blue* tight 5-point belt; *magenta* slack 5-point belt; *green*: slack 5-point belt and 30 mm shoulder panel gap. The latter test is considered not valid, because in the original NBDL tests there was no gap. In the graphs ISO corridors appear in *red*; derived corridors from P&C appear *red dotted*.

The internal neck loads of the NBDL tests were derived as explained in Philippens *et al.* (2004).

The plots are arranged such that NBDL and P&C responses can easily be compared. The responses of the same parameters are plotted next to each other, NBDL on the left and P&C on the right. Note that the scales of the left-hand and right-hand plots are identical. Presenting the plots this way shows that the head responses to the two test conditions are strikingly similar. Although pulses are different in NBDL and P&C, it appears that the neck acts as a mechanical filter and head responses are very similar. A noticeable difference is the slower response in NBDL. Also differences appear in the T1 response, see Figure 15and Figure 16. Considering the striking similarity (for this dummy, but possibly others as well) between head responses, there appears to be an incompatibility between NBDL and Patrick and Chou head - neck response requirements. This is demonstrated by the good performance of the dummy in the NBDL condition and the poor result in the P&C condition, see Table 7.

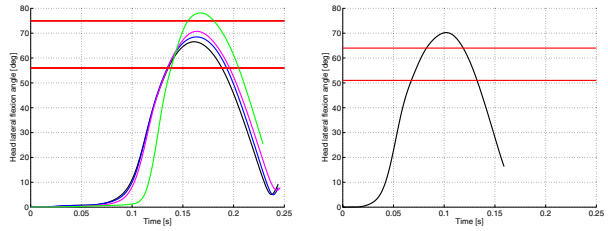

Figure 7. Head flexion angle NBLD (L), P&C.

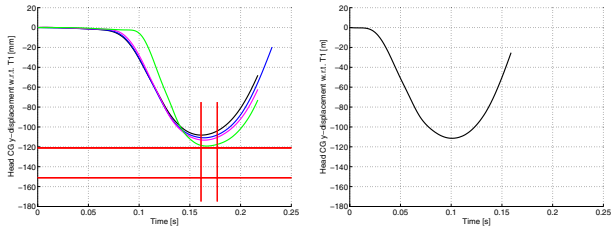

Figure 8 Head y-displacement NBLD (L), P&C.

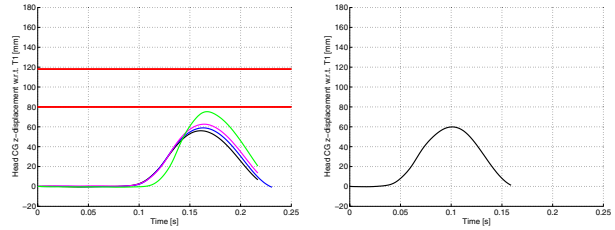

Figure 9. Head z-displacement NBLD (L), P&C.

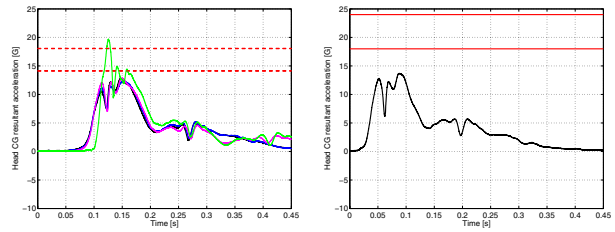

Figure 10. Head resultant acceln. NBLD(L), P&C.

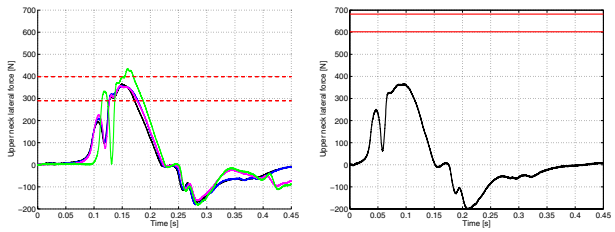

Figure 11. Head y OC force NBLD (L), P&C.

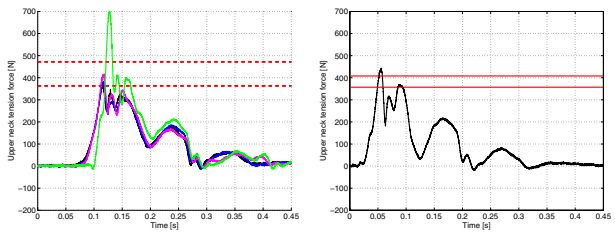

Figure 12. Head z OC force NBLD (L), P&C.

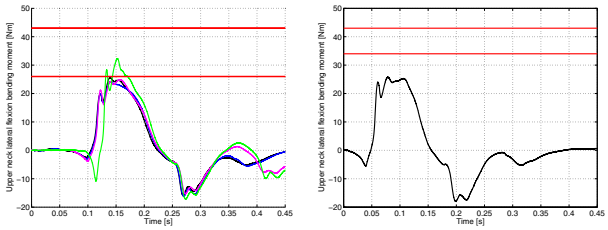

Figure 13. OC-x moment NBLD (L), P&C.

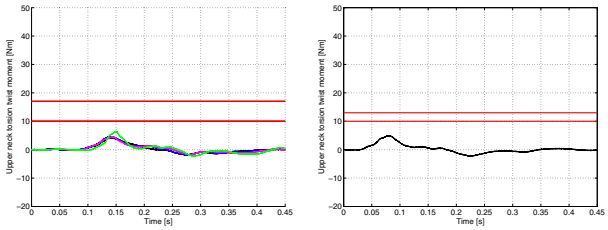

Figure 14. OC-z moment NBLD (L), P&C.

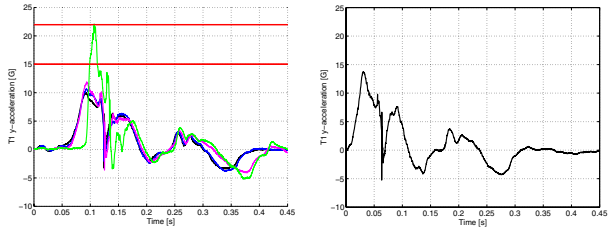

Figure 15. T1 y-acceleration NBLD (L), P&C.

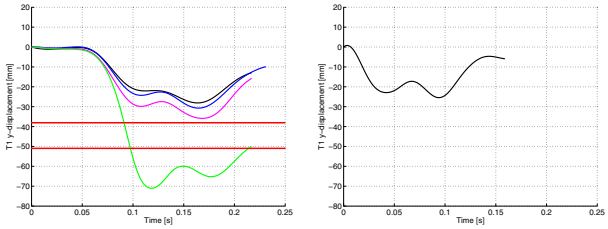

Figure 16. T1 y displacement NBDL (L), P&C.

The head and neck NBDL and P&C response requirements were further analysed for compatibility. The head lateral flexion angle should lie between 56 - 75º for NBDL and 51 - 64º for P&C. The overlapping corridor between NBDL and P&C is quite narrow (60º ± 6.6%). The NBDL resultant head acceleration can be calculated from NBDL a_y and a_z corridors and the mean a_x volunteer response reported in ISO TR9790 (6G). Doing so, the head resultant acceleration NBDL Head A_{res} 14 - 18G is not compatible with the P&C Head A_{res} 18 - 26G requirement. For free body motion such as a dummy head and neck, the neck loads and head acceleration have a direct correlation as long is there is no external force acting on the head. The neck loads can be derived from the product of head acceleration and head mass. Applying this simple equation allows comparison of NBDL vertical and lateral accelerations with P&C vertical and lateral neck loads. Using 3.7kg head mass, NBDL F_y 290 - 400N and P&C F_y 602 -682N. NBDL and P&C lateral head response requirements are completely incompatible. NBDL F_z 363 - 472N, P&C F_z 357 - 408N; vertical head response requirements are partly overlapping with a narrow corridor (385N ± 5.8%). The corridors for OC-x and OC-z moment are rather similar for NBDL and P&C, however NBDL are wider, as they are based on a larger data sample size (P&C is based on a single volunteer).

Table 7.
Neck ISOTR9790 biofidelity rating

Impact condition	Measurement	Average	Test	Body region
7.2 g sled impact NBDL	Peak horizontal Acc T1	5.0		
	Peak hor. Displ. T1/sled	5.0		
	Peak hor. Displ. head cg/t1	5.0		
	Peak vert. Displ. Head CG/T1	5.0		
	Time of max head excursion	10		
	Peak lateral Acc head cg	10		
	Peak vertical Acc head cg	8		
	Peak flexion angle	10		
	Peak twist angle	0.0		
	Peak OC lateral bending moment	6.7		
	Peak OC torsion twist moment	5.0		
			6.6	
6.7 G sled impact Patrick & Chou	Peak flexion angle	5.0		
	Peak bending X-moment @ OC	5.0		
	Peak bending Y-moment @ OC	0		
	Peak twist Z-moment	0		
	Peak shear PA (FX) @ OC	0		
	Peak FY @ OC	0		
	Peak FZ tension @ OC	5.0		
	Peak res. Acc. Head CG	5.0		
			2.9	
				4.9

Shoulder - The shoulder response was evaluated under three test conditions: the APR shoulder pendulum tests at 4.5 m/s, the NBDL 7.2 G sled impact and the WSU 8.9m/s padded sled impact on a load plate. The results are plotted in Figure 15 through Figure 19. In the APR pendulum tests the responses were normalised. The pendulum force exceeds the corridor slightly and the deflections stay below the corridor. The shoulder ISO rating for this test is 5. In the NBDL 7.2 G sled impact responses one clear outlier is visible, which was obtained with shoulder panel gap. This test is not valid. In NBDL the volunteer and dummy responses were not normalised. The T1 acceleration and the deflection are below the corridor. ISO rating for this test is 5.

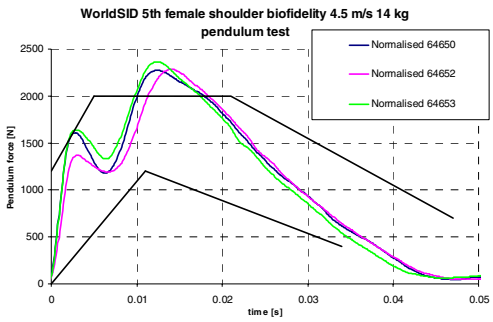

Figure 17. Pendulum force shoulder impact.

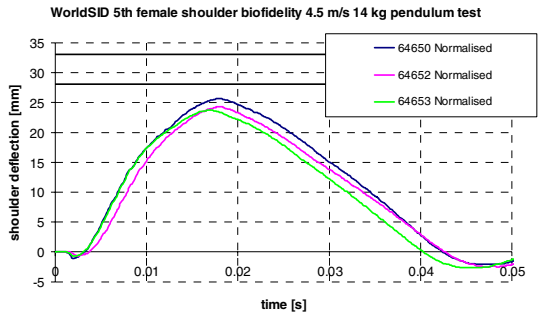

Figure 18. Shoulder deflection pendulum test.

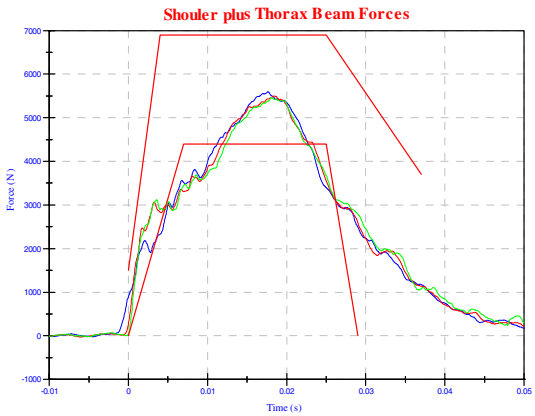

Figure 19. WSU 8.9 m/s padded shoulder and thorax force.

In the WSU 8.9 m/s padded sled impact the shoulder and thorax beam force is inside the upper corridor and the lower boundary is crossed. The response is very close to scoring 10 points in the ISO TR9790 rating. The overall shoulder biofidelity is 5.0 considering the three test conditions (out of four specified), see Table 8.

Table 8.
Shoulder ISOTR9790 biofidelity rating

Impact condition	Measurement	Average	Test	Body regio
4.5 m/s APR pendulum	Pendulum force-time	5.0		
	Pendulum Force			
	Peak shoulder deflection	5.0		
			5.0	
7.2 G sled NBDL	Peak horizontal Acc T1	5.0		
sled	Peak hor. Displ. T1/sled	5.0		
			5.0	
8.9 G WSU sled 23 PSI padded	shoulder + thoracic plate force	5.0		
			5.0	
				5.0

Thorax - The thorax biofidelity was evaluated in two pendulum and two sled test conditions. The results are shown in Figure 19 through Figure 23. All graphs show the same trend: the force responses are (almost) entirely inside the corridors. In some cases the lower boundaries are crossed and the duration of the response is on the short side; however, this was not confirmed in the Heidelberg 6.8 m/s rigid thorax response. The responses are very close to scoring 10 points in the ISO TR9790 rating. Slight lower corridor crossing was also visible in the PMHS original tests. The T1 acceleration is too high in the 4.3 m/s pendulum tests. The lower spine displacement in the padded 8.9 m/s WSU sled condition was inside the corridor in all three repeat tests.

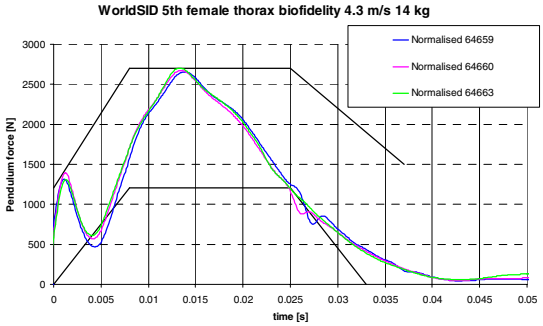

Figure 20. 4.3m/s 14kg thorax pendulum force.

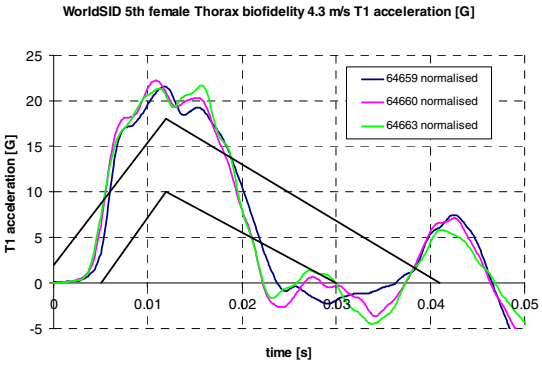

Figure 21. 4.3m/s 14kg thorax T1 acceleration.

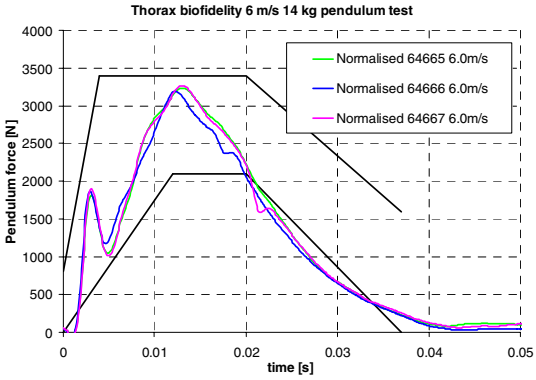

Figure 22. 6.0m/s 14kg thorax pendulum force.

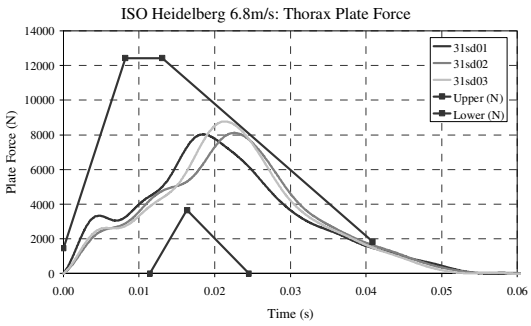

Figure 23. 6.8m/s Heidelberg thorax force ISO.

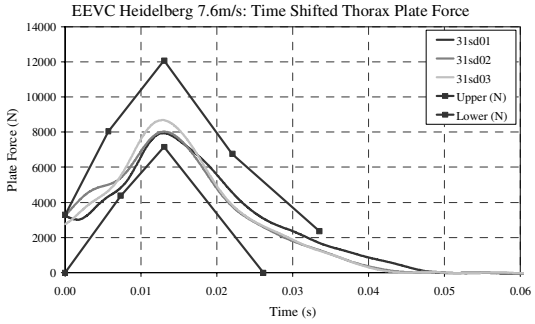

Figure 24: 6.8m/s Heidelberg thorax force EEVC.

The acceleration responses in the Heidelberg test are given in Table 9. Note that dummy rib1 corresponds with human rib4. The T1 and T12 spine responses are below the ISO targets, while the rib accelerations are above the ISO targets. Such response suggests that there may be a mass distribution problem, with too little mass on the outer circumference of the dummy and too much mass in the spine. This hypothesis is further supported considering that this dummy does not have damping material on the ribs, that the ribs themselves are made from a relatively low density alloy, and there is not much more material outside the ribs than a foam pad and a dummy suit. However the T1 acceleration in the 4.3 m/s pendulum test contradicts this hypothesis.

Table 9.
Peak lateral accelerations 6.8 m/s rigid sled test

Peak Lateral acceleration	ISO target	test1	test2	test3	CV %
T1	100-149	54.5	50.3	54.2	5.1
Rib 1	78-122	176	159	155	6.7
T12	87-131	54.6	53	63.9	10.3

The overall thorax responses are summarised in Table 10. The force-time responses of three tests are very close to scoring 10 points in the ISO TR9790 rating. The good performance of the thorax body segment is not fully reflected in the body segment rating of 6.3 according ISO TR9790. Note that this score is based on sub set of four out of six specified test conditions.

Table 10.
Thorax ISOTR9790 biofidelity rating

Impact condition	Measurement	Average	Test	Body region
4.3 m/s HSRI pendulum	Pendulum force	5.0		
	Peak T4 Y acc.	5.0		
			5.0	
6.0 m/s WSU/GML pendulum	Pendulum force	5.0		
			5.0	
6.8 m/s Heidelberg rigid sled	Thorax plate force	10		
	peak T1 Y acc.	3.3		
	peak T12 Y acc.	5.0		
	peak rib acc.	5.0		
			6.0	
8.9 m/s WSU sled 23 PSI padded	shoulder + thoracic plate force	5		
	Peak lateral displacement of T12	10		
			6.8	
				5.6

Abdomen - The abdomen biofidelity is evaluated in two Wayne State University sled test conditions at 6.8 m/s rigid and 8.9 m/s padded. The responses are shown in Figure 25 and Figure 26, the biofidelity rating is given in Table 11. The abdomen force is almost entirely in the corridor for the 6.8 m/s test and fully within the envelope of the 8.9 m/s test. The abdomen response, rated 8.5 in these tests, is rather good; however, only two out of five test conditions are considered for the abdomen.

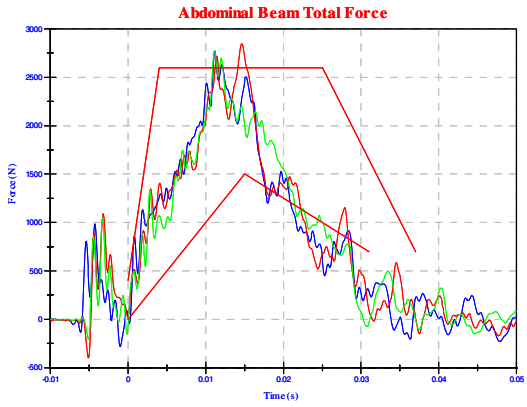

Figure 25. Abdomen force 6.8 m/s rigid WSU.

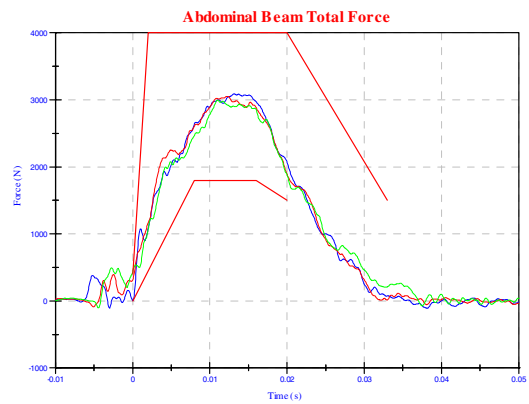

Figure 26. Abdomen force 8.9 m/s padded WSU.

Table 11.
Abdomen ISOTR9790 biofidelity rating

Impact condition	Measurement	Average	Test	Body regio
6.8 m/s WSU rigid sled	Abdominal plate force	5.0	**5.0**	
8.9 m/s WSU sled 23 PSI padded	Abdominal plate force	10	**10**	
				8.5

One particular outcome of the abdomen test was the poor repeatability of abdomen deflection in the sled tests (CV 23%) and the significant difference between upper and lower abdomen deflection, see Table 15. During the anthropometry evaluation it was found that the upper arm length did not meet the anthropometric target, see Figure 6. Figure 27 shows the position of the WorldSID small female on the sled and the relative position to the force beams. Note that the arm is in-between the torso and the load plates of the sled. The figure shows that lower end of the arm is coincident with the top of the lower abdomen and that the lower abdomen is not loaded through the arm. The unbalanced loading of the upper/lower abdomen in case the arm is in the load path, raises a concern of over-/under-assessment of injury. The other concern raised is that the interaction of the dummy with the load plate was different than the PMHS in the original tests. The poor repeatability of the lower abdomen is due to the small interaction with the load plate, resulting in small deflection and the relatively large influence of small variations. A second factor may be that, due to a small variation in arm position, there was more interaction with the arm in one test than in the other tests.

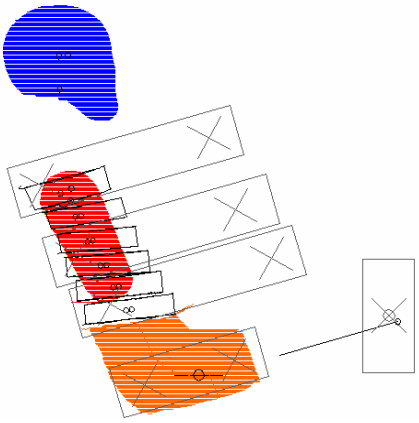

Figure 27. WorldSID small female position relative to WSU load plates.

Pelvis - The biofidelity of the pelvis was evaluated in seven test conditions, five of which were rigid and padded sled tests and two were linear guided and pendulum impactor tests. The linear guided impactor tests were performed with a mass of 10.26kg and the pendulum impactor tests were performed with a 14kg pendulum. The responses of the impactor tests were scaled to 10.14kg, using Equation (8).
The pelvis sled test responses are presented in Figure 28 through Figure 30 and Table 12. The responses are shown relative to EEVC as well as ISO corridors. The pelvis performs particularly well in the high speed padded and rigid sled tests and the low speed impactor tests. In these tests the force responses are inside the corridors. The acceleration responses are close to the corridors; the rigid Heidelberg accelerations are too high (high and low speed), WSU and Heidelberg high speed padded and WSU rigid low speed accelerations are below the corridors. No trend can be found in the pelvis accelerations.

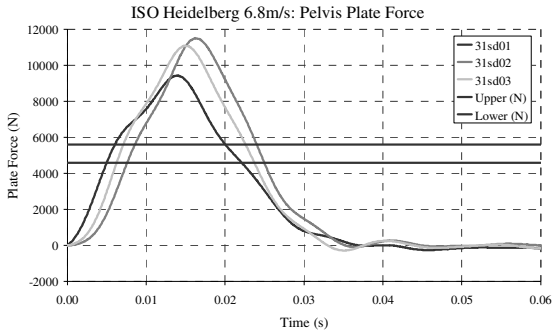

Figure 28. Pelvis Heidelberg 6.8 m/s rigid ISO

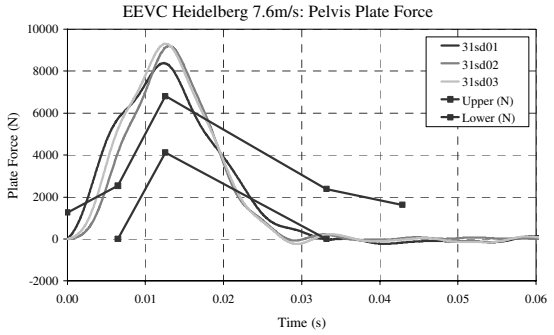

Figure 29. Pelvis Heidelberg 7.6m/s rigid EEVC.

The performance in the WSU 6.8 m/s rigid and the high speed impactor tests is reasonable. The performance is poor in the low speed rigid Heidelberg test in the ISO corridors and slightly better according EEVC corridors. No trend can be obtained from the pelvis force responses relative to impact velocity, as sled test and impactor tests show a contradicting trend. The different responses between tests may be explained by the different loading: in the impactor test the pelvis is loaded locally at the Greater Trochanter, in the Heidelberg tests all of the thigh and pelvis is loaded and in WSU only half of thigh is loaded and there is a knee impact plate.

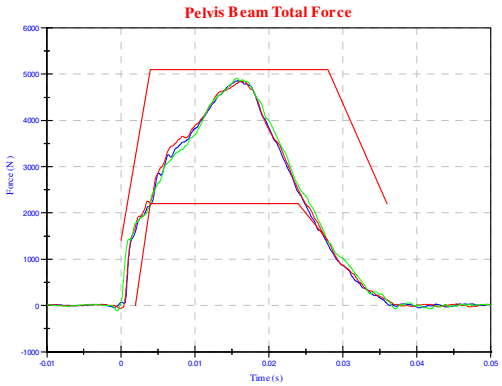

Figure 30. Pelvis WSU 8.9m/s padded

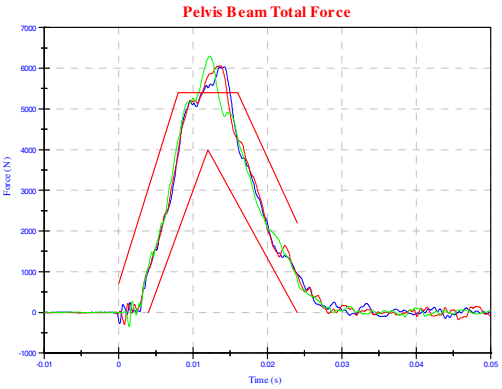

Figure 31. Pelvis beam force WSU 6.8m/s rigid ISO corridors

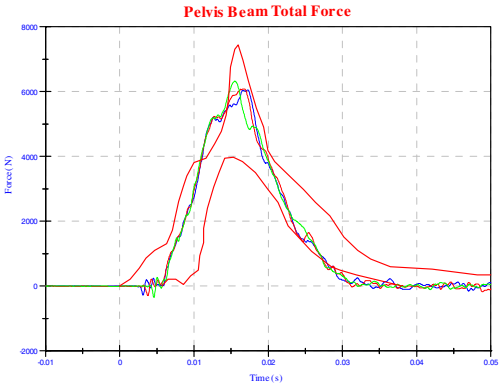

Figure 32 Pelvis beam force WSU 6.8m/s rigid EEVC corridors

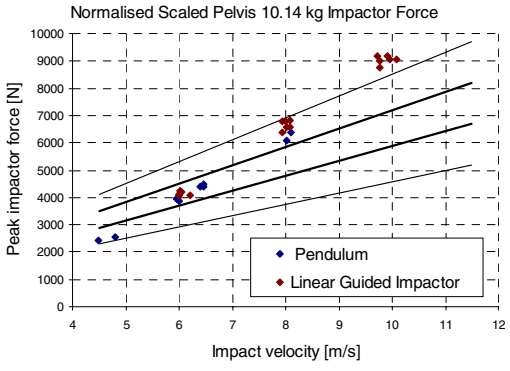

Figure 33. Normalised pelvis impactor forces

Table 12.
Summary pelvis sled test results

		Corridors		test1	test2	test3	CV%
Heid 6.8R	force	4.6	5.6	9.3	11.3	10.9	10.1
	acc.	78	95	99.3	101	102	1.2
Heid 8.9R	force	16.2	19.1	16.8	17.8	17.3	2.9
	acc.	118	143	162	166	164	2.7
Heid 8.9P	force	8.4	9.8	9.3	9.6	9.6	1.8
	acc.	75	93	68.2	71.9	70.5	2.7
wsu 6.8R	force	4	5.4	6.0	6.1	6.3	3.7
	acc.	105	142	101	96.2	102	1.7
wsu 8.9P	force	2.2	5.1	4.9	4.8	4.9	1.2
	acc.	80	110	76.6	76.7	74.3	1.8

Table 13.
Pelvis ISOTR9790 biofidelity rating

Impact condition	Measurement	Average	Test	Body regio
4.5 m/s 10.14 kg impact	Pendulum force	10	**10**	
11.5 m/s 10.14 kg impact	Pendulum force	0	**0**	
6.8 m/s Heidelberg rigid sled	Peak pelvic force Peak pelvic acc.	0.0 5.0	**2.2**	
8.9 m/s Heidelberg rigid sled	Peak pelvic force Peak pelvic acc.	10 5.0	**7.7**	
8.9 m/s Heidelberg padded sled	Peak pelvic force Peak pelvic acc.	10 5.0	**7.6**	
6.8 m/s WSU rigid sled	Peak pelvic force Peak pelvic Y acc.	5.0 5.0	**5.0**	
8.9 m/s WSU 23 PSI padde sled	Peak pelvic force Peak pelvic Y acc.	10 5.0	**7.8**	
				5.6

The ISO TR9790 pelvis biofidelity rating per test condition and overall is summarised in Table 13. The table shows some very good and some poor results, but does not clearly indicate how to improve further the pelvis segment biomechanical response. The overall pelvis biofidelity rating is 5.6 and does not meet the body segment target of 'good to excellent' biofidelity. Note that this score is based on sub set of seven out of thirteen specified test conditions; however the highest weighting factor tests were included in this sub set.

Biofidelity

The body segment and full dummy biofidelity is summarised in Table 14. The result is based on a sub-set of test conditions with high weighting factors and is a good indication of the dummy's biofidelity. The overall rating just exceeds the target of B > 6.5; however, not all body segments meet this target. Some of the responses, particularly for the thorax, are close to scoring 10 points rating. The overall result is

considered to be quite encouraging for a prototype dummy.

Table 14.
Summary ISOTR9790 Biofidelity Rating

Overall rating WorldSID 5th %-ile	
Head	10
Neck	4.9
Shoulder	5.0
Thorax	5.6
Abdomen	8.5
Pelvis	5.6
Overall rating	**6.7**

Repeatability

The repeatability of the dummy was evaluated by repeating the same test condition at least three times. Some of the results are presented in Table 15.Table 15. Table 17. In the Heidelberg sled test coefficients of variation were in the same order as in the WSU test.

Table 15.
WSU 6.8 m/s rigid sled internal measurement

Dummy segment	Magnitude	Mean	Sd	CV (%)
Thorax	T1 Acc. y (g)	45.3	1.8	4.0%
	T12 Acc. y (g)	68.6	5.2	7.6%
Ribs displacement [mm]	Shoulder	-59.1	0.25	0.4%
	Upper Thorax	44.5	2.1	4.6%
	Middle Thorax	47.3	0.7	1.5%
	Lower Thorax	44.7	1.5	3.4%
	Upper Abdomen	32.3	2.4	7.4%
	Lower Abdomen	10.5	2.4	23%
Pelvis	Acc. y (g)	78.9	1.3	1.7%
	Pubic Fy (N)	-1138	35	3.0%

Table 16.
WSU 6.8 m/s rigid sled external loads

Barrier beam	Mean	Sd	CV (%)
Shoulder Beam (N)	2772	98	3.5%
Thorax Beam (N)	4211	514	12.2%
Abdomen Beam (N)	2354	25	1.0%
Pelvis Beam (N)	7742	285	3.7%
Knee Beam (N)	10397	293	2.8%

Table 17.
14kg shoulder and thorax pendulum test

Parameter	Mean	Sd.	CV[%]
Shoulder deflection [mm]	24.6	1.0	4.1
Shoulder force [N]	2309	49	2.1
4.3m/s Thorax Rib 1 [mm]	15.9	0.3	1.6
4.3m/s Thorax Rib 2 [mm]	22.1	0.1	0.5
4.3m/s Thorax Rib 3 [mm]	20.2	0.2	1.1
4.3 m/s Pendulum force [N]	2678	25	0.9
4.3m/s T1 acceleration [G]	21.8	0.3	1.5
6.0m/s Thorax Rib 1 [mm]	26.9	1.2	4.5
6.0m/s Thorax Rib 2 [mm]	35.9	1.5	4.2
6.0m/s Thorax Rib 3 [mm]	34.0	1.2	3.6
6.0m/s Pendulum force [N]	3231	39	1.2

The WSU and Heidelberg padded test results were more repeatable then the rigid test results. Most results were well within the repeatability requirement of CV<7%. Some results do not meet the requirement. The CV of the thorax force beam in the WSU 6.8 m/s test was 12%. This result is attributed to differences in body segment contact orientation and timing due to differences in dummy sliding on the test bench. The high CV of the lower abdomen deflection was explained earlier in the paper. The pendulum tests are more repeatable then the sled tests.

Sensitivity

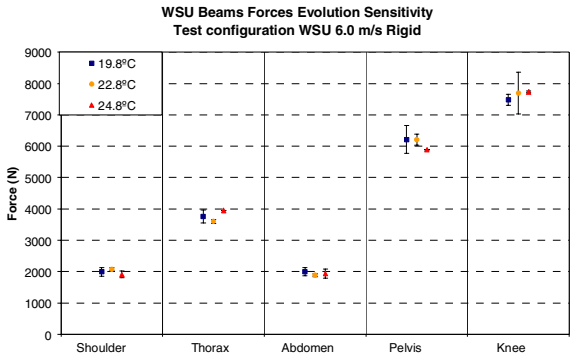

Figure 34. Temperature variation external measurements variability.

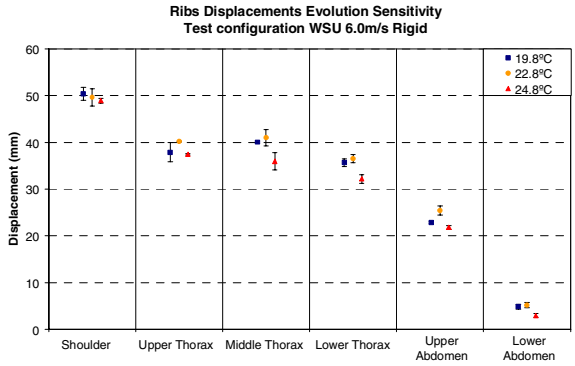

Figure 35. Temperature variation internal measurements variability.

Table 18
Variability of load responses

	Coefficient of variation (%)			
	Test 24.8ºC	Test 22.8ºC	Test 19.8ºC	All test 6.0 m/s
Shoulder Beam	4.02	1.55	4.72	4.70
Thorax Beam	0.00	1.23	3.99	4.59
Abdomen Beam	5.38	1.78	4.68	4.21
Pelvis Beam	0.12	2.06	5.05	3.70
Knee Beam	0.23	6.07	1.69	3.27

6.0m/s WSU sled tests were conducted at 20ºC, 23ºC and 25ºC environment temperature to evaluate the temperature sensitivity of the dummy. The results are shown in Figure 34 and Figure 35. The test results revealed no trends in dummy responses due to

temperature variation. The variations due to temperature variation were below 5% and were similar to the test-to-test variability, see Table 18.

Dummy prototype problems

The main problems occurring during the Aprosys evaluation are given below.
Tilt sensor problems were experienced due to loss of software after the PDA battery had fully drained.
Dummy battery charging remained a problem, even after exchange of new batteries. No battery charge indicator is available to the user. Battery charge problems seem to be related to the long off time between charges as dummies were transported between labs.
Wiring problems were experienced. All of them can be attributed to the smaller size of the dummy and reduced space in the sternum and particularly in the pelvis, where wires were crushed and a connector was damaged in the 10.3 m/s Heidelberg tests. The prototype dummy pelvis had a high wire content with one pubic, two femur, two femoral neck, and double sacro-iliac load cells and a tri-axial accelerometer adding up to 40 channels.
Some signals registered by the in-dummy DAS system presented a high level of noise. It was found that the CAC settings were set to high for the expected data to be collected.
During the Aprosys evaluation the rib permanent deformation was monitored between tests. The thorax ribs were settling 1-2 mm and then remained constant. The shoulder sustained permanent deformation continuously until the rib width came closer to the thorax ribs, unloading the shoulder rib. In the 10.3 m/s rigid Heidelberg tests the thorax ribs also sustained permanent deformation, but no ribs were broken. Also the shoulder load cell connector sustained damage in this test. The shoulder rib stop appears not to be protecting the rib. The Heidelberg tests were run without IR traccs to avoid damage. In the WSU 6.8 rigid tests two IR traccs were damaged.

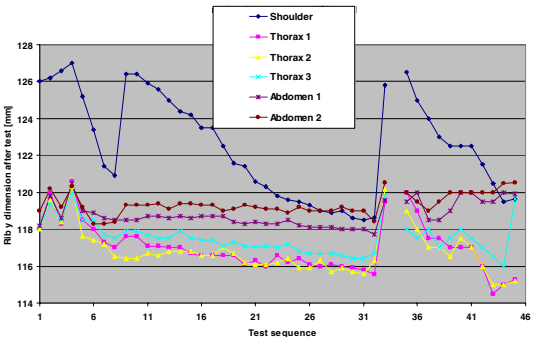

Figure 36. Rib permanent deformation record.

The IR-traccs in the thorax registered flat tops in the thorax compression (Figure 37). Also flat tops in the rib deflection were registered with the WorldSID small female dummy outside the Aprosys consortium.

The phenomena are believed to be related to forward deformation of the ribs relative to the spine and associated extension of the IR-traccs, (Hynd *et.al.* 2004). Flat top responses generally raise the concern whether the actual peak of the measured parameter is registered. Further, the IR-traccs are close to maximum range, even in moderate speed biofidelity tests.

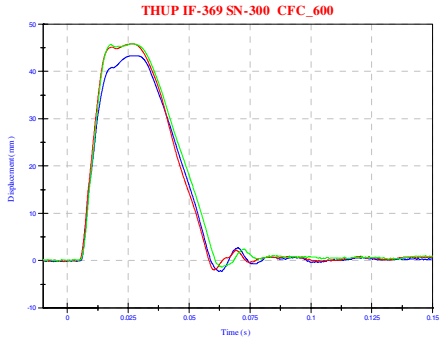

Figure 37. Upper rib deflection WSU 8.9 padded.

Also the shoulder deflection trace showed flat tops in the WSU tests. The shoulder string potentiometer is not recording the peak deflection, as shoulder rib accelerations exceeding 250 G were registered. The potentiometer is rated 50G, beyond which the string becomes slack.
Some problems were related to the half arm. The shoulder joint friction adjustment was difficult. The arm bone static bending stiffness of the dummy was compared analytically to human data based on Kemper *et.al.* (2005). The bending stiffness of the dummy humerus bone is much lower then the human target.

CONCLUSIONS and RECOMMENDATIONS

Conclusions

Two WorldSID small female prototype side impact dummies were extensively evaluated and tested to verify compliance of the dummy to its requirements. Some issues were found with the anthropometry, but these can be corrected. The overall biomechanical responses of the prototype just meets the target of good biofidelity (B>6.5), but not all body segments meet the biofidelity rating target. This is considered to be quite encouraging for a prototype dummy. However, some of the results are contradictory and do not provide clear guidance for improving the performance of the dummy . The repeatability of the dummy was good with a coefficient of variation generally below 5%. The sensitivity of the dummy to temperature variation was evaluated. The tests results revealed no trends in dummy responses in the temperature domain of the tests (20ºC -25ºC).

Recommendations for dummy update

Anthropometry - The abdomen and lower thorax mass shall be increased by 1.2kg. The lower leg should be redesigned to meet human anthropometry targets of mass, CoG location and target ratio of bone and flesh mass. The foot shall be redesigned to meet human anthropometry targets of mass and UMTRI surface shape and joint location. The half arm shall be redesigned to meet targets for total length, bone length and bone stiffness.

Biofidelity - The head skin thickness shall be tuned to meet the frontal impact response. The biofidelity targets for head-neck response appear to be conflicting and should be reviewed. The prediction of head injury as well as test data sample size should be prioritised when selecting biomechanical head-neck impact response specifications. Adopting the NBDL internal neck load corridors derived by Philippens *et al.* (2004) shall be considered.

Durability - Adequate fixation points for wires in the sternum and pelvis shall be provided. Wire lengths shall be optimised and wire gauge reduced if possible. Rib overload stops shall be designed for the shoulder and the thorax ribs.

Handling - The battery charging system shall be redesigned including a charge status indicator. The hip joint to iliac wing assembly shall be improved. The shoulder joint friction adjustment shall be improved.

Instrumentation - A rib deflection measurement system shall be developed to meet the following targets: 2d measurement of deflection in the rib plane; increased range of measurement exceeding 60mm; suitable for implementation in the shoulder, thorax and abdomen; suitable to act as rib overload protector.

Procedures - Pubic load shall be well controlled, as it is an injury assessment parameter. The certification procedure shall be updated to include pubic load measurement.

ACKNOWLEDGEMENTS

This work was supported through funding from: the European Commission, UK Department for Transport, MEC, DGUI-SEGVAUTO, and Dutch Ministry of Transport, Public Works and Water Management. In- dummy data acquisition system: DTS; Accelerometers: AUDI AG; Staff of test laboratories FTSS - INRETS - TNO - TRL - UMP-INSIA.

REFERENCES

Barnes A.S., Been B.W., Bermond F., Bortenschlager K., Caire Y., Carrol J.A., Compigne S., Hynd D. and Martinez L. (2004). "WorldSID 5th Female Requirements", APROSYS Document number AP-SP52 0007-D1.

Hynd D., Carrol J.A., BeenB.W. and Payne A.R., "Evaluation of the Shoulder Thorax and Abdomen of the WorldSID Pre-Production Side Impact Dummy", IMechE Vehicle Safety Conference 2004.

Irwin A.L., Mertz H.J., Ali M. Elhagediab A.M. and Moss S. (2002). "Guidelines for Assessing the Biofidelity of Side Impact Dummies of Various Sizes and Ages", SAE 2002-22-0016, Stapp Car Crash Journal, Vol. 46 November 2002, pp 297-319.

ISO (1997). ISO/TC22/SC12/WG5, Road Vehicles – Anthropometric side impact dummy – Lateral impact response requirements to assess the biofidelity, Technical Report 9790.

Kemper A., Stitzel J., Duma S., Matsuoka F. and Masuda M., "Biofidelity of the SID-IIs and a modified SID-IIs upper extremity: Biomechanical properties of the human humerus", Paper Number 05-0123.

Philippens M., Cappon H., and van Ratingen M., "Human volunteer head-T1 response for oblique impact conditions", International IRCOBI Conference on the Biomechanics of Impact. Graz, Austria, 2004.

Roberts A., Lowne R., Beusenberg M. and Cesari D. (1991). "Test procedures for defining biofidelity targets for lateral impact test dummies" 13th International Conference on Experimental Safety Vehicles, Paris, France, 04th to 07th November, 1991.

Schneider L.W., Robbins D.H, Pflüg M.A. and Snyder R.G. (1983). "Development of anthropometrically based design specifications for an advanced adult anthropomorphic dummy family." Final Report DOT-HS-806-715 NHTSA.

Wang Z.J., Been, B.W., Barnes A.S., Burleigh M.J., Schmidt A., Dotinga M. and Ratingen M.R.van (2007). "WorldSID 5th Percentile Prototype Dummy Development", SAE #2007-01-0701.

SCALABILITY OF HUMAN MODELS

Carmen Rodarius
Lex van Rooij
Ronald de Lange
TNO Science and Industry
The Netherlands
Paper No. 07-0314

ABSTRACT

The objective of this work was to create a scalable human occupant model that allows adaptation of human models with respect to size, weight and several mechanical parameters. Therefore, for the first time two scalable facet human models were developed in MADYMO. First, a scalable human male was created from an existing 50th percentile human occupant. But since the anthropometry between males and females differs too severely, a scalable human female was created as well to be able to obtain female models with different anthropometry.

Using these models in the MADYMO / Scaler, a target model anthropometry could be created either by defining an anthropometry set of 35 values, by defining 16 fixed scale factors or by using the GEBOD anthropometry database (BAUGHMAN, 1986). Additional to the geometric properties, the following mechanical properties were also scaled using appropriate scaling rules: mass, inertia, stiffness and contact characteristics. Several anthropometrically extreme models, ranging from small children to large adults, have been created using the 3 possible methods to provide the input. Direct definition of anthropometry values and definition of fixed scaling factors resulted in realistic scaled models, whereas using the GEBOD anthropometry database could lead to unrealistic ones, especially when scaling towards children.

A frontal crash application has been developed, using the original 50th percentile human occupant as released with MADYMO and two scaled male models of 65 kg and 85 kg weight with equal height as the base model, to demonstrate the benefit of the scalable models.

INTRODUCTION

Computers are getting faster and faster nowadays and possibilities for numerical simulations are increasing. Due to that, numerical automotive (impact) simulations are getting more and more important for the automotive industry, since they provide a cheap and effective way to help improving occupant safety on next generations of cars. In a crash, humans with different body sizes need to be protected rather than crash test dummies of only average sizes (HAPPEE ET AL., 1998, VAN HOOF ET AL., 2003). This results in the need for a scalable human occupant model, which should be easy to handle and can provide the possibility to adapt a models anthropometry due to the needs of the desired application, as was developed during this work.

GENERAL SCALING PROCEDURE

MADYMO / Scaler

The MADYMO / Scaler has been created to scale occupant models in MADYMO (DE LANGE, 2005). It allows the user to scale a model in three different ways:

- Specifying gender, mass and standing height for creating a model based on the GEBOD anthropometry database (BAUGHMAN, 1986)
- Specifying a data set of 35 anthropometry values according to Table 1
- Specifying direct scaling factors λ_x, λ_y, λ_z and λ_{xyz} for each dimension of the 14 scalable body sections of Table 2.

The definitions of the anthropometry values are given in the MADYMO Utilities Manual Release 6.3.1 (2006). With respect to the dimensions, x is always referring to the depth of a body section (e.g. “chest depth” for body region “thoracic spine”), y to its lateral width (e.g. “head breadth” for region “Head”) and z to its height (e.g. “Knee height seated” for region “lower leg”).

To obtain the scaling factors λ_x, λ_y and λ_z (in case they are not specified directly) the target anthropometry values X_i (or the values retrieved out of the GEBOD database) were divided by the correspond-

ing reference anthropometry values $X_{i,ref}$ given in the parameterised model file. (Equation 1)

$$\lambda_i = \frac{X_i}{X_{i,ref}} \qquad i = x, y, z \qquad \textbf{(1).}$$

These factors were mainly used to scale the models geometry and geometry based parameters as mass and moment of inertia. Additional to that the following parameters were scaled as well:

- Joint characteristics (stiffness, friction, damping and hysteresis)
- Contact characteristics
- All other force models

Therefore, the set of scaling parameters was extended with a scaling factor λ_{xyz}. This factor is calculated as third power root of λ_x, λ_y, λ_z (Equation 2)

$$\lambda_{xyz} = \sqrt[3]{\lambda_x \lambda_y \lambda_z} \qquad \textbf{(2).}$$

The scaling rules that were applied are to a great extend similar to those used for normalization and scaling (IRWIN AND MERTZ, 1997, VAN RATINGEN, 1997, MERTZ ET AL., 1989), though no "response corridors" but model parameters were scaled. All material parameters were assumed to be invariant with subject size.

Table 1.
Anthropometry data set for scaling

No	**Value**
1	Weight
2	Standing height
3	Shoulder height
4	Armpit height
5	Waist height
6	Seated height
7	Head length
8	Head breadth
9	Head to chin height
10	Neck circumference
11	Shoulder breadth
12	Chest depth
13	Chest breath
14	Waist depth
15	Waist breadth
16	Buttock depth
17	Hip breath, standing
18	Shoulder to elbow length
19	Forearm – hand length
20	Biceps circumference
21	Elbow circumference
22	Forearm circumference
23	Wrist circumference
24	Knee height, seated
25	Thigh circumference
26	Upper leg circumference
27	Knee circumference
28	Calf circumference
29	Ankle circumference
30	Ankle height, outside
31	Foot breath
32	Foot length
33	Hand breadth
34	Hand length
35	Hand depth

Table 2.
Body sections into which the model is divided

No	*Body Region*
1	Pelvis
2	Lumbar spine
3	Abdomen
4	Thoracic spine
5	Ribcage
6	Neck
7	Head
8	Clavicles
9	Upper arm
10	Lower arm
11	Hand
12	Upper leg
13	Lower leg
14	Feet

Note, when using GEBOD, weight and height have to be specified in either kilograms (KG) and meters (M) or percentiles (%tile).For more detailed information on the scaling tool see MADYMO Utilities manual Release 6.3.1 (2006)

Creation of the parameterized model files

The parameterized files were created using the existing MADYMO 50th and 5th percentile human (DE LANGE ET AL., 2005). The models are put in upright standing position, with horizontal arms (parallel to the y – axis) to simplify the scaling process (see Figure 2).

In reference space, two planes in each direction located at ± 1.50 m from the models H-point were implemented. These planes were needed in order to control standing height, seated height and shoulder breadth. Five ellipsoids were implemented at the pelvis, at the top of the head, at the bottom of the heel and one at each side of the shoulder. By measuring the distance of these ellipsoids relative to the appropriate planes, standing and seated height as well as the shoulder breadth were calculated and controlled by the MADYMO / Scaler during the actual scaling process, which ran through an optimization routine.

The MADYMO / Scaler utility already allowed scaling various dummy models (HAPPEE ET AL., 1998) and a pedestrian human model (VAN HOOF ET AL., 2003) based on ellipsoid geometry. Scaling an ellipsoid model was relatively simple since every ellipsoid could be scaled in each dimension by applying an appropriate scaling factor. No irregularities would occur with a skin mesh in the resultant model. The distance between two adjacent ellipsoids is always determined by a joint that connects the bodies, the ellipsoids are attached to. Therefore, also the overall geometry of an ellipsoid dummy model could be easily modified towards a scaled model by scaling the distances determined by those joints.

For a facet model, in general scaling could be applied in a similar way. Scale factors for each body region of Table 2 were calculated according to Equation 1 and 2 and the scaling was performed as mentioned above. However, for a facet model the overall geometry is not determined by ellipsoids, but by an continuous FE mesh covering different body sections and consisting of rigid elements. This resulted in different parts of the mesh being scaled with different scale factors for each dimension. Therefore in a first approach problems occurred since the originally smooth mesh contained many rough edges wherever the scaling factors changed moving from one body region to another. As an example this is explained for the elbow region. Since the upper arm is likely to get a different scaling factor than the lower arm, the mesh in the elbow region will be badly shaped if not adapted (Figure 1).

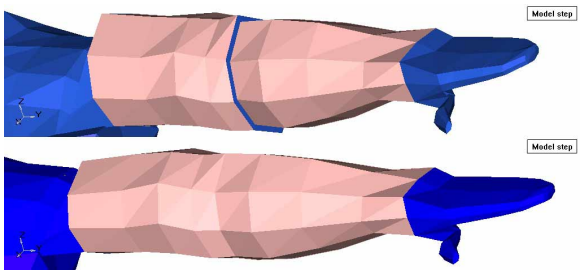

Figure 1. Scaled arm with (bottom) and without (top) mesh smoothing

The transition nodes of the lower arm were then not congruent any more with the transition nodes of the upper arm. To avoid this unwished effect, linear mesh smoothing functions were applied in these intersection areas.

Creation of a scaled model

In order to create a scaled human model, the three procedures mentioned before can be used:

- GEBOD
- User Defined (anthropometry data set)
- Fixed Scale Factors

In case most measures of the anthropometry of the target model are known, most reasonable results can be obtained using method two. If only weight and height of the target model are of interest, GEBOD can be used as well. Nevertheless, the anthropometry of models based on GEBOD should always be checked carefully since they often turned out to be unrealistic in some body parts like shoulder and upper leg. If so, the model could easily be corrected by a second scaling using the retrieved anthropometry data of the GEBOD model and correcting unrealistic scaling factors towards realistic ones.

It is not only possible, to scale the parameterized models towards adults, but also towards child anthropometry. As a base model, the male model can be scaled using a self defined anthropometry set. GEBOD is not suitable in this case, since it was often found to result in highly unsuitable models, especially when scaling towards very young children. This is exemplified in Figure 2 where both, a model of a three year old child created with GEBOD (left) and created with a self defined anthropometry data set based on the CANDAT database (right) (TWISK ET AL., 1993) is provided.

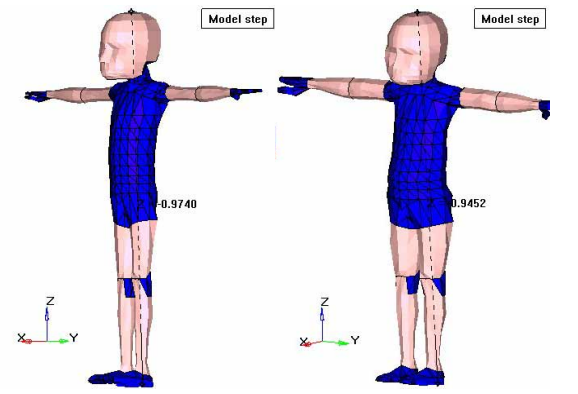

Figure 2. Child model resulting from GEBOD anthropometry (left) and from CANDAT anthropometry

In general, it is advised to use the female model only to scale towards adult females or teenage females that have reached puberty (app. age 13). The male model should only be used for male and child models. No appropriate outer geometry will be obtained otherwise due to too significant differences between male and female body shape, the latter which is absent with young children.

FRONTAL IMPACT SIMULATION

So far no validation of the mechanical impact behavior has been performed with the scaled models. To indicate the benefit of this work a frontal impact simulation was performed using two scaled models as well as the standard 50th percentile human occupant model.

Simulation model set up

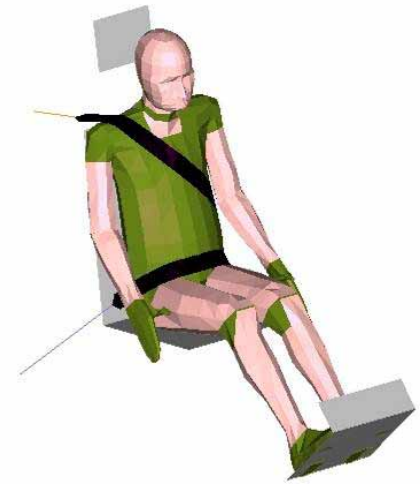

Figure 3. Simulation model set-up including the original 50th percentile human occupant

As simulation set up, the frontal impact application that is provided with MADYMO v6.3.1 was chosen. This model consists of a simple seat and a three point passenger belt system. The following human models were used within this application:

1. 50th percentile human occupant of 1.74 m standing height and 75.86 kg weight
2. Low mass model: Same size as 50th percentile human occupant, but 10 kg lighter
3. High mass model: Same size as 50th percentile human occupant, but 10 kg heavier

The models were created following the procedure described before. The scaling has been performed using the GEBOD anthropometry database and afterwards the models were corrected towards shoulder breath, upper leg length and circumference, neck circumference as well as chest depth. The simulation set up including the 50th percentile human occupant is shown in Figure 3, a side view of all 3 models in standing position is provided in Figure 4. For a better overview in all following pictures that contain all three models, the low mass model (pink) is shown on the left, the original 50th percentile human occupant model (green) in the middle and the high mass model (blue) on the right.

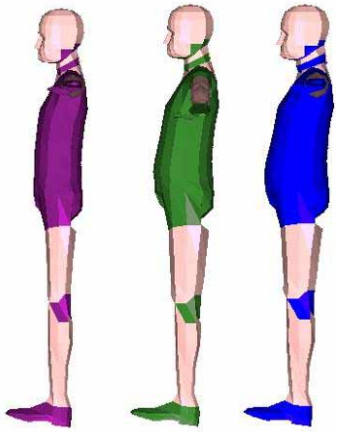

Figure 4. Side view: low mass (left), original (middle) and high mass human model (right) of 1.74 m standing height

All models are first settled into the seat and a separate belt fit is performed as presimulation to the actual impact simulation. The crash pulse represents a zero degrees full frontal impact of a mid-sized passenger car, as provided with the application. The initial position of the low mass and the high mass model in the seat with fitted belts is provided in Figure 5.

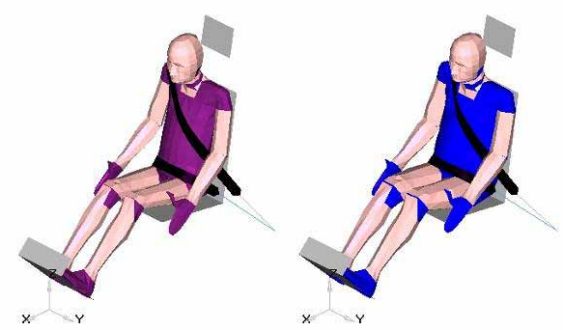

Figure 5. Initial position of the low mass (left) and high mass (right) human occupant model

Results

When looking at the kinetics, it can be seen, that during the impact simulation the low mass model rotated more and the high mass model less around the z axis than the original 50th percentile human occupant. Pictures of all three models at the end of the impact from different views are provided in Figure 6 to Figure 8.

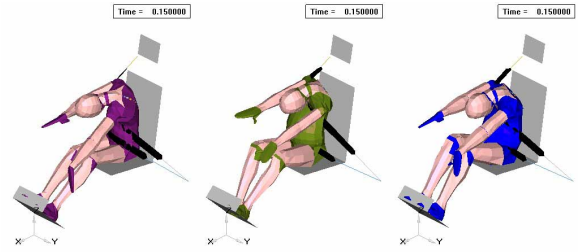

Figure 6. Isometric view of all three models at the end of the impact simulation (low mass model at the left, original model in the middle and high mass model at the right)

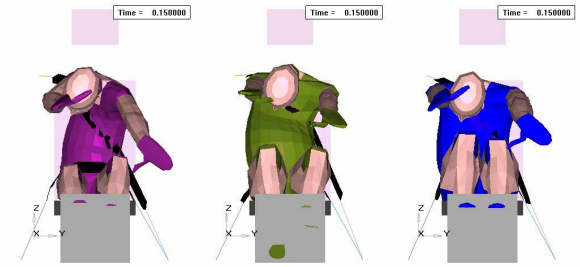

Figure 7. Frontal view of all three models at the end of the impact simulation (low mass model at the left, original model in the middle and high mass model at the right)

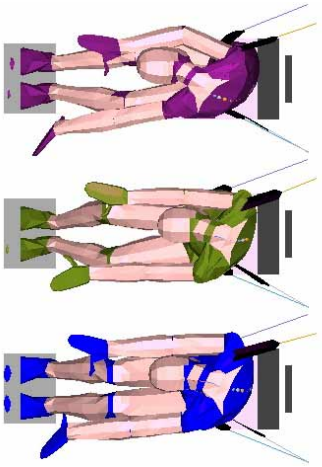

Figure 8. Top view of all three models at the end of the impact simulation (low mass model at the top, original model in the middle and high mass model at the bottom)

This is behavior is considered logic, since a low mass model has more space to move and less contact area with the belt than a high mass model because its less wide in lateral direction. As can be seen in Figure 8 the pelvis belt is also able to pull the low mass model most and the high mass model least back into the seat due to their masses. This also leads to more rotation of the model itself for a light human model.

Differences can as well be found when looking at the time history signals. In Figure 9 and Figure 10 an overview on some of the corresponding results is provided.

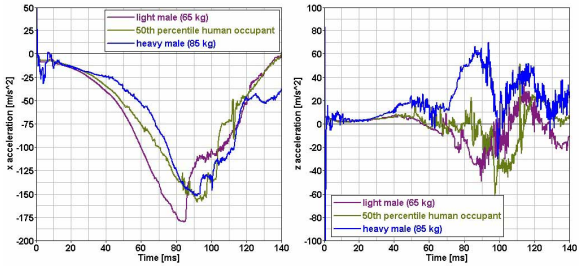

Figure 9. Pelvis x- and z- acceleration

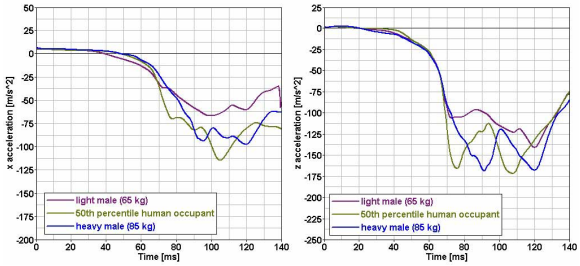

Figure 10. Head CG x- and z- acceleration

It can be stated, that in general the progression of the curves are comparable. The peak values are in the same range, but differ as expected according to the models mass.

Note, that the chosen application is very general and only a first indication on the usefulness of the scaleable models. The created models are not based on actual anthropometry data but out of GEBOD models that were corrected towards values that seamed feasible.

DISCUSSION

Recapitulating it can be stated that the created scalable models are suitable to obtain models that are not representing the available standard human occupants (5^{th} percentile female, 50^{th} and 95^{th} percentile male). In a basic frontal impact application differences could be found in the response of the scaled models and the original 50^{th} percentile human occupant. This indicates that scaled models are able to predict the response of occupants different from the standard models available in a better way. The main difference with respect to previous scalable models lies in the fact that now also models based on facet geometry can be obtained with scaling. Before, scaling was only possible for ellipsoid based models.

The main limitation of the models is that no age based material dependency is taken into account during the scaling. As a result, for example the response of created child models will not be completely biofidelic. Furthermore, the impact behavior of all models (injuries, range of motion, etc.) is not yet validated but only investigated briefly with 2 scaled models. In order to investigate whether scalable models are able to predict the behavior of an actual occupant more precisely than the standard models, two options could be taken into account:

- Comparison to PMHS sled tests
- Real accident reconstruction with known anthropometry data of the actual occupant

In order to investigate the influence of different parameters as neck circumference, neck to chin height or mass on the injury outcome, it might also be useful to perform model studies. Therefore, models could be created that only differ in certain parameters, investigated under one specific loading condition and their behaviors could be compared to the outcome of actual performed tests that can be found in literature.

However, it is assumed that future work with scalable human models will prove the benefit of this work for protection of non average sized occupants.

REFERENCES

Baughman L.D., “Development of an interactive computer program to produce body description data” University of Dayton, AFAMRL-TR-83-058, 1986

De Lange R., Rooij L. van, Mooi H., Wismans J., “Objective Biofidelity Rating of a Numerical Human Occupant Model in Frontal to Lateral Impact” Stapp Car Crash Journal (Vol. 49), 2005

Happee R., Haaster R. van, Michaelsen L., Hoffmann R., “Optimization of Vehicle Passive Safety for Occupants with varying Anthropometry” ESV Conference paper 98-S9-O-03, 1998

Hoof J. van, Lange R. de, Wismans J., “Improving Pedestrian Safety Using Numerical Human Models” Stapp Car Crash journal. Vol. 47, pp. 401-436. SAE Report No. 2003-22-0018, 2003

Irwin A.L., Mertz H.J., “Biomechanical bases for the Crabi and Hybrid III child dummies” SAE 973317, Stapp, 1997

MADYMO Utilities Manual Release 6.3.1, 2006

MADYMO Application Manual Release 6.3.1 2006

Mertz H.J., Irwin A.L., Melvin J.W., Stalnaker R.L., Beebe M.S., “size weight and biomechanical impact response requirements for adult size small female and large male dummies” SAE 890756, 1989

Ratingen M.R., Twisk D., Schrooten M., Beusenberg M.C., Barnes A., Platten G., “Biomechanically based design and performance targets for a 3-year old child crash dummy for frontal and side impact” SAE 973316, Child Occupant Protection Symposium, 1997

Twisk D., Beusenberg M., “Anthropometry of Children for Dummy Design” ECOSA Product Safety Conference, Amsterdam, 1993

CHARACTERIZING DIFFUSE BRAIN INJURIES FROM REAL-WORLD MOTOR VEHICLE IMPACTS

Narayan Yoganandan
Thomas A. Gennarelli
Frank A. Pintar

Medical College of Wisconsin
United States
Paper number 07-0338

ABSTRACT

This study characterized brain injuries with a focus on diffuse axonal injuries using the Crash Injury Research Engineering Network (CIREN) database, developed by the National Highway Safety Administration (NHTSA). Tier one and tier two medical- and crash-related data from 1997 to 2006 were used in the retrospective analysis. Diffuse axonal injuries injuries were assessed using the 1990 version of the Abbreviated Injury Scale. In addition, other brain injuries and bony trauma to this body region were extracted. Potential head contact data were determined based on an evaluation of medical information such as x-rays and CT scans. Crash-related variables such as change in velocity, principal direction of force, and impact modality were obtained.

Case-by-case analyses were grouped as a function of the number head injuries sustained by each occupant. Out of the 3,178 medical cases from 2,823 crashes, 67 occupants, 11 months to 85 years of age, sustained diffuse axonal injuries. Change in velocity ranged from 4 to 24 m/s. Twenty-eight passengers and 39 drivers and were involved in 49 lateral, 15 frontal, and three rear impacts. There were 32 female and 35 male occupants. In no case two occupants sustained diffuse axonal injuries in the same crash. Head contact was identified in a majority of occupants. Airbags were not attributed to be the cause of injury in more than 90% of the cases, implying its minimal role in severe head trauma. These preliminary findings appear to support the hypothesis that diffuse axonal injuries occur with impact loading to the head. In addition, this type of injury occurs more in side crashes than frontal impacts. Furthermore, these results suggest a decreasing trend for the incidence of diffuse axonal injuries in modern vehicular environments, possibly with newer technologies and increased restraint usage.

INTRODUCTION

Motor vehicle impacts continue to be a source of unintentional injury to the human head [1-4]. The recent brain injury symposium held in Washington, DC, in February 2007, emphasizes the importance of trauma to this region of the human body in vehicular environments. In neurosurgical and other clinical literatures, head injuries are commonly classified as open or closed depending on the integrity of the dura. Another classification is based on whether the injury is focal or diffuse [5]. Although national and international databases such as the Cooperative Crash Injury Study, CCIS, in England, and the National Automotive Sampling System, NASS, and Fatal Analysis Reporting System, FARS, in USA have been developed in the past, CIREN database provides opportunities to conduct detailed analyses of trauma from medical and clinical perspectives. Studies have begun to appear in published literature using this database. For example, a study on fractures of the second cervical vertebra was reproted using CIREN and NASS databases [6]. Injury mechanisms were derived based on the analysis of medical- and crash-related data from CIREN [7] Outcomes were correlated with clinical and laboratory studies [7, 8]. Recent presentations at CIREN meetings and the Society of Automotive Engineers – Government Industry conferences held in the United States have adopted a similar approach for analyzing injuries and injury mechanisms to other body regions. Chest injuries and injury mechanisms from pole-induced lateral impacts were described in 2006 [9].

Because head injuries continue to have significant societal impact and are a byproduct of motor vehicle crashes, similar analyses are needed. To the best of our knowledge, such studies for this body region are lacking in published literature. With this as a focus, the present preliminary study was designed to characterize brain injuries. Specifically, diffuse axonal injuries were characterized at the occupant

level using case-by-case analysis of crash- and medical-related information from CIREN database.

METHODS

All occupants with diffuse axonal injuries were included. Brain injuries were classified based on AIS 1990 definition [10]. This included both hemispheres of the cerebrum, cerebellum, and brainstem regions. No limit was placed on the principal direction of force or impact, the magnitude of change in velocity, occupant seating position, restraint availability or use, and occupant demographics. However, rollovers and ejections were excluded.

Medical information in the database included several evaluations. Pre-hospital data included emergency medical technician reports and trauma nurses notes. In addition, emergency room records, immediate and follow-up scans such as computed tomography and magnetic resonance images, operating room records, radiology/neuroradiology findings, and neurological status were included.

Each case was analyzed with a focus on injuries to the head. Case-by-case analyses at the occupant level were grouped into factors such as impact mode, i.e., frontal, side, and rear, and injury severity. Although injuries to other body regions were available, the current study focused on the head. Potential head contact suggesting impact load transfer was included in the characterization. In order to be consistent, the same team of clinical, biomechanics, and crash investigation personnel conducted the analysis. In the following sections, case and occupant are synonymously used.

DATA SOURCES

Information from CIREN database was used in the study. Tier one and tier two data were analyzed for the years 1997 to 2006. It should be noted that CIREN teams have been gathering data since 1996. Although current year data are available, because quality control and other requirements have not been completed, these data were omitted from the analysis. The number of head injuries sustained by each occupant was used as a basis in the analysis.

RESULTS

Between 1997 and 2006, 2,823 “structured case vehicles” and 3,178 “medical cases” were logged into the database. However, 2,618 structured vehicle cases were coded with digital information for data retrieval and analyses. The number of cases post quality control was 1823.

Out of the 3,178 cases in the database, 67 occupants were identified with diffuse axonal injuries with an incidence rate of 2.1%. No crash resulted in diffuse axonal injuries to more than one occupant.

Thirty-nine were drivers and 28 were passengers in the ensemble. Thirty-two were female and 35 were male occupants. Pregnant occupants were not involved. Occupant age ranged from 11 months to 85 years. Fifteen out of the 28 passengers were under 16 years of age and one was an eleven-month old occupant. Fourteen occupants sustained fatal injuries, and 53 were survivors. The cause of death was attributed to be head injury in 11 (79%) cases, aortic trauma in two cases, and internal trauma in one case.

Fifteen were frontal, 49 were lateral, and three were rear end impacts. Figure 1 shows the percentage distribution of these data. Of the 49 lateral impacts, one side impact involved the youngest occupant in the center-rear seating position, and 38 were near side and ten were far side impacted occupants.

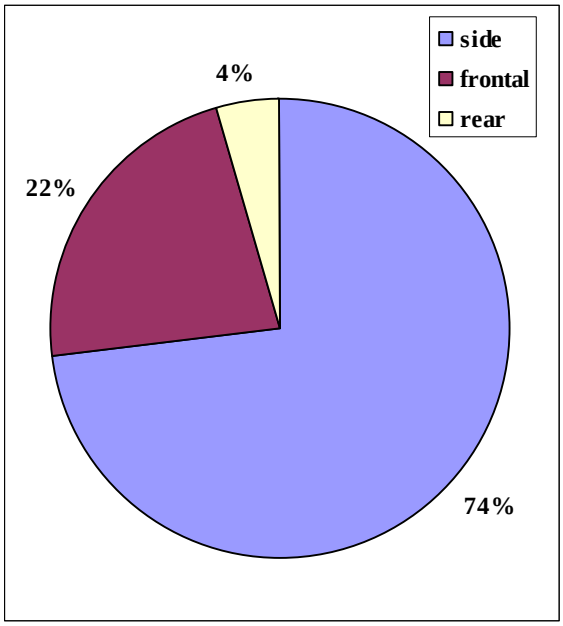

Figure 1: Distribution of injuries by impact mode.

The mean change in velocity was 11.2 m/s (standard deviation: ± 3.8, range 4.4 to 24.7 m/s) for the entire

ensemble. The average change in velocity for the frontal, side, and rear impacts were 11.5 ± 5.5, 10.9 ± 3.4, and 15.1 ± 2.5 m/s.

Out of the 67 occupants, six (9.0%) sustained single diffuse axonal injury. Three were frontal and three near side impacts in this subgroup. All diffuse axonal injuries were to the right or left cerebrum region. One side impact resulted in a fatal injury to the passenger, and noncontact was identified as the injury source for this occupant. Injury severity scores ranged from 26 to 66 in this subgroup. Table 1 summarizes other data.

Table 1.
Summary of data

# of injuries per occupant	# of occupants	# of fatalities	# of occupants with skull fracture	# of occupants with head contact	ISS range	# of impacts		
						frontal	side	rear
1	6	1	0	5	26 to 66	3	3	0
2	13	1	0	11	26 to 43	2	11	0
3	19	3	0	16	26 to 59	6	12	1
4	11	2	1	11	25 to 57	2	7	2
5	4	2	2	4	43 to 50	0	4	0
6	5	2	0	5	35 to 45	0	5	0
7	5	2	1	5	30 to 57	0	5	0

The remaining 59 (91%) occupants sustained at least one diffuse axonal injury and other brain injuries or bony trauma to the head. Table 1 shows the distribution of injuries and associated variables including head contact and skull fracture.

Thirteen (19.4%) out of the 67 occupants sustained two different types of head injuries. The first head trauma was a diffuse axonal injury to the cerebrum (12 cases) or cerebellum (one case). Out of the 13 cases, two were frontal, four were far side, six were near side, and one was an occupant in the center seat with side impact involvement. Rear end impact occupants were absent in this sub group. A far side driver was fatal and all other occupants were survivors. Head contact was identified in 11 (85%) cases. The diffuse axonal injury in one case was attributed to noncontact, and in the other case it was unknown. Injury severity scores ranged from 26 to 43 (Table 1).

Nineteen (28.4%) out of the 67 occupants sustained three different types of head injuries. The first head trauma was a diffuse axonal injury to the cerebrum in 17 cases, one was brain stem, and the other case involved the cerebellum. Head contact was identified in 16 (84%) cases. In one case the diffuse axonal injury was attributed to noncontact, and in the remaining two cases, head contact information was unknown. Three occupants sustained fatal injuries. Injury severity scores ranged from 26 to 59 (Table 1).

Eleven (16.4%) out of the 67 occupants sustained four different types of head injuries. The first head trauma was a diffuse axonal injury to the cerebrum in ten cases and cerebellum in another case. Although skull fractures were not identified in any case, AIS 3 severity orbit fracture occurred to one occupant. Out of the 10 cases, two were frontal, two were rear, and seven were side impacts. Head contact was identified in all cases. This included occupant-to-occupant contact in one case. Injuries to two occupants resulted in fatality. Injury severity scores ranged from 25 to 57 (Table 1).

Four (6.7%) out of the 67 occupants sustained five different types of head injuries. The first head trauma was a diffuse axonal injury to the cerebrum in all cases. Skull fracture occurred in two cases. All occupants sustained side impacts with head contact. Two occupant injuries were fatal. Injury severity scores ranged from 43 to 50 (Table 1).

Five (7.5%) out of the 67 occupants sustained six different types of head injuries. The first head trauma was a diffuse axonal injury to the cerebrum in all cases. Skull fractures were not identified in any case. All occupants sustained side impacts with head

contact. Two occupant injuries were fatal. Injury severity scores ranged from 35 to 45 (Table 1).

Five (7.5%) out of the 67 occupants sustained seven different types of head injuries. The first head trauma was a diffuse axonal injury to the cerebrum in all cases. Skull fracture occurred to one occupant. All five occupants sustained side impacts with head contact. Two occupant injuries were fatal. Injury severity scores ranged from 30 to 57. Figure 2 shows the cumulative distribution as a function of number of head injuries sustained by each occupant. More than one-half of the occupants sustained three or less head injuries (Table 1).

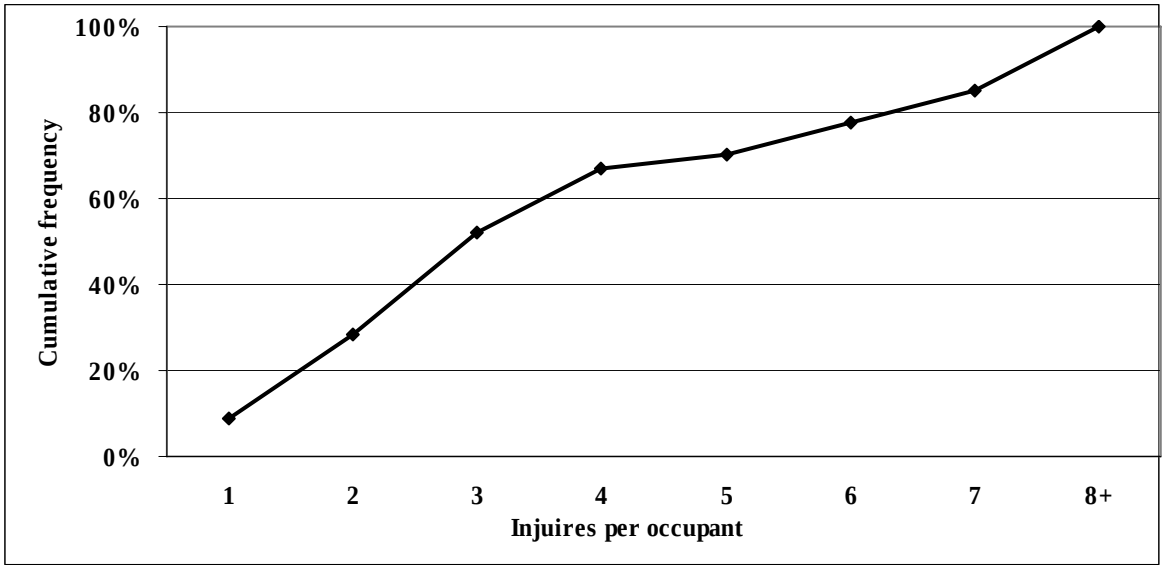

Figure 2: Injury distribution as a function of the number of head injuries sustained by each occupant.

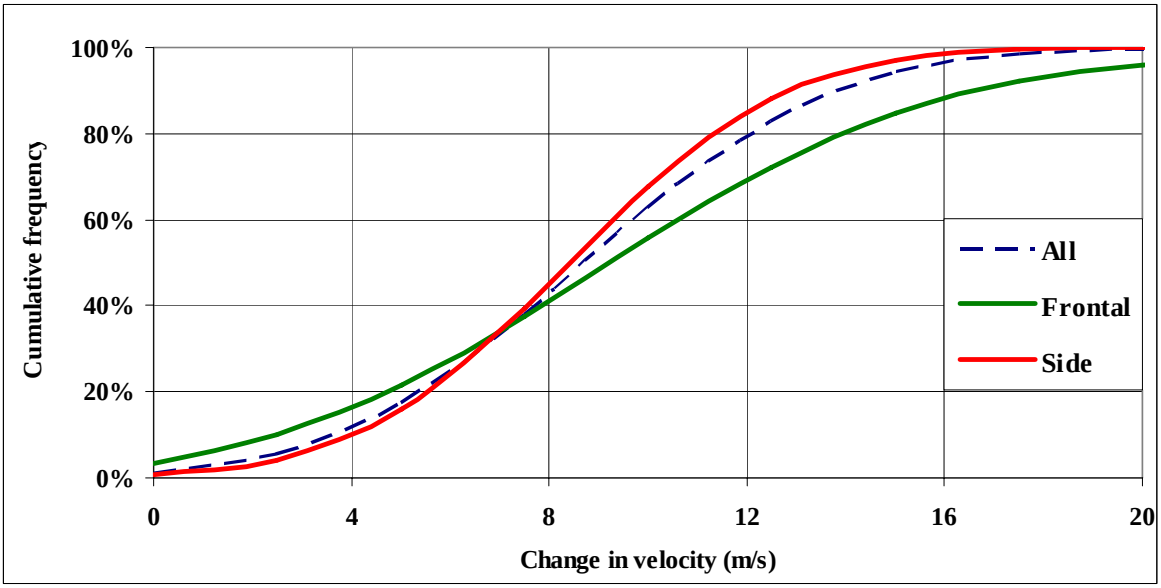

Figure 3: Cumulative frequency of the change in velocity as a function of impact mode.

Figure 3 shows the cumulative frequency distribution of the change in velocity for the entire ensemble, and for frontal and side impacts. More than one-half of the crashes had a change in velocity of 10 m/s or less.

DISCUSSION

As described in the earlier section, more medical cases than case vehicles were logged in the database. The database consists of two main components, i.e., structured case vehicles and individual medical cases. A case vehicle may include more than one occupant. Data entry is done through CIREN and NASSMAIN applications. The former focuses on medical aspects and the latter focuses on crash and vehicle data. A case can be initiated by entering data in either application. However, the two applications remain segregated until a medical case is linked to the corresponding crash case. Thus, a crash case can be associated with more than one medical case. The potential for a 'one-to-many' relationship between a crash case and multiple medical cases explains differences between the number of crash and medical cases in the database.

The quality control of a medical case in this database is involved because of the availability of clinical information such as x-rays and CT. The availability of actual images in the database, along with medical records such as operating room documents and radiology reports, facilitates a more comprehensive analysis (example, injury type) of crash- and clinical-related information. As emphasized, the present study characterized diffuse axonal trauma on an occupant-to-occupant basis, a first step in such analysis. Further analyses such as determining the most commonly associated brain injury with the diffuse axonal trauma and potential variations as a function of impact mode and change in velocity are needed for a more comprehensive understanding of the injury biomechanics.

One of the criteria for case selection is the vehicle model year (less than seven years at the time crash). The current data selection process limits to six years. Although this feature may bias data collection, it has advantages for gathering and analyzing data from recent model years, examining effects of potential crashworthiness improvements, and continuing prospective evaluations of US Federal government Standards. From this viewpoint, gathering of such data is necessary. Presently, eight nation-wide teams are developing a comprehensive, i.e., clinical and crash database with this as a basis, and its uniqueness should assist in assessing performance of more recent model year vehicles. It should however be noted that, because data are gathered from few teams, and are not population based, general estimates cannot be obtained. A more conventional database such as NASS should be used to analyze data from an epidemiological perspective. However, a distinct limitation of NASS is the limited availability of medical records, a critical aspect in studying brain trauma, especially diffuse axonal injuries.

As indicated in the Introduction, the present analysis is limited to the characterization of diffuse axonal injuries. Thus, cases were selected only if an occupant sustained this type of injury. While it is possible and necessary to analyze injury data based on factors such as restraint use/availability, crash severity and mode, being a preliminary study, the analysis is focused mainly at the occupant level. This was achieved by describing other head injuries in association with diffuse axonal trauma.

A small percentage of occupants (less than ten) sustained this type of brain injury without any other accompanying head trauma (Table 1). All occupants with the exception one fatality sustaining the injury due to head contact indicate that single diffuse axonal injury in the motor vehicle environment is most likely associated with contact loading to the head in both frontal and side crashes.

In occupants sustaining more than one head injury associated with diffuse axonal injury as the most severe trauma, as shown in table 1, head contact was again identified in a significant majority of the cases, further emphasizing the role of contact loading. Therefore, it can be hypothesized that diffuse axonal injuries occurs with the transfer of impact loading during the dynamic event, and this observation is independent of crash modality. In addition, the occurrence of minimal number of skull fractures, despite direct loading to the head, suggests that the impact force transmitted is below bony tolerances while exceeding the threshold of diffuse axonal trauma [11]. The presence and increased use of modern restraint systems may account for the decrease in bony pathology.

It is important to include crash-related engineering and medical records in the assignment and evaluation of diffuse axonal injuries as this terminology has been used somewhat loosely in clinical practice. Although the injury has been described, defined, and investigated in the laboratory by the clinical author of this paper and others in the literature, and identifiable on imaging, patient evaluation is critical [5, 12-24].

The present characterization relied on injury coding according to AIS 1990 version. The coding scheme has changed since 2005 as the Injury Scaling team headed by Genneralli has incorporated procedures that include clinical correlation in conjunction with radiological data [25]. From this perspective, no single clinical discipline can conclusively determine and report that the injury belongs to the diffuse axonal type. The next logical step would be to process current data with the new coding scheme. With continuing addition of cases to the database and recoding current data, a more appropriate analysis of head injuries can be made. This is considered as a future research topic.

Although NASS and FARS databases have been in vogue before CIREN and are population-based, these databases were not used because of the lack of required medical records to conduct the retrospective analysis. From a biomechanical perspective, injuries associated with head contact found in significant majority of cases imply the role of direct impact load transmission as a potential trauma mechanism. This is supported by laboratory studies wherein direct load transmission is necessary to reach the high angular acceleration level associated with this type of injury [26]. The study, using first generation mathematical simulations, showed the importance of impact loading of the head to attain injury threshold levels reported in published experimental research. Contact loading mechanism has also been supported by international epidemiological studies [27]. The present characterization from a more recent database and modern vehicle environments further reinforces this conclusion. In addition, because of sample size constraints, the characterization underscores the need to gather similar data from other countries for epidemiological interpretations.

In this limited database, the present preliminary findings appear to support the hypothesis that diffuse axonal injuries occur with impact loading to the head. In addition, this type of injury occurs more in side crashes than frontal impacts. Airbags are not the injury causal agent in a considerable majority of cases (more than 90%), implying its minimal role in severe head trauma. These results suggest a decreasing trend for the occurrence of diffuse axonal injuries in modern vehicular environments, possibly with newer technologies and increased restraint usage.

ACKNOWLEDGEMENTS

This study was supported in part by U.S. Department of Transportation National Highway Traffic Safety Administration DTNH22-05-H-41001. It was also supported by the Department of Veterans Affairs Medical Research. The material presented in this manuscript represents the position of the authors and not necessarily that of the associated organizations. The assistance of Dale Halloway is acknowledged.

REFERENCES

1. Rutland-Brown, W., J.A. Langlois, K.E. Thomas and Y.L. Xi, Incidence of traumatic brain injury in the United States, 2003. J Head Trauma Rehabil, 2006. 21(6): p. 544-8.
2. Sosin, D.M., J.E. Sniezek and D.J. Thurman, Incidence of mild and moderate brain injury in the United States, 1991. Brain Inj, 1996. 10(1): p. 47-54.
3. Sosin, D.M., J.E. Sniezek and R.J. Waxweiler, Trends in death associated with traumatic brain injury, 1979 through 1992. Success and failure. Jama, 1995. 273(22): p. 1778-80.
4. Waxweiler, R.J., D. Thurman, J. Sniezek, D. Sosin and J. O'Neil, Monitoring the impact of traumatic brain injury: a review and update. J Neurotrauma, 1995. 12(4): p. 509-16.
5. Gennarelli, T.A. and D.F. Meaney, Mechanisms of primary head injury, in Neurosurgery, R. Wilkins and S. Rengachary, Editors. 1996, McGraw Hill: New York. p. 2611-2621.
6. Yoganandan, N. and F.A. Pintar, Odontoid fracture in motor vehicle environments. Accid Anal Prev, 2005. 37(3): p. 505-14.
7. Yoganandan, N., J.L. Baisden, D.J. Maiman and F.A. Pintar, Type II odontoid fracture from frontal impact: case report and biomechanical mechanism of injury. J Neurosurg Spine, 2005. 2(4): p. 481-5.
8. Mouradian, W., V.J. Fietti, G. Cochran, J. Fielding and J. Young, Fractures of the odontoid: a laboratory and clinical study of mechanisms. Orthop Clin North Am, 1978. 9(4): p. 985-1001.
9. Pintar, F., Characterizing occupant injuries in narrow-object side impacts. in SAE Government/Industry Meeting. 2006: Washington DC.
10. AIS, The Abbreviated Injury Scale. 1990, American Association for Automotive Medicine: Arlington Heights, IL. 74 pp.
11. Yoganandan, N., F.A. Pintar, A. Sances, Jr., P.R. Walsh, C.L. Ewing, D.J. Thomas and R.G. Snyder, Biomechanics of skull fracture. J Neurotrauma, 1995. 12(4): p. 659-68.
12. Adams, J.H., D. Doyle, I. Ford, T.A. Gennarelli, D.I. Graham and D.R. McLellan,

Diffuse axonal injury in head injury: definition, diagnosis and grading. Histopathology, 1989. 15(1): p. 49-59.
13. Adams, J.H., D.I. Graham and T.A. Gennarelli, Head injury in man and experimental animals: neuropathology. Acta Neurochir Suppl (Wien), 1983. 32: p. 15-30.
14. Adams, J.H., D.I. Graham, T.A. Gennarelli and W.L. Maxwell, Diffuse axonal injury in non-missile head injury. J Neurol Neurosurg Psychiatry, 1991. 54(6): p. 481-3.
15. Gennarelli, T.A. and D.I. Graham, Neuropathology of the Head Injuries. Semin Clin Neuropsychiatry, 1998. 3(3): p. 160-175.
16. Gennarelli, T.A., L.E. Thibault, J.H. Adams, D.I. Graham, C.J. Thompson and R.P. Marcincin, Diffuse axonal injury and traumatic coma in the primate. Ann Neurol, 1982. 12(6): p. 564-74.
17. Gennarelli, T.A., L.E. Thibault, R. Tipperman, G. Tomei, R. Sergot, M. Brown, W.L. Maxwell, D.I. Graham, J.H. Adams, A. Irvine, and et al., Axonal injury in the optic nerve: a model simulating diffuse axonal injury in the brain. J Neurosurg, 1989. 71(2): p. 244-53.
18. Graham, D.I., J.H. Adams, D. Doyle, I. Ford, T.A. Gennarelli, A.E. Lawrence, W.L. Maxwell and D.R. McLellan, Quantification of primary and secondary lesions in severe head injury. Acta Neurochir Suppl (Wien), 1993. 57: p. 41-8.
19. Graham, D.I., J.H. Adams and T.A. Gennarelli, Mechanisms of non-penetrating head injury. Prog Clin Biol Res, 1988. 264: p. 159-68.
20. Margulies, S.S. and L.E. Thibault, An analytical model of traumatic diffuse brain injury. J Biomech Eng, 1989. 111(3): p. 241-9.
21. Margulies, S.S. and L.E. Thibault, A proposed tolerance criterion for diffuse axonal injury in man. J Biomech, 1992. 25(8): p. 917-23.
22. Margulies, S.S., L.E. Thibault and T.A. Gennarelli, Physical model simulations of brain injury in the primate. J Biomech, 1990. 23(8): p. 823-36.
23. McIntosh, T.K., D.H. Smith, D.F. Meaney, M.J. Kotapka, T.A. Gennarelli and D.I. Graham, Neuropathological sequelae of traumatic brain injury: relationship to neurochemical and biomechanical mechanisms. Lab Invest, 1996. 74(2): p. 315-42.
24. Meaney, D.F., D.T. Ross, B.A. Winkelstein, J. Brasko, D. Goldstein, L.B. Bilston, L.E. Thibault and T.A. Gennarelli, Modification of the cortical impact model to produce axonal injury in the rat cerebral cortex. J Neurotrauma, 1994. 11(5): p. 599-612.
25. AIS, The Abbreviated Injury Scale. 2005, American Association for Automotive Medicine: Arlington Heights, IL. p. 75 pp.
26. Meaney, D., L. Thibault and T. Gennarelli. Rotational brain injury tolerance criteria as a function of vehicle crash parameters. in IRCOBI. 1994. Lyon, France.
27. Morris, A., A. Hasan, M.M. Mackay and J. Hill. Head injuries in lateral impact collisions. in IRCOBI. 1993.

BIOMECHANICAL ANALYSIS OF HARD TISSUE RESPONSES AND INJURIES WITH FINITE ELEMENT FULL HUMAN BODY MODEL

Jay Zhijian Zhao, Gopal Narwani
TK Holdings Inc.
United States
Paper Number 07-0354

ABSTRACT

This paper summarizes the development activities on the finite element full human body model, improving upon last 19th ESV publication (ESV 05-0399). The updated Takata Human Model for an average adult male has anatomical details of skeleton and major soft tissues in all the body parts—head, neck, shoulder, thorax, abdomen, pelvis, lower and upper extremities. The arteries and veins as well as sciatic nerves in pelvis, thigh and tibia regions were also modeled. The model's responses of all the body parts were validated against published or in-house PMHS test data of twenty tissue material tests and forty-seven pendulum, drop or sled tests under frontal, side and oblique and rear impacts. A method similar to those defined in the ISO-TR9790 lateral biofidelity rating procedures was applied for evaluation of the model biofidelity. The overall biofidelity rating of the model is good (8.1).

Biomechanical analysis using this model has been made on fractures of femur, tibia, clavicle and lumbar vertebra under different test conditions. The bone fractures were assessed by both, the localized stress-strain characteristics as well as the global force-deflection responses. This analysis indicates that the maximum Von-Mises stress (MVMS) should be a good injury indicator for the bones with high cortical indices, independent of load directions. For the vertebral bodies with very low cortical index (1-3%), the ultimate strain of the trabecular bone may be considered as indicator for the bone fractures.

INTRODUCTION

Occupant injury assessment tools are essential to research and development of advanced occupant restraint systems. Traditionally, Anthropomorphic Test Devices (ATDs) have been used in laboratories to evaluate the restraint system performance. In recent years human body models have been developed as an important tool to help assess restrained occupant injuries which could not be evaluated by the ATDs due to their biofidelic deficiencies. The human body finite element model for an average adult male reported earlier [1], was one such tool for injury analyses of the thorax, abdomen and shoulder of a belted occupant. However, this model was not fully biofidelic and thus needed to be further developed.

A biofidelic full human body model requires two essential elements: the anatomical structures and the material characterization of human. All the human (hard and soft) tissues of which injuries were observed in field should be modeled in the anthropometrical details and their physical material properties should be investigated.

As an applicable occupant injury assessment tool the human model was required to be fully validated for its biofidelity. Such validations, as per Yang et al. [2], should be carried out against the cadaveric or human volunteer tests data in a variety of impact conditions such as frontal, side, rear, and oblique for all the body regions at three levels: the component (tissue), the subsystem (body part), and the system (whole-body), to ensure their predictive accuracy for human responses and computation robustness.

Human hard tissues are those that have become mineralized, or having a firm intercellular substance, e.g., cartilage and bone. The human model should have predictive capabilities for their fractures. Although great efforts have been made so far to develop the modeling techniques and fracture prediction capabilities for such human bony parts as skull [3], cervical spine [4], thoracic ribs [5], bones of the pelvis and the lower limb [6], the injury measures and thresholds in terms of strain or stress at the local tissue level were still not well established, and the co-relationship between the injury measures and tolerances in terms of measurable global indicators and those in terms of local strain or stress were not fully understood.

From the existing biomechanical research results we knew that two kinds of human bones—the trabecular and the cortical have much different microstructures, material properties and strengths. The modulus of the

cortical bones can be 100-1000 times higher than that of the trabecular bones. The stiffness, strength and tolerance of a piece of bone are dependent on the cortical index which is the combined cortical thickness divided by the thickness of the bone. The thickness of the cortical shell, again, varies from bone to bone, region to region, and even varies with age and gender. For example, the shafts of femur and tibia have the cortical index of 1, on the other hand, the lumbar vertebral bodies (L1-L5) have average cortical thickness of only 0.3mm (or about 1% of cortical index) [7]. In between, the clavicle cortical index decreases from 0.6 at 25 years-old to about 0.38 at 80 years-old for female, and from 0.5 at 25 years-old to about 0.3 at 80 years-old for male [8]. Studying these bones whose cortical indices vary from 0.01 to 1 could help us understand better the fracture mechanisms and tolerances of the human hard tissues.

This research pursued the following objectives:

1. to construct a full human body model including the anatomical details of skeleton and major soft tissues in all the body parts (head, neck, shoulder, thorax, abdomen, pelvis, lower and upper extremities); and to complete full validations on the model's biofidelity at the component, subsystem and system levels under various loading/impact conditions;
2. using the model to analyze the fracture mechanisms and tolerances of femur, tibia, clavicle and lumbar vertebra in terms of both global measures and local strain or stress in order to better understand injury mechanisms and tolerances of the human hard tissues.

CONSTRUCTION OF A BIOFIDELIC MODEL

Great efforts have been made to update the earlier version of the 50th% male human model [1] to a full biofidelic model. The completed development work can be explained in three sections: the anatomical modeling, the tissue material modeling, and the model biofidelity validation.

Anatomical Modeling

Additional modeling work for the anatomical structures in all the following body regions is described briefly below.

The Head - The skull, modeled in three layers (inner, diploe, outer) in solid elements, was partitioned as multiple zones representing bones of Frontal, Parietal, Occipital, Temporal, Sphenoid, Maxilla+Ethmoid, and Mandible. The finer element sizes of the average 2.5mm were meshed in the whole brain region. Currently, the Cerebrospinal fluid (CSF) was modeled in three layers of solid elements materialized with the fluid-like behavior defined by LSDYNA MAT_ELASTIC_FLUID material type. However, different modeling methods are being explored for local failure estimations.

The Neck - The occipital condyle was modeled, adding more ligaments and membranes (Alar, Cruciate, Alantooccipital, Tectorial, Apical). The Capsule of zygapophyseal joints between C2-3, C3-4, C4-5, C5-6, C6-7 were defined as combination of solids contact interfaces and 2D membrane ligaments. Five cervical ligaments (anterior longitudinal, posterior longitudinal, joint capsules, ligamentum flavum, interspinous) were modeled as 2D membrane elements. Ten pairs of neck muscles (Sternocleidomastiod, Sternothyroid, Sternohyoid, Thyrohyoid, Omohyoid, Trapezius, Scalene, Splenius, Levator scapulae, Platysma) were modeled as combination of solids and 1D Discrete element with the LSDYNA Hill-type muscle material model.

The Thorax - The original rib cage model was divided into anterior, lateral, and posterior segments as the same defined by Stitzel et al. [9] to take into account of the regional variation of stiffness and strength of the rib cortical bone.

The Shoulder – The clavicle bones were re-modeled in the finer mesh sizes of average 1.2 mm to better predict the fracture. All the ligaments, tendons, and muscles connecting the Clavicle, Sternum and Ribcage, Acromion, Scapula and Humerus were thus re-meshed to ensure integrity of the whole shoulder structures.

The Abdomen – The lower abdomen were reconstructed to adapt to the updated pelvis. The abdominal aorta and inferior vena cava were modeled.

The Pelvis and The Upper and Lower Extremities – New full finite-element sub-models for the pelvis, the lower extremities and the upper extremities were constructed. The anthropometrical data of all the bony parts in these three body regions were obtained from two resources: 1) the full-color cross-section image data of the Visible Human Male Subject segmented by in-house 3D-Doctor software; or 2) the MRI male subject data from Wayne State University. Additional tissues segmented by using

the 3D-Doctor and meshed by using Hypermesh included the Sciatic nerves coming from the lower spines (L4-5, S1-3) through its Common fibula division and Tibial nerve in the thigh and knee regions, the main arteries of thigh and knee (External Iliac, Femoral, Deep, Anterior and Posterior Tibial), and all the knee ligaments (ACL, PCL, MCL, LCL). All the segmented data were scaled to 50th% male size based on the UMTRI data.

The hard tissues modeled in the pelvis region included lumbar, sacrum and coccyx, ilium, ischium, pubis, symphisis pubica, and acetabulum. The sacroiliac joint was modeled as tied surfaces. The hip joints were modeled as combination of the hip joints ligaments (ligament of femur head, the capsular ligaments), the synovial membranes and contact between the femur head and acetabulum. The pelvis bones were directly connected to lower abdomen hollow organs, fats and outer skins. Two joints in each of the knee were carefully modeled: the femoro-patellar joint consisting of the patella, patellar and quadriceps tendons, and the patellar groove; the femoro-tibial joint consisting of the femur condyle and articular cartilage, the tibia and fibula and meniscus, as well as the ligaments of ACL, PCL, MCL, LCL. The synovial membranes were modeled as surfaces for soft contacts.

All pieces of bones and major ligaments in the body regions of lower leg, ankle/foot, upper and lower arms and elbow, wrist and hands were modeled. The cortical bones in the shaft of the long bones (femur, tibia and fibula) were modeled as solid elements, and those in the head/condyle region were modeled as shells with varying regional thickness measured by using 3D-Doctor software or from the literature. All the trabecular bones were modeled in solid elements.

Along their routes, the branches of the main arteries/nerves were modeled as discrete spring elements, and the connections among these nerves/arteries and their surrounding muscles were modeled with the method of tied nodes. The skins and muscles of the lower limb were meshed as solid elements which were tied with the bony structures.

The updated human model is fully deformable representing an average adult male with weight of 77.8Kg. It consists of 154,142 elements, 113,349 nodes, and 701 components for the tissues. Figure 1 shows this model.

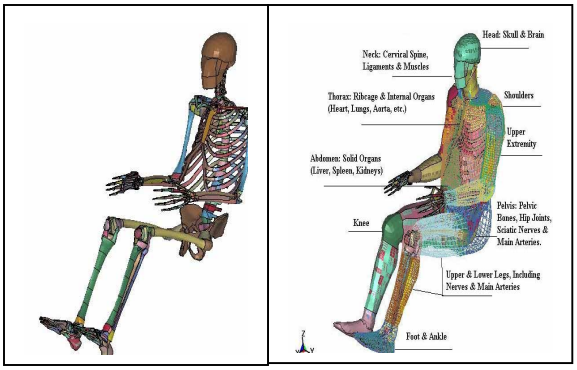

Figure 1. The updated Takata Human Model. Left-Skeleton; Right-Full body.

Tissue Material Modeling

There are 589 material cards in total with sixteen material models (constitutive laws) defined in this updated human body model. Table 1 summarizes the material models used for the tissue components.

Table 1 The Material Models and Cards in the Model

Material Model	Tissues	Total
01-Elastic	The connective tissues being not easily injured	275
01-Elastic Fluid	CSF	1
03-Plastic Kinematic	Other connective tissues	37
06-Viscoelastic	Brain, abdominal solid organs	13
09-Null	Internal contact interfaces	7
20-Rigid	Local coordinate base	1
24-PiecewiseLinearPlasticity	Ligaments, tendons	133
34-Fabric	Capsule membranes	6
57-LowDensityFoam	Hollow organ inserts	3
62-ViscousFoam	Skin, body fats	18
81-PlasticitywithDamage	Cortical bones	28
105-Damge 2	Trabecular bones, cartilages	37
129-LungTissue	Lungs, heart	2
SB1-Seatbelt	Tendons	13
DS4-SpringNonlinearElastic	Artery branches	5
DS15-SpringMuscle	Neck Muscles	10
ALL	--	589

The material properties or parameters in the material models were determined in three ways: 1) directly from the published tissue material tests data; 2) from our tissue test component model correlations; and 3) from our body impact subsystem model correlations.

The directly applied tissue material property data were selected from the cadaver or live porcine tissue coupon tests. Examples of such coupon tests were for the rib cortical shells [9], the cervical and lumbar

spine ligaments [10, 11], the scalp and brain tissues and the skull (inner and outer tables and diploe) [12], the shoulder ligaments of OC, CC, SC joints [13], the auricular and costal Cartilage [14], and the cortical shells of Femur, Tibia, Fibula, Humerus, Radius, and Ulna [15], etc.

However, quite a few biomechanical tests were performed at the tissue component (consisted of a group of tissues) level. In addition, the existing published tissue material property data, especially of the soft tissues, varied in wide range due to different subjects, test conditions and methods. Considered these uncertainties we selected the biomechanical tests for those tissues which were primary load carriers inside the body or easily sustained injuries. FE models for each of the test configurations were constructed and the test procedures were simulated. The model outputs defined according to the measurements were correlated with the test data. Through this process the material properties of these tissues were determined or estimated. Table A-1 in Appendix A lists all such simulated material tests in total of 20 that came from 10 studies involving 2 skull/brain tissue tests, 4 neck tissue tests, 4 thorax tissue tests, 3 abdomen organs tests, 1 clavicle tests, 4 lower extremity long bone tests, and 2 lumbar vertebra and disc tests. Table A-1 provides the information of the test conditions, the correlated responses and correlation quality grades (1-5, 1-unacceptable; 5-best; determined as explained in notes of Table A-1), and the references.

From the two ways described above, most of the tissue material properties defined in the model could be determined or estimated. For those of the modeled human tissues which were not tested in either coupon or component material tests, their material properties were estimated from the body impact subsystem model correlations.

Model Biofidelity Evaluation

Seven body regions (head, neck, shoulders including upper extremities, thorax, abdomen including lumbar, KTH, lower leg including ankle/foot) were validated against a set of the PMHS drop or pendulum and sled tests. These biomechanical tests included 47 in total from 22 studies that involved 5 head tests, 7 neck tests, 5 thorax tests, 5 abdomen tests, 5 shoulder tests, 5 KTH tests, 2 lower leg tests, 5 ankle tests, 6 lumbar tests, and 2 whole body sled tests. The selected tests data covered in a variety of impact energies and directions (frontal impacts-25; side/oblique impacts-16; rear impacts-3; axial-4).

The method for evaluation of biofidelity of the human model was similar to those defined in the ISO-TR9790 lateral biofidelity rating procedures [16]. The biofidelity rating calculation of each body region was defined by ISO as expressed in Eq. (1)

$$B_i = \frac{\sum_{j=1}^{m} V_{i,j} \left(\sum_{k=1}^{n} W_{i,j,k} R_{i,j,k} \Big/ \sum_{k=1}^{n} W_{i,j,k} \right)}{\sum_{j=1}^{m} V_{i,j}} \quad (1)$$

where $V_{i,j}$ were the weighting factor for each test condition for a given body region; $W_{i,j,k}$ were weighting factor for each response measurement for which requirement was given; $R_{i,j,k}$ were the rating of how well a given response meets its requirement. R=10 if response meets requirement; R=5 if response is outside requirement but lies within one corridor width of requirement; R=0 if neither of the above two is met. The overall rating for a given model was calculated via Eq. (2)

$$B = \frac{\sum_{i=1}^{7} U_i B_i}{\sum_{i=1}^{7} U_i} \quad (2)$$

where B was the overall rating which have a value between 0 (unacceptable) and 10 (excellent); B_i were the biofidelity rating of each of body regions; U_i were the weighting factors for the biofidelity rating of each of body regions.

To simply the rating calculation procedures we assigned all of the weighting factors $V_{i,j}$, $W_{i,j,k}$ and U_i equal to 1, which means that all the measured responses in each of the selected tests were equally treated, and that each of all the body regions were considered equally important.

All the test conditions, the measurements, the model's responses and the ratings $R_{i,j,k}$, as well as test data resource are summarized in Table A-2 and A-3 in Appendix-A. In Table A-3 the ratings of each response for a relevant body region were included in Eq.(1) while the external force measurements (marked NA in Table A-3) were excluded from the rating calculation. Table A-4 summarizes the biofidelity rating results for the body regions of the human model.

According to the ISO five biofidelity rating classifications, the biofidelity is considered as excellent if the rating scale is between 8.6^{+}-10, and as good if the scale between 6.5^{+}-8.6. The model achieved excellent biofidelity rating scores in the body region of Thorax (9.4). All the other body

regions (scored 7.2-8.6) achieved good biofidelity score. The overall biofidelity rating of the human model is good (8.1).

HARD TISSUE INJURY ANALYSIS

Based on the results of the bio-tests simulations listed in Table A-1, A-2, A-3, we summarize our findings from the hard tissue injury analysis particularly for femur, tibia, lumbar vertebra, and clavicle. The material properties of these bones in the sub-models are tabulated in Table B-1 in Appendix B.

Analysis of the 3-Point A-P Bending Tests on Femur and Tibia

In this study, static 3-point anterior-posterior (A-P) bending tests on femur and tibia were simulated. The model-predicted force-displacement curves of these bones were compared with the measured data [15], as shown in Figure 2.

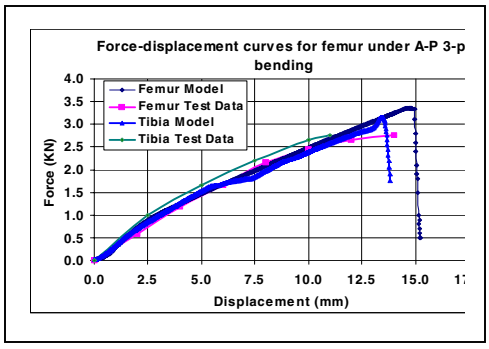

Figure 2. Comparison of the model predicted and the measured load force vs. displacement curves of the femur and tibia under quasi-static 3-point bending. The test data referred to [15].

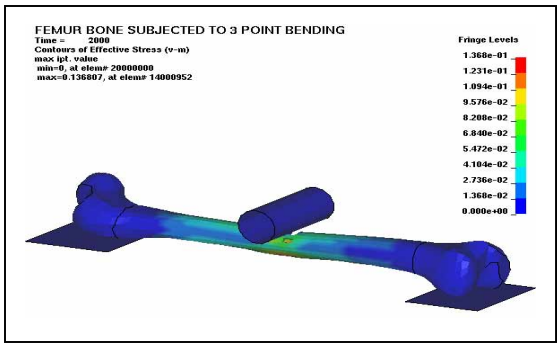

Figure 3. The stress contour of the femur under quasi-static 3-point bending at the failure time.

The simulations showed that corresponding to each of the peak forces in Figure 2 failure occurred in the shaft center of the femur or the tibia, where maximum stresses of the femur or tibia occurred as shown in Figures 3-4.

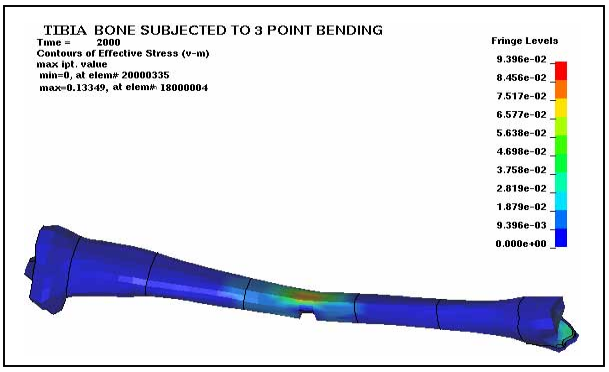

Figure 4. The stress contour of the tibia under quasi-static 3-point bending at the failure time.

Table 2 summarizes the calculated failure forces, maximum Von-Mises stresses and the failure strains of femur and tibia under the simulated A-P 3-point bending test conditions. It is noted here that in both cases the failure stresses are around 130MPa while the failure strains are around 1.3%.

Table 2 The calculated failure forces, stresses, and strains of the femur and the tibia

Tissue	Failure Force (KN)	Failure Stress (MPa)	Failure Strain (%)
Femur	3.3	136.8	1.4
Tibia	3.2	133.5	1.3

Analysis of the Compression Tests on the Lumbar Vertebrae

In this study, the compression tests on isolated lumbar vertebrae L1-L5 reported by Yoganandan et al. [17] were modeled. In the test set-up, a compressive load was uniformly applied to the vertebral body at a constant speed of 2.5 mm/s to about 50% of its original height. Figure 5 shows the model predicted force-deformation curve compared with the measured ones of L2, L3, L4 and L5 [17]. It was seen that the force-deformation curve of the vertebra had a plateau in which the large plastic deformation of the trabecular bone occurred.

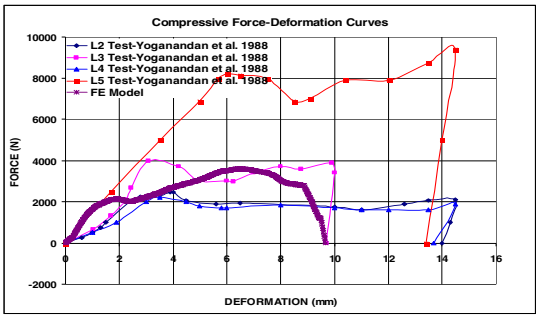

Figure 5: Comparison of the model predicted and measured force-deformation curves [17] of the lumbar vertebral bodies under quasi-static compressive loading.

Figure 6 shows that the maximum stresses were in the circumferential edge of the endplate where failure occurred.

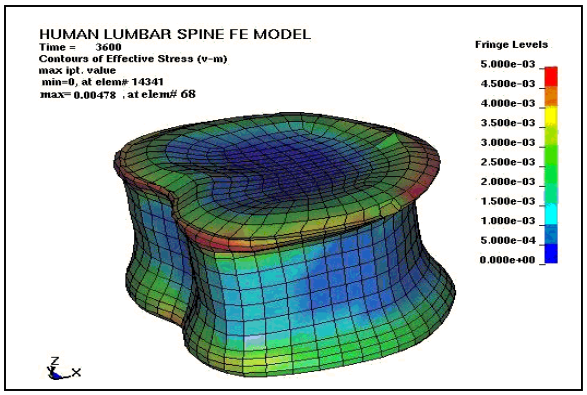

Figure 6. The stress contour of the lumbar vertebral body under quasi-static compressive loading at the failure time.

Table 3 summarizes the calculated failure force (the value when the force dropped significantly), maximum Von-Mises stresses of the vertebral bones and the failure strains of the trabecular bone under the compressive loading. It was interesting to see from the simulation that before the failure force a few percent of cortical and trabecular bone elements had already failed. The vertebral trabecular bone along carried about 70% of the total loads. Thus the failure stress and strain reflected dominantly the material characteristics of the trabecular bone.

Table 3 The calculated failure forces, stresses, and strains of the vertebra L3

Tissue	Failure Force (KN)	Trabecular Failure Stress (MPa)	Trabecular Failure Strain (%)	Cortical Failure Stress (MPa)
Vertebra L3	2.8	4.8	25.4	112.7

Clavicle Fracture Analysis

Clavicle three-point bending tests analysis

Quasi-static cadaver clavicle three-point bending tests were simulated. Table 4 compares the model outputs with the test results reported by Bolte et al. [43] and Probasta et al. [18].

Table 4 compares the model predicted maximum load force, stiffness, average failure stress and maximum deflection with the test data [18, 43].

Source	Maximum Force (N)	Stiffness (N/mm)	Max. Deflection (mm)	Failure Stress (MPa)
Bolte's Average [43]	681.7	147.2	4.6	N/A
Proubasta's Average [18]	485.6	94.8	5.0	N/A
Model	529.9	99.6	5.3	125.0

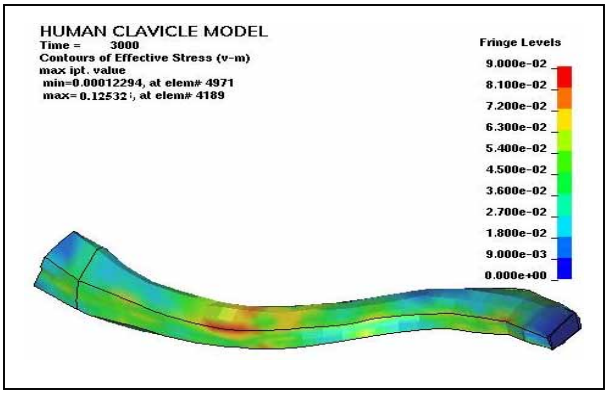

Figure 7. The stress contour of the clavicle under 3-point bending.

Figure 7 shows the stress contour of the clavicle under 3-point bending at the failure moment. The clavicle fractured in the center of shaft body where the maximum Von-Mises stress was 125MPa.

Analysis of pendulum side impacts to shoulders

The tests of the pendulum side impacts to PMHS shoulders conducted by Bolte [43] and Compigne [19] were simulated. In Compigne's test set-ups, the PMHS were struck using a 23.4kg impactor fitted with a rigid rectangular shaped impacting plate in lateral and oblique (±15°) directions at different impact velocities (1.5-6 m/s). In Bolte's test set-ups, the left shoulder of PMHS was impacted with a 23 kg pneumatic ram (20cmX15cm, padded with a 5cm thick piece of Arcel foam) in lateral and oblique (15°, 30°) directions at impact speeds from about 4 to 7.5 m/s.

Figures 8-9 show the correlation of the model predicted acromion-to-sternum deflections and the

impact forces with the Bolte's [43] and Compigne's test results [19].

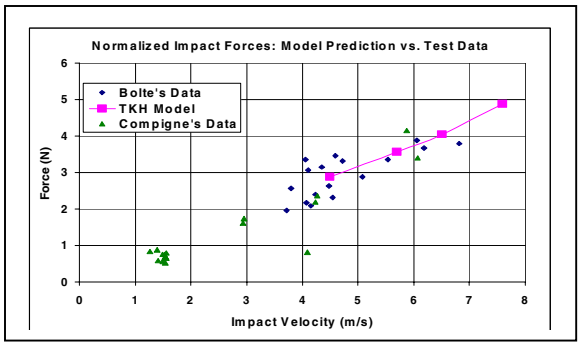

Figure 8. Comparison of the model predicted Acromion-to-Sternum deflections varying with impact velocities with the test data [19, 43].

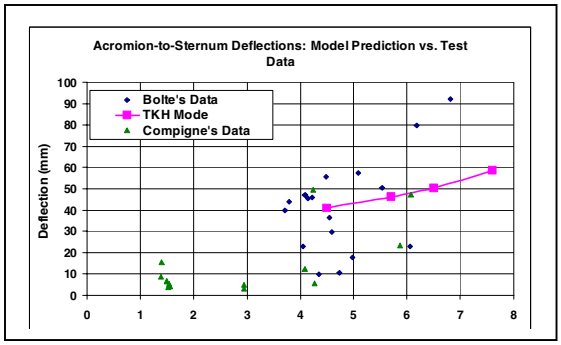

Figure 9. Comparison of the model predicted forces varying with impact velocities with the test data [19,43].

Table 5. Model Predicted Injury Numbers for PMHS Pendulum Side Impact Tests

Impact Velocity (m/s)	Max. Force (N)	Acr-To-Sternum Def. (Mm)	Max. Stress (MPa)
4.5	2.87	40.8	90.9
5.7	3.56	46.4	104.7
6.5	4.05	50.3	121.4
7.6	4.87	58.5	130.8

Table 5 correlates the maximum forces, the acromion-to-sternum deflections and the model-predicted maximum Von-Mises stresses of the clavicle responding to different pendulum impact speeds. At 6.5 m/s impact speed, the calculated acromion-to-sternum deflection was 50.3 mm while the maximum Von-Mises stress exceeded 120MPa, at which the bone fractured in the simulation. The past research concluded that under lateral impacts to PMHS shoulders 47 mm of the acromion-to-sternum deflection predicted a 50% probability of clavicle fracture or AIS 2+ shoulder injury. This study indicated that at failure the clavicle experienced the Von-Mises stress of more than 120 MPa.

DISCUSSION

In this study, all the investigated three bones (femur, tibia, clavicle) with high cortical indices (above 0.4) fractured consistently in the range of 120-130MPa of maximum Von-Mises stress (MVMS) of the cortical bones. This suggested that the MVMS can be a good injury indicator for these high cortical index bones, independent of load directions. The threshold of 120-130 MPa matched Stitzel's ultimate stress data from the rib cortical bone coupon tests [7].

For the vertebral bodies with very low cortical index (1-3%), the ultimate strain of the trabecular bone may be considered as indicator for the bone fractures.

More experimental studies are needed to confirm these analytical findings.

CONCLUSIONS

The updated Takata Human Model for an average adult male has the detailed bony and soft tissues in all the body regions. The overall biofidelity rating of the model is good (biofidelity rating score 8.1).

The results of simulated 3-point bending tests for the bones (femur, tibia, clavicle) with high cortical indices (0.4-1.0) showed that all of them fractured at 120-130MPa of the maximum Von-Mises stress (MVMS). Additional simulations for the lateral impacts to PMHS shoulders at different speeds of 4.5-7.6m/s concluded that 47 mm of the acromion-to-sternum deflection corresponded to 120MPa of the MVMS in the clavicle. All these results suggested that the MVMS be a good injury indicator for these high cortical index bones, independent of load directions.

The results of simulated compression tests on isolated lumbar vertebral body L3 with very low cortical index (~0.01) showed that the deformation pattern and fracture characteristics of the vertebral body were very similar to those of the trabecular bone of the body. The ultimate strain of the trabecular bone may be considered as indicator for fractures of the low cortical-index bones.

These analytical findings are worthy to be further investigated experimentally.

ACKNOWLEGEMENT

The authors would like to gratefully acknowledge, to Dr. King Yang and Dr. Jong Lee at Bioengineering

Center of Wayne State University, and Tadayuki Ato of Takata Corporation, Japan, for their valuable advice and support for this research. Special thanks to Dr. Richard Kent and Jason Forman at University of Virginia for providing the cadaver sled test data used for the human sled model correlation.

The authors also wish to acknowledge Aditya Belwadi in WSU and Shivakumar Chandrasekharan in Takata for their modeling support of this research.

REFERENCES

[1] Jay Zhijian Zhao and Gopal Narwani, "Development of a Human Body Finite Element Model for Restraint System R&D Applications", 19th ESV Conference, Paper# 05-0399, 2005.

[2] Yang, K.H., Hu, J.W., White, N.A., King, A.I., Chou, C.C. and Prasad, P., "Development of Numerical Models for Injury Biomechanics Research: A Review of 50 Years of Publications in the Stapp car Crash Conference", Stapp Car Crash Journal, Vol. 50, 2006-22-0017, 2006.

[3] Ruan, J. and Prasad, P., "The Effects of Skull Thickness Variations on Human Head Dynamic Impact Responses", Stapp Car Crash Journal, Vol. 45, 2001-22-0018, 2001.

[4] Meyer, F., Bourdet, N., Deck, C., Willinger, R., Raul J.S., "Human Neck Finite Element Model Development and Validation against Original Experimental Data", Stapp Car Crash Journal, Vol. 48, 2004-22-0008, 2004.

[5] Tamura, A., Watanabe, I., Miki, K., "Elderly Human Thoracic FE Model Development and Validation", 19th ESV Conference, Paper# 05-0229, 2005.

[6] Untaroiu, C., Darvish, K., Crandall, J., Deng, B., Wang, J-T., "A Finite Element Model of the Lower Limb for Simulating Pedestrian Impacts", Stapp Car Crash Journal, Vol. 49, 2005-22-0008, 2005.

[7] Rotzel, H., Amling, M., Pösl, M., Hahn, M., Delling, G., "The Thickness of Human Vertebral Cortical Bone and Its Changes in Aging and Osteoporosis: A Histomorphometric Analysis of the Complete Spinal Column from Thirty-Seven Autopsy Specimens", J. Bone and Mineral Research, 12(1): 89-95, 1997.

[8] Helelä, T., "Age-dependent Variations of the Cortical Thickness of the Clavicle", Annals of Clinical Research, 1:140-143, 1969.

[9] Stitzel, J.D., Cormier, J.M., Barretta, J.T., Kennedy, E.A., Smith, E.P., Rath, A.L., Duma, S.M., "Defining Regional Variations in the Material Properties of Human Rib Cortical Bone and Its Effect on Fracture Prediction", Stapp Car Crash Journal, Vol. 47, 2003-22-0012, 2003.

[10] Yoganandan N., Pintar F. A., Kumaresan S., "Biomechanical Assessment of Human Cervical Spine Ligament", Stapp Car Crash Journal, Vol. 42, 983159, 1998.

[11] Pintar, F., Yoganandan, N., Meyers, T., Elhagediab, A., Sances Jr. A., "Biomechanical Properties of Human Lumbar Spine Ligaments", J. Biomechanics, 25(11):1351-1356, 1992.

[12] Melvin, J.W, McElhaney, J.H., Roberts, V.L., "Development of a Mechanical Model of the Human Head-Determination of Tissue Properties and Synthetic Substitute Materials", Stapp Car Crash Journal, Vol. 14, 700903, 1970.

[13] Koh, S.W., Cavanaugh J.M., and Leach J.P., Rouhana, S.W., "Mechanical Properties of the Shoulder Ligaments under Dynamic Loading", Stapp Car Crash Journal, Vol. 48, 2004-22-0006, 2004.

[14] Roy, R., Kohles, S.S., Zaporojan, V., Peretti, G.M., Randolph, M.A., Xu, J., Bonassar, L.J., "Analysis of Bending Behavior of Native and Engineered Auricular and Costal Cartilage", J. Biomedical Material Research, 68A: 597-602, 2004.

[15] Yamada, H., Strength of Biological Materials, Williams & Wilkins Inc., Baltimore, 1970.

[16] ISO-TR 9790, Road Vehicle Anthropomorphic Side Impact Dummy-Lateral Impact Response Requirements to Assess the Biofidelity of the Dummy, 1999.

[17] Yoganandan, N., Pintar, F., Sances, A. Jr., Maiman, D., Myklebust, J., Harris, G., Ray, G., "Biomechanical Investigations of the Human Thoracolumbar Spine", SAE Paper #881331, 1988.

[18] Proubasta, I.R., Itarte, J.P., Cáceres, E.P., Liusá, M.P., Gil, J.M, Planell, J.A.E., Ginebra, M.P.M., "Biomechanical Evaluation of Fixation of Clavicular Fractures", J. Southern Orthopaedic Association, 11(3):148-52, 2002.

[19] Compigne S., Caire, Y., Quesnel, T., Verriest, J-P., "Non-Injurious and Injurious Impact Response of the Human Shoulder Three-Dimensional Analysis of Kinematics and Determination of Injury Threshold", 48th Stapp Car Crash Conference, 2004-22-0005, 2004.

[20] Arbogast, K.B., Meaney, D.F., Thibault, L.E., “Biomechanical Characterization of the Constitutive Relationship for the Brainstem”, Stapp Car Crash Journal, Vol. 39, #952716, 1995.

[21] Nightingale, R., Winkelstein, B.A., Knaub, K.E., Richardson, W.J., Luck, J.F., Myers, B.S., “Comparative Strengths and Structural Properties of the Upper and Lower Cervical Spine in Flexion and Extension”, Journal of Biomechanics 35: 725-732, 2002.

[22] Yoganandan N. and Pintar F.A., "Biomechanics of Human Thoracic Ribs", Transactions of the ASME, Vol. 120, pp. 100-104, February 1998.

[23] Yen, M. R.T., “Development of Thorax Model Sub-project-C: Mechanical Properties of Human Heart, Lung and Aorta.” Ph.D. Thesis of the Department of Biomedical Engineering of University of Memphis, September, 1999.

[24] Tamura, A., Omori K., Miki, K., Lee, J.B., Yang, K.H., King, A.I., “Mechanical Characterization of Porcine Abdomen Organs”, Stapp Car Crash Journal, Vol. 46, 2002-22-0003, 2003.

[25] Keyak, J.H., Rossi, S.A., Jones, K.A., Skinner, H.B., “Prediction of Femoral Fracture Load Using Automated Finite Element Modeling”, Journal of Biomechanics, 31:125-133, 1998.

[26] Gordon, S., Yang, K.H., Mayer, P., Mace, A., Kish, V., Radin. E., “Mechanism of Disc Rupture”, Spine, 16(4): 450-456, 1991.

[27] Allsop, D.L., Warner, C.Y., Schneider. D.C., Nahum, A.M., “Facial Impact Response–A Comparison of the Hybrid III Dummy and Human Cadaver”, Stapp Car Crash Journal, Vol. 32, 881719, 1988.

[28] Yoganandan, N. Zhang, J., Kuppa, S., Eppinger, R.H., "Biomechanics of Lateral Skull Fracture", IRCOBI Conference Proceedings, September 2003.

[29] Trosseille X., Tarriére, C., Lavaste, F., Guillon, F., Domont, A., "Development of a F.E.M. of the Human Head According to a Specific Test Protocol, Stapp Car Crash Journal, Vol. 36, 922527, 1992.

[30] Hardy, W.N., Foster, C.D., Mason, M.J., Yang, K.H., King, A., Tashman, S., “Investigation of Head Injury Mechanisms Using Neutral Density Technology and High-Speed Biplanar X-Ray”, Stapp Car Crash Journal, Vol. 45, 2001-22-0016, 2001.

[31] Chris A. Van Ee, Nightingale, R.W., Camacho, D.L.A., Chancey, V.C., Knaub, K.E., Sun, E.A., Myers, B.S., “Tensile Properties of the Human Muscular and Ligamentous Cervical Spine”, Stapp Car Crash Journal, Vol. 44, 2000-01-SC07, 2000.

[32] Pintar, F. A., Yoganandan N., Voo, L., Cusick, J.F., Maiman, D.J., Sances, Jr., A., “Dynamic Characteristics of the Human Cervical Spine”, Stapp Car Crash Journal, Vol. 39, 952722, 1995.

[33] Thunnissen, J., Wismans, J., Ewing, C.L., Thomas, D.J., "Human Volunteer Head-Neck Response in Frontal Flexion: A New Analysis", Stapp Car Crash Journal, Vol. 39, 952721, 1995.

[34] Wismans J. and Spenny, C.H., “Performance Requirements for Mechanical Necks in Lateral Flexion”, Stapp Car Crash Journal, Vol. 27, 831613, 1983.

[35] Viano, D.C., Hardy, W.N., King, A., “Response of the Head, Neck, and Torso to Pendulum Impacts on the Back”, J. Crash Prevention and Injury Control, 2(4):289-306, 2001.

[36] Kroell, C. K., Schneider, D.C. and Nahum, A.M., "Impact Tolerance and Response of the Human Thorax", Stapp Car Crash Journal, Vol. 15, 710851, 1971.

[37] Kroell, C.K., Schneider, D.C. and Nahum, A.M., "Impact Tolerance and Response of the Human Thorax II." Stapp Car Crash Journal, Vol. 18, 741187, 1974.

[38] Viano, D.C., "Biomechanical Responses and Injuries in Blunt Lateral Impact." Stapp Car Crash Journal, Vol. 33, 892432, 1989.

[39] Kent R., Lessley, D., Sherwood, C., “Thoracic Response to Dynamic, Non-Impact Loading from a Hub, Distributed Belt, Diagonal Belt and Double Diagonal Belts.” Stapp Car Crash Journal, Vol. 48, 2004-22-0022, 2004.

[40] Cavanaugh, J.M., Nyquist, G.W, Goldberg, S.J., King, A.I.,, “Lower Abdominal Tolerances and Responses.” Stapp Car Crash Journal, Vol. 30, 861878, 1986.

[41] Hardy, W., Schneider, W. and Rouhana, S.W., “Abdominal impact Response to Rigid-Bar, Seatbelt, and Airbag Loading.” Stapp Car Crash Journal, Vol. 45, 2001-22-0001, 2001.

[42] Bendjiella, F., Walfisch, G., Fayon, A., Tarriere, C., APR Biomechanical Data, Nanterre, France, 1984.

[43] Bolte IV, J.H., Hines, M.H., Herriot, R.G., McFadden, J.D., and Donnelly, B.R., "Shoulder

Impact Response and Injury Due to Lateral and Oblique Loading." Stapp Car Crash Journal, Vol. 47, 2003-22-0003, 2003.

[44] Guillemot, H., Got, C., Besnault, B., Coz, J.Y.L., Robin, S., Lavaste, F., Lassau, J.-P., "Pelvic Injuries in Side Impact Collisions: A Filed Accident Analysis and Dynamic Tests on Isolated Pelvic Bones", 41st Stapp Car Crash Journal, Vol. 41, 973322, 1997.

[45] Rupp, J.D., Reed, M.P., Van Er, C.A., Kuppa, S., Wang, S.C., Goulet, J.A., Schneider, L.W., "The Tolerance of the Human Hip to Dynamic Knee Loading", Stapp Car Crash Journal, Vol. 46, 2002-22-0011, 2002.

[46] Haut, R.C., Atkinson, P.J., "Insult to the Human Cadaver Patellofemoral Joint: Effects of Age on Fracture Tolerance and Occult Injury", Stapp Car Crash Journal, Vol. 39, 952729, 1995.

[47] Hayashi, S., Choi, H.-Y., Levine, R.S., Yang, K.H., King, A.I., "Experimental and Analytical Study of Knee Fracture Mechanisms in a Frontal Knee Impact", Stapp Car Crash Journal, Vol. 40, 962423, 1996.

[48] Dhaliwal, T.S., Beillas, P., Chou, C.C. Prasad, P., Yang, K.H., King, A.I., "Structural Response of Lower Leg Muscles in Compression: A Low Impact Energy Study Employing Volunteers, Cadavers and the Hybrid III", Stapp Car Crash Journal, Vol. 46 2002-22-0012, 2002.

[49] Crandal, J.R., Portier, L., Petit., P., Hall, G.W., Bass, C.R., Klopp, G.S., Hurwitz, S., Pilkey, W.D., Trosseille, X., Tarrière, C., Lassau, J.-P., "Biomechanical Response and Physical Properties of the Leg, Foot and Ankle", Stapp Car Crash Journal, Vol. 40, 962424, 1996.

[50] Rudd, R., Crandall, J., Millington, S., Hurwitz, S., Höglund, N., "Injury Tolerance and Response of the Ankle Joint in Dynamic Dorsiflexion", Car Crash Journal, Vol. 48, 2004-22-0001, 2004.

[51] Forman, J., Lessley, D., Kent, R., Bostrom, O., Pipkorn, B., "Whole-body Kinematic and Dynamic Response of Restrained PMHS in Frontal Sled Tests", Stapp Car Crash Journal, Vol. 50, 2006-22-0013, 2006.

APPENDIX A Results of Material Modeling and Biofidelity Evaluation of the Takata Human Model

Table A-1 Summary of the bio-tissue test simulations for determining the material properties

Body Region	Tissue	Test conditions	Correlated Responses	Correlation quality*	Ref
Head	Cerebrum, Brainstem	Oscillating shear test over 20-100Hz and stress relaxation test at 7.5%	Stress-strain curve and Stress relaxation curve	4	[20]
Neck	OC-C1-C2 FSU	Quasi-static flexion and extension loadings.	Moment My vs. Rotation angle measure at C2.	4	[21]
Neck	C5-C6 FSU	Quasi-static flexion and extension loadings.	Moment My vs. Rotation angle measure at C6.	4	[21]
Thorax	Rib	3-point bending at quasi-static rate of 2.5 mm/min.	Max. load and deflection	4	[22]
Thorax	Heart	Biaxial tensile tests for cadaver heart samples	Average stress-strain curve	5	[23]
Thorax	Aorta	Biaxial tensile tests for cadaver aorta samples	Average Stress-strain curve	4	[23]
Thorax	Lungs	Biaxial tensile tests for cadaver lung samples	Average Stress-strain curve	5	[23]
Abdomen	Liver	Uniaxial compression to porcine liver at three loading rates *0.001/s, 0.05/s, 0.5/s)	Average Stress-strain curve	5	[24]
Abdomen	Kidney	Uniaxial compression to porcine kidney at three loading rates *0.001/s, 0.05/s, 0.5/s)	Average Stress-strain curve	5	[24]
Abdomen	Spleen	Uniaxial compression to porcine spleen at three loading rates *0.001/s, 0.05/s, 0.5/s)	Average Stress-strain curve	5	[24]
Shoulder	Clavicle	3pt bending tests at 0.5 mm/sec	Stiffness and failure load	5	[18, 43]
KTH	Femur Shaft	Quasi-static 3-pt bending tests	Load force vs. Deflection curve	5	[15]
KTH	Femoral head	Quasi-static loading to femoral head.	failure load	3	[25]
Lower Leg	Tibia & Fibula	Quasi-static 3-pt bending tests	Load force vs. Deflection curve	5	[15]
Lumbar Spine	Vertebra	Compressive loading at 2.5 mm/sec	Load force vs. Deformation curve	4	[17]
Lumbar Spine	Disc	Quasi-static compressive loading cyclically at 15.Hz up to 3mm.	Stiffness	4	[26]

* The correlation quality grades (1-5) are defined as follows: 1-unacceptable: the peaks and phases of the two curves behaviors totally different. 2-poor: the peaks and phases of the two curves do not match but trends are similar. 3-fair: both peaks and phases of the two curves differ within the range of 30%. 4-good: both peaks and phases of the two curves differ within the range of 20%. 5-excellent: both peaks and phases of the two curves differ within the range of 10%.

Table A-2 Summary of the PMHS drop or pendulum tests and biofidelity rating results for the body regions

Body region	Impact direction	Test conditions	Response	Requirement	Results	Rating	Ref.
Head	F	14.5kg 20mm rod impact to frontal bone at drop height of 460-915mm.	Force-Deformation curves	(2.5KN, 5.5KN) at 5 mm deformation	5.4 KN at 5mm	10	[27]
Head	F	14.5kg 20mm rod impact to Zygoma bone at drop height of 305-610 mm.	Force-Deformation curves	(1.4kN, 2.0KN) at 20mm	1.9KN at 20mm	10	[27]
Head	F	14.5kg 20mm rod impact to Maxilla bone at drop height of 305-610 mm.	Force-Deformation curves	(0.8KN, 1.8KN) at 20mm;	1.3KN at 20mm	10	[27]
Head	L	Head drop laterally to a 40-durometer padding place (50mm-thickness) at 6.5 m/s	Average peak force and displacement	Force: 8.4±1.4KN; Displ: 15.0±2.3mm	7.9KN, 16.4mm	10	[28]
Head	F	A rod impact to face in the antero-posterior direction at 7m/s. Test#MS428-2.	Intracranial pressures: Frontal	87KPa at 11ms	91.7 KPa at 10ms	10	[29]
Head	F	A rod impact to face in the antero-posterior direction at 7m/s. Test#MS428-2.	Intracranial pressures: Occipital	-11.4KPa at 9ms	-13.4KPa at 9ms	5	[29]
Head	F	A rod impact to face in the antero-posterior direction at 7m/s. Test#MS428-2.	Intracranial pressures: Lateral	39.8KP at 11ms	40.5KPa at 10ms	10	[29]
Head	F	A rod impact to face in the antero-posterior direction at 7m/s. Test#MS428-2.	Intracranial pressures: 3rd Ventricle.	30KPa at 10ms	27.8KPa at 10ms	10	[29]
Head	F	Suspended Head accelerated and impacted to a padded linear-piston impostor at 2 m/s. Test#C755-T2:	Brain targets X-Z displacements at sagittal plane	Figure 6 in [26]	maximum difference 28%	0	[30]
Neck	A	Eccentricity tensile loading to cervical spine at 2mm/s at free cranial end condition	Force vs Displacement	225KN at 7.5 mm	270KN at 7.5mm	5	[31]
Neck	A	Compressive loading to cervical spine by a padded plate at 2.5 m/s.	Force-deformation	Force-deformation corridor in Figure 6 [32]	Stay in between the corridors	10	[32]
Neck	F	Analyzed test data of head-neck to T1 relative motion responding to the 15.6G frontal sled pulse.	Head CG to T1 relative displacements X,Z	Head X (140mm,165mm) Head Z (200mm,225mm)	Head X 190 mm Head Z 235 mm	5	[33]
Neck	L	Analyzed test data of head-neck to T1 relative motion responding to the 7g lateral sled pulses.	Head CG to T1 relative displacements Y,Z	Head Y (120mm,141mm) Head Z (60mm,90mm)	Head Y 120 mm Head Z 51 mm	10	[34]
Neck	R	23.4 kg 150mm disk impact to rear skin at the level of T1 at 4.4 m/s.	Impact force history	(2.5KN, 3.8KN) in 8.5-10.0 ms	3.7KN at 13mm	5	[35]
Neck	R	23.4 kg 150mm disk impact to rear skin at the level of T1 at 4.4 m/s.	Head CG X-displacement	(125mm, 200mm) at 120ms	195mm at 120ms	10	[35]
Neck	R	23.4 kg 150mm disk impact to rear skin at the level of T1 at 4.4 m/s.	Head CG Z-displacement	(-24mm,45mm) at 120ms	35mm at 120ms	10	[35]
Neck	R	23.4 kg 150mm disk impact to rear skin at the level of T1 at 4.4 m/s.	Head rotation	(15deg, 65deg) at 120ms	31deg at 120ms	10	[35]
Neck	R	23.4 kg 150mm disk impact to rear skin at the level of T1 at 6.6 m/s.	Impact force history	(4KN, 6KN) at 10ms	5.8KN at 13ms	5	[35]
Neck	R	23.4 kg 150mm disk impact to rear skin at the level of T1 at 6.6 m/s.	Head CG X-displacement	(80mm, 280mm) at 80ms	160mm at 80ms	10	[35]
Neck	R	23.4 kg 150mm disk impact to rear skin at the level of T1 at 6.6 m/s.	Head CG Z-displacement	(-35mm,30mm) at 70ms	65mm at 70ms	0	[35]
Neck	R	23.4 kg 150mm disk impact to rear skin at the level of T1 at 6.6 m/s.	Head rotation	(20deg, 75deg) at 120ms	33deg at 80ms	10	[35]
Thorax	F	23.4kg 152mm disk at 6.5 m/s to center of thorax	Force-Deflection curve	Corridor	4.17KN at 72.1mm.	10	[36, 37]
Thorax	L	23.4kg 152mm disk at 30 degree oblique at 6.7 m/s to left side of thorax	Force-Deflection curve	Corridor	2.93KN at 73.3mm.	10	[38]
Thorax	F	UVA hub loading to thorax	Force-Deflection curve	Corridor	2.3KN at 65mm.	10	[39]

Thorax	F	UVA diagonal belt loading to thorax	Force-Deflection curve	Corridor	2.1KN at 37mm.	10	[39]
Thorax	F	UVA distributed loading to thorax	Force-Deflection curve	Corridor	4.1KN at 56mm.	10	[39]
Abdomen	F	32 kg bar at 6.1 m/s to lower abdomen.	Force-Deflection curve	Corridor: (2.16KN,4.2KN) at 120mm	4.5KN at 120mm	5	[40]
Abdomen	F	48kg rigid bar rigid-bar test at 9 m/s to free back cadavers	Force-Deflection curve	Corridor: (7KN,11.5KN) at 140mm	9.7KN at 137mm	10	[41]
Abdomen	L	23.4 kg disk at 30 degree oblique at 6.5 m/s to right side of upper abdomen.	Force-Deflection curve	Corridor: (3KN,4.5KN) at 100mm	5KN at 98.4mm	5	[38]
Abdomen	F	Close proximity surrogate airbag loading to midabdomen of fixed-back cadaver.	Force-penetration curve	Corridor: (2.5KN, 5KN) at 10mm	3KN at 10mm	10	[41]
Abdomen	F	Seat belt loading at 3.2m/s maximum to midabdomen of free-back cadaver.	Force-penetration curve	Corridor: (3.5KN, 4.4KN) at 50mm	3.8KN at 48.3mm	10	[41]
Shoulder	F	23 kg 150mm disk impact to left shoulder at 4.5 m/s.	Force-time history	Corridor: (1.6KN, 2.7KN) at 11ms	1.8KN at 11ms	10	[42]
Shoulder	L	23 kg 200X1500mm ram impact to left shoulder at 4.4 m/s.	Force vs Acromion-Acromion Deflection	Corridor: (2.1KN, 2.8KN) at 25mm	2.1KN at 25mm	10	[43]
Shoulder	O	23 kg 200X1500mm ram 15-Deg oblique impact to left shoulder at 4.4 m/s.	Y-Force vs Acromion-Acromion Y-Deflection	Corridor: (1.1KN, 1.7KN) at 15mm	1.8at 15mm	5	[43]
Shoulder	O	23 kg 200X1500mm ram 15-Deg oblique impact to left shoulder at 4.4 m/s.	X-Force vs Acromion-Acromion X-Deflection	Corridor: (0.4KN, 0.6KN) at 27mm	0.35KN at 27mm	5	[43]
Shoulder	O	23 kg 200X1500mm ram 30-Deg oblique impact to left shoulder at 4.4 m/s.	Y-Force vs Acromion-Acromion Y-Deflection	Corridor: (1.28KN, 1.44KN) at 15mm	1.56at 15mm	5	[43]
Shoulder	O	23 kg 200X1500mm ram 30-Deg oblique impact to left shoulder at 7.6 m/s.	X-Force vs Acromion-Acromion X-Deflection	Corridor: (0.79KN, 0.92KN) at 50mm	0.67KN at 50mm	5	[43]
KTH/Pelvis	L	23.4 kg rigid pendulum impact at 5.2m/s laterally to pelvis of seated cadavers.	Force-Deflection curve	Corridor: (5KN,8KN) at 40mm	4.6KN at40mm	10	[38]
KTH/Pelvis	L	23.4 kg rigid pendulum impact at 9.8m/s laterally to pelvis of seated cadavers.	Force-Deflection curve	Corridor: (10KN,15KN) at 50mm	17KN at 50mm	5	[38]
KTH/Pelvis	L	3.4 kg rigid ball impact to the acetabulum of isolated cadaver pelvic bones at 4 m/s.	Force-time history	Corridor: (1.7KN, 3.5KN) at 2.5ms	2.2KN at 2.5ms	10	[44]
KTH/Pelvis	F	270kg padded pendulum impact to KTH complex at 1.2m/s.	Force-time history	Corridor: (4KN, 10KN) at 30ms	6.6KN at 30ms	10	[45]
KTH/Knee	F	4.5 kg rigid pendulum impact to isolated knee with 6 different velocities from 1-6m/s.	Max. Force vs. Impact energy	2KN at 3J; 8KN at 61J	2.3KN at 3J; 8.2KN at 61J	10	[46, 47]
LLF/Lower leg	L	1.84 kg 145X45mm bar impact laterally to the lower leg below knee at 2.56 m/s.	Max Force & Penetration	5.96 KN at 22 mm	5.88KN at 19mm	10	[48]
LLF/Lower leg	R	1.72 kg 145X45mm bar posterior-anterior impact the lower leg at 2.56 m/s.	Max Force & Penetration	0.48 KN at 34mm	0.45KN at 28mm	5	[48]
LLF/Ankle	F	Quasi-static dosiflexion loading to ankle.	Moment vs Angle curve	69 N-m at 45deg	68N-m at 45deg	10	[49,50]
LLF/Ankle	F	Quasi-static plantarflexion loading to ankle.	Moment vs Angle curve	37 N-m at 65deg	39N-m at 65deg	10	[49]
LLF/Ankle	L	Quasi-static Inversion loading to ankle.	Moment vs Angle curve	12 N-m at 45deg	13 N-m at 45deg	10	[49]
LLF/Ankle	L	Quasi-static Eversion loading to ankle.	Moment vs Angle curve	40 N-m at 40deg	33 N-m at 40deg	5	[49]
ABD/Lumbar	A	Quasi-static compressive loading to lumbar spine at 8mm/s.	Z-Force-Displacement corridor	(0.4KN,1.5KN) at 3mm	0.9KN at 3mm	10	**
ABD/Lumbar	A	Quasi-static tensile loading to lumbar spine at 8mm/s.	Z-Force-Displacement corridor	(0.08KN,0.22KN) at 2 mm	0.26Kn at 2 mm	5	**

ABD/Lumbar	F	Quasi-static anterior shear loading to lumbar spine at 4mm/s.	X-Force-Displacement corridor	(0.1KN,0.37KN) at 10mm	0.18KN at 10mm	10	**
ABD/Lumbar	F	Quasi-static posterior shear loading to lumbar spine at 4mm/s.	X-Force-Displacement corridor	(0.15KN,0.5KN) at 10mm	0.22KN at 10mm	10	**
ABD/Lumbar	F	Quasi-static flexion loading to lumbar spine at 5deg/s.	y-Moment vs Angle corridor	(30NM,80NM) at 6 deg	37NM at 6deg	10	**
ABD/Lumbar	F	Quasi-static extension loading to lumbar spine at 5deg/s.	y-Moment vs Angle corridor	(20NM,75NM) at 6 deg	33NM at 6deg	10	**

* KTH--Knee Thigh & Hip; LLF--Lower Leg & Foot; ABD—Abdomen.

** In-house data

Table A-3 Summary of the PMHS sled tests and biofidelity rating results for the whole body

Test conditions	Response measurement	Test Results	Model	Body Region	Rating	Ref.
Driver case[1]	Upper Shoulder belt force	(3.59KN,4.24KN)	3.58KN	NA	**10**	[51]
Driver case[1]	Lower Shoulder belt force	(2.39KN,2.65KN)	2.49KN	NA	**10**	[51]
Driver case[1]	Lap belt force	(1.72KN,2.18KN)	1.67KN	NA	**5**	[51]
Driver case[1]	Left Knee bolster force	(1.84KN,3.42KN)	3.2KN	NA	**10**	[51]
Driver case[1]	Right Knee bolster force	(1.6KN,3.3KN)	3.6KN	NA	**10**	[51]
Driver case[1]	Head CG X-displacement	(254mm,325mm)	335 mm	Head	**10**	[51]
Driver case[1]	Head CG Z-displacement	(45mm,60mm)	64 mm	Head	**5**	[51]
Driver case[1]	Shoulder X-displacement	(164mm,278mm)	242mm	Shoulder	**10**	[51]
Driver case[1]	Shoulder Z-displacement	(-8 mm,-24 mm)	-40mm	Shoulder	**5**	[51]
Driver case[1]	Pelvis CG X-displacement	(65mm,158mm)	88mm	KTH	**10**	[51]
Driver case[1]	Pelvis CG Z-displacement	(64mm,66mm)	46 mm	KTH	**5**	[51]
Driver case[1]	Knee X-displacement	(20mm,54.3 mm)	64 mm	KTH	**5**	[51]
Driver case[1]	Knee Z-displacement	(38 mm,85mm)	32 mm	KTH	**5**	[51]
Driver case[1]	Chest Deflection from Upper chest band	(40 mm,60mm)	33 mm	Thorax	**10**	[51]
Driver case[1]	Right Rib8 compression from Lower chest band	(12.5 mm,55mm)	21 mm	Thorax	**10**	[51]
Passenger case[2]	Upper Shoulder belt force	(2.9KN,4.5KN)	3.88KN	NA	**10**	[51]
Passenger case[2]	Lower Shoulder belt force	(2.1KN,2.65KN)	2.5KN	NA	**10**	[51]
Passenger case[2]	Lap belt force	(1.83KN,2.04KN)	1.87 KN	NA	**10**	[51]
Passenger case[2]	Head CG X-displacement	(254mm,329mm)	335 mm	Head	**10**	[51]
Passenger case[2]	Head CG Z-displacement	(225 mm,267 mm)	200 mm	Head	**5**	[51]
Passenger case[2]	Shoulder X-displacement	(115mm,230mm)	180 mm	Shoulder	**10**	[51]
Passenger case[2]	Shoulder Z-displacement	(-60mm,100mm)	-25 mm	Shoulder	**10**	[51]
Passenger case[2]	Pelvis CG X-displacement	(-25 mm, 60mm)	75 mm	KTH	**5**	[51]
Passenger case[2]	Pelvis CG Z-displacement	(0mm,-18mm)	-21 mm	KTH	**5**	[51]
Passenger case[2]	Knee X-displacement	(-20 mm,60mm)	80 mm	KTH	**5**	[51]
Passenger case[2]	Knee Z-displacement	(30mm,80mm)	50 mm	KTH	**10**	[51]
Passenger case[2]	Chest Deflection from Upper chest band	42 mm	32 mm	Thorax	**5**	[51]
Passenger case[2]	Right Rib8 compression from Lower chest band	(17.5mm,40mm)	21.5 mm	Thorax	**10**	[51]

1--PMHS in a driver position, restrained with force limited 3 point belts plus airbag (FLB+AB), under 48 kmph mid-size sedan crash pulse

2 -- PMHS in a passenger position, restrained with traditional (no force limit) 3 point belt (SB), under 29.8 kmph mid-size sedan crash pulse.

Table A-4 The biofidelity ratings of the Takata Human Model

Index	Body Region	Biofidelity Rating
1	Head	8.3
2	Neck	7.5
3	Shoulder	7.5
4	Thorax	9.4
5	Abdomen	8.6
6	KTH	7.3
7	Lower Leg	8.3
Overall		8.1

APPENDIX B

Table B-1 The Material Properties of the modeled femur, tibia, lumbar vertebra, and clavicle

Tissue	Material Model	Density(kg /mm^3)	E (GPa)	Poisson Ratio	Yield Stress (GPa)	Ep (GPa)	Failure Strain	Thickness (mm)
Clavicle cortical	24	2.00E-06	6.26	0.3	0.0626	4.78	0.0225	2.75
Clavicle trabecular	105	1.00E-06	0.010	0.35	0.002	0.005	0.22	--
Clavicle cartilage	24	1.10E-06	0.020706	0.45	0.0062	0.001		--
Lumbar vertebra trabecular	105	1.00E-06	0.02	0.3	0.00319	0.0	0.244	--
Lumbar vertebra cortical	81	1.41E-06	7.46	0.3	0.056	0.23	0.03	0.3
Femur shaft cortical	24	1.95E-06	17.6	0.315	0.088	4.8	0.014	5.0 (solid)
Femur condyle trabecular	105	1.00E-06	0.292	0.3	0.035	0.106	0.14	--
Femur condyle cortical	81	1.95E-06	17.6	0.315	0.0668	4.5	0.02	2-4 vary
Tibia shaft cortical	81	1.95E-06	20.3	0.315	0.0964	4.5	0.013	4.75 (solid)
Tibia condyle trabecular	105	1.00E-06	0.292	0.3	0.035	0.09	0.14	--
Tibia condyle cortical	81	1.95E-06	17.6	0.315	0.0668	4.5	0.02	2-4 vary

A PROPOSED SIDE IMPACT ATD BIO-FIDELITY EVALUATION SCHEME USING CROSS-CORRELATION APPROACH

Guy S. Nusholtz
Timothy P. Hsu
Lynn C. Byers
DaimlerChrysler Corporation
United States
Paper Number 07-0399

ABSTRACT

ISO/TR9790 has been in existence for some years for evaluating the bio-fidelity of side impact ATD's (ISO/TR 9790, 1999). NHTSA recently generated a new method for creating bio-fidelity corridors. The method was different from the ISO method, by incorporating statistics and the time relationships into the evaluation equation and automating the process (Maltese et al. 2002). Although both the ISO and NHTSA methods exhibit a number of strengths, they also have weaknesses. This paper attempts to build on these two methods and develop an ATD assessment method which offers added objectivity and is based on a statistical process. Improvements were explored in several key areas to address the existing numeric issues (Hsu et al., 2005). This process bases itself on the statistical correlations between the post-mortem human subject (PMHS) data. Validation of the scheme is performed using PMHSs as "pseudo dummies". A simple formula is proposed for ranking the bio-fidelity of the dummy, resulting in a score from 0-10, with 10 being the best.

INTRODUCTION

Since the 1950's various mechanical human surrogates, or Anthropomorphic Test Devices (ATD), have been used for assessing the potential for injury in vehicle crash tests. These ATD crash test dummies have become more sophisticated, complex, and potentially more human-like through the years, but still provide only very limited estimations of what might occur in a real life crash. In order to improve this prediction, efforts have been made through the years to make the ATDs more bio-fidelic. However, an omni-directional dummy has not been developed. Instead, dummies have been created for each type of impact, resulting in a variety of different ATDs in frontal, side, and rear impacts. For some of these impact types, a whole family of ATD sizes has been developed.

Each of these ATDs has its own set of performance requirements, calibration procedures, and response corridors that have been developed in an attempt to make the dummy better mimic a human, as well as ensuring repeatability of responses. Many attempts have been made to determine the level of bio-fidelity. Tests have been performed using PMHSs to gather information on what injury response would be in certain loading situations. The difficulty however, lies in how to correlate the findings from these tests with those of the ATDs, i.e., determining how accurately an ATD crash test dummy response represents "real" human injury.

In 1989, the International Standards Organization (ISO) first published ISO/TR 9790, which defined a bio-fidelity evaluation approach for side impact dummies (Figure 1). Defining a method to standardize the determination of bio-fidelity was a big step forward. However, the actual method required some level of subjectivity and the resulting corridors were large, allowing the acceptability of a large amount of variation in the results.

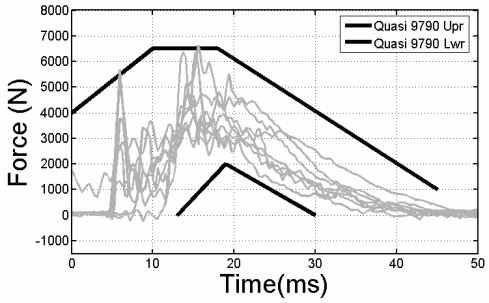

Figure 1. Typical ISO bio-fidelity corridor.

In an effort to reduce the subjectivity and improve upon the ISO method, Maltese et al., at the National Highway Traffic and Safety Administration (NHTSA), published a new method for creating bio-fidelity corridors. This method used a statistical cumulative variance approach to align the signals, which were then averaged. A corridor was then automatically created, with its boundaries defined as plus and minus one standard deviation from the mean of the aligned signals. Thus this created a tighter

corridor, which in general, better resembled the shape of the test data curves (Figure 2).

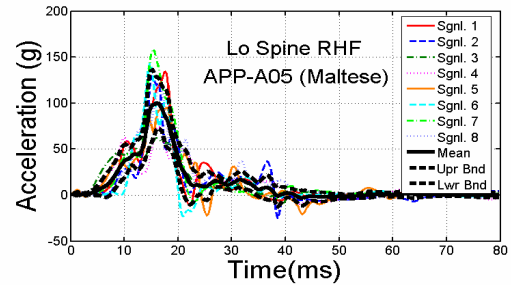

Figure 2. Typical Maltese bio-fidelity corridor.

Although this method appeared to remove some of the human intervention found in the ISO method, it too had shortcomings (Hsu et al. 2005). The selection of the standard signal with which to align the others, still involved some subjectivity. The method for aligning the curves involved variability in time shifting, which could destroy relative timing information and in some situations the resulting corridor lacked physical meaning.

This paper presents a statistical, correlation based method that builds upon the work incorporated into the ISO and Maltese methods. One notable difference in this new method is that it does not generate physical corridors. Instead it examines and compares the magnitude, shape, and phase relationships of the curves to determine the level of similarity. It then calculates a simple bio-fidelity score, based on these cross-correlation comparisons. This method avoids the issues caused by subjective evaluation, time shifting, and variable time history lengths. It is fully automatic and updatable. This bio-fidelity score should be more statistics based, straightforward, and representative of actual bio-fidelity than the existing methods.

CROSS-CORRELATION BASED APPROACH

As discussed, current dummy evaluation methods have areas that could be improved. In an earlier study (Hsu et al. 2005), several areas for improvement were identified. Among them, the use of a correlation method to better preserve the signal characteristics and to resolve issues resulting from time shifting, manual standard curve selection, and inconsistency in the integration time period. The proposed method aims at forming a more objective, scientific, statistically meaningful and easily applicable ATD assessment alternative.

Areas of Improvement

This approach attempts to address the following areas key to a broader scientific method in evaluating the side impact ATD:

- Incorporation of statistical correlations
- Reduction of manual intervention
- Incorporation of complete time history
- Reduction of numeric issues
- Automation of the process and improvement of process robustness

The approach proposed does not require a fixed set of PMHS data (one or greater is required). Rather, a continuously updatable set of PMHS data is used. The scheme does not shift the data as is done in Maltese's method. It is believed that the correlation method will take care of the relative timing information by using phase correlation coefficients. By eliminating time shifting, the potential destruction of relative timing information is avoided.

Steps

A flow chart of the proposed process is shown below.

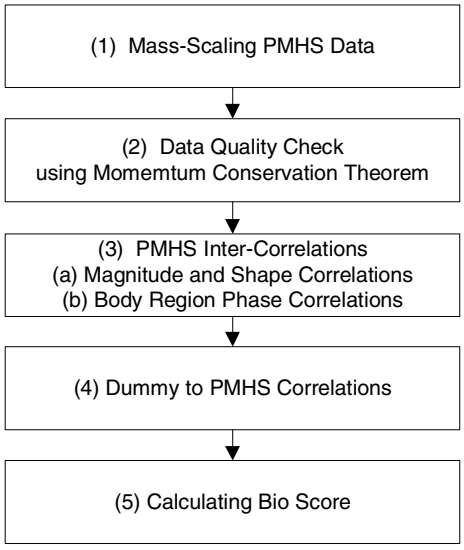

The steps to obtain the biofidelic score of an ATD consist of mass-scaling the PMHS data, scrutinizing the data using the momentum conservation theorem, calculating the magnitude, shape, and phase correlations of the PMHSs and the dummy, comparing the correlations of the dummy to the averages of that of the PMHSs (magnitude and shape), obtaining the relative phase differences between different body regions of the dummy and of

each PMHS, and calculating the bio-fidelity score of the dummy using a multifactor based formula.

Data used in the study are from NHTSA's biomechanical research program portfolio on its public websites. Figure 3 shows a typical sled test set-up. Figures 4 and 5 show some typical signal traces for PMHSs and dummies in sled tests. The data was mass-scaled to account for the different sized PMHSs. Since no time shifting is performed, all of the relevant signal timings are preserved.

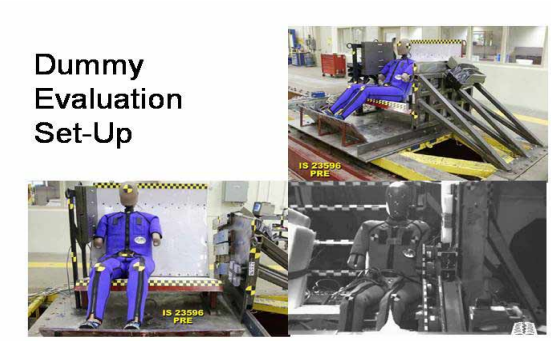

Figure 3. Typical set-up for NHTSA's biomechanical tests.

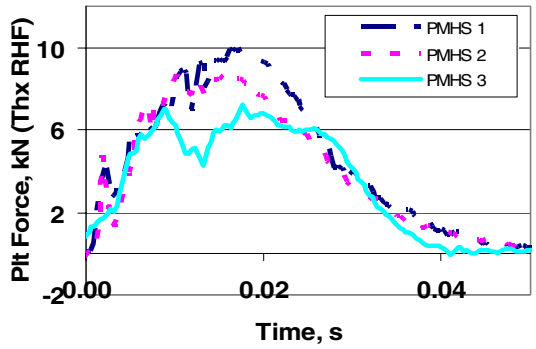

Figure 4. Typical PMHS test time histories.

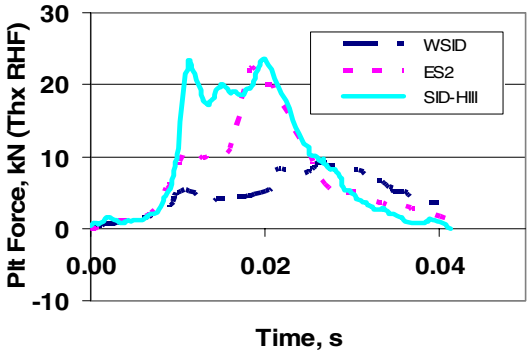

Figure 5. Typical dummy test time histories.

(1) Mass-Scaling PMHS Data

The PMHS data is mass-scaled using Eppinger's technique (Eppinger et al. 1984). The scaling process is described by Maltese (Maltese et al. 2002).

(2) Data Quality Check

Before the correlations are calculated, corrupted signals need to be identified and removed to ensure the quality of the process. ISO/TR9790 does this similarly by removing from the data sets the PMHSs which sustained severe rib fractures. In the approach herein, data are scrutinized using the momentum conservation theorem. The process is done to the force data, based on the theory that the summation of the force over time for a particular test condition should be relatively consistent from test to test. The same is true for the acceleration data, assuming equivalent masses can be considered constant and then applying Newton's theorem, ***F=m*a***. This way, the contamination due to instrumentation malfunction or improper calibration can be singled out easily. Since the energy inputs are the same for the group of PMHSs under the same test conditions, the integration of the response time histories from that group should yield the same value over time based on the momentum conservation theorem (Equation 1.):

$$m * V = \int F dt \qquad (1).$$

i.e., for a set test condition, the velocity and the integration of the force over time should yield the same results. Those PMHSs that deviate from the majority of the group when integrated indicate that they either have different momentum, incorrect set-ups, an error in the data acquisition process due to miscalibration, a bad connection, or a static interference issue. The signals whose integrations

deviate from the majority of the group are dropped. e.g., an arbitrary 20% has been chosen as the threshold for data elimination. Those having greater than 20% deviations from the group mean are considered to be outliers, or bad data. Only the data meeting the momentum conservation equation are used for the subsequent bio-fidelity evaluation. For the purpose of illustration, a set of thorax rigid plate high speed plate force signals is plotted in Figures 6 and 7. Five out of the six tests in the graph have similar momentum, while the one with the dashed line has distinctly different integration results. All data except that test are then used for the correlation analysis.

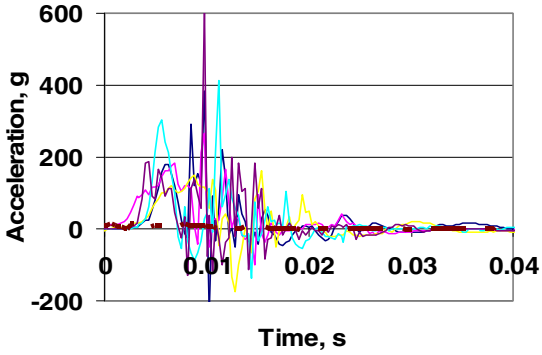

Figure 6. PMHS signals used for dummy evaluation before integration and drop of bad data.

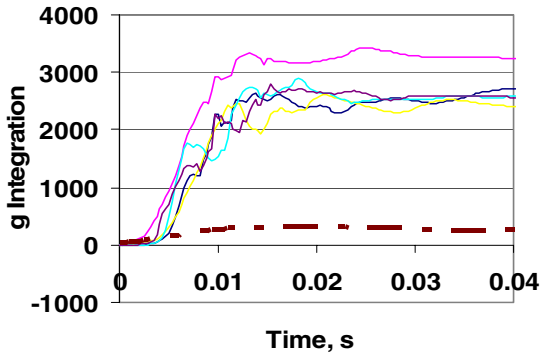

Figure 7. PMHS signals used for dummy evaluation after integration. The test with a dashed line is dropped as a result of failing the momentum conservation theorem.

(3) PMHS Inter-Correlations

After the clean-up process, the correlation baseline from the PMHSs can be established. The cross-correlations between the PMHSs themselves are calculated using the following methods. Three quantitative indicators are utilized (Figure 8). They are magnitude, shape, and phase correlations, as described by Xu (Xu 2000).

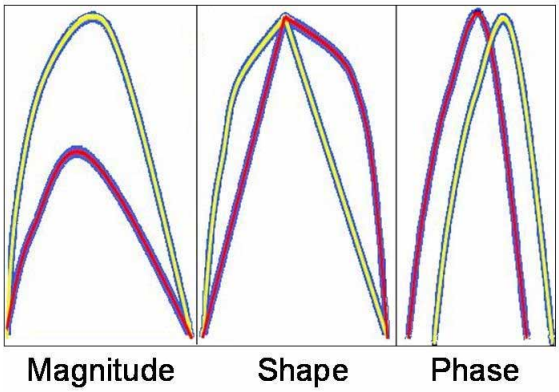

Figure 8. Schematic representation of three cross-correlation indicators.

(3a) Magnitude and Shape Correlations

Mathematically, the magnitude and shape correlations of the PMHSs are between 0 and 1, with one indicating that the two signals are identical (Figures 9 & 10).

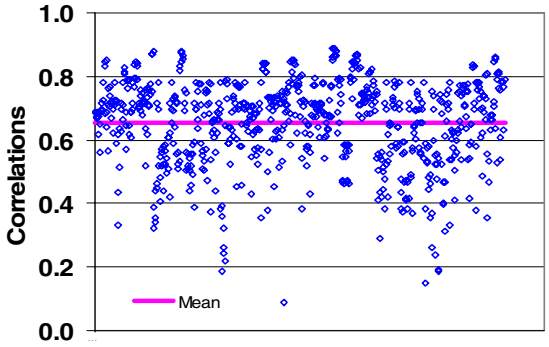

Figure 9. Typical scatter of magnitude cross-correlation coefficients of PMHS test data.

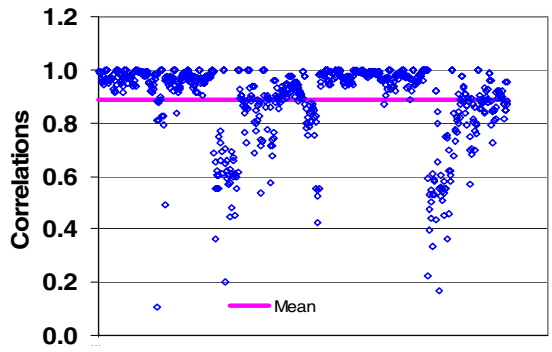

Figure 10. Typical scatter of shape cross-correlation coefficients of PMHS test data.

The correlations are calculated in the following way to achieve reasonable and balanced numeric results. First, the one to one correlations between every two PMHSs, including itself, are calculated.

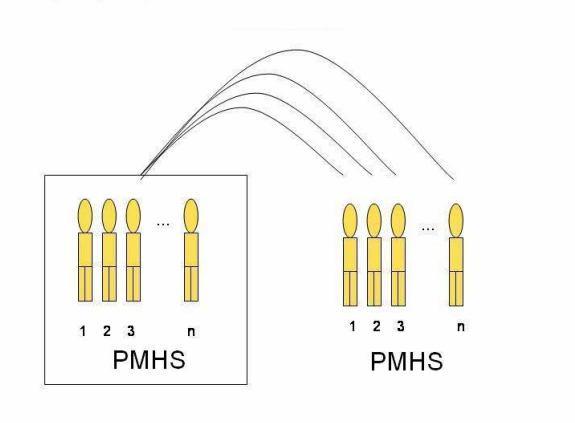

Figure 11. Magnitude and shape cross-correlation calculation.

Their sums are averaged. In averaging the sums, including or not including the auto-correlations (the cross-correlations of a PMHS with itself) yields slight differences in outcome, but is believed to be minimal (Figures 12 & 14).

Tables 1 and 2 show some correlation calculations from PMHS data in 9.8 mph tests using the PHF (Padded High speed Flat/no offset) test condition. The average of all PMHSs is shown in the top row, and the PMHS with the worst correlation is shown in the second row. As mentioned above, those time histories failing the momentum conservation guidelines are already excluded from the calculation.

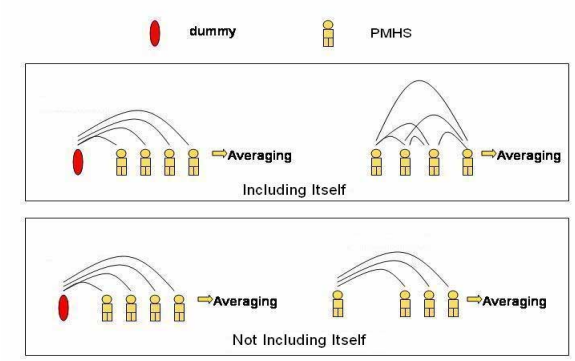

Figure 12. Two schemes for collective correlation calculations.

Table 1.
Example magnitude correlation results for three different body regions (not normalized)

BIO-FIDELITY BASED ON MAGNITUDE - PHF			
	Thorax	Abdomen	Pelvis
PMHS(ave)	0.8185	0.9164	0.8841
PMHS(wst)	0.7265	0.7104	0.8650
SID	0.2683	0.6232	0.5762
ES-2	0.5950	0.8160	0.7198
WSID	0.7212	0.7246	0.8729

(3b) Body Region Phase Correlations

While the time history magnitude and the time history shape correlations are based on a PMHS local body region, the phase relationships are compared between different anatomical regions (Figure 13). Phases between the different body regions of each PMHS are also averaged and the duration calculated. The reason for this is that it has been seen that the relative timing between body regions in a crash is critical for representing human body kinematics during an impact event.

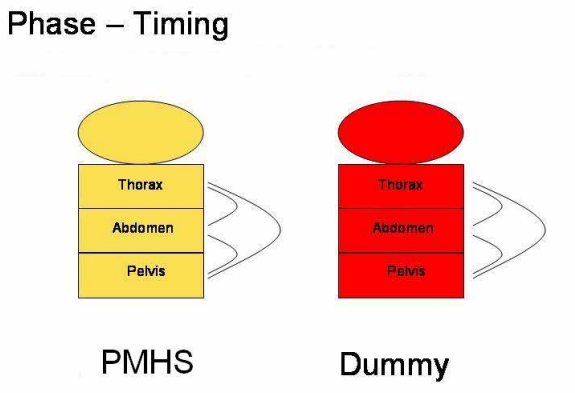

Figure 13. Schematic representation of phase correlation calculation.

(4) Dummy to PMHS Correlations

As the next step, a dummy's correlations to each and every PMHS are calculated similarly to the way the inter-PMHSs correlations are calculated. Some earlier/prototype test data for SID, ES-2 and WorldSID are used here as an example.

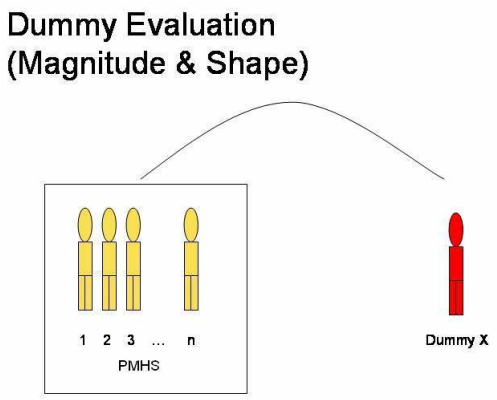

Figure 14. The dummy time history is checked against each PMHS time history in the process.

The average of the magnitude, shape and phase correlations of the dummy to each of the PMHSs is obtained. These results are shown in Tables 1, 2 and 3, in the bottom three rows.

To check the dummy's bio-fidelity, theoretically either the worst PMHS performer, the best PMHS performer or the average of a PMHS group can be used as the threshold. Which is more appropriate, or more truly reflects the dummy's bio-fidelity, is yet to be determined. Nevertheless, the procedures are the same for either method. Only the results from the averaged PMHSs are shown in Table 1. In the following discussion, the average PMHS method is used for the purpose of describing the process. If using the best or worst PMHS is deemed to be more appropriate, it can be easily implemented without the need to change the formula.

(5) Calculating the Bio Score

A few variations in the dummy evaluation scheme formulation can be used, as long as the main objective remains to effectively measure the closeness of the ATD's responses to those of the PMHSs. In the proposed approach, after the correlations of inter-PMHSs and between dummy and PMHSs are calculated, summed, and averaged, the ratios of the two averages are used for the bio-fidelity score calculations. Equation 2 is proposed for that purpose. In Equation 2, the scaling factor of 10 is used to yield a score of 0 to 10.

The magnitude and shape correlations are normalized by dividing the average PMHS to dummy correlation by the average PMHS to PMHS correlation (Table 2). For the phase correlation contribution, the coefficients are normalized according to Equations 5, 6 and 7. They represent results as a function of total duration, as well as the time lags between different body regions.

$$Bio\ Fidelity\ Score\ =\ [RMAG * RSHA * RPHA] * 10 \qquad (2).$$

where,

$$RMAG\ =\ Ratio\ of\ Average\ Magnitude\ Cross\ Correlations\ of\ Dummy\ to\ PMHS\ to\ that\ of\ PMHS\ to\ PMHS \qquad (1.0,\ if\ >1.0) \qquad (3).$$

$$RSHA = Ratio\ of\ Average\ Shape\ Cross\ Correlations\ of\ Dummy\ to\ PMHS\ to\ that\ of\ PMHS\ to\ PMHS \quad (1.0,\ if > 1.0) \qquad (4).$$

$$RPHA = Ratio\ of\ RPHA1\ of\ Dummy\ to\ PMHS\ to\ that\ of\ PMHS\ to\ PMHS \quad (1.0,\ if > 1.0) \qquad (5).$$

$$RPHA1 = \sum \frac{DURDIFF}{Duration} \qquad (6).$$

where,

$$DURDIFF = Duration - Absolute\ Phase\ Differences\ Between\ Body\ Regions \qquad (7).$$

Table 2.
Example magnitude correlation results for thorax (normalized)

MAGNITUDE - Thorax PHF		
		Normalized
PMHS(ave)	0.8185	
PMHS(wst)	0.7265	
SID	0.2683	0.3278
ES-2	0.5950	0.7269
WSID	0.7212	0.8811

All three key indicators are represented in the formula and given equal weights. The formulation of the equation yields a score of 10 when the subjects to be compared are identical and a score of 0 when they are statistically completely unrelated. The evaluation thus ties the closeness of the ATD impact response time history of a given anatomical structure to that of the impact response time history of the human surrogates using a numeric score defined as the bio-fidelity score. If the ATD's statistical relationships to the PMHSs are equal to or greater than those between the PMHSs, the ATD's bio-fidelity is considered to be excellent. If it is below the statistical relationships of the PMHSs then that is considered to have low bio-fidelity.

Example

The sled data for the PHF test condition (Padded, High speed /8.9 mph, Flat/no offset) from some earlier/prototype SID-3, ES-2, and WorldSID tests are used to show the process of the bio-fidelity evaluation scheme being proposed (Tables 3 and A1).

The magnitude and shape correlations of the dummy to the PMHSs are compared to the averages of the PMHSs by dividing the correlations of the dummy to the PMHSs by that of the PMHSs. In Table A1, R8C4 (Row 8 Column 4) divided by R5C4 results in R12C4, and R9C4 divided by R5C4 results in R13C4, etc. If the quotient is greater than one, one is used instead. The same is done with the shape correlations (row 12-14, column 6, etc.). The relative phase differences between different body regions of each PMHS are obtained (timing differences shown in ms in the example, row 5 col 8), as well as the duration of each signal (time between the first zero crossing before and after the peak time, row 5 col 9). Note that those results are yet to be updated with newly available SID-3, ES-2, and WorldSID data.

Table 3.
Example magnitude, shape, and phase correlation results for thorax (not normalized).

		Magnitude	Shape	Phase	Duration (period)
Thorax (Not Normalized)					
	PMHS(ave)	0.8185	0.9960	0.3189	53.75
	PMHS(wst)	0.7265	0.9920		
	SID	0.2683	0.9767	5.0900	
	ES-2	0.5950	0.9895	5.5800	
	WSID	0.7212	0.9872	7.0100	

Process Verification

The sensitivity of the formula parameters is studied in the process by using PMHS data as "dummy" data. Theoretically when PMHS data are used as "dummy' data and plugged into the formula, they should yield a good or passing score because they are the very data used as the baseline to form the dummy evaluation equations. To confirm this, several trials are run to examine the robustness and practicability of the method. The scheme is verified using several arbitrarily picked PMHSs as "pseudo dummy" data.

Discussion

Differences exist between ISO9790, Maltese's method, and the cross-correlation based approach proposed by this study, e.g. the corridor definitions and the way dummies are judged. ISO9790 does not shift the signals. Maltese's method shifts the time histories based on the minimum cumulative variance relative to a master time history. ISO corridors often contain all the normalized response data within its corridors while the Maltese corridors use the signal mean plus and minus one standard deviation as the upper and lower boundaries. Three key differences between ISO9790, the Maltese method, and the approach herein are the algorithms used, the corridor definitions, and the way dummies are judged. Table A2 gives a brief summary of differences between the three evaluation schemes.

Summary

A cross-correlation based evaluation scheme is proposed. The statistical characteristics of the relationship between human surrogate and ATD impact response time histories are used to evaluate the ATD's bio-fidelity. The evaluation is done by determining if the ATD impact response time history of a given anatomical structure is statistically similar to that of the impact response time history of the anatomical structure in the human surrogates used for comparison. Three key parameters are used: magnitude correlation, shape correlation, and the phase relationship between different anatomical regions. The data relevancy is determined by kinematical factors such as conservation of momentum. The proposed approach eliminates the requirements for time shifting. The process is similar to the cumulative variance technique used in Maltese's method. It continues the work of Maltese with respect to reducing the human intervention in the existing bio-fidelity rating schemes.

Using this proposed bio-fidelity evaluation scheme, if an ATD's statistical relationships to the PMHSs are equal to or greater than the statistical relationships between PMHSs, it is considered to be bio-fidelic. If the statistical relationships are in the same ranges as that of the PMHSs, it is considered to be acceptable. If it is below the PMHSs, it is considered to have low bio-fidelity.

The process discussed in this paper is merely the framework of a side impact dummy evaluation scheme. Complete evaluation of a particular dummy requires additional work to finalize and test the scheme. Also, the proposed scheme at the time of this publication is not ready to be used for dummy design guidance. In other words, although the proposed approach certainly provides a tool for dummy evaluation, it does not provide provisions for dummy development targets. There is no corridor or curve to design a dummy to, as the ISO and Maltese methods have. Additional work will be needed to develop a similar design tool.

Further Work

More work remains to be done before this approach will be in its final form. At this time, a complete evaluation of a dummy is yet to be performed. On one hand, a more comprehensive PMHS database is needed. Without that, a reasonable statistical meaning of the scheme can not be achieved. Fortunately, thanks to the approach's flexibility, the scheme can be easily updated as additional data becomes available. On the other hand, how the correlation method should be formulated to achieve the best representation of the dummy's bio-fidelity remains to be further explored. How the weights should be applied to achieve the best balance of all the relevant factors in the formula, (i.e. how the three correlation indicators should be weighed and combined and

whether their product or summation should be used) remains to be answered. In addition, where to draw the line between the acceptable or not-acceptable ATDs is also somewhat subjective in the proposed approach. Whether a physical corridor or a score should be used as the rating tool remains to be decided. Whether the power statistics, T-square or some other approach should be used is to be studied as well. Whether the test data should be screened for adequacy, and how that should be done, is yet to be agreed upon by researchers in the field. All in all, there is a lot of work yet to be done, but this proposed ATD evaluation scheme provides a promising alternative in applying correlation tools in side impact dummy bio-fidelity evaluation.

ACKNOWLEDGEMENT

Sincere appreciation goes to Bruce Donnelly and Kevin Moorhouse of VRTC for their support in reviewing the material and providing valuable insights, to Matt Maltese for his insights and valuable suggestions, and to Heather Rhule for providing the electronic data for the study.

REFERENCES

Eppinger, R.H., Marcus, J.H., and Morgan, R.M., (1984) Development of dummy and injury index for NHTSA's thoracic side impact protection research program. Proc. SAE Government/industry Meeting, pp. 983-101 1. Society of Automotive Engineers, Warrendale, PA.

Hsu, T.P., Nusholtz, G.S. (2004) 31st Annual international Workshop on Human Subjects for Biomechanical research

Hsu, T. P, Nusholtz, G. S. (2005) Considerations of Bio-fidelity Corridors for Lateral Impacts, SAE Technical Paper Series 2005-01-0308, April 11, 2005

Irwin, A. L.; Sutterfield, A.; Hsu, T. P.; Kim, A.; Mertz, H. J.; Rouhana, S. W.; Scherer, R. (2005) Side impact response corridors for the rigid flat-wall and offset-wall side impact tests of NHTSA using the ISO method of corridor development. Occupant Safety Research Partnership, Mich. 34 p. Stapp car crash journal. Vol. 49 (Nov. 2005) p. 423-456.

ISO/TR9790. (1999) Road Vehicles Anthropomorphic Side Impact Dummy - Lateral Impact Response Requirements to Assess the Bio-fidelity of the Dummy. International Standards Organization, American National Standards Institute, NY, NY.

Maltese, M. R.; Eppinger, R. H.; Rhule, H. H.; Donnelly, B. R.; Pintar, F. A.; Yoganandan, N. (2002) Response corridors of human surrogates in lateral impacts. National Highway Traffic Safety Administration, Washington, D.C./ Wisconsin Medical College, Milwaukee/ Veterans Affairs Medical Center, Milwaukee, Wisc. 31 p. Stapp Car Crash Journal, Vol. 46, Nov. 2002, p. 321-351.

Rhule, H. H.; Maltese, M. R.; Donnelly, B. R.; Eppinger, R. H.; Brunner, J. K.; Bolte, J. H.. (2002) Development of a new bio-fidelity ranking system for anthropomorphic test devices. National Highway Traffic Safety Administration, Washington, D.C./ Transportation Research Center, East Liberty, Ohio. 36 p. Stapp Car Crash Journal, Vol. 46, Nov. 2002, p. 477-512.

Xu, L.; Agaram, V.; Rouhana, S.; Hultman, R. W.; Kostyniuk, G.W.; McCleary, J.; Mertz, H.; Nusholtz, G.S.; and Scherer, R.. (2000) Repeatability Evaluation of the Pre-Prototype NHTSA Advanced Dummy Compared to the Hybrid III, SAE Technical Paper Series 2000-01-0165, March6-9, 2000

APPENDIX A

Table A1.
Sample results of bio-fidelity score calculation

	1	2	3	4	5	6	7	8	9	10
1										Score
2	PHF									Scales of 0-10
3				Magnitude		Shape		Phase	Duration (period)	10 being the most Biofidelic
4	Thorax									
5		PMHS	ave Mag	0.8185	ave. shape	0.9960	ave phase	0.3189	53.75	
6		PMHS	wst Mag	0.7265	wst shape	0.9920				
7										
8		SID		0.2683		0.9767		5.0900		
9		ES-2		0.5950		0.9895		5.5800		
10		WSID		0.7212		0.9872		7.0100		
11										
12	Normalized	SID		0.3278		0.9806		0.9107		2.9
13	Normalized	ES-2		0.7269		0.9935		0.9015		6.5
14	Normalized	WSID		0.8811		0.9912		0.8748		7.6
15										
16	Abdomen									
17		PMHS	ave Mag	0.9164	ave. shape	0.9945	ave phase	0.2706	42.19	
18		PMHS	wst Mag	0.7104	wst shape	0.9937				
19										
20		SID		0.6232		0.9736		5.4911		
21		ES-2		0.8160		0.9830		5.4018		
22		WSID		0.7246		0.9809		6.2500		
23										
24	Normalized	SID		0.6801		0.9790		0.8755		5.8
25	Normalized	ES-2		0.8904		0.9884		0.8776		7.7
26	Normalized	WSID		0.7907		0.9863		0.8574		6.7
27										
28	Pelvis									
29		PMHS	ave Mag	0.8841	ave. shape	0.9965	ave phase	0.2296	40.00	
30		PMHS	wst Mag	0.8650	wst shape	0.9934				
31										
32		SID		0.5762		0.9844		6.4732		
33		ES-2		0.7198		0.9926		4.6429		
34		WSID		0.8729		0.9850		6.6518		
35										
36	Normalized	SID		0.6517		0.9879		0.8430		5.4
37	Normalized	ES-2		0.8142		1.0000		0.8890		7.2
38	Normalized	WSID		0.9873		1.0000		0.8385		8.3

Due to lack of data availability, some of the results shown are not based on a complete data set.

Table A2.
Comparison of different side impact dummy evaluation schemes

	ISO/TR9790	Maltese	Correlation
Evaluation	Expert evaluation	Statistical variance	Statistical correlation
Data screening	Severe rib fracture eliminated	No data exclusion	Irrelevant data eliminated through the momentum conservation theorem
Corridors	Upper and lower corridors	Mean +/- one standard deviation corridors	No physical corridors
Alignment	Manual alignment with some relative timing conservation	Alignment based on minimum variance	Alignment through correlation phase indicator
Processing	Manual processing	Automatic processing	Automatic processing
Numeric issues	No known numeric issues	The standard curve selection leading to variability	No known numeric issues
Numeric issues		Negative corridor issue	
Numeric issues		Some irregular corridors (zero corridor width) or corridors with less physical meaning	
Numeric issues		Sometimes unstable outcome due to integration time window	
Update	Update with new test data cumbersome	Updatable	Easily updatable
Manual work	More human interventions	Less human interventions	Minimum human intervention
Design guideline	Provides design guidance	Provides design guidance	Does not provide design guidance

COMPARISON OF KINEMATIC AND THORACIC RESPONSE OF THE 5TH PERCENTILE HYBRID III IN 40, 48 AND 56 KM/H RIGID BARRIER TESTS

Suzanne Tylko
Dominique Charlebois
Transport Canada
Canada
Alain Bussières
PMG Technologies
Canada

Paper Number 07-0506

ABSTRACT

Full-scale crash tests were conducted to investigate the correlation between the 5th percentile Hybrid III dummy kinematics and chest response at three test speeds. A total of 20 comparative full frontal rigid barrier tests were conducted at 40, 48 and 56 km/h with the dummies placed in the front and rear outboard seating positions.

As test speed increases to 56 km/h, the forward excursion and rotation of the thorax increases significantly. This rotation combined with chest jacket distortions inhibits the accurate measurement of chest deflection. The influence of the seat characteristics and belt geometry at peak load are explored.

A new multi-point sensing device, known as the RibEye is introduced in full-scale rigid barrier tests to evaluate the role of multi-point sensing in enhancing the accuracy of chest deflection measurements. This new instrumentation may significantly reduce the sensitivity to belt placement associated with traditional single point measurements.

An impulse calculation method to evaluate the load management capability of restraint systems is proposed.

INTRODUCTION

In 2001 the Government of Canada published in the Canada Gazette, a Notice of Intent to change the Canadian Motor Vehicle Safety Standard for frontal protection (CMVSS 208). The department strives to harmonize motor vehicle safety standards with the U.S., except in cases where harmonization would lead to the relaxation of an existing safety requirement.

The CMVSS 208 currently requires that the peak chest deflections for the Hybrid III 50th male remain below 50 mm for frontal rigid barrier tests conducted at up to 48 km/h. Complete harmonization with the U.S. FMVSS 208 would mean increasing the allowable chest deflection limit to 63 mm for the male and adopting a limit of 52 mm for the 5th percentile female. Raising the limit for chest deflection to levels that are beyond the magnitudes measured in vehicles would negate the benefit of including chest deflection as an injury criterion. A lower limit scaled to the 50th male is needed for the 5th percentile female.

Transport Canada has been engaged in the conduct of research to investigate the characteristics of the chest under belt and or combined belt and airbag loading conditions to identify the factors affecting chest response in the 5th percentile ATD. A study on the effects of breast anthropometry on chest response was reported in Stapp 2006 (Tylko, S. et al). During the course of this investigation it became evident that chest deflection did not increase linearly between 40 and 56 km/h FFRB tests. The dummy behaved differently at higher test speeds.

As the test speed is increased the extent of forward excursion and rotation about the torso belt is amplified and torsion of the jacket with respect to the rib cage becomes more noticeable. Observation of the high-speed video indicated that the dummies rotated outboard as they approached the limit of forward excursion thus redirecting the load away from the single point measurement sensor in the sternum.

A new multi-point sensing system was added to the instrumentation of the dummy to assist in the characterization of load application. The paper presents the preliminary multi-point measurements and the results of an alternative approach used to investigate the kinematics of the dummy and the influence that this may have on chest response.

METHODOLOGY

Crash Tests

Frontal rigid barrier tests were carried out at 40, 48 and 56 km/h with model year 2006 - 2007 vehicles. The Hybrid III 5th percentile female anthropometric test device (ATD) manufactured by Denton ATD and FTSS were seated in the front and rear outboard seating positions. Test set-up, vehicle preparation, and dummy positioning for the front seat were done in accordance with the respective sections of the FMVSS 208 requirements for the full frontal rigid-barrier tests (FFRB).

The rear doors were removed to provide optimized camera views of the dummy kinematics. Video cameras were attached to the vehicle as shown in Figure 1. Pre and post-test dimensions were obtained to monitor for B-pillar displacement during the test should it occur.

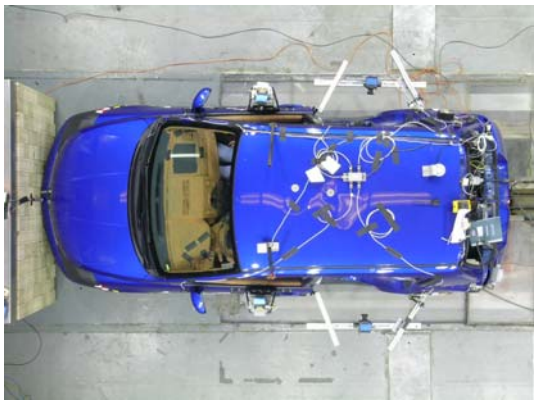

Figure 1: Plan view of camera locations.

Instrumentation and Video Imaging

Data were recorded at 10kHz and filtering was performed in accordance with SAE J211. High-speed videos at 1000 frames/second were obtained and included lateral views of the front seat occupants; lateral and a frontal view of the rear seat occupants. Overhead camera views of the occupants were obtained for one vehicle with a retractable roof (convertible).

The baseline instrumentation in the dummies included a tri-axial accelerometer at the head CG, a 6-axis load cell at the upper and lower neck and lumbar spine; a 3-axis clavicle load cell; tri-axial accelerometers at the upper, mid and lower spine and pelvis; accelerometers at the top mid and lower sternum; and single axis load cells in the femurs. The chest potentiometer was supplemented with either the THUMPER kit consisting of four IR-TRACCs (**I**nfra**R**ed – **T**elescoping **R**od for **A**ssessment of **C**hest **C**ompression) or the RibEye for multi-point sensing.

RibEye

The RibEye is an electro-optical system developed by Boxboro Systems and Denton ATD for the measurement of rib deflections. The first production version was developed for Transport Canada for use in the 5th Female Hybrid III ATD. The RibEye measures the X and Y locations of 12 points on the ribcage using optical triangulation at a sampling rate of 10 kHz. Light emitting diodes (LEDs) can be attached to the ribs anywhere within the measurement range, offering much greater measurement flexibility than the traditional fixed sensors. Two light angle detectors are mounted on the sides of the spine box while the RibEye controller, is mounted in the spine box. The RibEye controller auto adjusts the brightness of each LED to enhance accuracy. After the angle data is acquired, the controller calculates the X and Y position of each LED by triangulation and reports the data in millimeters with an accuracy of 1 mm.

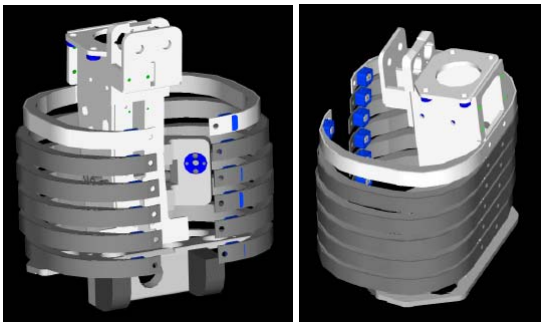

Figure 2: RibEye sensor & light detector location.

RESULTS

RibEye Chest Deflection

Tests were conducted with the RibEye installed in a Denton 5th percentile Hybrid III ATD. The 12 sensors were located on each rib at approximately 60 mm from the centerline of the sternum. By comparison, the four IR-TRACCs are attached at approximately 30 mm from the centerline of the sternum. As shown in Table 1, the majority of the tests were conducted in the rear seat to investigate the RibEye response in belt only loading conditions. Two driver tests were also conducted to evaluate the RibEye performance in combined belt and airbag loading conditions and compare this to the pure belt loading responses.

Table 1: Tests conducted with the RibEye

FFRB Test Speed			
Position	40 km/h	48 km/h	56 km/h
11		1	
13		1	
14	1	1	
16	2	1	4

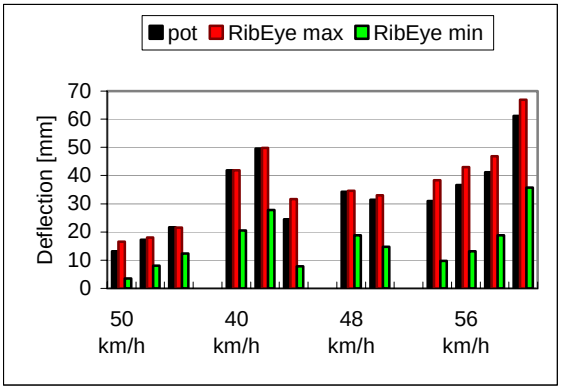

Figure 3: Comparison of peak chest deflection measured at potentiometer to peak RibEye measurement for rear seat, belt only.

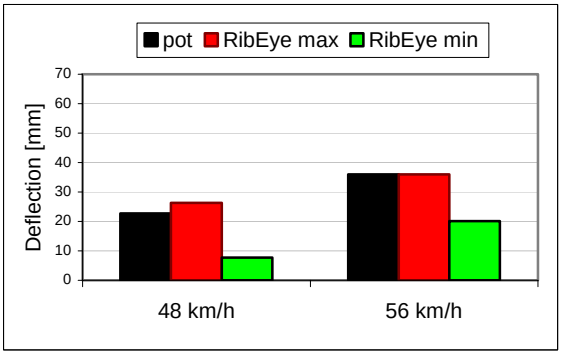

Figure 4: Comparison of peak chest deflection measured at potentiometer to peak RibEye measurements for a driver at 48 and a driver at 56 km/h with belt & airbag.

As can be seen in Figure 3 the discrepancy between the deflection measurement of the potentiometer and the RibEye measurement of the individual ribs increases as test severity is increased. The first series of bars represent the measurement results obtained in a soft car-to-car test whereas the tests at 40, 48 and 56km/h were all FFRB tests conducted with the dummy seated in the rear seat. The RibEye detected greater peak deflections than the potentiometer in all tests that were conducted at 56km/h. This confirms the greater out-of-plane motion that was observed in the videos of the higher test speed tests. Figure 4 illustrates the effect of combined belt/ airbag loading in the two tests that were conducted with the dummy seated in the driver seat.

Crash videos were reviewed to determine the belt drape. Tests were classified, as having belt routing that was close to the neck, at the mid-shoulder and distal to the shoulder. RibEye measurements were normalized as a function of potentiometer measurement and plotted for both sides of the ribcage.

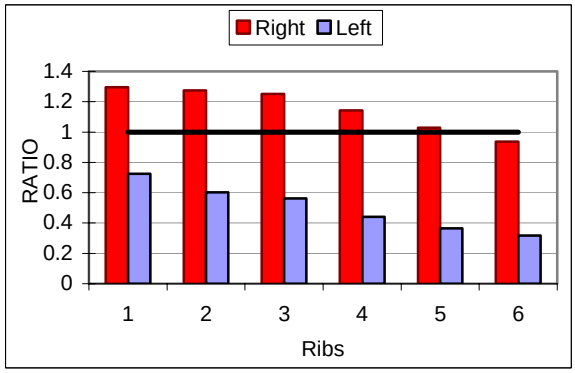

Figure 5: Potentiometer measure normalized to the individual RibEye deflection values for a belt that passes close to the neck. Left rear passenger.

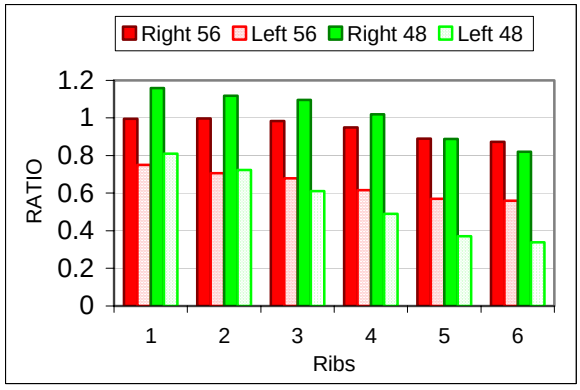

Figure 6: Potentiometer measure normalized to the individual RibEye deflection values for drivers with belt and airbag loading at 48 & 56 km/h.

Figure 5 is an example of the type of deflection pattern that is observed when the belt lies close to the neck. In this example the rear passenger dummy was seated behind the driver in a 40km/h FFRB test. The greatest rib deflection is observed on the right side of the rib cage. Figure 6 displays the deflection pattern observed when the belt and the airbag load the chest. In the 56km/h test the chest was evenly loaded however, in the vehicle that underwent the 48km/h test the videos confirmed that the shoulder belt was

very close to the neck resulting in higher peak upper rib deflections relative to the central potentiometer.

The RibEye system was able to consistently characterize the asymmetrical deformation of the chest for the belted loading conditions. An ATD seated behind the driver will have greater deflections on the right side of the chest as it rotates into the belt and outboard. Similarly for the passenger seated behind the front passenger, deflections will be greater on the left side of the thorax.

The system was found to track the belt position at peak load rather well. When the belt was close to the neck, the RibEye/ potentiometer ratio was greater than unity and progressively dropped in magnitude from the upper ribs down to the lower ribs. However, as the belt moved away from the neck and towards the middle of the shoulder, the normalized ratio for the lower ribs approached unity and was more evenly distributed from top to bottom. The sample contained only one vehicle model where the belt was clearly draped at the extremity of the shoulder. It was not possible therefore to draw any conclusion from this test since the lap belt penetrated the dummy abdomen.

Interference with the potentiometer resulted in data loss during the initial trials of the system. However the problem was rectified with a slight adjustment of the sensors. Data loss was also observed to occur occasionally in more severe test conditions with the lower rib channels. The data loss was likely related to the upward displacement of the abdominal insert.

Kinematic Analysis & Chest Deflection

Removal of the rear doors made it possible to obtain a full lateral view of the dummies as they engaged the seat cushion and restraint system in the rear seats. Generally the motion of the ATD's can be described as:

a) Translation of the upper body and pelvis with minimal vertical motion; or

b) Rotation of the upper body about the lap belt with large vertical displacement into the seat cushion.

The initial loading phase of the lumbar spine force appears to be a good indicator of these motions as each of these kinematic behaviors is associated with a distinctive time history trace. Figure 7 displays sample time history traces of the lumbar spine force in the vertical axis for three different vehicle seats associated with this motion. In the case of translation the vertical lumbar spine is in compression, early in the event as the pelvis and thighs of the dummy rapidly engage the seat cushion and belt. Extension of the spine follows during rebound resulting in a clean sinusoidal trace. Figure 8 displays samples of time history traces for lumbar spine forces for four different vehicle seats wherein rotation was the principal motion. In these examples the lumbar spine is in extension at the onset of the loading phase. Observation of the videos suggests that this initial extension is characterized by a forward ramping of the pelvis; the dummy has less contact with the seat cushion and almost appears to become airborne in some cases. This motion early in the event contributes to spring-like oscillations of the dummy. The seatbelt and seat are discordant and there is substantially more out of plane motion than in the cases where translation is the predominant motion. Consequently, there is a greater tendency of lap belt migration into the abdominal cavity and greater opportunity for the head to strike the surrounding structure. The lumbar spine force response is dependant on seat and restraint system but does not appear to be affected by test severity.

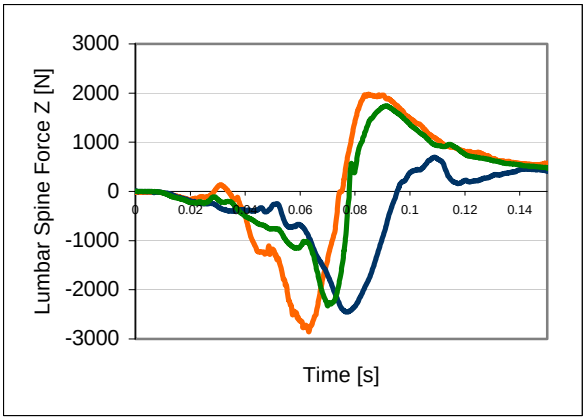

Figure 7: Time history traces of lumbar forces in dummies characterized by a translational motion in rear seats.

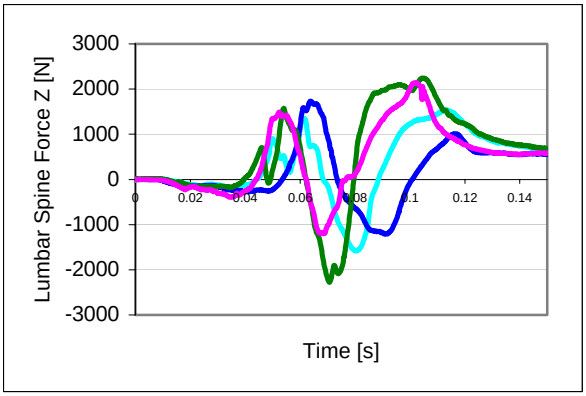

Figure 8: Time history traces of lumbar forces in dummies characterized by a rotational motion in rear seats.

The lumbar force time history may also be used to qualify, or explain the chest deflection measured at the potentiometer. The example shown in Figure 9 illustrates the interaction that occurs between chest deflection and the dummy kinematics. The time history traces presented are from a 56km/h test where the ATD was in the right front passenger seat. The chest deflection stops and remains constant at the moment that tension in the lumbar spine is released. There is no further deflection because the dummy is sliding downward into the seat. While this kinematic timing may be effective in reducing chest deflection, the risk of lap belt intrusion into the abdominal cavity may be increased.

Figure 10 illustrates the relationship between the lumbar spine forces and chest deflections at 48km/h and 56 km/h in the same vehicle model. As speed is increased the character of the traces remains unchanged but the magnitude is amplified. In this case the vertical force does not explain the observed difference in deflection.

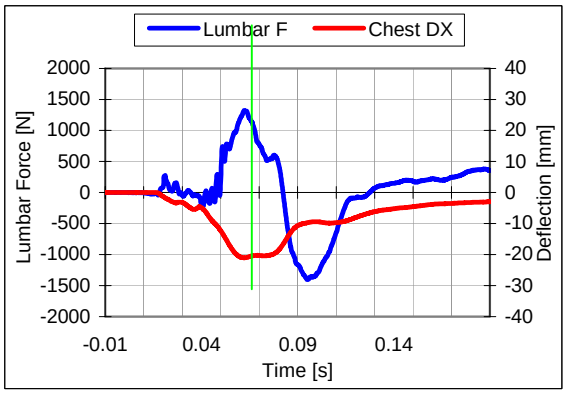

Figure 9: Time history trace of lumbar force and chest deflection for the front right passenger with seatbelt and airbag in a 56km/h FFRB test.

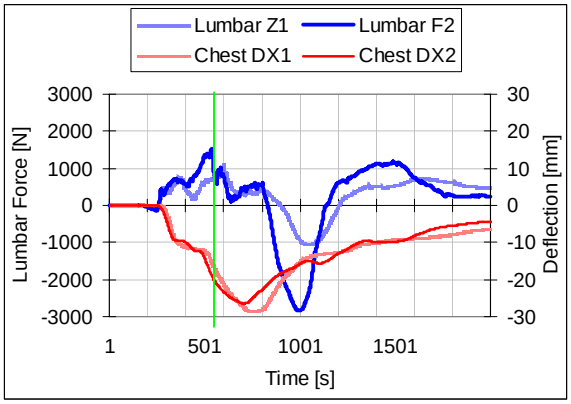

Figure 10: Time history trace of lumbar vertical force and chest deflection for the driver with belt /airbag in a 48 & 56km/h FFRB test.

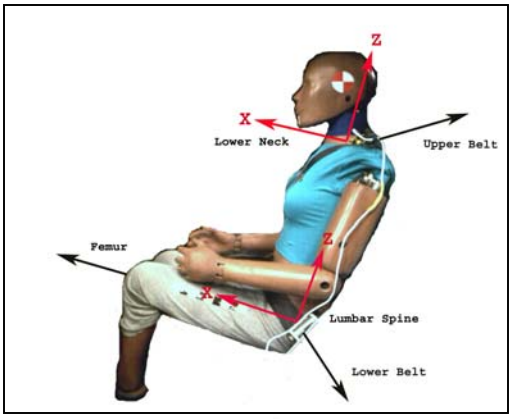

Figure 11: Free body diagram of forces included in the calculations.

Load Management

Comparison of dummy responses can be quite complex to carry out particularly when the dummies are in different vehicles, seat positions and exposed to different test speeds. Ideally, a comparison of the load distribution between the dummy and the restraint system could help quantify the energy management capabilities of a particular restraint system. Furthermore, qualification of load paths could help explain why deflection does not necessarily increase with increasing test speeds.

The individual force channels for the neck, pelvis, femurs, and lap and shoulder belt were integrated in time and summed as a function of time to provide an estimate of the total impulse in time. Figure 11 shows a free body diagram of the forces. Since this was a preliminary investigation calculations were restricted to two dimensions F_x and F_z. Comparisons were conducted with two FTSS 5th percentile Hybrid III dummies. The equations used for the calculations are presented in the Appendix.

Four separate comparisons will be presented as follows:

1. 2 drivers, 2 vehicle models;
2. Driver & passenger same vehicle crash;
3. Right front & right rear passengers same vehicle crash.
4. 2 drivers, same vehicle model two test speeds

The first sample includes a comparison of two dummies seated in the driver seat of two vehicles undergoing a FFRB test at 48 km/h. The dummies were each restrained by a seatbelt and an airbag. Figure 12 displays the loads on the belt in the solid color and the loads on the dummy in the shaded color. The test labeled as A and colored blue, indicates that more force was exerted on the dummy

than on the belt. In fact, the shoulder belt force, which was 3.5 kN for the driver was relatively low given that the chest was compressed to 38 mm. The driver clearly had femur contact with the knee bolsters since the femur loads were of the order of 4 kN in this test. In contrast, the belt forces for test B shown in red were significantly greater than the sum of the forces on the dummy. The dummy experienced very little load application. The seatbelt in this vehicle seems to have provided better energy management.

In the next plot, Figure 13 shows that the difference in chest deflections was 11 mm and that the chest in test A in blue was loaded more rapidly, more abruptly than in test B. In Figure 14, the third and final plot of the comparison, the two chest acceleration traces are overlaid, the blue trace or test A displays a more rapid drop and is noisier than the red trace of test B but the chest clips are equal. Overall the plots suggest that the restraint system in test B offered better chest protection.

The second sample is a comparison of a dummy in the driver seat and a dummy in the right front passenger seat of the same vehicle in a 56km/h FFRB test. Both dummies were restrained with the seatbelt and the airbag.

In Figure 15 the loads on the driver shown in shaded red are greater than the loads on the belt (solid red). The loads on the driver rose much more rapidly and were greater than the sum of the loads on the passenger shown in the shaded blue. The loads on the passenger belt shown by the solid blue trace were much greater than the loads on the passenger. The passenger therefore, appears to have exerted more force on the belt than the driver. The driver left femur load was above 8kN, the lumbar spine force was 3kN while the axial tension in the neck for the driver was above 2kN (N_{te} of 0.98) in this test, hence with such large loads transmitted above and below the chest it is not surprising to see that the chest was by-passed altogether.

Deflection for the driver, shown in red in Figure 16 was only 19 mm while for the passenger the chest deflection, shown in blue was 26 mm. Figure 17 displays the time history trace for the chest acceleration in red for the driver and in blue for the passenger. The onset of chest acceleration for both dummies were equal, however, beyond the initial peak the responses were quite different. The chest clip did not reflect the differences observed in the acceleration responses between the driver and passenger nor did they provide any indication that the load paths were away from the chest for driver and involved the chest for the passenger.

The third sample is a comparison of a dummy seated in the right front passenger seat with a dummy seated in the rear right passenger seat of a vehicle that underwent a FFRB test at 40 km/h. The front seat passenger is restrained with a seatbelt and airbag and the rear dummy is belted only.

Figure 18 illustrates the loads transmitted to the front passenger dummy in blue and the rear passenger dummy in red. Both belt load curves were well above the two dummy load curves. The sum of the dummy forces was slightly greater for the rear passenger but both dummy traces displayed a similar trend. This particular vehicle has firm seats and good belt geometry. The lumbar spine vertical forces for both the front and rear dummy are in compression early in the loading phase and there is good engagement between the pelvis and the seat cushion. The video analysis suggests a controlled deceleration of the dummies.

The deflections are shown in Figure 19. With the exception of the pretensioner response observed in the blue trace for the front passenger the shape of the traces were very similar. Deflection for the rear seat passenger shown in red was greater than for the front seat passenger seat by approximately 7 mm.

Figure 20 displays the chest acceleration traces, the pretensioner and load limiting effects of the front seatbelt shown in blue, cause a more gradual deceleration of the chest. Though the difference in chest clip is only 5g, the rear occupant is decelerated more rapidly and without interruption.

The final sample is a comparison of two dummies seated in the driver seats of two identical vehicle models tested in a 48 km/h and 56km/h FFRB crash. The blue traces represent the 48km/h test while the red trace represents the 56km/h test in all three graphs. Figure 21 indicates that the belt loads in both tests were comparable during the first 100 ms.. The sum of forces for the dummy was greater in the 56km/h test.

In Figure 22 the peak deflection measured at 56km/h, shown in red, was 26mm compared to 29mm for the 48km/h test. The chest acceleration traces in Figure 23 indicate a more rapid and slightly longer deceleration at 56km/h, yet there is only a 3g difference in chest clip.

While deflections were lower at 56km/h, the sum of impulses on the driver suggest that load paths were redirected to regions other than the chest in the higher severity crash test.

Sample 1

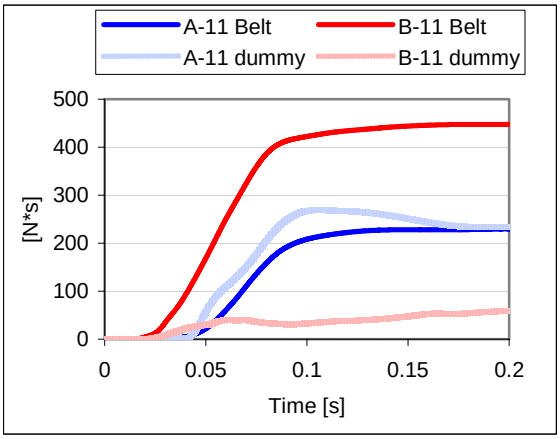

Figure 12: Comparison of load distribution for the dummy and the seatbelt for drivers in two 48km/h FFRB tests.

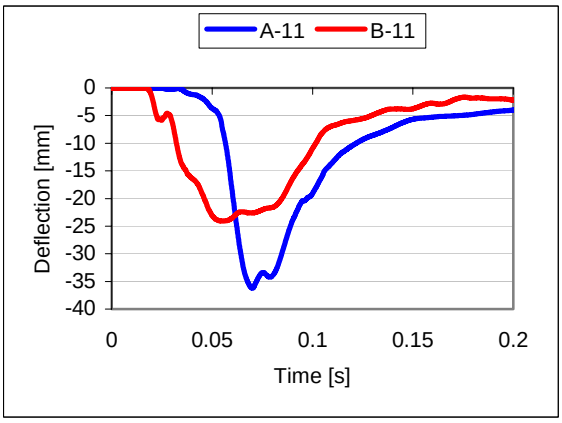

Figure 13: Corresponding chest deflections recorded in the two 48km/h FFRB tests.

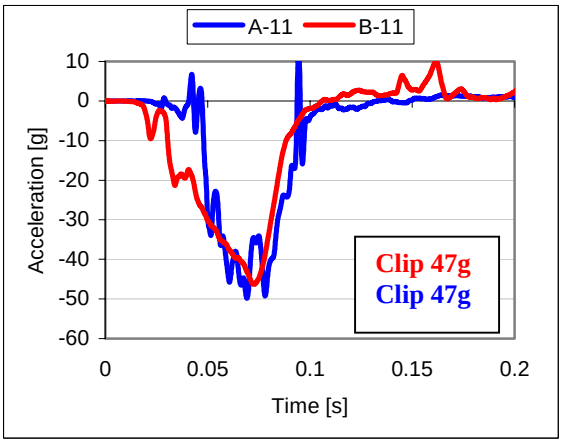

Figure 14: Corresponding chest accelerations recorded in the two 48km/h FFRB tests.

Sample 2

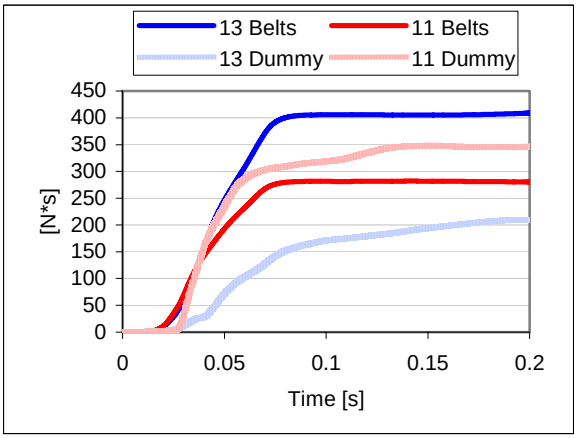

Figure 15: Comparison of load distribution for the dummy and the seatbelt for the driver and front passenger into a 56km/h FFRB test.

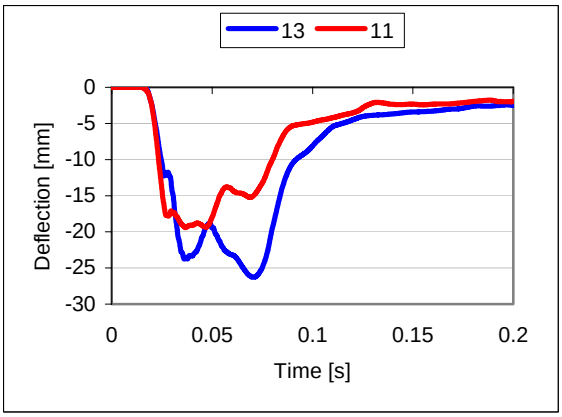

Figure 16: Corresponding chest deflection recorded in the 56km/h FFRB test.

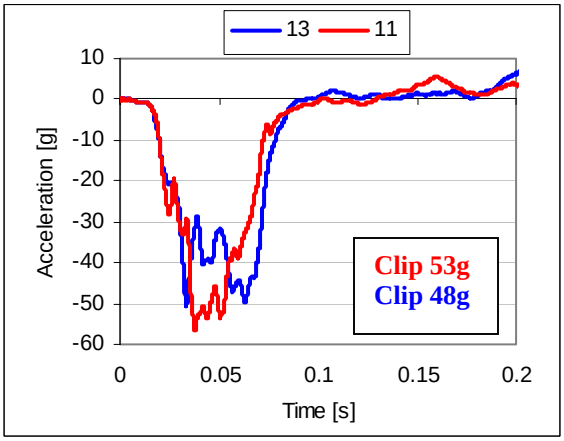

Figure 17: Corresponding chest accelerations recorded in the 56km/h FFRB test.

Sample 3

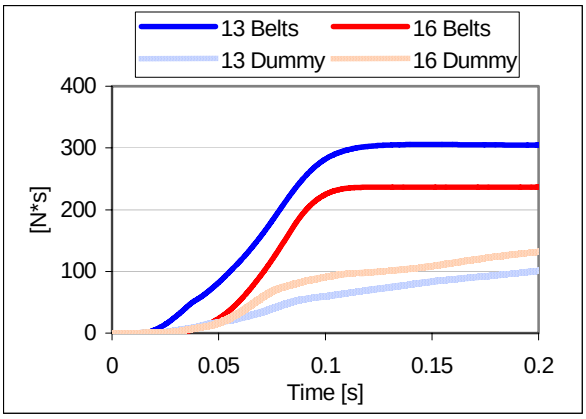

Figure 18: Comparison of load distribution for the dummy and the seatbelt for the right front and rear passenger in a 40km/h FFRB test.

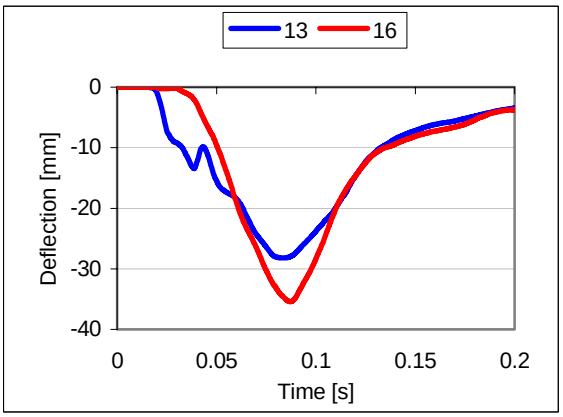

Figure 19: Corresponding chest deflections recorded in the 40km/h FFRB test.

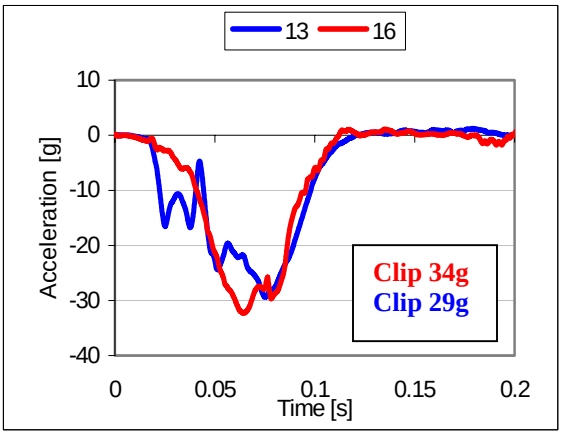

Figure 20: Corresponding chest accelerations recorded in the 40km/h FFRB test.

Sample 4

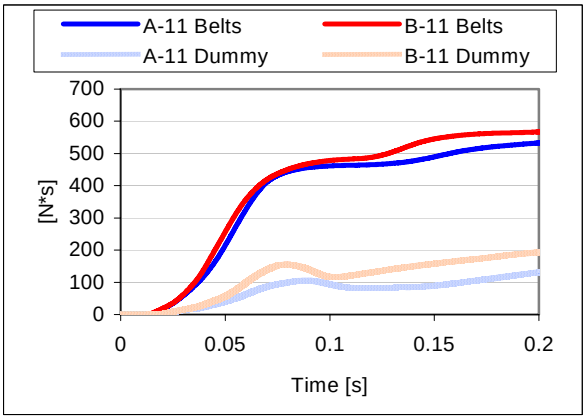

Figure 21: Comparison of load distribution for the dummy and the seatbelt for the drivers in 48km/h and 56km/h FFRB tests.

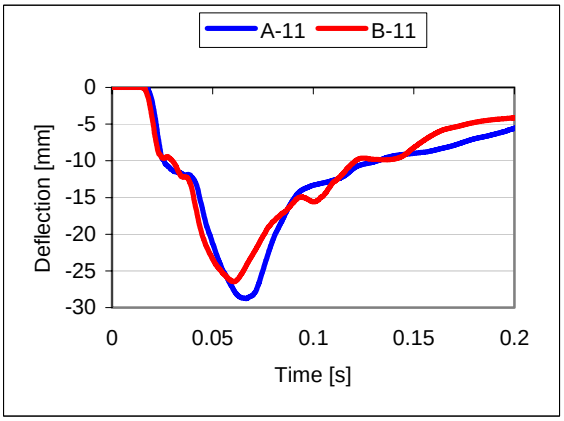

Figure 22: Corresponding chest deflections recorded in the 48km/h and 56km/h FFRB tests.

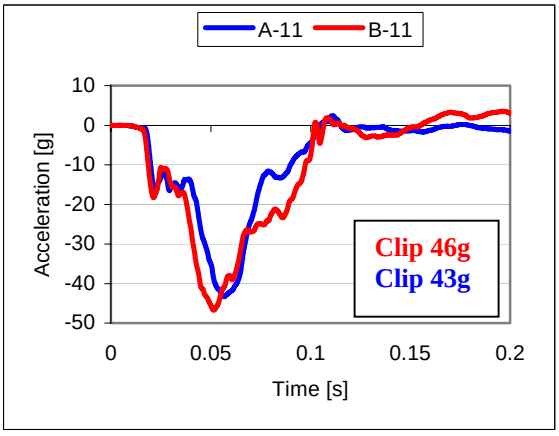

Corresponding chest accelerations recorded in the 48km/h and 56km/h FFRB tests.

DISCUSSION & CONCLUSION

Comparative testing with the Hybrid III 5th female dummy was conducted at 40, 48 and 56km/h to gain a better understanding of the effects of dummy kinematics and load distribution paths. New instrumentation capable of measuring deflection in two dimensions at 12 locations along the ribs of the dummy thorax will greatly facilitate the characterization of the chest response. The preliminary trials carried out in this test series suggest that this system could prove useful in delimiting belt routing on the chest. Asymmetrical loading particularly in more severe test conditions appears to be quantifiable with this system. Further testing under controlled conditions, should be conducted in order to determine where the sensors are best positioned to achieve optimal measurements. While the optical sensors require a clear line of sight, interference due to obstruction does not appear to be a problem unless belt intrusion and abdominal insert displacement occurs.

The lumbar spine force time history trace is a good indicator of seat and restraint performance. Video images confirm that lumbar force compression early in the event is associated with better seat cushion and seatbelt engagement and results in a more controlled deceleration. This signature trace is independent of test speed. Examination of the relationship between lumbar force and chest deflection time history traces can also, in certain vehicle models, help explain an unexpected reduction or increase in chest deflection since it reflects the vertical displacement of the dummy. Though not included in this study, the addition of anterior superior iliac spine load cells could provide a better definition of lap belt interaction with the pelvis and abdomen of the dummy.

The forces at the neck, lumbar spine and femurs were used to estimate the total impulse in time detected by the dummy and the total impulse in time measured in the seatbelt. Based on this exploratory exercise the method appears to offer the possibility of estimating the proportion of impulse from the crash that is directed to the dummy and the proportion transmitted to the belt. Measurements of direct load applications such as force and chest deflection are authoritative indicators of dummy load paths. Global measures such as acceleration clips provide only a snapshot in time and do not adequately describe the severity or duration of the loading event. The identification of load restrictions to key body regions could eventually provide a more comprehensive systems approach to the evaluation of occupant protection systems. Further applications of this method to a larger sample of crashes will be completed to validate the process and establish correlation with existing injury criteria.

ACKNOWLEDMENT

The authors would like to acknowledge Renault, Denton ATD and the staff of PMG Technologies for their assistance in the conduct of this study.

The opinions expressed and conclusions reached are solely the responsibility of the authors and do not necessarily represent the official policy of Transport Canada.

REFERENCES

Canada Gazette Part I Department of Transport, Motor Vehicle Safety Act, Notice of Intent to Amend Section 208, 'Occupant Restraint Systems in Frontal Impact,' of the *Motor Vehicle Safety Regulations*" June 30, 2001, page 2359.

Tylko S., Charlebois, D., Bussières, A., Dalmotas, D., The Effect Of Breast Anthropometry On The Hybrid III 5th Female Chest Response, Stapp Car Crash Journal, *Vol. 50 (November 2006)*

APPENDIX

Impulse calculation equations:

$$pulseZ(t_i) = \sum_{t=0}^{t=0.2}\left[\int_{t}^{t+i} Fz_{neck} + \int_{t}^{t+i} Fz_{lumbar}\right]$$

$$pulseX(t_i) = \sum_{t=0}^{t=0.2}\left[\int_{t}^{t+i} Fx_{neck} + \int_{t}^{t+i} Fx_{lumbar} \int_{t}^{t+i} F_{femur}\right]$$

$$pulseDummy(t_i) = \sqrt{pulseX^2 + pulseZ^2}$$

$$pulseBelt(t_i) = \sum_{t=0}^{t=0.2}\left[\int_{t}^{t+i} F_{LAP} + \int_{t}^{t+i} F_{UPPER}\right]$$